# INFORMATION TO USERS

This manuscript has been reproduced from the microfilm master. UMI films the text directly from the original or copy submitted. Thus, some thesis and dissertation copies are in typewriter face, while others may be from any type of computer printer.

**The quality of this reproduction is dependent upon the quality of the copy submitted.** Broken or indistinct print, colored or poor quality illustrations and photographs, print bleedthrough, substandard margins, and improper alignment can adversely affect reproduction.

In the unlikely event that the author did not send UMI a complete manuscript and there are missing pages, these will be noted. Also, if unauthorized copyright material had to be removed, a note will indicate the deletion.

Oversize materials (e.g., maps, drawings, charts) are reproduced by sectioning the original, beginning at the upper left-hand corner and continuing from left to right in equal sections with small overlaps. Each original is also photographed in one exposure and is included in reduced form at the back of the book.

Photographs included in the original manuscript have been reproduced xerographically in this copy. Higher quality 6" x 9" black and white photographic prints are available for any photographs or illustrations appearing in this copy for an additional charge. Contact UMI directly to order.

## UMI®

Root Strength, Colluvial Soil Depth, and Colluvial Transport

on Landslide-Prone Hillslopes

Kevin Michael Schmidt

A dissertation submitted in partial fulfillment of the
requirements for the degree of

Doctor of Philosophy

University of Washington

1999

Program Authorized to Offer Degree:  Department of Geological Sciences

UMI Number: 9944177

Copyright 1999 by
Schmidt, Kevin Michael

**UMI**

In presenting this thesis in partial fulfillment of the requirements for the Doctoral degree at the University of Washington, I agree that the Library shall make its copies freely available for inspection. I further agree that extensive copying of the dissertation is allowable only for scholarly purposes, consistent with "fair use" as prescribed in the U.S. Copyright Law. Requests for copying or reproduction of this dissertation may be referred to UMI Dissertation Services, 300 North Zeeb Road, P.O. Box 1346, Ann Arbor, MI 48106-1346, to whom the author has granted "the right to reproduce and sell (a) copies of the manuscript in microform and/or (b) printed copies of the manuscript made from microform."

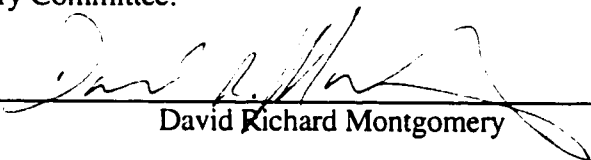Signature _Kevin M Schiff_

Date _August 19, 1999_

University of Washington
Graduate School

This is to certify that I have examined this copy of a doctoral dissertation by
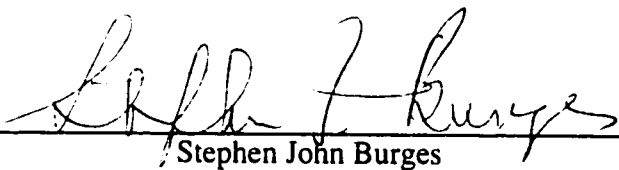
Kevin Michael Schmidt

and have found that it is complete and satisfactory in all respects,
and that any and all revisions required by the final
examining committee have been made.
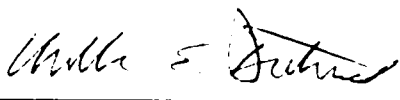
Chair of Supervisory Committee:

David Richard Montgomery

Reading Committee:

Stephen John Burges

William Eric Dietrich

Date: August 19, 1999

University of Washington

Abstract


Root Strength, Colluvial Soil Depth, and Colluvial Transport

on Landslide-Prone Hillslopes


Kevin Michael Schmidt

Chairperson of the Supervisory Committee:

Associate Professor David R. Montgomery

Department of Geological Sciences

I evaluate factors governing shallow-soil, slope stability in forested landscapes by measuring root strength, colluvial soil depth, colluvial soil transport, and topography within the Oregon Coast Range. Cohesive root reinforcement within different vegetation communities was quantified by determining the tensile strength, species, depth, orientation, relative health, and root-area-ratio for all root threads $\geq 1$ mm in diameter. Examination of 41 sites, including soil pits and landslides triggered during 1996, reveals that cohesion values within clear cuts are uniformly $< 10$ kPa, while cohesion values range from $< 2$ kPa in industrial, anthropogenically altered forests with significant understory and deciduous vegetation to over 150 kPa in old growth forests dominated by coniferous vegetation.


Colluvium depth measurements (n = 721) over a 12,400 $m^2$ headwall area range from 0 to > 3m. Near the ridgetop, at small upslope drainage areas, saprolite is preserved (up to 1m thick) and the bedrock surface is characterized by closed depressions (> 2 m deep and 6 m in diameter) filled with colluvium. At large upslope drainage areas colluvium is thin, saprolite is absent, and the bedrock surface is devoid of depressions. I observed no

correspondence between local slope and colluvium depth. Regional geographic-information-system-based, slope stability assessments using measured colluvium depths predict localized areas of potentially unstable ground that are concordant with observed landslide locations.

Differential tilting of 212 piezometer standpipes emplaced to varying depths within a 43° catchment reveals a general inverse relationship between sediment transport rate and below-ground length of standpipe. Measurements made over 860 m$^2$ provide a four to nine year record of surface sediment velocities ranging from 0 to greater than 10 cm yr$^{-1}$ with mean annual volumetric fluxes varying from 20 to 44 cm$^3$cm$^{-1}$ yr$^{-1}$. Bedrock-to-soil production rates inferred through measurements of i) the gradient of the volumetric colluvial transport vector delineate a median production rate of 0.14 mm yr$^{-1}$ and ii) the magnitude of topographic divergence surrounding bedrock outcrops and the coefficient of diffusivity delineate a median production rate of 0.07 mm yr$^{-1}$. No inverse dependence between production rate and depth of colluvial soil cover was discernible.

# TABLE OF CONTENTS

# LIST OF FIGURES

v

# LIST OF TABLES

# LIST OF SYMBOLS

| | |
|---|---|
| $A$ | upslope contributing drainage area |
| $A_b$ | basal area of landslide |
| $A_c$ | area over which creep or slow mass wasting acts |
| $A_l$ | lateral area of landslide headscarp |
| $A_r$ | cross-sectional area of roots |
| $A_s$ | cross-sectional area of soil |
| $A_r / A_s$ | root area ratio |
| $\alpha$ | angle of shear distortion of root thread across a shear zone |
| $\alpha_p$ | inclination of piezometer standpipe relative to a vertical plane |
| $b$ | unit topographic contour width |
| $b_*$ | constant in exponential function of root regrowth ($c_{rrg}$) |
| $\beta$ | convergence angle between the orientation of the hollow axis and the down-gradient orientation of the adjacent side slopes |
| $c$ | cohesion arising from roots and/or soil |
| $c_b$ | cohesion along basal surface of landslide |
| $c_l$ | cohesion along lateral perimeter of landslide |
| $c_r$ | apparent cohesion contributed by root strength |
| $c_{rb}$ | apparent cohesion provided by roots along basal surface of landslide |
| $c_{rd}$ | apparent cohesion provided by decaying roots |
| $c_{rl}$ | apparent cohesion provided by roots along lateral perimeter of landslide |
| $c_{rrg}$ | apparent cohesion provided by post-harvest root regrowth |
| $c_s$ | cohesion contributed by soil |

| | |
|---|---|
| $c_{sb}$ | cohesion provided by soil along basal surface of landslide |
| $c_{sl}$ | cohesion provided by soil along lateral perimeter of landslide |
| $d$ | diameter of root thread |
| $e$ | elevation of the bedrock-colluvium interface |
| $-\partial e/\partial t$ | conversion rate of bedrock to colluvial soil arising from the lowering of the elevation of the bedrock-colluvium interface ( $e$ ) |
| $g$ | gravitational acceleration |
| $\gamma^*(\bar{h})$ | semivariogram function |
| $h$ | saturated portion of colluvium |
| $\bar{h}$ | vector separating points in semivariogram function [ $\gamma^*(\bar{h})$ ] |
| $h_1$ | horizontal displacement length of piezometer standpipe |
| $k$ | constant in root regrowth ( $c_{rrg}$ ) |
| $K$ | coefficient of diffusion |
| $l$ | empirical constant in conversion rate of bedrock to colluvial soil ( $-\partial e/\partial t$ ) |
| $l_h$ | hollow axis length |
| $L_h$ | horizontal displacement of piezometer standpipe |
| $L_s$ | slope parallel displacement of piezometer standpipe |
| $m$ | exponent of upslope drainage area ( $A$ ) |
| $M$ | relative degree of soil saturation |
| $M_c$ | critical proportion of saturated regolith necessary to trigger landsliding |
| $n$ | exponent of ground surface slope ( $S$ ) |
| $P_o$ | empirical constant in conversion rate of bedrock to colluvial soil ( $-\partial e/\partial t$ ) |
| $\rho_r$ | dry bulk density of rock |
| $\rho_s$ | dry bulk density of colluvial soil |

| | |
|---|---|
| $\rho_{ss}$ | saturated soil bulk density |
| $\rho_w$ | bulk density of water |
| $\phi$ | internal friction angle of colluvial soil |
| $q$ | effective steady-state rainfall rate |
| $q_c$ | critical steady-state rainfall necessary to induce landsliding |
| $\bar{q}_m$ | sediment mass transport rate |
| $\bar{q}_s$ | volumetric colluvial transport rate |
| $Q$ | discharge of water through colluvial soil |
| $Q_s$ | sediment transport capacity |
| $Q_{spr}$ | landscape sediment production rate |
| $R_{80}$ | 80% of total cohesion provided by roots less than or equal to $d$ |
| $S$ | ground surface slope |
| $S_{sr}$ | shear strength of soil-root composite |
| $\sigma$ | normal stress arising from weight of landslide mass |
| $t$ | time |
| $t_r$ | tensile strength of root thread per unit area of soil |
| $T$ | depth-integrated, saturated soil transmissivity |
| $T_r$ | tensile strength of root thread |
| $\tau$ | shear stress arising from gravitational weight of landslide mass |
| $\theta$ | ground surface slope |
| $u$ | pore-water pressure |
| $u_*$ | downslope velocity of colluvial soil |
| $z$ | ground surface elevation |
| $\nabla z$ | topographic gradient |

| | |
|---|---|
| $\nabla^2 z$ | topographic curvature |
| $z_s$ | vertical colluvium thickness |
| $z_{sc}$ | critical colluvium depth for landslide initiation |
| $z_{s*}$ | vertical depth below ground surface |
| $\left(\dfrac{\partial z}{\partial t}\right)_{ls}$ | erosion rate arising from sediment transport via landsliding |
| $Z$ | underground length of piezometer standpipe |

# ACKNOWLEDGMENTS

# CHAPTER 1: SEDIMENT PRODUCTION AND TRANSPORT IN STEEP, FORESTED LANDSCAPES

## STATEMENT OF PURPOSE

My objective is to evaluate the magnitude and spatial variability of factors governing shallow-soil, slope stability in forested landscapes. I aim to characterize root strength, colluvial soil depth, topography, and colluvial soil transport rates within landslide-prone hillslopes of the Oregon Coast Range. By using field data in geographic information system (GIS) models linking digital terrain, near-surface hydrology, cohesive root reinforcement, and colluvial soil depth, I seek to refine our ability to determine the location, timing, and processes of landslide generation as well as examine some of the influences of industrial forestry on landslide susceptibility.

## RESEARCH OBJECTIVES

The location of bedrock outcrops and the distribution of soil over a landscape reflects the interaction between topography, biologic activity, hydrology, and material properties. The magnitude and spatial variability of sediment production and transport on hillslopes sets rates of bedrock weathering, slow mass movement, and landsliding. Figure 1.1, a simplified sediment budget, depicts some of the linkages between geomorphic processes and the results of measurements and modeling presented here. In transport-limited environments, colluvial soil produced from the underlying bedrock either i) accumulates *in situ* or ii) transports via slow mass movement. One potential sediment conveyance route to the channel network is solely by slow mass movement, sometimes called "creep", or other diffusive transport processes. For example, soil may be transported by freeze-thaw, rainsplash, bioturbation, or rheologic creep mechanisms from

the hillslopes and into the valley bottoms where fluvial transport processes dominate. Alternatively, landslide processes may transport sediment to the channel network. Once colluvium accumulates to some sufficient depth, either locally or by accretion from upslope, it may be transported into the fluvial system by landsliding. Landslides can significantly control landscape evolution by introducing large volumes of sediment and debris to the channel network, incising into bedrock, and exposing bedrock to subaerial weathering. Landslide initiation, though, is governed by numerous factors including: hydrology (e.g., distribution and magnitude of positive pore pressures), topography (e.g., gradient and curvature), and material properties (e.g., soil depth, cohesive reinforcement from vegetation, and internal angle of friction).

Here I present detailed field measurements motivated by multiple theoretical frameworks to document and evaluate rates of sediment production and transport in the context of shallow-soil slope stability. The research presented spans a broad range of topics related to hillslope sediment transport and landscape evolution. To investigate the influence of cohesive reinforcement provided by vegetation, chapter 2 presents detailed field measurements of root characteristics in different land use types in the context of landsliding. Research presented in chapter 3 discusses the morphology of the ground and bedrock surfaces relative to observed patterns of colluvial soil and saprolite distribution that are thought to reflect the removal of sediment via landsliding and slow mass movement. Field measurements of colluvial soil depth are applied in a GIS to evaluate the influence of soil depth on predicted landslide susceptibility in comparison to mapped landslides. For a transport-limited environment to persist, the rate of colluvial soil production must equal or exceed the rate of slow mass movement. Short-term colluvial soil transport rates, vertical velocity profiles, and sediment fluxes, discussed in chapter 4, are inferred from measurements of differentially displaced piezometer standpipes. Additionally, colluvial soil

production rates and processes responsible for the patterns of observed bedrock outcrops are deduced using two methods in chapter 4.

*Vegetation characteristics and cohesion attributable to root strength*

**Chapter #2**    I quantified cohesion variability attributable to vegetation within landslides and pits to address the following:

a)  the magnitude of spatial variability of cohesion on individual hillslopes and between different vegetation communities;

b)  the relationship between root strength and vegetation condition;

c)  the variability of root strength within industrial forests;

d)  the correlation between simple age classifications derived from the oldest tree in a region and landslide susceptibility;

and

e)  the time period of recovery following forest stand replacement.

I explore the role of cohesion variability provided by roots by documenting root strength in unharvested old growth stands in natural forests, mature second growth stands in industrial forests, recent clear cuts, and recent herbicided clear cuts.

*Soil depth and topographic attributes*

**Chapter #3**    I measured saprolite and colluvial soil depth over a headwall region to address the following:

a)  the spatial variability of colluvial soil depth;

b)  the spatial variability of saprolite;

c) the correlation between colluvium depth and morphologic attributes of the ground and bedrock surfaces;

d) the difference between measured depths and depths predicted with a sediment transport model solely portraying diffusive processes;

e) the topographic attributes specific to regions of inferred landslide-dominated sediment transport;

and

f) the influence of spatially variable colluvial soil thickness on physics-based slope stability predictions.

I use measured colluvial soil depths to gauge the magnitude of possible over-estimation of observed landslide source regions defined by a GIS-driven slope stability model. I compare documented patterns of landsliding with model outputs using assumed, predicted, and field-measured colluvium depths.

*Spatial variation in sediment flux and bedrock-to-soil production rates*

**Chapter #4** I measured the displacement of differentially tilted piezometer standpipes, material bulk densities, and topographic attributes over a headwall region to address the following:

a) the spatial variability of short-term diffusive sediment transport;

b) the relationship between diffusive sediment transport and gradient of the bedrock and ground surfaces;

and

c) the velocity-depth profiles of diffusive sediment transport.

Short-term diffusive sediment transport rates reported here are representative of individual stochastic biologic disturbances and rheologic creep examined over a 4 to 9 year time scale. These measurements are consistent with transport rates characteristic of geologic time scales inferred from radiocarbon dating of basal colluvium.

I also apply a theoretical model approximating the conservation of mass in the continuity equation with measurements of i) the spatial distribution of sediment flux and ii) the distribution of colluvium and bedrock outcrops with respect to the magnitude of topographic divergence to address the following:

a) the spatial variability in bedrock-to-soil production rates;

b) the variation in bedrock-to-soil production rate with overlying colluvium depth; and

c) the distribution of bedrock outcrops with respect to topographic curvature.

As quantitative estimates of the colluvial production rate are few, I compared estimates of the soil production rate and its variability with overlying soil cover with values determined by dating soil with cosmogenic isotopes in the same study area.

STUDY AREA

Extending a research tradition initiated by researchers at the University of California at Berkeley led by Dr. W. E. Dietrich, I selected areas in the Oregon Coast Range to conduct my research (figure 1.2). Research presented in chapter 2 details root strength measurements within different vegetation communities and land use histories in the three open circles represented on figure 1.2. Research presented in chapters 3 and 4, documenting the distribution of soil depth, sediment transport, and bedrock-to-soil production, was conducted on Mettman Ridge northeast of Coos Bay (represented by

asterisk on figure 1.2). Although the measurements and results presented here are specific to the Oregon Coast Range, the interpretations are likely to be applicable to a variety of soil-mantled, forested landscapes.

Numerous prior geomorphic studies have focused on the Oregon Coast Range with research examining fluvial (Beschta, 1978; Dietrich and Dunne, 1978; Beschta, 1984; Seidl and Dietrich, 1992; Personious et al., 1993), hillslope (Swanston and Swanson, 1976; Dietrich and Dunne, 1978; Benda, 1987; Montgomery, 1991; Reneau and Dietrich, 1991; Montgomery, 1994; Anderson et al., 1997; Montgomery et al., 1997; Torres et al., 1998; Heimsath, 1999; Roering et al., 1999), and tectonic processes (Kelsey and Bockheim, 1994; Kelsey et al., 1994). The area is largely underlain by the Eocene Tyee formation that is characterized by arkosic, feldspathic and micaceous, rhythmically bedded sandstones with mudstone and siltstone interbeds (Snavely et al., 1964; Lovell, 1969). The combination of soil-mantled, steep slopes and heavy winter rains makes this region prone to landsliding. Landslides in shallow soil that mobilize into debris flows act as an important sediment transport link between the hillslopes and alluvial channels (e.g., Swanston and Swanson, 1976; Keller and Swanson, 1979) and can be a dominant landscape forming processes (Dietrich and Dunne, 1978; Seidl and Dietrich, 1992). Through radiocarbon dating of basal colluvial material, Reneau and Dietrich (1991) suggested the landscape may be in a dynamic equilibrium such that colluvial soil in the region is eroding at roughly the same rate as it is being produced from the underlying bedrock. Radiocarbon dating of charcoal at the colluvium/bedrock interface implies the natural frequency of debris flows in this area ranges from thousands to tens of thousands of years (Benda and Dunne, 1987; Reneau and Dietrich, 1991), the influence of industrial

forestry likely increases the frequency (Swanson et al., 1977; Ketcheson and Froehlich, 1978; Gresswell et al., 1979).

Intense industrial forestry combined with landslide-producing storms in 1996 provide the unique opportunity to evaluate the influence of land use practices on landsliding in the Oregon Coast Range (Robison et al., 1997, 1999; Schmidt et al., 1997). Two notable storm sequences in 1996 caused thousands of landslides, loss of human life, and subsequent controversy over land management practices. One storm sequence in February 1996 triggered numerous debris flows in the central and northern portions of the range. According to the Newport, Oregon rain gauge (NOAA/NWS network) the February 6 - 8, 1996 storm produced 212 mm of rain with a maximum daily total of 78 mm. During November 1996, a similar storm hit the southern portion of the range triggering widespread landsliding from Coos Bay east towards Roseburg (figure 1.2). My own rain gauge measurements document that the storm of November 16 - 18, 1996 in the Coos Bay area produced 225 mm of rain with a maximum 24-hr total exceeding 150 mm.

As the regolith in the region is predominantly a friction-dominated, cohesionless material (Yee and Harr, 1977; Schroeder and Alto, 1983; Burroughs, 1985; Wu et al., 1988b), any loss of cohesion caused by the decay of roots likely influences slope stability. In response to the 1996 landslide-producing storms, I quantified root strength within hand-dug pits and landslide headscarps to investigate cohesive root reinforcement in various vegetation communities. Working in the same region, the Oregon Department of Forestry (ODF) also instigated ground-based, field surveys over 145 mi (233 km) of channel length documenting over 550 landslides in a 46 mi$^2$ (120 km$^2$) area composed primarily of industrial forest lands (Robison et al. 1997, 1999). The objective of the research by

Robison et al. was to evaluate the influence of commercial forest practices on landslide frequency. One particular result of the ODF research was that in some areas roughly equal numbers of landslides initiated from clear cuts less than nine years old and industrial forests. In other areas, Robison et al. report that clear cuts expressed an average landslide density 5.4 times that detected in more mature industrial forests. As only small parcels of old growth forest remain in the region, it is difficult to determine the geologic background rate of landsliding from equivalent topography in different land use types. Robison et al. (1997, 1999) did not make any quantitative measurements of the roots exposed in landslide headscarps; instead they simply noted the presence of roots or lack thereof, and the dominant vegetation types.

## BACKGROUND RESEARCH

I build upon a wide range of published research that identified some of the variables governing hillslope morphology, diffusive sediment transport, mass wasting via landsliding, cohesive reinforcement provided by roots, and the influence of land use on sediment transport.

*Factors governing shallow-soil slope stability*

It has long been recognized that highly-mobile, fast-moving (up to 60 km/hr) landslides termed debris flows (slurries of soil, rock, vegetation, and water) (Varnes, 1978) occur during high intensity storms or periods of prolonged rainfall (Caine, 1980; Cannon, 1988). Subsurface flow governs the spatial extent of saturated areas, which in turn affects the runoff distribution and magnitude of positive pore-water pressures (Dunne and Black, 1970; Dunne et al., 1975). Hollows, sites of topographic convergence at the upslope tip of channel networks, focus both sediment and subsurface water flow and are thus preferential sites of debris flow initiation (Hack and Goodlett, 1960; Hack, 1965; Johnson and Rahn,

1970; Campbell, 1975; Reneau and Dietrich, 1987). Relative slope stability over a hillslope, though, is a function of topography, colluvium thickness, hydraulic conductivity, subsurface flow orientation, presence of macropores or bedrock fracture flow, and the material strength arising from the internal friction angle of the colluvium as well as cohesion attributable to the colluvial soil and root strength. The infinite slope model, a one-dimensional analysis of a slice on the sides of which the stresses are assumed as being equal and opposite in direction and magnitude (e.g., Selby, 1993) simplifies the above factors in the following expression:

$$\rho_{ss}gz_s \sin\theta\cos\theta = c_s + c_r + (\rho_{ss} - \rho_w M)gz_s \cos^2\theta\tan\phi \qquad (1.1)$$

in which $\rho_{ss}$ is the saturated soil bulk density, $g$ is gravitational acceleration, $z_s$ is the vertical colluvium thickness, $\theta$ is the hillslope angle, $c_s$ is the soil cohesion, $c_r$ is the apparent cohesion contributed by root strength, $\rho_w$ is the density of water, $M$ is the relative degree of saturation within the soil, and $\phi$ is internal friction angle of the soil. The term to the left represents the driving stress while the terms on the right hand side of equation represent the resisting stresses. Seepage is presumed to be slope parallel and the pore pressure term, $M$, links the slope stability of equation 1.1 with hillslope hydrology and regolith depth such that:

$$M = h/z_s \qquad (1.2)$$

where $h$ is the saturated portion of colluvium. Increased pore-water pressures within the soil mantle subsequently cause a reduction of the effective normal resisting stresses within

the material. Hence, all else being equal, regions on a hillslope with large $M$ values are more prone to landsliding.

Most estimates of the likelihood of landsliding require *a priori* knowledge or assumptions regarding such factors as the hydrologic response to rainfall ($M$), cohesion attributable to root strength ($c_r$), and soil depth ($z_s$). Numerous approaches define landslide susceptibility based on multivariate correlations between mapped landslides and physical attributes (Neuland, 1976; Carrara et al., 1977; 1982; 1991; Carrara, 1983; Mark, 1992). Other analyses define landslide susceptibility based on hillslope morphology, material properties, and geologic structure (Brabb et al., 1972; Campbell, 1975; Hollingsworth and Kovacs, 1981; Seeley and West, 1990; Ellen et al., 1993; Derbyshire et al., 1995). Landslide susceptibility can also be assessed based on empirical relationships between pore-water pressure, rainfall, and soil strength. For example, the U.S. Geological Survey designed a real-time system for issuing landslide warnings in the San Francisco region of California that is built on empirical and theoretical relations between antecedent moisture, rainfall intensity/duration relationships for a storm sequence, and the occurrence of prior observed landsliding (Keefer et al., 1987).

Alternatively, numerous physics-based models exist to characterize hydrologic factors and relative slope stability (e.g., Okimura, 1982, 1983; Okimura and Ichikawa, 1985; Iverson and Major, 1986; Okimura and Nakagawa, 1988; Reid et al., 1988; Reid and Iverson, 1992; Iverson et al, 1997). In particular, Okimura and Ichikawa (1985) and Okimura and Nakagawa (1988) use a grid-based digital elevation model in conjunction with a finite difference model of shallow subsurface flow. Models coupling digital terrain data, near-surface water flow, and slope stability approximations based on variants of equation 1.1 in a GIS generate process-based predictions of the relative landslide potential.

The steady-state hydrologic models of Dietrich et al. (1993) and Montgomery and Dietrich (1994) determine the relative soil saturation based upon modeling concepts originally introduced by Beven and Kirkby (1979), Okimura and Ichikawa (1985), O'Loughlin (1986), and Okimura and Nakagawa (1988). Beven and Kirkby (1979) suggested that patterns of soil saturation could be related to topographic controls such as the ratio of the upslope area drained per unit contour length at a point divided by the local surface gradient. The hydrologic model TOPOG presented by O'Loughlin (1986) builds on this observation to conceptually route subsurface flow through a digital elevation model based on the topographic convexity and upslope drainage area. The critical soil saturation required to generate landsliding is thus a function of the steady-state rainfall, upslope contributing area, local ground surface gradient, soil thickness, soil transmissivity, cohesive reinforcement, and the internal angle of friction. Relative slope stability is typically analyzed for the simplistic case of soils with spatially constant cohesion, thickness, and saturated conductivity. To assess the regional influence of topographic control on shallow landsliding, Montgomery et al. (1998) use a data set of mapped landslides in 14 watersheds covering almost 3000 $km^2$ in the Pacific Northwest. Based on comparisons of mapped landslides with model outputs, Montgomery et al. (1998) conclude the model performed best in steep watersheds underlain by shallow bedrock while the poorest model performance was generally located in low-gradient watersheds underlain by glacial deposits.

Relative slope stability is also a function of the prior anthropogenic activities in a region. Increased landslide frequency, for example, is commonly attributed to the removal of vegetation (Swanson et al., 1977; Gresswell et al., 1979; Wu et al., 1979; Sidle, 1992; De Rose et al., 1993). In the western Cascade Range of Oregon landslide frequency in clear cuts was increased by a factor of 2.8 over forested areas (Swanson and Dyrnesss, 1975),

presumably resulting from vegetation removal. Numerous studies examined the relationships between landslide frequency and land use practices in the Mapleton area of the central Oregon Coast Range (figure 1.2) (Swanson et al., 1977; 1981; Ketcheson and Froehlich, 1978; Gresswell et al., 1979; Schmidt et al., 1997). In November 1975, a three-day storm totaling 19.7 cm of rainfall triggered over 250 landslides in a 400-ha area near Mapleton (Swanson et al., 1977; Gresswell et al., 1979). Swanson et al. (1977, 1981) report that the mass erosion rate based on landslide inventories over a 10 to 15 year period in the Mapleton area is 4 times higher in clear cuts than forests. Similarly, Ketcheson and Froelich (1978), also working in the Mapleton area, report an increase of 4 times the mass erosion rate resulting from landslides in clear cuts while research by Gresswell et al. (1979) indicates that for an individual storm the proportion of landslides delivering sediment to channels was over 9 times higher in clear cuts than undisturbed land. For a concise compilation of similar studies documenting increased post-timber harvest rates of landsliding in other regions see Sidle et al. (1985).

Construction of logging roads on steep hillslopes and the subsequent concentration of surface water runoff over relatively impermeable surfaces also leads to increased landslide frequencies (Dyrness, 1967; Swanston and Swanson, 1976; Yee and Harr, 1977; Gresswell et al., 1979; Reid, 1981; Reid et al., 1981; Reid and Dunne, 1984; Montgomery, 1994). From mapping in the Oregon Cascades, Dyrness (1967) concludes that 72% of the landslides identified were associated with roads and that the spatial density of landslides per unit area was 300 times greater along roads than in unharvested forests without roads. In a study examining the Mapleton area in the Oregon Coast Ranges, Swanston et al. (1977) conclude the landslide rate associated with roads is 120 times higher than forests. Gresswell et al. (1979), though, report that the road-related landslide frequency in the Mapleton area is only 7 times higher that the rate from uncut hillslopes. Gresswell et al.

ascribe this relatively low road-related landslide frequency to previous sediment evacuation triggered by an earlier storm and subsequent remediation of road drainage.

The majority of the studies discussed here, concluding increased landslide frequencies following timber harvest, are based on analyses from aerial photographs in different land use types. Pyles and Froehlich (1987) raised the concern that mature forest canopies, characteristic of the Pacific Northwest, may conceal landslides. Hence aerial photograph analyses comparing landslide frequencies of recent clear cuts and mature forest stands may erroneously conclude that clear cuts express higher landslide frequencies because landslides are potentially concealed by forest canopies. The researcher's ability to identify landslides, however, depends on the density of the forest canopy, scale of the aerial photographs, size of the landslide source volume and runout path, the amount of vegetation regrowth since landsliding, and the angle of sunlight illumination. In the Pacific Northwest, field observations indicate that the identification of landslides even in clear cuts is obscured by rapid regrowth (< 5 yrs) of the understory vegetation. Hence, depending on the timing of the photographs relative to the landslides, the number of landslides may be underestimated in both forested and clear-cut lands. Additionally, the effectiveness of leaving uncut trees in steep, topography near the drainage divide of a watershed ("headwall leave area") on reducing landslide frequency has also been questioned. Skaugset et al., (1993) and Martin et al, (1996) proposed that landslide frequencies from clear cut and forested headwalls are statistically equivalent. These "headwall leave area" studies, however, are based on extremely small sample sizes where the vegetation density, effective root cohesion, relative health of the trees, or detailed attributes of the topography were not documented. Thus, the effectiveness of headwall leave areas at reducing landslide frequency remains ambiguous.

*Impacts of shallow-soil landsliding*

The impact of landsliding within shallow soil is influential in the socio-political, biological, and geological realms in humid mountainous regions throughout the world. Triggered by severe rainstorms, landslides that transform into debris flows can travel several kilometers from the point of initiation, incorporating downstream material and increasing in volume. Originating on steep slopes, debris flows can impact a significant portion of the channel network and thus pose a significant hazard to life and property. The January 1982 storm in the San Francisco Bay Area of California, for example, initiated 18,000 landslides (principally debris flows) causing 25 fatalities and $66 million in property damage (Ellen et al., 1988). Similarly, Fleming and Taylor (1980) estimate that landslide costs resulting from the winter of 1968 - 1969 in the San Francisco Bay Area totaled about $56 million. The influence of debris flows on loss of life and property are especially caustic where urbanization encroached into steep, landslide-prone landscapes. Heavy rains during November 1996 in the Oregon Coast Range triggered thousands of landslides, damaged roads, and killed six people living adjacent to steep hillslopes.

As landsliding in mountainous landscapes can comprise a significant portion of the local sediment transport (Swanston and Swanson, 1976; Dietrich and Dunne, 1978; Swanson et al., 1982), increased landslide frequencies arising from land use practices may also impact the fluvial system. In the Oregon Coast Range, Seidl and Dietrich (1992) suggested that debris flow scour is instrumental in eroding into bedrock channels. In the same region, Swanson and Lienkaemper (1978) noted that debris flows are important conveyers of woody debris and sediment into high order channels. The hypothesis has been suggested that some river channels may be starved of large woody material and that introduction of debris by landsliding is necessary for rejuvenating or maintaining fish

habitat (Everest and Meehan, 1981; Reeves et al., 1995). The impact on ecology and sediment transport, however, may be an issue of frequency and magnitude such that large volumes of debris arrive in the channel network synchronously in the context of geologic time. Alternatively, sedimentation produced from mass movements can deteriorate downstream water quality as well as aquatic spawning and rearing habitat for both resident and anadromous fish species.

Damage to fish gills caused by high levels of fine suspended sediment induces high mortality levels or alter behavior patterns in fish populations (Cardone and Kelley, 1961; Herbert and Merkens, 1961; Phillips, 1971). An 11 year study of three small watersheds in the Oregon Coast Range by Brown and Krygier (1971) determined that sediment production to channels doubled after road construction (before logging) in one watershed and was tripled after burning and clear-cutting in another watershed. Similarly, an in-stream monitoring program in the Oregon Coast Range by Beschta (1978), recording the response of small watersheds to road building and clear-cutting, demonstrates a significant increase in suspended sediment yields above background values following clear-cutting. Beschta credited the increase in sediment yield to a combination of both road-related and in-unit landslides. Alteration of river channel morphology also occurs in response to increased sediment yields. Building on relationships described by Schumm (1971, 1973), Beschta (1981) documented a change in channel characteristics in response to accelerated mass soil erosion such that increased sediment loads aggraded the channel bed and increased the channel widths.

The response of a landscape to disturbances arising from land use may be used as an analogy for landscape response to climate change, disease, or fire. On a global scale

land use may considerably increase sediment yields. For example, Judson (1981)

estimates that alluvial sediment delivery rates into the oceans increased in response to the

onset of intensive agriculture, grazing, and other human activities from an initial value of 10

billion Mg yr$^{-1}$ to between 25 and 50 billion Mg yr$^{-1}$. Even though deciphering causes of

soil loss is a complicated function of erosion via wind and water, climate, tectonics,

vegetation cover, and anthropogenic influences (e.g., Kirkby, 1980), agricultural practices

are typically thought to accelerate soil erosion rates (e.g., Cumberland, 1947; Loudermilk,

1950; McCaskill, 1973; Dunne et al., 1978; Dudal, 1981; Lal, 1982; Brown and Wolf,

1984; Sidle et al., 1985).


*Vegetation characteristics and cohesion attributable to root strength*

The use of vegetation to stabilize hillslopes can be traced back at least to the Ming

Dynasty of China. Lee (1985) reports that in 1591 an engineer named Pan in China

planted willows to stabilize embankments. Likewise, Záruba and Mencl (1982) describe

accounts of vegetation use to control erosion in Europe during the 1800's. Croft and

Adams (1950) link landsliding to forestry practices, suggesting the loss of root strength in

areas of timber harvest increased landslide frequency in Utah. Numerous studies in the

late 1960's and early 1970's alluded to the destabilizing influence of post-timber harvest

decreases in root strength on rates of landsliding (e.g., Bishop and Stevens, 1964;

Swanston, 1967, 1969, 1970; Gray, 1970, 1973). Bishop and Stevens (1964) determined

that in coastal Alaska the number of landslides increased more than 4.5 times within the 10

years following clear-cut logging. The majority of the subsequent research in the 1970's

attributed post-harvest increases in landslide frequency to measured decreases in root

strength following timber harvest (O'Loughlin, 1974a; Burroughs and Thomas, 1977;

Ziemer and Swanston, 1977). Ziemer and Swanston (1977), studying the root strength of

Western hemlock (*Tsuga heterphylla*) and Sitka spruce (*Picea sitchensis*) in southeast

Alaska, concluded that a 32% loss of strength of the smaller diameter roots occurs rapidly during the first 2 years after cutting. Furthermore, they noted that after 4 years many of the smaller diameter roots had completely decayed and by 10 years post-harvesting even the largest diameter roots lost appreciable strength. In addition, laboratory experiments document that the presence of roots increases the shear strength of a soil (Kassiff and Kopelovitz, 1968; Endo and Tsuruta, 1969; Manbeian, 1973; Waldron, 1977; Waldron and Dakessian, 1981; Waldron and Dakessian, 1982; Waldron et al., 1983). Kassiff and Kopelovitz (1968) report the relative strength provided by roots with ends that are fixed in the soil provide more resistance than roots with un-anchored ends. Furthermore, Kassiff and Kopelovitz (1968), as well as Endo and Tsuruta (1969), established the significant relation that the shear strength of root-reinforced soils increases in proportion to the density or cross-sectional areas of roots within the soil.

Burroughs and Thomas (1977) quantified the root density and the post-timber harvest decline in root strength for two varieties of Douglas-fir: the Coastal Douglas-fir (*Psuedotsuga menziessii*) in the Oregon Coast Range and the Rocky Mountain variety of Douglas-fir (*Psuedotsuga menziessii* var. *glauca*) in central Idaho. They compared roots intersecting a vertical trench midway between trees from old growth Douglas-fir trees (100 to 200 years old) to roots sampled from Douglas-fir stumps within clear cuts ranging from 2 to 111 months in age. The thread strength of individual roots was determined using a specially constructed device that held root ends in place with hydraulic pressure. Although Burroughs and Thomas (1977) examined roots with inside bark diameters ranging from 0.4 mm to 10 cm in the field, their root strength testing device was limited to a maximum diameter of 14.3 mm. A comparison between strength tests conducted by Burroughs and Thomas (1977) in the Oregon Coast Range and O'Loughlin (1974) in British Columbia indicates that the strength of equivalent diameter, live Coast Douglas-fir root threads is

remarkably similar over the Pacific Coast region. Timber harvest, however, alters both the thread strength and the density of roots within a soil. Field measurements by Burroughs and Thomas (1977) in the Oregon Coast Range revealed that the number of roots per area of soil decreased markedly within the first 3 years following timber harvest. Additionally, the tensile strength of the individual root threads decreased rapidly within the first 3 years after cutting. Significantly, Burroughs and Thomas surmise that by 48 months after cutting, a 1 cm diameter root loses 74% of its live strength. From their data indicating a decrease in both the number of small diameter roots and the thread strength, Burroughs and Thomas resolve that roots less than 1 cm in diameter most effectively influence post-timber harvest slope stability. Furthermore, the authors inferred that the rapid decrease in the strength of small diameter roots after cutting is most influential at the lateral edges of the root system where roots from neighboring plants commonly intertwine and co-occupy soil. Where shallow soils overlie relatively impermeable bedrock, intertwining root systems may weave the regolith together, forming a patchwork "quilt" joined at the lateral edges of the root systems. As distal roots decay after cutting, the diameter of individual root networks constricts, resulting in isolated root systems that are separated by regions of reduced root reinforcement.

In landmark papers, Wu (1976) and Wu et al. (1979) quantified hillslope stability in coastal Alaska before and after timber harvest and determined that post-cutting root decay significantly reduced the shear strength of hillslopes. Although Wu measured the strength of individual root threads, monitored pore water pressures, and determined strength properties of the soil through both laboratory and *in situ* tests, the largest contribution was the introduction of a theoretical model to quantify root strength. Independently, Wu (1976) and Waldron (1977) presented analogous models to portray the shear strength of the soil-root system such that the shear strength contribution from roots

is considered as a cohesive reinforcement. The models analyze root reinforcement as a composite material of elastic root fibers with relatively high tensile strength embedded in a soil matrix with a lower tensile strength where frictional resistance to shear is provided by the soil-root contact. Deformation-induced shear is resisted by tension in the root fiber that is resolved into a normal component that increases the confining stress on the shear plane and a shear component that directly resists shear. The models assume that the maximum tensile strength of the root thread is mobilized during failure, requiring that the root ends remain fixed across the shear zone either because they are long enough to be anchored outside the width of the shear zone or that the frictional resistance between the root and the surrounding soil exceeds the tensile strength of the root. Field examination of broken, exposed roots in the shear planes by Wu (1976) support the validity of this assumption.

The theoretical framework offered by these models allows for the calculation of root cohesion solely from measurements of the tensile strength of root threads of varying diameter, the cross-sectional areas occupied by roots and soil, and the angle of internal friction of the soil. The validity of the model is supported with direct shear tests performed by Waldron (1977) on soils reinforced by alfalfa (*Medicago sativa*), barley (*Hordeum vulgare*), and yellow pine (*Pinus ponderosa*) roots. Likewise Wu et al. (1979) defend the conceptual model by comparing laboratory and *in situ* direct shear tests on soils in Alaska reinforced by Sitka spruce (*Picea sitchensis*), Western hemlock (*Tsuga heterophylla*), and yellow cedar (*Chamaecyparis nootkatensis*). Subsequent laboratory experiments by Shewbridge and Sitar (1990) concluded that limit equilibrium methods using only the development of tension in the reinforcements, such as the one described above, are preferable to analyses that do not account for the influence of the reinforcement properties.

I use the model presented by Wu (1976) and Waldron (1977) in chapter 2 to assess detailed measurements of root cohesion mobilized during landsliding in different vegetation communities and land use histories. In addition I collected data regarding species, diameter of broken and intact roots, the depth and orientation of rooting, and the topographic attributes representative of the position on the hillslope. Although studies have documented the tensile strength of individual root threads for coniferous trees (Burroughs and Thomas, 1977; Ziemer and Swanston, 1977; Wu et al., 1979; Commandeur and Pyles, 1991), no research investigates the cumulative strength provided by trees, shrubs, and understory vegetation. Hence I estimate the spatial variation of root strength provided by all roots $\geq 1$ mm diameter within different vegetation communities to address the hypothesis of Burroughs and Thomas (1977) that post-harvest root strength is characterized by isolated root systems of low cohesion.

*Soil depth and topographic attributes*

The distribution of soil over a landscape and the morphology of the landscape itself reflect the processes of soil production and erosion. On steep, soil mantled landscapes the distribution of colluvial soil results from the interplay between slow mass movement, landsliding, and soil production. Although field observations (e.g., Hack and Goodlett, 1960; Hack, 1965) and quantitative modeling (e.g., Dietrich et al., 1995) support the inference that landsliding preferentially occurs in accumulations of thick colluvial soil, measurements of the spatial variation of colluvium depth over a landscape are uncommon.

Noteworthy studies documenting colluvial soil depth are Trustrum and De Rose (1988), De Rose et al. (1991; 1993), and De Rose (1996) in Taranaki, New Zealand. Working in an area underlain by Tertiary silty sandstone that was deforested by European settlers in the late 1800's, Trustrum and De Rose (1988) developed a regolith

chronosequence and determined that regolith depth increased logarithmically with time since landsliding. In an area geomorphically similar to my field area, Trustrum and De Rose (1988) document a correspondence between the regolith depth and topographic curvature such that thick deposits were located in hollows while the interfluves were covered by a thin mantle. In the same study area, De Rose et al. (1991, 1993) recognize that mean regolith depths are inversely correlated with mean profile slope. Also using Taranaki as a field site, De Rose (1996) concludes that the residence times of regolith decrease from greater than 26,000 years on low gradient (< 31°) hillslopes to less than 1000 years on steep hillslopes > 40°.

Examining soil derived from granitic rock in Japan, Okimura (1983, 1989), Iida and Okunishi (1983), and Iida and Tanaka (1997) inferred "potential failure layers" and colluvial soil depth from cone penetrometer data. Data derived from cone penetrometers were used to infer approximate regolith thickness through correlations between the resistance to penetration and dry bulk density. Dry bulk density is a function of the degree of weathering. Hence the works of Okimura (1983; 1989), Iida and Okunishi (1983), and Iida and Tanaka (1997) are not direct measures of regolith thickness but rather represent the distribution of bulk density used to infer regolith depth. Iida and Okunishi (1983) recognize a weak relation between average slope angle and inferred regolith thickness. Okimura (1989), however, presents results that show no clear association between regolith depth and slope gradient or upslope contributing drainage area. In a study written in Japanese, Iida and Tanaka (1997) document that inferred regolith depth is greatest in areas of relatively planar topography.

Reneau and Dietrich (1987), as well as Dunne (1991), discuss the influence of landsliding on patterns of regolith depth over a landscape. That is, the evacuation of

regolith within hollows is usually incomplete and higher landslide frequencies on the lower portions of hillslopes lead to progressive thinning of the regolith with increasing distance from the drainage divide or upslope contributing drainage area. A power function of the upslope drainage area, $A$, and the ground surface slope, $S$, has been used to approximate this relation such that the transport capacity, $Q_s$, is expressed as:

$$Q_s = KA^m S^n \qquad (1.3)$$

where $K$, the diffusion coefficient, is a constant representing the material's resistance to erosion while $m$ and $n$ are widely debated constants that are typically assumed $\geq 0$ (e.g., Kirkby, 1971; Smith and Bretherton, 1972; Seidl and Dietrich, 1992; Howard, 1994). The exponent $m$ represents a discharge-drainage area relation that is weighted by the importance of discharge on transport capacity while $n$ reflects the significance of topographic gradient. Kirkby (1971) reasoned that the transport law of equation 1.3 could successfully represent slow mass movements such as creep, surface wash, and stream transport by varying the exponents $m$ and $n$. Similarly, Smith and Bretherton (1972) use variants of equation 1.3 to conceptually model drainage basin evolution.

Quantitative models of hillslope development (e.g., Culling, 1963; Kirkby, 1971; Howard, 1994) customarily infer rates of sediment transport from ground surface attributes. Building on this research, Dietrich et al. (1995) proposed a soil production model to predict the spatial variation of colluvium based on a mass balance between soil production from the underlying bedrock and the vector divergence of diffusive soil transport. Assuming a linear transport law, the change in the colluvium thickness is related

to the bedrock lowering rate and the local gradient in sediment flux through the continuity equation such that:

$$\frac{\partial(\rho_s z_s)}{\partial t} = \rho_s K \nabla^2 z - \rho_r \frac{\partial e}{\partial t} \qquad (1.4)$$

where $\rho_s$ and $\rho_r$ are the dry bulk densities of colluvial soil and rock, $z$ is the ground surface elevation, $\nabla^2 z$ is the topographic curvature, $e$ is the elevation of the bedrock-colluvium interface, and $t$ is time. The first term in the mass conservation of equation 1.4 is the change in colluvium thickness with time, the second term is the divergence of colluvial transport assuming that sediment transport is driven by linear diffusion, and the last term is the conversion rate of bedrock to colluvium arising from the lowering of the elevation of the bedrock-colluvium interface, $-\partial e/\partial t$. Equation 1.4 thus represents the mass balance of soil thickness variability in response to the dynamic balance between the downslope changes in the rate of sediment transport and the soil production rate. Dietrich et al. (1995) applied the model in a grass and chaparral landscape in coastal California and concluded that model predictions mimic the regolith distribution in the field site: narrow ridges were observed to have the thinnest soils while thick accumulations were observed in the valleys. Furthermore, Dietrich et al. (1995) compared observed landslide locations with distributions of landslide susceptibility using predicted regolith depths. For their coastal California field site, the predicted distributions of instability correlated well with mapped landslide locations.

Recent efforts to apply digital terrain-based models to estimate landslide susceptibility consistently predict areas of apparent equivalent landslide hazard as being much larger than the actual area of instability in a given storm (Carrara et al., 1991; Ellen et

al.. 1993; Montgomery and Dietrich, 1994; Pack and Tarboton, 1997; Montgomery et al., 1998). Studies examining the relationships between observed landslide locations and predictions using variants of the model presented by Montgomery and Dietrich (1994) include: i) Pack and Tarboton (1997) studying landslides in British Columbia, ii) Dietrich and Montgomery (unpublished) analyzing landslides of the Noyo Basin in northern California, and iii) Dietrich and Montgomery (unpublished) examining landslides in the Mettman Ridge area near Coos Bay, Oregon. Results from these studies support the inference that regional, GIS-based models smooth the natural irregularity in actual patterns of landsliding and tend to over-estimate the spatial extent of potential landslide source areas for a given storm. Dietrich et al. (1995), Wu and Sidle (1995), and Montgomery et al. (1997) suggested that spatial variability in such factors as soil depth, root strength, hydraulic conductivity, angle of internal friction, and cohesion can account for why specific sites are more landslide prone. Hence, landslide hazard maps generated from GIS-based models using either assumed or modeled colluvial soil depths identify a large number of potential landslide source regions covering a significant portion of the landscape. Not all sites, though, have sufficient accumulations of colluvium to initiate landsliding; typical landslide-producing storms generate landslides in a small fraction of the hollows in a region.

In chapter 3 I explore the hypothesis submitted by Dietrich et al. (1995), Wu and Sidle (1995), and Montgomery et al. (1997) that spatially variable regolith depth influences patterns of slope stability. I measured high-resolution topography and depths of saprolite and colluvial soil over Mettman Ridge, a landslide-prone headwall (asterisk in figure 1.2). Additionally, I use a variant of the model presented by Dietrich et al. (1993) and Montgomery and Dietrich (1994) to investigate the correlation between colluvium distribution over a landscape and regional GIS-based predictions of slope stability.

Furthermore, if the predictive soil depth model postulated by Dietrich et al. (1995) is accurate, one can hypothesize the potential distribution of soil resulting solely from diffusive sediment transport. Through observations of hillslope sediment transport in my field area over a 7-year period, I propose that diffusive transport processes and landsliding are responsible for the bulk of the sediment transport. If true, the difference between measured soil depths (representative of diffusive and landslide processes) and predicted depths (representative solely of diffusive processes) should provide an approximation of the material removed from the hillslope via landsliding. Measured regolith depths are thus compared to depths predicted from the diffusion-based model presented by Dietrich et al. (1995) to infer a landslide transport rate of the form expressed by equation 1.3.

*Spatial variation in sediment flux rates*

The concept that topography influences rates of sediment transport via slow mass movement is easily traced to early geomorphic research by Davison (1889), Davis (1892), and Gilbert (1909). Davis (1892) suggested that creep rates of soil increase relative to hillslope gradient. On soil-mantled landscapes, Gilbert (1909) hypothesized that the downslope convexity of hillslopes results from slope-dependent transport processes. Where gravity is the sole impetus responsible for sediment transport, hillslopes theoretically increase in steepness with increasing distance from the drainage divide, hence resulting in a convex, one-dimensional profile. The form of a hillslope profile thus depends on the spatial distribution and relative rates of the soil production and sediment transport rates. Quantitative models of hillslope development, presented by Culling (1960, 1963), Scheidegger (1961), and Kirkby (1971), typically presume that sediment flux over a hillslope is linearly proportional to the topographic gradient, $\nabla z$, such that:

$$\bar{q}_s = -K\nabla z \qquad (1.5)$$

in which $\bar{q}_s$ is the volumetric colluvial transport rate. Although field measurements of sediment transport on moderate slopes ($< 0.6$ m m$^{-1}$) are consistent with equation 1.5 (Schumm, 1967; McKean et al., 1993; Granger et al., 1996), documentation of any linear relation between sediment flux and hillslope gradient on steep slopes ($> 0.8$ m m$^{-1}$) is lacking. In addition, recent research proposes that the relation between diffusive sediment transport and topographic gradient may be non-linear over steep hillslopes (Martin and Church, 1997; Roering et al., 1999).

High surface transport rates occur where disturbance is concentrated within the upper portion of the colluvial soil. Such disturbances may originate from temperature changes (freeze-thaw), shrinking and swelling of clays, bioturbation, or soil moisture variations (e.g., Davison, 1889; Davis, 1892; Kirkby, 1967). Davison (1889) attributed transport by creep to an expansion of a sloping soil mass and subsequent deflation of the soil resulting from repeated cycles of freeze-thaw and granular movement at the surface.

Two velocity profiles are commonly associated with diffusive hillslope transport: i) the velocity profile predicted from the theory of Davison (1889), depicting highest transport rate at the surface that decline approximately exponentially with depth below the surface and ii) a modified exponential profile presented by Kirkby (1967). Kirkby (1967) proposed a theoretical model of soil creep, and evaluated the model using laboratory experiments and measured creep rates in Scotland. Kirkby thought the profile suggested by Davison ignores gravitational forces. Adding gravity-driven shear to the exponential velocity profile of Davison, Kirkby (1967) suggests a profile resembling plug flow from the ground surface to an intermediate depth of soil combined with an exponential decline in velocity at greater soil depths. Measured velocity profiles over short time scales, however,

exhibit complex patterns of deformation within the regolith (Young, 1960; Kirkby, 1967; Selby, 1974; Lewis, 1976; Young, 1978; Jahn, 1981; Moeyersons, 1988; Yamada, 1997) that resemble neither the Davison (1889) nor the Kirkby (1967) profiles.

Chapter 4 discusses the results of an opportunistic study evaluating the spatial variation of inferred sediment transport, velocity-depth profiles, and their relation to topographic attributes on Mettman Ridge. Using differentially displaced piezometer standpipes emplaced to varying depths in a steep catchment, I infer sediment flux rates representative of event-based transport over a 4 to 9 year period. Although initially installed to monitor near-surface hydrology, piezometer standpipes were also used as coarse displacement markers. Short-term rates inferred from standpipe displacements are similar to long-term rates determined from dating of basal colluvium by Reneau and Dietrich (1991). The inferred transport rates are used to evaluate the validity of linear slope dependent transport (e.g., equation 1.5) on steep hillslopes.

*Bedrock-to-soil production rates*

Soil production from bedrock is a function of the rates of mechanical, biological, and chemical lowering of the bedrock surface ($-\partial e/\partial t$ in equation 1.4). Mechanical processes loosening pieces of *in situ* bedrock and entraining them into the overlying soil include the biotic influences of burrowing and tree throw while abiotic influences include freeze-thaw, gravity induced shear deformation, and chemical-biological dissolution-induced collapse.

Numerous researchers proposed that the thickness of overlying colluvium influences the rate of bedrock-to-soil conversion (Gilbert, 1877; 1909; Culling, 1963; Young, 1963; Carson and Kirkby, 1972; Young, 1972; Armstrong, 1976; Ahnert, 1977;

1987; Cox, 1980). Gilbert (1877) initially hypothesized that soil production rates from the underlying bedrock should decrease with overlying soil depth as thick deposits act to insulate the bedrock from disturbance. Armstrong (1976) and Ahnert (1977) suggested an exponential relationship represents the decreased efficacy of processes converting rock to soil with increasing soil cover. Alternatively, a "humped" or bell-shaped polynomial function (Gilbert, 1877; Ahnert, 1967; Carson and Kirkby, 1972) can be used to portray a maximum soil production occurring under moderate soil depths. Where mechanical disruption converts rock to soil, a finite soil cover is likely necessary to allow for the burrowing of animals or growth of large tree roots. Under these scenarios, exposed rock produces less soil than areas covered by soil. Similarly, Young (1963) and Culling (1965) proposed hyperbolic relationships for the relationship between soil production and depth of overlying soil cover. Although numerous theoretical models exist to describe the relation between overlying soil thickness and soil production, quantitative measurements are rare. Dietrich et al. (1995) present an approach to infer soil production rates from attributes of the landscape, the relative densities of the soil and rock, and the coefficient of diffusivity. Using the conceptual framework presented by Dietrich et al. (1995), Heimsath et al. (1997) measured *in situ* cosmogenic concentrations in central coastal California and on Mettman Ridge in the Oregon Coast Range (Heimsath, 1999) to examine the variation of colluvium production with overlying colluvium depth.

Motivated by the conceptual framework presented in Dietrich et al. (1995) (equation 1.4), chapter 4 discusses estimations of the bedrock-to-soil conversion rate through measurements of i) the gradient of the volumetric colluvial transport vector inferred from displaced piezometer standpipes and ii) the magnitude of topographic divergence and the coefficient of diffusivity. Contrary to the numerous theories on the relationship between soil production and overlying soil cover, soil thickness appears to

have little influence on rates of soil production on Mettman Ridge. Additionally, I compare

the soil production rates reported here with those determined on Mettman Ridge by

(Heimsath, 1999) through cosmogcnic isotope dating of colluvial deposits.


## SYNOPSIS OF RESULTS

Although it is generally accepted that roots mechanically reinforce hillslopes in

forested landscapes, chapter 2 documents the spatial variability of cohesion within different

vegetation communities. The study sites in the Oregon Coast Range exhibit great spatial

variability of cohesion with values ranging from < 2 kPa in industrial forests with

significant understory and deciduous vegetation to over 150 kPa in unharvested forests

dominated by coniferous vegetation. Cohesion values representative of clear cuts are

uniformly < 10 kPa. Anthropogenic disturbances arising from timber harvesting,

intentional burning, herbiciding, and replanting modify the cohesion furnished by roots

through changes in the species, density, and health of the vegetation. For instance, the

measured strength of live Douglas-fir roots in a commercially thinned forest was reduced

relative to trees not impacted by thinning operations. Moreover, certain industrial forests

express species compositions, cohesion values, and root diameter distributions that more

closely resemble attributes of clear cuts than natural, non-commercial forests.

Mathematical simulations using a topographically driven hydrologic routing model and a

two-dimensional slope stability approximation reveal that the critical proportion of the

saturated regolith and steady-state rainfall necessary to induce landsliding are lower for the

clear-cut sites and commercial forests than for unharvested, natural forests. At particular

sites, the decrease in root strength arising from prior land use persists for at least a decade.

The implications of a disturbance legacy arising from commercial timber harvesting should

be considered when comparing rates of landsliding initiating from forests with different

land use histories to geologic background rates.

The measured distribution of saprolite and colluvium, discussed in chapter 3, is consistent with a process regime shift on Mettman Ridge (asterisk in figure 1.2) such that near the drainage divide sediment transport is infrequent, saprolite is preserved, and the uprooting of trees creates depressions in the bedrock surface 1 to 2 m deep and 6 m in diameter. At large contributing drainage areas, a higher frequency of sediment transport yields homogeneously thin deposits of colluvium, an absence of saprolite, and a relatively smooth bedrock surface. Comparing measured colluvium depths with depths predicted from a diffusion-based model of sediment transport that does not include transport via landsliding reveals an over-estimation of predicted depths in regions of topographic concavity and large contributing drainage areas. A sediment transport power law, determined from topographic attributes at each colluvium depth measurement, was approximated by subtracting measured depths from predicted depths to appraise the thickness of colluvium evacuated from the headwall. The form of the transport law representative of a steep catchment is: $\left(\dfrac{\partial z}{\partial t}\right)_{ls} = 0.08A^{0.5}S^{1}$, where $\left(\dfrac{\partial z}{\partial t}\right)_{ls}$ is expressed in units of m yr$^{-1}$ X 10$^{-4}$ and the constant has units of m$^{-1}$ yr$^{-1}$ X 10$^{-4}$. GIS-based, slope stability assessments using a detailed digital elevation model (< 3 m grid spacing), assumed homogeneous colluvium depths of 1 m, and predicted colluvial soil depths tend to over-estimate the surface area of observed landslide source areas. Similar slope stability assessments using measured soil depths result in predictions of unstable areas that more closely correspond to observed landslides because the topographic influence of landslide potential is modified by site-specific conditions.

Chapter 4 discusses sediment transport rates inferred from differential tilting of 212 polyvinylchloride (PVC) piezometer standpipes emplaced to varying depths within a

steep, colluvium-mantled catchment on Mettman Ridge. Substantial variation of sediment transport exists within a general inverse relationship between downslope sediment transport rate and below-ground length of standpipe. Measurements made over an 860 $m^2$ area provide a four to nine year record of sediment transport estimates resolved through simple trigonometric relations and angular measurements of differentially tilted piezometer standpipes. Transport rates determined by grouping together all 212 standpipes express a high degree of spatial variability, an exponential decline of sediment transport rate with length of below-ground pipe, and surface, downslope sediment transport rates ranging from 0 to greater than 10 cm $yr^{-1}$. Field observations reveal that those sites displaying the highest transport rates are located adjacent to recent bioturbation by mountain beavers. Assuming linear displacement between the piezometer inlet and ground surface, an annual flux rate of 44 $cm^3 cm^{-1} yr^{-1}$ was determined from the integral of mean displacement for all piezometers on the hillslope with non-zero displacement, a value similar to estimates based on longer-term hollow infilling rates. Using a site-specific density-depth function, the corresponding mass transport rate across a unit length of contour is 4.2 tonnes $m^{-1} yr^{-1}$. The exponential form of the velocity-depth profile, expressed by the regional data set, is used to represent the displacement of individual piezometers. The corresponding mean and median annual sediment fluxes are 18.5 and 10.6 $cm^3 cm^{-1} yr^{-1}$, respectively.

Chapter 4 also details estimates of the bedrock-to-colluvium conversion rate on Mettman Ridge are determined through measurements of i) the gradient of the volumetric colluvial transport vector and ii) the magnitude of topographic divergence and the coefficient of diffusivity. Field measurements of differentially displaced piezometer standpipes over a 860 $m^2$ area, representing the spatial variability of the volumetric colluvium flux over a 9 year period, delineate a median bedrock-to-colluvium production rate of 0.14 mm $yr^{-1}$. Mapping of colluvium depth and detailed topographic surveying over

a 12,400 m$^2$ area are used to calculate a median soil production rate of 0.07 mm yr$^{-1}$ for areas of topographic divergence surrounding bedrock outcrops. Topographic curvature and colluvium depth exhibit only a weak inverse relationship on divergent topography. Furthermore, no pronounced dependence between bedrock-to-colluvium production rate and depth of overlying colluvium cover was discernible. Nonetheless, the correspondence between the median colluvium production rates determined here and sediment yields for the same area inferred from bedrock exfoliation rates, hollow infilling rates, and displaced piezometer standpipes suggest the landscape is in an approximate steady state condition.
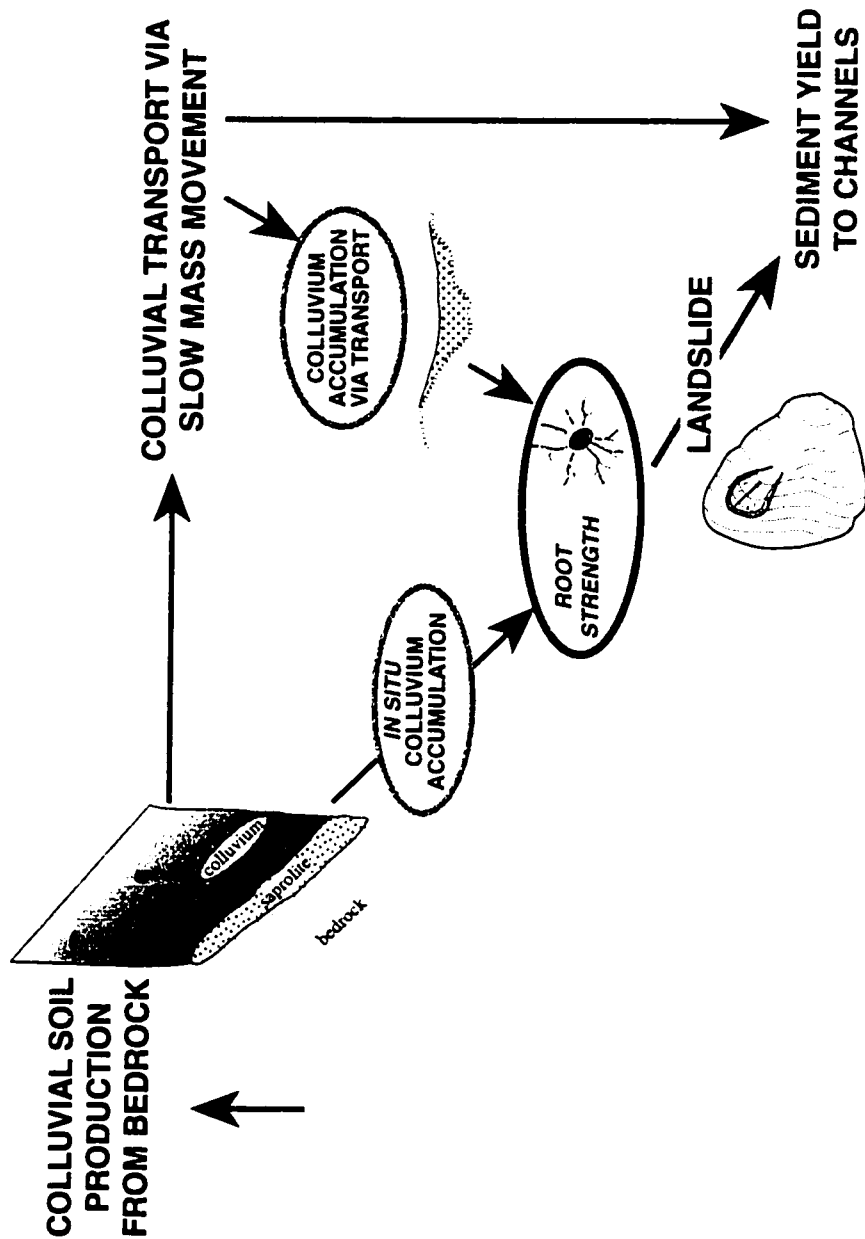
Figure 1.1    Simplified sediment budget depicting relationship between colluvial soil production, sediment transport via slow mass movement, and landsliding. Landsliding is partially governed by low root strength, thick soil depths, or high pore water pressures. Although not explicitly depicted, hydrologic conditions influence the entire simplified sediment budget. For simplicity, the process where transport occurs by gravitational sliding of individual grains over bedrock surfaces is not considered in this discussion as I examine soil-mantled landscapes characteristic of transport-limited environments.

Figure 1.2    Shaded relief map showing study region (open circles and asterisk) in the central Oregon Coast Range where thousands of landslides occurred during winter storms of 1996. The Mapleton District is comprised of federal and private lands, the study area directly northeast of Coos Bay is comprised of the Elliot State Forest (ESF) and private timber land, while the region west of Roseburg is entirely private. The large asterisk represents the Mettman Ridge study area.

Pacific
Ocean

Mapleton

Eugene

44° N

10 km

ESF

Coos
Bay

Roseburg

43° N

124° W

123° W

Oregon Coast Range

Oregon

N

0    200 km
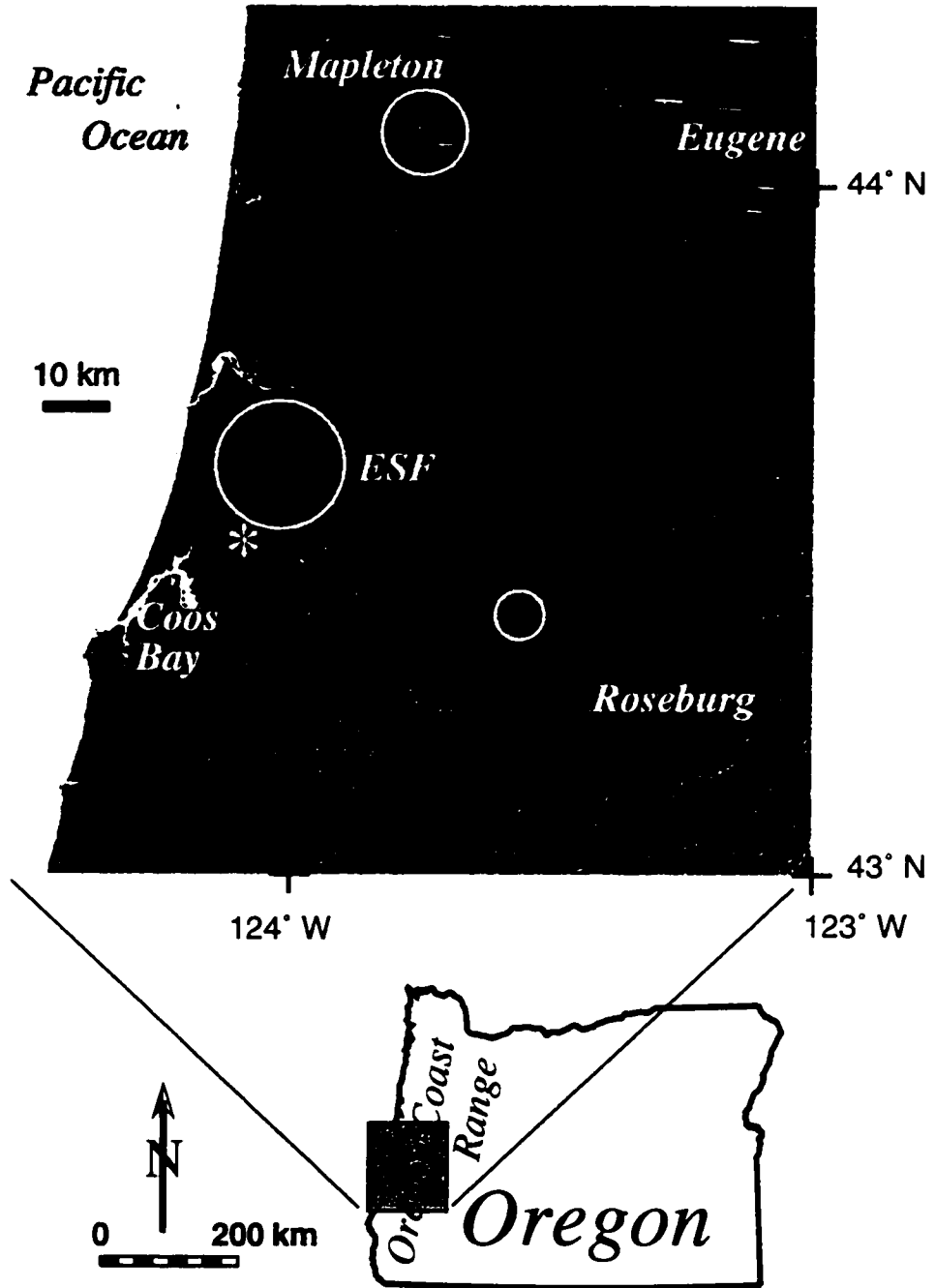
# CHAPTER 2: ROOT STRENGTH VARIABILITY IN FORESTED LANDSCAPES AND SUSCEPTIBILITY TO SHALLOW LANDSLIDING

ABSTRACT

It is generally accepted that roots mechanically reinforce hillslopes in forested landscapes, but the spatial variability of cohesion among and within different vegetation communities (natural forests, industrial forests, and clear cuts) remains relatively undocumented. Determining the influence of roots on landslide susceptibility is extremely pertinent to forest management because landslide frequencies may be sensitive to timber harvesting or post-logging herbicide application intended to eradicate understory vegetation. Anthropogenic influences on the species, density, and health of vegetation arising from timber harvesting, fire, herbiciding, and replanting strongly influence the cohesion furnished by roots. To address the issue of spatial variability in root cohesion, I examined all root threads $\geq 1$ mm in diameter (with bark) exposed within 41 sites including soil pits and headscarps of landslides triggered during large storms in February and November of 1996 in the Oregon Coast Range. I estimate the cohesive strength provided by roots within different vegetation communities by determining the tensile strength, species, depth, orientation, relative health, and the density of roots within an area of colluvium. The region exhibits great spatial variability of cohesion with values ranging from < 2 kPa in industrial forests with significant understory and deciduous vegetation to over 150 kPa in undisturbed forests dominated by coniferous vegetation. Cohesion values representative of clear cuts are uniformly < 10 kPa. Moreover, certain industrial forests express species compositions, cohesion values, and root diameter distributions that more closely resemble attributes of clear cuts than natural forests. Simulations using an idealized hydrologic routing model and a two-dimensional slope stability equation reveal

that the critical proportion of the saturated regolith and steady state rainfall necessary to induce landsliding are lower for the clear cut sites and industrial forests than for unharvested, natural forests. At particular sites, the decrease in root strength arising from prior land use can persist for at least a decade. The implications of this disturbance legacy should be considered when comparing rates of landsliding from industrial forests to geologic background rates. In order to examine the debris flow susceptibility of forests with different land use histories, one must appraise the considerable spatial variability in root strength arising from differing vegetation communities in addition to uniform age classifications.

## INTRODUCTION

Perhaps one of the most striking features of landsliding within shallow soils of forested landscapes is that for any given landslide-producing storm, only a small portion of the potentially unstable areas actually generate landslides. Recent efforts to apply digital terrain-based models to estimate landslide susceptibility consistently predict areas of potential landslide hazard as being much larger than the actual area of instability in a given storm (Carrara et al., 1991; Ellen et al., 1993; Montgomery and Dietrich, 1994; Pack and Tarboton, 1997; Montgomery et al., 1998). Dietrich et al. (1995), Wu and Sidle (1995), and Montgomery et al. (1997) suggested that spatial variability in such factors as soil depth, root strength, hydraulic conductivity, angle of internal friction, and cohesion can account for why specific sites are more prone to landsliding. As vegetation provides an effective cohesion to the soil through the binding action of roots, the magnitude of cohesion can profoundly increase the stability of low-cohesion, granular soils. Hence, variability of effective cohesion across the landscape could significantly alter patterns of landslide susceptibility.

Seemingly uniform forests exhibit considerable variability in patterns of observed landsliding. Landslide susceptibility across a landscape varies substantially with differing topographic controls, hydrologic response, and material resistance. However, the role of spatial variability in effective cohesion is relatively unconstrained in the context of mass wasting assessments. Even though root strength should vary generally with vegetation type, the mosaic of stand density and vegetation composition in forested landscapes reflects the growing conditions and history of disturbance such as tree senescence, fire, climate change, disease, climate, and land use such as grazing or logging (Franklin and Dyrness, 1969). This mosaic is dynamic in time and space with a continual turnover of individuals and species in response to external forcing factors. Furthermore, as the network of roots mirrors the above ground vegetation mosaic, the apparent cohesion provided by roots to the soil is strongly tied to the legacy of the land. It is commonly recognized that forest clearing can increase the frequency of landsliding (e.g., Sidle, et al., 1985) and in the Oregon Coast Range contemporary landslide rates and sediment yields in areas of recent clear-cut timber harvesting exceed pre-industrial rates by at least several fold (Brown and Krygier, 1971; Ketcheson and Froehlich, 1978; Swanson et al., 1981).

To estimate cohesion provided by roots at a specific location *a priori* is complex because a) the growth habits of trees are highly variable, even within one species growing in different environments (Coppin and Richards, 1990), and b) root thread diameter, density, geometry and relative health are highly diverse (Wu, 1995). It is difficult to predict the magnitude of variation of root cohesion over varying length scales because root morphology and distribution reflects both biological mechanisms and their disruption by environmental factors (Deans and Ford, 1983). Furthermore, documented root

distributions and morphologies are highly variable (Bannan, 1940; Smith, 1964; Eis, 1974; McMinn, 1974; Böhm, 1979; Eis, 1987). Thus, cohesion values are typically back-calculated because field measurements are time consuming and regional coverage is difficult to obtain.

Although a range of cohesion values have been determined for different forest communities (e.g., Endo and Tsuruta, 1969; Burroughs and Thomas, 1977; Wu et al., 1979; Ziemer, 1981; Riestenberg and Sovonick-Dunford, 1983), single values are typically adopted for regional slope stability calculations. The adoption of spatially invariant cohesion values may be inappropriate where root distributions vary greatly. If landslides were found to occur in the forest within "gaps" of low root strength or in areas where the root strength declined substantially due to decay as hypothesized by Burroughs and Thomas (1977), this would improve the understanding of why certain portions of the landscape initiate landslides while others remain stable. To constrain the variability of cohesion I quantified the root strength mobilized during landslide initiation and within pits on stable ground to address the following questions:

- Is there a relationship between root strength and average vegetation condition?

- Is the variation within vegetation communities less than the variation between individual communities?

- How variable is root strength within the entity collectively referred to as a "forest"? Moreover, are simple age classifications based on the oldest tree in a region adequate to represent landslide susceptibility?

- How long is the time period of recovery following stand replacement?

- On a regular rotation interval of clear cutting, will industrial forests attain cohesive reinforcement from roots similar to those of old growth forests?

Here I explore the role of variability of cohesion provided by roots in controlling landslide locations by documenting root strength in unharvested old growth stands of natural forests, mature second growth stands in industrial forests, recent clear cuts, and recent clear cuts that were herbicided.

## THEORY AND METHODS

Roots produce an effective or apparent cohesion via root fiber reinforcement that can influence shallow-soil, slope stability. The stabilizing influence of roots to the soil is supported by landslide inventories that note an increase in landslide frequency following vegetation removal (Bishop and Stevens, 1964; Gray and Megahan, 1981), laboratory experiments on rooted, artificially reinforced, and fallow soil (Takahashi, 1968; Endo and Tsuruta, 1969; Waldron, 1977; Waldron and Dakessian, 1981; 1982; Gray and Ohashi, 1983; Waldron et al., 1983; Shewbridge and Sitar, 1989; 1990), slope stability analyses of field data (Swanston, 1970; Burroughs and Thomas, 1977; Ziemer and Swanston, 1977; Riestenberg and Sovonick-Dunford, 1983; Wu et al., 1988a; 1988b; Terwilliger and Waldron, 1991; Riestenberg, 1994) and numerical modeling analyses (Wu et al., 1979; Sidle, 1992; Krogstad, 1995).

Following the work of Endo and Tsuruta (1969), O'Loughlin (1974), and Waldron (1977) I assume that the primary influence of root strength can be expressed as a cohesion term in the Mohr-Coulomb equation where the soil-root composite shear strength, $S_{sr}$, is expressed by:

$$S_{sr} = c_s + c_r + (\sigma - u)\tan\phi \qquad (2.1)$$

such that $c_s$ is the soil cohesion, $c_r$ is the apparent cohesion from root reinforcement, $\sigma$ is the normal stress due to the weight of the soil and water of the sliding mass, $u$ is the soil pore-water pressure, and $\phi$ is the internal friction angle of the regolith uninfluenced by the presence of roots (e.g., Wu, 1995). A forest soil is a composite material consisting of root fibers of relatively high tensile strength and adhesion within a granular matrix of colluvium with a much lower tensile strength. The binding action of roots increases the strength of the soil-root mass by enhancing the confining stress and resistance to sliding (e.g., Waldron, 1977). The root network serves to distribute the local stress by transferring the load to regions of lower stress where tangential forces are carried by friction or by bonding between the fibers and the surrounding matrix. Loss of cohesion occurs when either the bond between root and soil is exceeded and the roots pull out of the soil matrix or by rupture of the root thread in tension or shear.

I quantify the interaction between root threads and the soil matrix using a simple model that considers roots as elements that cross a slip plane perpendicularly. I adopt this procedure for determining the increase in shear strength of the soil due to root reinforcement from Wu (1976), Waldron (1977), and Wu et al. (1979). The limit equilibrium analysis assumes the ultimate thread strength is mobilized. The mobilization of tensile resistance in the fibers translates into a shear strength increase in the soil with a tangential component that directly resists shear and a normal component that increases the confining stress on the shear plane such that:

$$c_r = t_r(\cos\alpha \tan\phi + \sin\alpha) \tag{2.2}$$

where $t_r$ is the average tensile strength of the root thread of a given species per unit area of

soil, and $\alpha$ is the angle of shear distortion across a shear zone (figure 2.1).

The average tensile root strength per unit area of soil, $t_r$, is expressed as:

$$t_r = \sum_{i=1}^{n} T_{ri}(A_r / A_s) \qquad (2.3)$$

where $T_r$ is the tensile strength of an individual root thread (figure 2.1); $A_r / A$ is the root

area ratio or fraction of soil cross-sectional area of soil, $A_s$, with a root of cross-sectional

area $A_r$; and $n$ is the number of roots in area $A_s$. Field measurements of root extraction

force (Anderson et al., 1989) and laboratory analyses on the effects of roots on shearing

resistance (Kassiff and Kopelovitz, 1968; Waldron and Dakessian, 1982; Gray and

Ohashi, 1983) substantiate the premise that extraction force is related to root cross-

sectional area. In addition, Shewbridge and Sitar (1990) recommend the use of limit

equilibrium methods based on the development of tension within the reinforcing fibers

such as the method adopted here. Sensitivity analyses indicate that values of

$\cos\alpha \tan\phi + \sin\alpha$ in equation 2.2 can be approximated as 1.2 for 25 $^\circ< \phi < 40^\circ$ and $40^\circ <$

$\alpha < 70^\circ$ (Wu, 1976 and Wu et al., 1979). Results of Waldron (1977) and Wu et al. (1979)

confirm that $\alpha$ varies at most between 45$^\circ$ and 70$^\circ$ and $\phi$ values for the colluvium in the

study area generally range between 35$^\circ$ to 44$^\circ$ (Yee and Harr, 1977; Schroeder and Alto,

1983; Burroughs, 1985; Wu et al., 1988a). Assuming that the different roots are loaded to

approximately the same stress, equation 2.2 can be modified to determine the total cohesion such that:

$$c_r = 1.2 \sum_{i=1}^{n} T_{ri}(A_{ri} / A_s) \qquad (2.4)$$

Adopting this approach I assume: 1) the tensile strength of the fibers is fully mobilized, not just bond failure between the soil and root; 2) $\phi$ is unaffected by root reinforcement; 3) all roots break simultaneously; 4) roots are perfectly flexible and initially oriented perpendicularly across the shear zone (figure 2.1); 5) increases in cohesion are directly proportional to $A_r / A_s$; and 6) shear deformation is restricted to a narrow zone (figure 2.1). With respect to assumption (1), I include only those roots in landslide headscarps that broke as a result of landsliding, evidence that their strength was fully mobilized. I may, however, overestimate cohesion estimates for pits because I include all root threads intersecting the walls of the pit. Laboratory analyses by Endo and Tsuruta (1969) substantiate assumption (2). During landsliding, it is likely that not all roots in a cross section of soil are loaded to their ultimate tensile strengths simultaneously; I may overestimate root strength in landslides characterized by slow deformations where roots progressively fail. All the landslides I investigated in this study, however, mobilized into debris flows and thus it is likely that most landslides initiated rapidly in response to high intensity rainfall with quasi-synchronous failure of the majority of the root threads. Laboratory tests by Gray and Ohashi (1983) reveal that reinforcing fibers oriented perpendicular to a shear zone provide comparable reinforcement to randomly oriented fibers, supporting assumption (4). Roots aligned parallel to the direction of maximum tensile force receive the largest load and fail first, although when a large amount of multi-

branched root material is present, the applied load causes the soil-root mass to behave as a unit (Coutts, 1983). The results of Gray and Ohashi (1983) indicate that shear strength increases are directly proportional to $A_r / A_s$, while Shewbridge and Sitar (1989) and Jewell and Wroth (1987) argue that the strength increase in reinforced soil is slightly nonlinear. That is, I may overestimate cohesion at sites with high values of $A_r / A_s$. I presume that deformation is restricted to a narrow shear zone (assumption 6 and figure 2.1). Shewbridge and Sitar (1989) determined that shear zone width increases with increased reinforcement concentration, stiffness, or soil bond strength. Within wide shear zones, the shear strains in the soil and the stresses in the reinforcing fibers are decreased. In summary, my cohesion estimates may be overestimated in pits where I quantify strength based on all roots intersecting the pit, not just those that broke as a result of landsliding, and at sites with slow, progressive strain.

Using the procedure outlined above I quantify root strength based on exhaustive field measurements. The resulting estimate of the effective cohesion attributable to root strength is input easily into slope stability analyses and provides systematic results which can be used to assess relative root contributions in different land use types and vegetation conditions. Although more complex root strength models exist, they often require time-consuming excavations to document the branching character of the root network (Wu et al., 1988b). I adopted a relatively simple model as my goal was to document the variability of cohesion over large areas at a great number of sites.

*Field methods*

To obtain field-based estimates of root strength in landslide headscarps and pits, I determined the root area ratio and cumulative root strength for separate species of vegetation. In order to calculate the cohesion specific to individual species, I carried out tensile strength tests for thread diameters up to 6.5 mm for twelve characteristic species in the field area which are listed in table 2.1. I trimmed sample roots from the plant, measured diameters including bark, clamped one end of the roots to a calibrated spring and loaded roots evenly by hand to failure in tension similar to the procedure described in Wu et al. (1979). Spring extension determines the associated tensile force. Regression curves of the strength vs. root diameter data were subsequently used to extrapolate root strength for threads > 6.5 mm in diameter.

I measured characteristics of all roots with diameters $\geq 1$ mm in regions with differing vegetation communities. Field-measured root attributes include: species, depth relative to the ground surface, orientation of root relative to landslide headscarp or pit, whether the root is alive or decaying, and area of colluvium over which roots act. Live and decaying roots were identified based on their color, texture, plasticity, adherence of bark to woody material, and compressibility. For example, live Douglas-fir (*Pseudotsuga menziesii*) roots have a distinctive, crimson-colored inner bark darkening to a brownish red in dead Douglas-fir roots. Both colors are fairly distinctive. Live roots exhibited plastic responses to bending and strong adherence of bark while dead roots displayed brittle responses to bending and poor adherence of bark to the underlying woody material. All dead roots in forested areas and dead understory roots in clear cuts are assumed to have zero cohesion because I do not know when the plant died. Hence, calculated root strengths are conservative on the low side. Supporting this assumption, I measured strengths of

decaying root threads within clear cuts and found that their strength was significantly lower than their ultimate living strength. Because I did not systematically characterize the decay function of all the species in the area, I characterize the strength of conifer roots within clear cuts with the Douglas-fir decay function defined by Burroughs and Thomas (1977). For a discussion on how to calculate decreased root thread strengths based on the time since cutting see the text surrounding equation 2.13 and Burroughs and Thomas (1977).

STUDY AREA

Numerous studies document landsliding of the shallow soil mantle within the Oregon Coast Range (Burroughs and Thomas, 1977; Pierson, 1977; Swanson et al., 1981; Amaranthus et al., 1985; Benda, 1987). Furthermore, research documents that many of these landslides occur during intense rainfall and subsequently mobilize into debris flows (Pierson, 1977; Montgomery et al., 1997). The landscape of the Oregon Coast Range is highly dissected with narrow ridgetops, steep slopes (32 - 47°), and local relief typically less than 1000 m (figure 1.2). Debris flows are a primary sediment transport mechanism in the region over geologic time (Dietrich and Dunne, 1978). The Oregon Coast Range has also been the focus of intense industrial forestry with accelerated landsliding after logging and road construction (e.g., Swanston and Swanson, 1976). The wet, mild maritime climate has a strong coastal influence with mean annual precipitation totals of 1500 to 3000 mm occurring mainly during the winter (Corliss, 1973). This research was motivated by 1996 storms in the Oregon Coast Range that caused thousands of landslides, loss of human life, and subsequent controversy over land management practices. A storm in February 1996 triggered numerous debris flows in the central and northern portions of the coast range, including the Mapleton area in figure 1.2. According to the Newport, Oregon rain gauge (NOAA/NWS network) west of the Mapleton study area, the February

6 - 8, 1996 storm produced 212 mm of rain with a maximum daily total of 78 mm. During

November 1996, a similar storm hit the southern Oregon Coast Range triggering

widespread landsliding from Coos Bay east towards Roseburg (figure 1.2). My own rain

gauge measurements document that the storm of November 16 - 18, 1996 in the Coos Bay

area produced 225 mm of rain with a maximum daily total over 150 mm. As a result of

both these storms, the Oregon Department of Forestry (ODF) initiated ground-based, field

studies to map and characterize over 400 landslides surveyed over 50 $mi^2$ (130 $km^2$)

(Robison et al., 1997; 1999). One particular result of the ODF research was that roughly

equal numbers of landslides initiated from clear cuts and forests. To investigate this

unexpected result, I used the ODF maps to locate landslides in order to quantify root

strength in various vegetation communities.

I examined 41 sites in areas of topographic convergence within three areas depicted

by the open circles in figure 1.2. All sites are underlain by arkosic, feldspathic and

micaceous, rhythmically bedded sandstones with mudstone and siltstone interbeds of the

Eocene Tyee or Flournoy formations (Lovell, 1969). The colluvial soils derived from these

units are nonplastic, gravely sands embodying large sandstone clasts up to 50 cm in

diameter. Continual mixing and downslope transport due to intense bioturbation and tree

throw precludes development of soil structure on these steep hillslopes. The sites are

located within private, state, and federal land exhibiting a wide variety of management

techniques and varying levels of anthropogenic disturbance. I examined landslides

occurring in November 1996 located directly northeast of Coos Bay in the Elliot State

Forest (ESF), in private timber lands northeast of Coos Bay, and in private timber lands

northwest of Roseburg. Farther north in the Mapleton District, a composite of federal and

private lands, I examined landslides triggered during February 1996. I visited landslides

within seven months of each storm, prior to the decay of the small diameter roots and degradation of the landslide headscarps. Measured roots were either in landslide headscarps triggered by storms in 1996, or in pits dug by hand in areas of topographic convergence. My aim was to represent sites in the common vegetation communities of the region.

The "Tsuga heterophylla" vegetation zone, extending from British Columbia south to the Klamath Mountains, delineates once vast stands of Douglas-fir and Coastal Western Hemlock (*Tsuga heterophylla*) and as such is important to timber production (Franklin and Dyrness, 1969). A wide variety of coniferous, hardwood, and understory species exists within this vegetation community. All the coniferous and most of the hardwood vegetation is characterized by a single upright trunk which branches in the upper part to form a crown. In contrast, the understory vegetation can be fairly dense with many well-branched stems within 2 m of the ground surface. In table 2.1 I identify twelve dominant species of conifer, hardwood, and understory vegetation for which I directly measured the strength of individual root threads. Root strength regression curves for an additional sixteen associated species of vegetation were correlated to the dominant species (shown by indented brackets in table 2.1).

Within the larger Tsuga heterophylla zone exist subsets of vegetation communities that form in response to local conditions. My research quantifies cohesion in a wide variety of different vegetation communities with varying density, species composition, and health/condition. I hesitate to label land use categories strictly as a function of stand age because this label can belie a complicated history. Instead I separate sites based on their level of anthropogenic disturbance. Eight categories associated with the style of

measurement and local management-related activities were identified for the 41 study sites (table 2.2): 1) pit in natural forest with trees > 200 years old (n=3), 2) back-calculation of natural forest condition with trees > 200 years old from clear-cut landslide (n=2), 3) blow-down-induced landslide in natural forest with trees > 200 years old (n=2), 4) pit in industrial forest <100 years old thinned approximately 30 years ago (n=2), 5) landslide in industrial forest with varying levels of disturbance: prior clear cutting with planting of seedlings after harvest > 43 years ago, prior clear cutting without subsequent planting > 80 years ago, perfunctory selective thinning in the 1960's, and fire (n=15), 6) pit in clear cut ranging in age from 6 to 11 years (n=8), 7) landslide in clear cut ranging in age from 6 to 10 years (n=8), 8) pit in herbicided clear cut < 4 years old (n=3). The end-member sites of natural or "old growth" forests (categories 1 - 3) were selected to provide a spectrum of root strength within an unharvested, unimpacted forest. Natural forests are dominated typically by Douglas-fir (*Pseudotsuga menziesii*), western hemlock (*Tsuga heterophylla*), vine maple (*Acer circinatum*), and sword fern (*Polystichum munitum*). The diameter at breast height of Douglas-fir trees within categories 1 - 3 typically ranges between 0.5 to 1.5 m. Here I use the term industrial forest (categories 4 and 5) to denote stands of trees in the Mapleton District and Elloit State Forest that are significantly influenced by land management such as: previous timber harvesting, commercial thinning of timber, or intentional use of fire (much of the vicinity was burned in the late 19th Century to flush game and clear land). Industrial forests consisted of a mosaic of conifers (Douglas-fir and western hemlock), hardwoods [Oregon maple (*Acer macrophyllum*) and red alder (*Alnus rubra*)], and understory vegetation. Within category 5, landslides in the commercial lands of the Mapleton District and Elloit State Forest, the mean number of live hardwood trees (primarily red alder and Oregon maple) within 12 m surrounding a landslide headscarp exceeded that of live coniferous trees (Douglas-fir and western hemlock) (table 2.3). The mean number of nearby (i.e., < 12 m) live hardwoods ranges between roughly 3 and 7 trees

per landslide while the number of live coniferous trees is only 1 to 3.5 trees per landslide. The diameter at breast height of live conifers (0.63 - 0.81 m), though, exceeds that of live hardwoods (0.16 - 0.21) for both sites. Clear cuts less than 11 years old (categories 6 - 8) are distinguished by an abundance of understory vegetation, red alder, and planted conifer seedlings. I determined cohesion in landslide source volumes, areas of wind-induced blow down, and in hand-dug pits greater than 1 $m^2$ extending to the colluvium/bedrock interface. All landslides are "in-unit" failures, that is none are directly related to roads.

## RESULTS

Examination of roots emanating from landslide headscarps revealed that the vast majority grow parallel to the ground surface. In response to the relatively steep gradients, roots appear to preferentially orient opposite to the downslope gravitational attraction. The associated tensile or compressive forces may stimulate roots to thicken in the upslope direction and function as anchors. Large taproots extending downward into saprolite and fractured bedrock are absent because roots in moist soils with high groundwater levels spread laterally to form plate or disk-like root masses. The observed lateral roots of plate root systems, which grow close to the ground surface, experience higher bending stresses than highly tapered roots of heart or tap systems, and as a result the root wood of plate systems is stronger (Stokes and Mattheck, 1996). Field observations illustrate that root networks of the twelve dominant species (table 2.1) vary from fine fibrous systems through intricate branched systems and that growth habits of trees and understory vegetation was highly variable, even within one species growing in different environments.

I noted a preponderance of exposed, blunt stubs of broken roots in the exposed walls of recent landslide headscarps (figure 2.2), solid evidence that roots broke prior to

pulling out of soil matrix (also identified by Wu, 1976 and Gray and Leiser, 1982). Blunt ends often protruded up to tens of centimeters from the headscarp face. Wu et al. (1988a) conclude that soil resistance for roots at shallow depths and relatively weak soil is not sufficient to prevent roots from straightening out during soil shear. Therefore, root threads with high tortuousities will straighten prior to snapping, and will therefore result in a length of root jutting out from the headscarp. Furthermore, longer roots mobilize their maximum force at higher displacements than shorter ones because pullout resistance rises with root length until the breaking strength of the root is reached (Waldron and Dakessian, 1981; Ennos, 1990). In highly branched root systems, the ample density of roots per unit area of soil enables tension to be transferred rapidly to the soil via shear before root pull out occurs (Ennos, 1990). In the runout path of the subsequent debris flows, however, I noted that the intact root tendrils are extremely abraded by the passage of debris. Hence roots outside of the landslide source volume attest to an evacuation of soil from around the root network or a pulling out of the roots from the soil matrix.

I generated twelve strength curves characterizing both the primary and secondary vegetation (table 2.1) in the study area (figure 2.3). Thread strength increases with diameter such that second order polynomial regression curves best fit the data. Measurement of root length before and after strength testing reveals that plastic deformation prior to brittle failure produced strains of 5 to 10%. In addition to root diameter, strength variation within a given species may arise from growing environment (Burroughs and Thomas, 1977), growing season (Hathaway and Penny, 1975), or root orientation where those roots growing uphill are stronger than downhill oriented roots (Schietchtl, 1980). These environmental factors engender changes in tracheid length, specific gravity, fibril angle, and cellulose content; all influencing the amount of material

resisting applied stress (Ifju and Kennedy, 1962). Environmental variations are clearly expressed in the case of Douglas-fir subject to varying land-use histories (figure 2.3). Healthy Douglas-fir roots were measured in unharvested, natural forests and in areas of 7 to 8 year old planted seedlings after clear felling. In portions of the ESF the yarding-cable, thinning operations in the 1960's damaged tree canopies and scarred trunk bark. Subsequent fungal infestation appears to have weakened the trees and the roots chronicle this disturbance with lower thread strengths. Because I do not know the spatial extent of the damaged roots resulting from this thinning operation within the ESF, I carried out all analyses using the ultimate (healthy) root strength.

My root thread strengths agree with other studies specific to the Oregon Coast Range. For example, Commandeur and Pyles (1991) report that Douglas-fir roots have an average tensile strength of 17 MPa (tensile load divided by cross-sectional area for a 3 mm diameter root). In comparison, my strength curve produces a tensile strength of 15.3 MPa for a 3 mm diameter thread. Similarly, Burroughs (1985) reports the force required to pull an entire sword fern plant out of a vertical soil face averages 1.7 kPa. Using my measured average density of sword fern roots (650 1 mm threads/m$^2$) and an average radius of 0.5 m for the influence of roots attributable to a single plant, I predict the cohesion attributable to an individual sword fern to be 2 kPa.

Although the majority of colluvium depths in landslide-prone areas range from 0.5 to 1.5 m, average rooting depths are constrained to the upper 0.5 m of regolith (figure 2.4 and table 2.2). Average rooting depths were determined by calculating the arithmetic mean of all the root thread depths at a site. Similarly, roots of deciduous trees in the eastern United States typically extend to depths up to 0.5 m (Stout, 1956; Riestenberg, 1987). The

fact that most roots are within the upper 0.5 m of colluvium highlights the lack of tap roots or deeply penetrating roots in the Oregon Coast Range and reinforces the approximation of a two-dimensional slope stability analysis. The sites with the greatest mean rooting depths are not located in mature forests, but rather in clear cuts dominated by thimbleberry (*Rubus parviflorus*), vine maple, and Oregon maple. Maximum colluvium thickness typically ranges from < 0.5 m on topographic noses to < 3 m in hollows (Pierson, 1977; Montgomery et al., 1997; see also Chapter 3).

*Cohesion and vegetation community*

The root area ratio ( $A_r / A_s$ in equations 2.3 and 2.4) provides a measure of the density of roots within the colluvium. An examination of all the roots, both live and decaying, reveals that values of $A_r / A_s$ are similar throughout the vegetation communities with values ranging from $10^{-4}$ to $10^{-2}$ (figure 2.5A). That is, sites within clear cuts and industrial forests have maximum root densities similar to those of natural forests in this study and values determined in other regions (Riestenberg, 1994; Wu, 1995). In contrast, if only the proportion of live roots is considered, the values of $A_r / A_s$ for clear cuts and industrial forests markedly drop below $10^{-3}$ (figure 2.5B). The significant reduction in values of $A_r / A_s$ for live roots in the clear-cut landslide category indicates a large fraction of decaying roots. As the vast majority of decaying roots in clear cuts are directly linked to nearby stumps, anthropogenic influences actively decrease the density of live roots from that similar to natural forests.

Figure 2.6 depicts the effective cohesion determined from up to thousands of roots per site (table 2.2) in different vegetation communities growing under variable conditions.

All values reported are calculated with equation 2.4 along the lateral boundaries of the

landslide or pit (basal cohesion in the landslide scars was insignificant). Similar to figure

2.5B, clear differences emerge between the eight categories in table 2.2. For instance,

cohesion in herbicided slopes in recent clear cuts are well below 3 kPa, over an order of

magnitude lower than values for natural forests which can exceed 100 kPa (figure 2.6A and

table 2.2). The disturbance of understory vegetation during clear cutting and subsequent

herbiciding suppresses available root strength. While significant overlap in cohesion exists

between sites in clear cuts and industrial forests, the mean and standard deviation of natural

forest sites is distinctly separated from clear cut and industrial forest sites (figure 2.6). The

student t-test reveals that mean values for each category are statistically distinct (confidence

level $\alpha = 0.05$), the industrial forest and clear-cut sites are more closely related than the

natural forest sites and either the clear cut or industrial forest sites. Comparison of

cohesion within natural and industrial forests reveals a discrepancy, with mean values

separated by up to an order of magnitude (table 2.2).

Areas of blow down in natural forests represent sites where destabilization by

increased pore-water pressures is augmented by a lever-arm influence from the length of

falling tree. The wind pressure on trees generated by the bulk aerodynamic resistance of

vegetation on air flow above the plant canopy (Hsi and Nath, 1970) is not considered in my

analyses. The representative cohesion for blow-down induced landslides in natural forests

(mean 25.6 kPa) is relatively lower than values for the natural forest pits; blow-down

induced landslides may preferentially occur in areas of lower than average cohesion. As

the blow down sites are located on the low end of the cohesion distribution of natural

forests, it may be that the trees are weak or distressed. Similarly, field observations of

industrial forests attest to a preferential location of landslides within areas of low cohesion expressed as gaps in the root network (Roering et al., in prep).

In general, my cohesion values are comparable to previously published values, except for the natural forest sites which are considerably higher (mean 99.9 kPa) (tables 2.2 and 2.4). Burroughs and Thomas (1977), in a study also located in the Oregon Coast Range, document a range of cohesions between 7.5 and 17.5 kPa, limited to roots less than 10 mm in diameter. The cohesion values determined by Burroughs and Thomas (1977) may be lower than the actual total cohesion because they limited their investigation to roots < 10 mm in diameter. Even though Burroughs and Thomas (1977) restrict their study to a narrow range of root diameters, their cohesion values remain higher than my mean total cohesion representative of industrial forests.

Cohesion values of old growth sites may overestimate strength because I neglect the pull-out resistance of the soil-root bond. While measurements in headscarps include only those roots broken by the landslide, cohesion estimates in pits include all roots intersecting the plane of the pit wall. For large diameter roots the thread strength may exceed the resistance of the soil-root bond (Stolzy and Barley, 1968; Waldron and Dakessian, 1981) and the full root strength would not mobilize in the event of a landslide. It is difficult to quantify soil-root pull-out resistance over large areas because of the branching, lateral network of roots, presence of root hairs, and interlocking nature of roots from separate plants. Field observations indicate that roots are not straight and smooth, but rather exhibit tortuous growth paths that can be firmly anchored. Moreover, I have field observations in landslide headscparps of broken, live roots up to 122 mm in diameter for Douglas-fir roots, 87 mm for vine maple roots, 69 mm for western hemlock roots, and 42

mm for red alder roots. For comparative purposes, if I assume thread strengths of roots >
30 mm in diameter exceed the soil-root resistance, I limit the contribution of cohesion to
the smaller size fraction of roots. This approach underestimates strength because when
soil shearing causes roots to slip through the soil, they still contribute a reinforcing
increment (Waldron and Dakessian, 1981). Limiting the contribution of strength to the
size class of roots between 1 and 30 mm decreases cohesion in the undisturbed forest pits
from 151.89 to 46.2 kPa, from 94.32 to 42.40 kPa, and does not affect the value of 50.77
kPa from a site with no roots > 20 mm. Even with the imposed diameter bound, values for
natural forests (mean 46.5 kPa) remain substantially above those for industrial forests.

Besides varying between vegetation communities, cohesion is also spatially variable
over distances of only a few meters (figure 2.7). In performing field measurements of the
roots within landslide headscarps, I divided landslide headscarps into polygons of similar
soil depth and a typical length of 2 m. Cohesion for each polygon was determined
separately. Based on the field-defined polygons, industrial forests exhibit widely varying
maximum cohesion values over short distances (up to 80 kPa) with the punctuated, local
cohesion maxima corresponding to anchors provided by conifers or hardwood trees. In
contrast, clear cuts display values uniformly less than 25 kPa with numerous measurements
< 1 kPa. Thimbleberry, possessing an extensive root network, is a primary source of
cohesion in clear cut sites. Values from landslide scars within clear-cuts also stratify
roughly in relation to time since timber harvest (figure 2.7). Consistent with the local
cohesion maxima in clear cuts is the positive correlation between cohesion and time since
harvesting where cohesion values >10 kPa are all located in areas of 9 to 11 year old
regrowth (figure 2.8). It appears as if 5 to 10 years after harvest is necessary for
coniferous and hardwood vegetation to provide cohesions greater than 10 kPa.

The greater source volume perimeters displayed by clear cut sites in figure 2.7 translates to clear-cut landslides having larger landslide source volumes than industrial forests (figure 2.9). If this relation is common to the entire area, sediment yields from clear cuts will be substantially larger than from industrial forests. Curiously, a landslide situated at a cut boundary within an industrial forest has a volume more characteristic of clear cuts than the remainder of the industrial forest landslides (figure 2.9). Previous research, however, indicates that source volumes are generally smaller in grassland and brush than in forests (Selby, 1976; Lehre, 1982; Reneau and Dietrich, 1987).

Factors limiting cohesion are the species of vegetation, density of plants, and diameter of roots. Figure 2.10 associates the contribution of cohesion from individual vegetation strata (i.e., conifer, hardwood, and understory) for each vegetation community. While the component of cohesion contributed by hardwood and understory vegetation is limited to less than 12 kPa, those sites with cohesion values over 15 kPa are dominated by coniferous vegetation (figure 2.10). Furthermore, cohesion in natural forests is dominated by coniferous vegetation while cohesion within industrial forests has a strong contribution from understory and hardwood vegetation. Hence, industrial forestry appears to produce a shift toward a greater proportion of hardwood and understory vegetation, with the Mapleton forest characterized by a large proportion of hardwoods and the ESF having a strong understory component. Cohesion within clear-cut sites has an even smaller component arising from coniferous vegetation, with approximately equal contribution from coniferous and understory vegetation.

Figure 2.11 depicts the relationship between root diameter and total cohesion at measurement sites, and shows that natural forests attain higher cohesion values by having both a higher density of small diameter roots and a greater overall maximum diameter roots to provide strength. For comparison, 1 mm diameter roots alone generate 1 - 7 kPa in natural forests while roots up to 10 mm in diameter are required within clear cuts and industrial forests to attain only 1 kPa. The presence of dead roots is evident in the plateau expressed by curves representing clear-cut landslides; even though large diameter roots are present at a site they provide little additional strength. The summary figure at the base of figure 2.11 represents boundaries encompassing the curves for natural forests, industrial forests, and clear cuts. Notable overlap exists between industrial forest sites and both clear cut and natural forests. Marginal overlap exists between clear cut and natural forest sites.

Averaging sites within a vegetation community, figure 2.12 shows a distinct separation of vegetation communities with mean root diameter and proportion of total measured strength. For example, 80% percent of the total root strength in herbicided clear-cut slopes arises from roots < 5 mm in diameter (figure 2.13). In contrast, 80% percent of the total strength in natural forest pits originates from roots < 65 mm in diameter, an order of magnitude difference between these end members. Similarly, sites of blow down receive a significant proportion of their total strength from larger diameter roots. Curiously, a strong overlap exists between clear cut landslides and industrial forest landslides in the ESF; the site of the 1960's yarding-cable thinning operation. The forests in the Mapleton area exhibit diameters approaching those of natural forests. The industrial, second growth forests in the ESF have lower cohesion values (similar to recent clear cuts) because they have smaller root diameter distributions and a large proportion of understory and hardwood vegetation.

*Slope stability modeling*

To compare the individual measured cohesion values reported above with respect to relative slope stability, I must incorporate site-specific representations of the topography and hydrologic routing. Hydrologic response to a given rain storm and slope stability, though, vary across the landscape in response to topographic curvature, hillslope gradient, and local cohesion. I therefore use field measurements characterizing the local topography to evaluate differences in the observed and predicted root strengths and back-calculated hydrologic conditions at failure.

Shallow-soil slope stability is typically approximated as a one-dimensional problem where apparent cohesion is limited to the unique case of basal anchoring. Numerous researchers, however, recognize that an infinite slope approximation ignores the contribution of roots along the perimeter of a landslide mass (Riestenberg and Sovonick-Dunford, 1983; Wu, 1984a; Burroughs, 1985; Reneau and Dietrich, 1987; Terwilliger and Waldron, 1991). As my own field observations document the majority of roots grow slope parallel with few anchoring into the bedrock surface, I adopt a two-dimensional, limit-equilibrium stability analysis that includes cohesion acting over a basal surface and the lateral perimeter of a landslide source volume. The influences of buttressing and arching on the soil arising from root mats are neglected because I cannot reproduce the pre-landslide configuration of roots within the landslide source volume.

The shear stress, $\tau$, acting over the basal area of the landslide, $A_b$, is represented by:

$$\tau = A_b \rho_{ss} g z_s \sin\theta \cos\theta \qquad (2.5)$$

where $\rho_{ss}$ is the saturated, sediment bulk density, $g$ is gravitational acceleration, $z_s$ is the vertical colluvium thickness, and $\theta$ is the ground surface slope. The resisting force is approximated as:

$$S_{sr} = c_l A_l + c_b A_b + A_b (\rho_{ss} - \rho_w m) g z_s \cos^2\theta \tan\phi \qquad (2.6)$$

where $c_l$ is the sum of the cohesion provided by the soil ($c_{sl}$) and the roots ($c_{rl}$) along the lateral perimeter with lateral area $A_l$, $c_b$ is the basal cohesion comprised of the sum of soil cohesion ($c_{sb}$) and the root cohesion ($c_{rb}$), $\rho_w$ is the bulk density of water, and $M$ is the ratio of the saturated portion of colluvium ($h$) to the total colluvium depth ($z_s$). At a factor of safety of unity (ratio of the resisting to driving forces), $\tau = S_{sr}$ and equations 2.5 and 2.6 are equal. Solving for the critical proportion of saturated regolith necessary to trigger landsliding, $M_c$ yields

$$M_c = \frac{c_l A_l + c_b A_b + A_b \rho_{ss} g z_s \cos^2\theta \tan\phi - A_b \rho_{ss} g z_s \sin\theta \cos\theta}{A_b \rho_w g z_s \cos^2\theta \tan\phi} \qquad (2.7)$$

Gathering similar terms results in:

$$M_c = \frac{c_l A_l + c_b A_b}{A_b \rho_w g z_s \cos^2 \theta \tan \phi} + \frac{\rho_{ss}}{\rho_w} \left( 1 - \frac{\tan \theta}{\tan \phi} \right) \tag{2.8}$$

Values of $M_c$ greater than unity (i.e., $h > z_s$) indicate that pore water pressures exceeding hydrostatic are required to initiate landsliding.

The hydrologic model used here to determine the relative degree of saturation estimates steady-state, shallow subsurface runoff driven by local topographic controls (O'Loughlin, 1986). This model includes variables that are easily measured in the field: upslope drainage area, contour width through which water in the upslope drainage area flows, and the upslope gradient (figure 2.14). Discharge of water, $Q$, through the regolith is:

$$Q = q \frac{A}{b} \tag{2.9}$$

where $q$ is the effective steady-state rainfall rate (rainfall minus evapotranspiration with no leakage into the bedrock) and $\frac{A}{b}$ is the drainage area per unit contour width (figure 2.14). Assuming Darcy flow parallel to the ground surface, the saturated proportion of the regolith at failure, $M_c$, may be expressed as:

$$M_c = \frac{qA}{Tb \sin \theta} \tag{2.10}$$

where $T$ is the depth-integrated, saturated soil transmissivity and $\sin\theta$ is the head gradient driven by the ground surface slope. For more detailed discussions of the model, its assumptions, and performance see Dietrich et al. (1993; 1995), Montgomery and Dietrich (1994), and Montgomery et al. (1998).

Using equations 2.8 and 2.10 to solve for $(q/T)_c$ yields:

$$\left(\frac{q}{T}\right)_c = \frac{b\sin\theta}{A}\left[\frac{c_l A_l + c_b A_b}{A_b \rho_w g z_s \cos^2\theta\tan\phi} + \frac{\rho_{ss}}{\rho_w}\left(1 - \frac{\tan\theta}{\tan\phi}\right)\right] \tag{2.11}$$

The ratio $(q/T)_c$ represents the magnitude of the apparent rain storm, $q$, to the subsurface ability to convey water downslope, $T$ required to initiate landsliding. The larger the $q$ relative to $T$ the more likely the soil is to saturate thus decreasing slope stability. If values of $T$ were constrained through measurements of soil depth and hydraulic conductivity, one could simply solve for the critical steady-state rainfall necessary to induce landsliding, $q_c$. As values of $T$ are unconstrained and likely to vary considerably, I opt to solve for the ratio $(q/T)_c$.

Using site specific field measurements, I solve equation 2.11 for the local hydrologic conditions, $(q/T)_c$, under varying vegetation communities (figure 2.15). All sites are modeled with the following attributes: $\phi = 40°$, $c_{rl}$ is the site specific value plotted in figure 2.6 and table 2.2, $c_{sl} = c_{sb} = 0$, $\rho_w = 1000$ kg/m$^3$, and g = 9.81 m/s$^2$. As my field

observations document negligible basal cohesion arising from roots within landslides $(c_{rb}$

$= 0)$, the term $(c_b A_b)$ is neglected. Internal friction angles for soils derived from Tyee

formation sandstones vary from 35° to 44° (Yee and Harr, 1977; Schroeder and Alto, 1983;

Burroughs, 1985; Wu et al., 1988a) and the soil is cohesionless (Yee and Harr, 1977).

Although $\rho_s$ varies as a function of depth below the ground surface, I use a single value of

$\rho_s = 1600$ kg/m$^3$ to represent the saturated bulk density. The resulting estimation of

hydrologic conditions reveals a threshold of $-\log(\frac{q}{T}) = 3.7$ separates landslides within

clear cuts from industrial forest landslides (figure 2.15). Assuming that the transmissivity

is invariant, low values of $-\log(\frac{q}{T})$ correspond to high steady-state rainfalls necessary to

cause instability while high values of $-\log(\frac{q}{T})$ correspond to low critical steady-state

rainfalls. Thus, clear cut sites are both unconditionally unstable (predicted to be unstable

without rainfall) and susceptible to landsliding under smaller or more frequent storms.

Natural forest sites possess lower values of $-\log(\frac{q}{T})$ and hence require higher rainfall

intensities to initiate landsliding. For comparison, digital terrain modeling in conjunction

with observed landslide locations in British Columbia determined that a value of $-\log(\frac{q}{T})$

$= 3.3$ accounted for 91% of the landslides (Pack and Tarboton, 1997). Studies of the

Noyo Basin in northern California document that 90% of the landslide scars correspond to

$-\log(\frac{q}{T})$ values less than 2.5 (Dietrich and Montgomery, unpublished). Similarly,

Montgomery and Dietrich (1994) determined that a threshold of $-\log(\frac{q}{T}) = 2.5$ accounted

for the 84% of the landslides in the Mettman Ridge area near Coos Bay, Oregon.

Furthermore, Dietrich and Montgomery (unpublished) report a $-\log(\frac{q}{T})$ value of 3.1 for slides triggered by the February 1996 storm in the Oregon Coast Range. Although the above mentioned $-\log(\frac{q}{T})$ values are based on model calculations that neglect cohesion, the values determined here indicate that the threshold $-\log(\frac{q}{T})$ values for landsliding in industrial forests is roughly 2.5 while that for clear-cut landslides is 3.7.

Viewed slightly differently, the critical wetness or the proportion of the saturated regolith required to cause instability in different vegetation communities is positively correlated with local cohesion (figure 2.16). Equation 2.10 predicts that clear cut sites require less than half of the regolith to be saturated to trigger landsliding. In contrast, values of $M_c$ range from 0.01 to 2 for industrial forests and from 2 to almost 30 for natural forests. Thus all clear cut and most industrial forest landslides require the least amount of rainfall, failing under hydrostatic pore pressures, whereas sites in natural forests require pore pressures greater than that attainable by simple saturation of the soil column to trigger landsliding.

The magnitude of available root strength is a key variable determining how close a site is to the threshold of stability. Assuming a cohesionless soil and a factor of safety of unity, the lateral root strength necessary for stability at can be represented as:

$$c_l A_l = A_b g z_s \cos\theta [\rho_{ss} \sin\theta - (\rho_{ss} - \rho_w M)\cos\theta \tan\phi] \tag{2.12}$$

Through the use of equation 2.12 I compare the predicted root force necessary for stability with the measured value (observed cohesion multiplied by area over which roots act) for different vegetation communities (figure 2.17). This approach does not provide unique results because the predicted root forces are based on $-\log(\frac{q}{T})$ values determined from the measured cohesions. This exercise can, however, highlight how close sites are to the threshold of stability. Attribute variables are the same as in figure 2.15 except that I assume identical hydrologic parameters ($-\log(\frac{q}{T}) = 3.1$, a value that best fits the data and is an approximate mean value from figure 2.15; mean $-\log(\frac{q}{T})$ for industrial forest =2.66; clear cut =4.02, all sites =3.34). Overall, the industrial forests better fit the prediction. That is, industrial forests plot closer to threshold of stability represented by the dashed line in figure 2.17. Sites of blow down and natural forests are well within the stable field and are unlikely sites to generate landslides. The industrial forestry site with the poorest fit to the model predictions, is located in the ESF where I first recognized the degrading influence of selective harvesting on Douglas-fir root strength. Clear cut sites plot far from the threshold in the unstable field, with root forces required for stability two to forty-four times the measured root forces. The deviation between strength required and that measured in the field reinforces the interpretation that clear cut slopes are more susceptible to landsliding in response to lower intensity rainfall.

## DISCUSSION

My field data demonstrate both substantial variability in cohesion within a given vegetation community and that cohesion variability between certain communities of vegetation exceeds the variability within vegetation communities. Mean cohesion values for

herbicided slopes and clear cuts, for example, are distinctly lower than natural forests. In addition, the spatial variability of maximum cohesion values along landslide perimeters within clear cuts is a great deal less than within natural and industrial forests. Thus, if debris flows opportunistically exploit gaps in the root network, clear cuts and industrial forests have a greater landslide susceptibility because they posses wider gaps as well as lower overall cohesions. Furthermore, landslides in clear-cuts tend to have larger initial source volumes and thus may trigger long run-out debris flows. This association highlights the importance of well established understory and hardwood vegetation to provide a spatially continuous root mat. Understory vegetation in recent clear cuts (< 11 years old) attain maximum cohesion values of about 10 kPa (figures 2.8, 2.10, and table 2.2), a value that may greatly increase stability. Field observations of reduced cohesion following herbiciding, in conjunction with modeling results by Sidle (1992) indicating that the suppression of understory vegetation drastically reduces slope stability, demonstrate a high likelihood of adverse effects from herbicide application.


Certain industrial forests exhibit cohesion values, species associations, and root diameter distributions that more closely resemble clear cuts than natural forests. The disturbance legacy within industrial forests arises from previous clear cuts and selective timber harvesting, fires set intentionally to flush game and clear vegetation, and the introduction of non-native insects and diseases. The overlap in cohesion values between industrial forests and clear cuts (figure 2.6) may indicate that landslides initiate from industrial forests because they possess vegetative cover with relatively low cohesion. Furthermore, it seems as if the response time to timber harvest may persist for at least a 100 years. Some areas in the ESF that were cut at the turn of the century, for example, presently maintain a veritable monoculture of red alder, that based on the species of

remaining stumps, replaces a mixed conifer forest. More recently, damage resulting from yarding-cables and the removal of trees during thinning operations are seen to persist for at least 30 years. A study by Zavitkovski and Stevens (1972) in the Oregon Coast Range documents that the dry weight of red alder roots is at a maximum for a 60 year old tree. Hence, landslide susceptibility may increase in areas such as the ESF dominated by a large proportion of > 60 year old red alder trees. Determining the natural condition of old growth forests is a formidable task because few unharvested natural forests remain and they are small in size. It seems clear, however, that the relative productivity of a forest and hence the underlying root strength is not simply a function of time. Therefore, labeling forest stands simply by the age of the oldest living tree obscures the local history of the land while contributing inadequate insight to the local landslide susceptibility. Stand age classifications, then, provide a basis of understanding that should be augmented with insight into the stand condition.

*Root decay and regrowth*

A lag time from timber harvesting to landsliding is commonly associated with the decay of roots (Rice and Krammes, 1970; Burroughs and Thomas, 1977; Ziemer and Swanston, 1977; Ziemer, 1981; O'Loughlin and Ziemer, 1982; Fahey et al., 1988; Hendrick and Pregitzer, 1993; Fahey and Arthur, 1994). The response time of root decay and regrowth following disturbance, however, can differ greatly over a landscape. In areas with roughly equivalent topographic and hydrologic characteristics, those sites with a long duration of suppressed root strength are more prone to landsliding during large magnitude storms. I use cohesion measurements obtained just after landsliding, back-calculated cohesion values representative of conditions prior to timber harvest, and the proportion of understory, hardwood, and coniferous vegetation from two sites located in close proximity

to one another to heuristically portray site specific response to disturbance in order to emphasize variations in cohesion at sites of the same age.

The total root cohesion after timber harvest is a function of a) the declining component from the decay of roots present prior to cutting plus b) the increasing contribution from roots of vegetation established after cutting. The strength contributed by decaying roots, $c_{rd}$, of Douglas-fir was proposed by Burroughs and Thomas (1977) to be expressed by the following function:

$$c_{rd} = 1.04(2.516d)^{1.8-0.06\sqrt{t}}$$

(2.13)

where $d$ is the root thread diameter (mm), t is time (months), and $c_{rd}$ is expressed in kPa. For simplicity, I uniformly apply the Douglas-fir decay function in equation 2.13 to all conifers and hardwoods. By assuming that the understory component available for decay at the time of cutting is zero, I therefore underestimate the total strength at the time of cutting. The contribution of cohesion from the establishment of post-harvest root regrowth, $c_{rrg}$ (kPa), from understory, hardwood, and coniferous vegetation can be defined as an exponential function with the form:

$$c_{rrg} = ke^{b_* t}$$

(2.14)

such as that depicted in figure 2.8 where e is the base of natural logarithm, $k$ is set by the regression in figure 2.8, and $b_*$ is determined from the cohesion at a given time since cutting. Sidle (1991) suggests, however, that a sigmoid relationship is more appropriate than an exponential representation for vegetation regrowth after timber harvest because exponential functions generate unrealistically high cohesions at large values of t. Unfortunately, I cannot utilize the more realistic sigmoid relationship because I lack specific knowledge regarding the time to the inflection point marking decreased root regrowth rates or the value of cohesion at the that time. Based on figures 2.8 and 2.10 I can, though, infer that understory and hardwood vegetation attain a maximum value of about 10 kPa. Projected cohesion values > 10 kPa are thus solely a function of the presence of coniferous vegetation.

Two sites in the field area west of Roseburg, located on the same headwall, with roughly equivalent topographic controls express distinct vegetation regrowth patterns: 1) regrowth at one site is dictated solely by understory regrowth with little establishment of coniferous vegetation, and 2) understory regrowth is complimented by abundant conifers and hardwoods (figure 2.18). In figure 2.18 the cohesion values at $t = 0$ are back-calculations of pre-logging values based on diameters of observed decaying hardwood and conifer roots emanating from stumps adjacent to the slide scar. The cohesion values at the time of landsliding are based on the measured components of decaying pre-logging roots and the re-establishment of new vegetation. The inflection points expressed by the total regrowth and total curves correspond to the projected time at which the understory vegetation attains the ceiling of 10 kPa inferred from figure 2.10. Cohesion values after the time of landsliding are theoretical projections based on the amount and species of vegetation present at the time cohesion was measured. The two cases reveal stark

differences in the re-establishment of the same "age" second growth forest. The site dominated by understory vegetation (upper plot) is limited to cohesion values < 15 kPa for at least 18 years while the site with abundant hardwood and conifer vegetation regenerates cohesion to pre-cutting levels within 16 years. Thus simply inferring root strength values from a simple age designation for a given stand of trees may belie a more complex relationship between root reinforcement and time since disturbance.

The window of landslide vulnerability is a function of the decay time to a critical cohesion value low enough to allow for landsliding and the duration of time spent below the critical value (Ziemer and Swanston, 1977; Ziemer, 1981). In areas of equivalent topographic and hydrologic settings, the temporal window of landslide vulnerability is shorter where vegetation and hence roots become quickly established. The planting of conifer seedlings immediately post-cutting should act to narrow the window of vulnerability. As a gauge to the duration of this window, previous research reports it may take 15 to more than 25 years for a regenerating clear cut lodgepole pine forest in California to restore 50% of its original root strength (Ziemer, 1981). As revealed in figure 2.18, the window of vulnerability marked by low cohesion values is tied strongly to site-specific conditions. Moreover, an unexplored issue is whether the initial conditions immediately post-cutting are the same for natural and industrial forests. That is, the window of vulnerability to landsliding may be greater for industrial forests where initial cohesion values are lower and the subsequent exponential decline of cohesion to critical values occurs over a shorter time period. The question, though, remains as to whether under a commercial harvesting cycle cohesion values recover to levels similar to those of a natural forest.

In the context of slope stability modeling the implications of high spatial and temporal variability in cohesion values are enormous. Typical landslide hazard analyses impose a given, uniform value of cohesion across the landscape. Bracketing high and low values of cohesion furnishes the best and worst case scenarios but cannot reliably locate exact landslide source regions producing landslides in a given storm. Cohesion data of the type presented here can help to identify specific landslide hazards but field measurements are time consuming and thus aid little in regional scale predictions. When evaluating the predictions of regional slope stability models, though, one must be aware of the site-specific variations in order to understand why certain areas of high predicted hazard produce landslides while other areas of high predicted hazard do not.

CONCLUSION

Root area ratio, thread diameter, species of vegetation, and proportion of live roots are salient vegetation characteristics controlling cohesion in the central Oregon Coast Range. Variation in root strength between different vegetation communities is notable and quantifiable. Although combined root area ratios of both live and decaying roots are similar for all the vegetation communities, root area ratios representative of live roots are greatly reduced in clear cuts and industrial forests. As the live roots in clear cuts and industrial forests are comprised of a significant proportion of hardwood and understory vegetation, it appears as if some older industrial forests > 43 years old may not establish substantially more stable ground than recent clear cuts. In fact, the average cohesion for landslides within industrial forests (7.5 ± 5.1) is only twice that of landslides in clear cuts < 11 years old (3.8 ± 3.3). Suppressed cohesion within industrial forests may reflect the local history or disturbance legacy arising from fire, commercial thinning, or partial conversion of conifer to hardwood forest. In contrast, average cohesions values of natural

forests ranged from 25 to 99 kPa. Natural forests with no history of previous timber harvest expressed such high root strengths that only unusually strong winds causing blow down or very excessive pore pressures could cause instability. As few such areas remain in the Oregon Coast Range, characterizing the spatial variability and regrowth of roots after disturbance within industrial forests is essential.

The conversion of old growth, unharvested forests to industrial forests may trigger significant increases in the rates of landsliding, although one should expect significant spatial variability because landslide susceptibility is extremely site dependent. Even though < 11 year old clear cuts have cohesions ranging up to 10 kPa, simulations that couple an idealized hydrologic routing model with a two-dimensional slope stability model indicate that clear cuts are more susceptible to landsliding in smaller magnitude storms than either industrial or natural forests because of reduced cohesion. Furthermore, the results determined here support the "window of vulnerability" concept but suggest that in some localities root strength recovery may be arrested by the presence of dense understory and hardwood vegetation which effectively extends the opening of such a window. Root strength recovery within clear cuts was seen to be an exponential function of the time since timber harvesting for the first decade after harvesting. The limited data on herbicided clear cut sites indicates that the practice of herbiciding decreases effective cohesion, acting to extend the window of vulnerability. Moreover, a refined classification of vegetation is necessary to augment stand age designations to establish the intricate association between landsliding and vegetation. Future research surrounding these issues could utilize data on the density of timber per given area or remote sensing information to characterize the amount of cohesion and its spatial variability in a geographic information system. Such an

approach could be used to better assess risks posed by timber harvest plans in landslide prone regions.
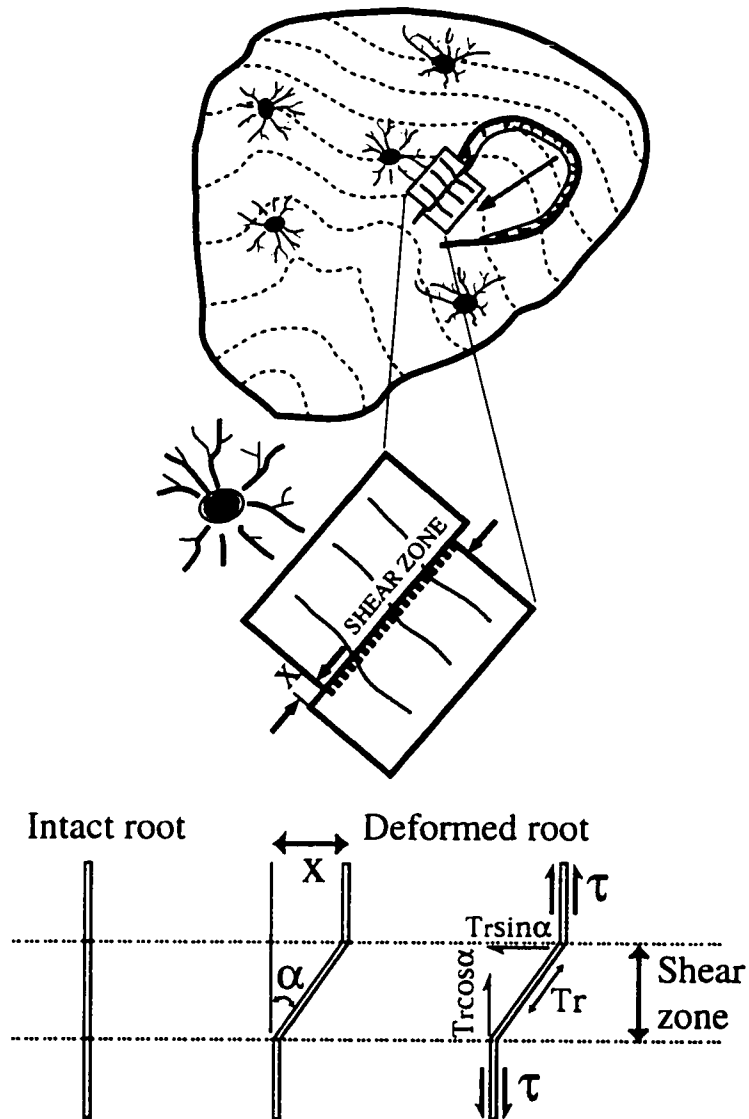
Figure 2.1    Idealized topography with cross sections of tree trunks and roots emanating toward a potential shear zone on the lateral margin of a landslide.    Horseshoe-shaped landslide headscarp shows deformation of flexible, elastic roots extending perpendicularly across shear zone, displaced laterally by an amount X, and distorted by angle $\alpha$.    Shear strength increase in soil arising from roots is expressed as

$c_r = T_r(A_r / A_s)(\cos\alpha\tan\phi + \sin\alpha)$.    (For definition of variables see discussion with equations 2.1 through 2.4).

Figure 2.2     Photograph of broken roots (highlighted in white) in landslide source region within Elliot State Forest.  Roots crossing boundary between stable ground and landslide source volume did not simply pull out of soil matrix, but broke during the landslide.  Note 2 m tall person for scale in center and absence of roots on the basal surface of the landslide.
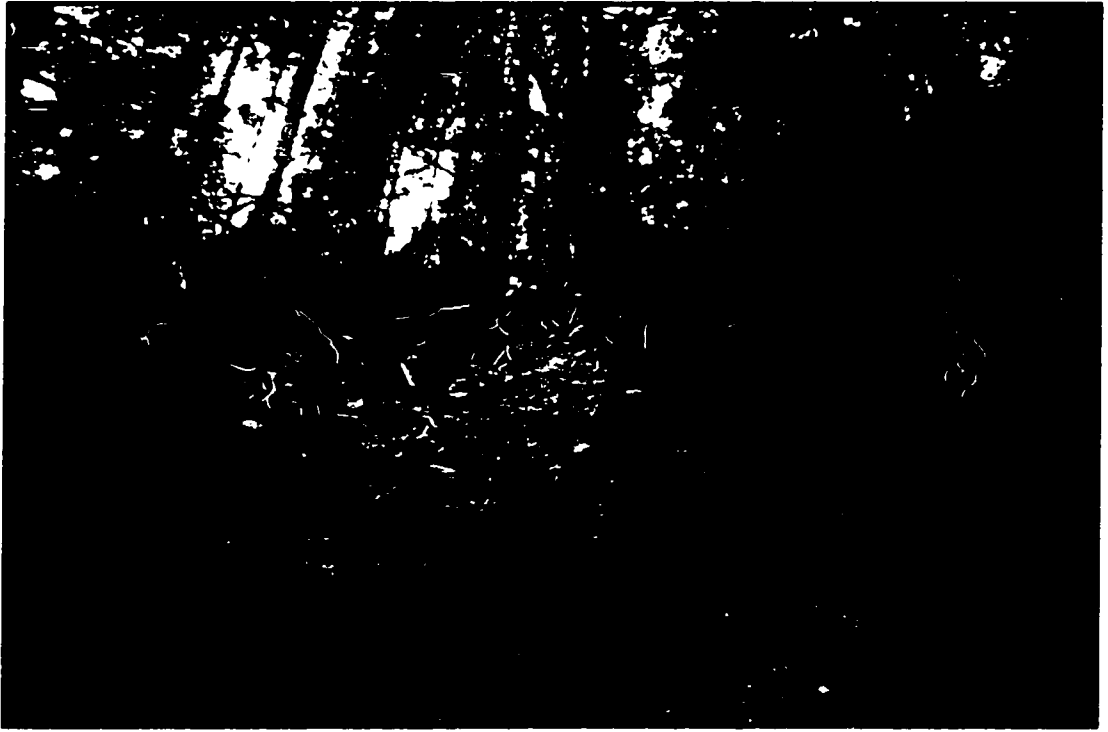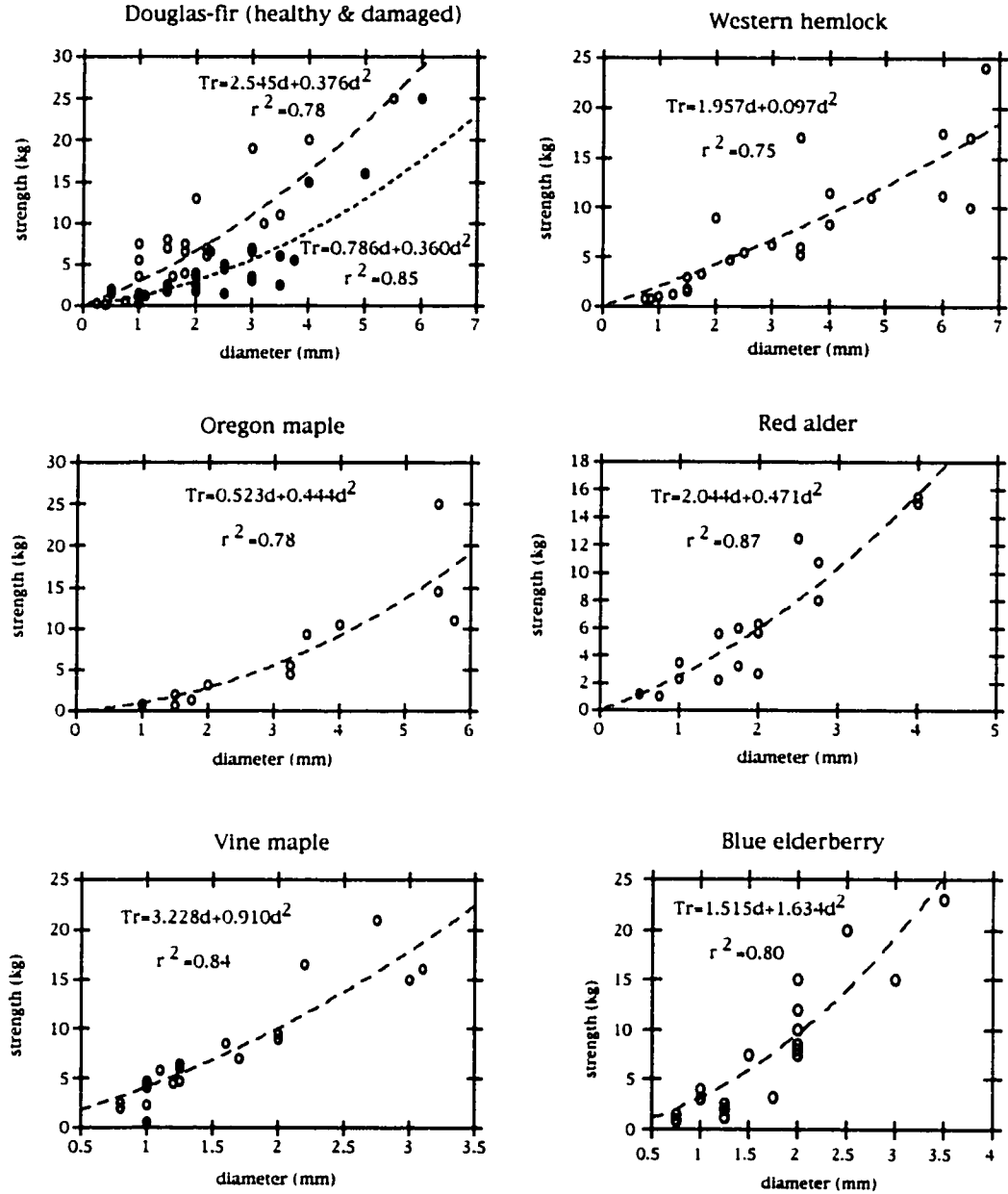
Figure 2.3    Critical tensile strength of individual root threads of varying diameter for the twelve primary species of vegetation (table 2.1). Second order polynomial regressions ($T_r = ad + bd^2$) plotted as dashed line with associated regression coefficients; $T_r$ is the tensile strength of the individual root thread (kg), $d$ is the root thread diameter (mm), while $a$ and $b$ are constants. Root diameter measurements include outer bark. Note significant decrease in strength for live roots of Douglas-fir trees damaged in thinning operation during the 1960's, denoted by solid circles.
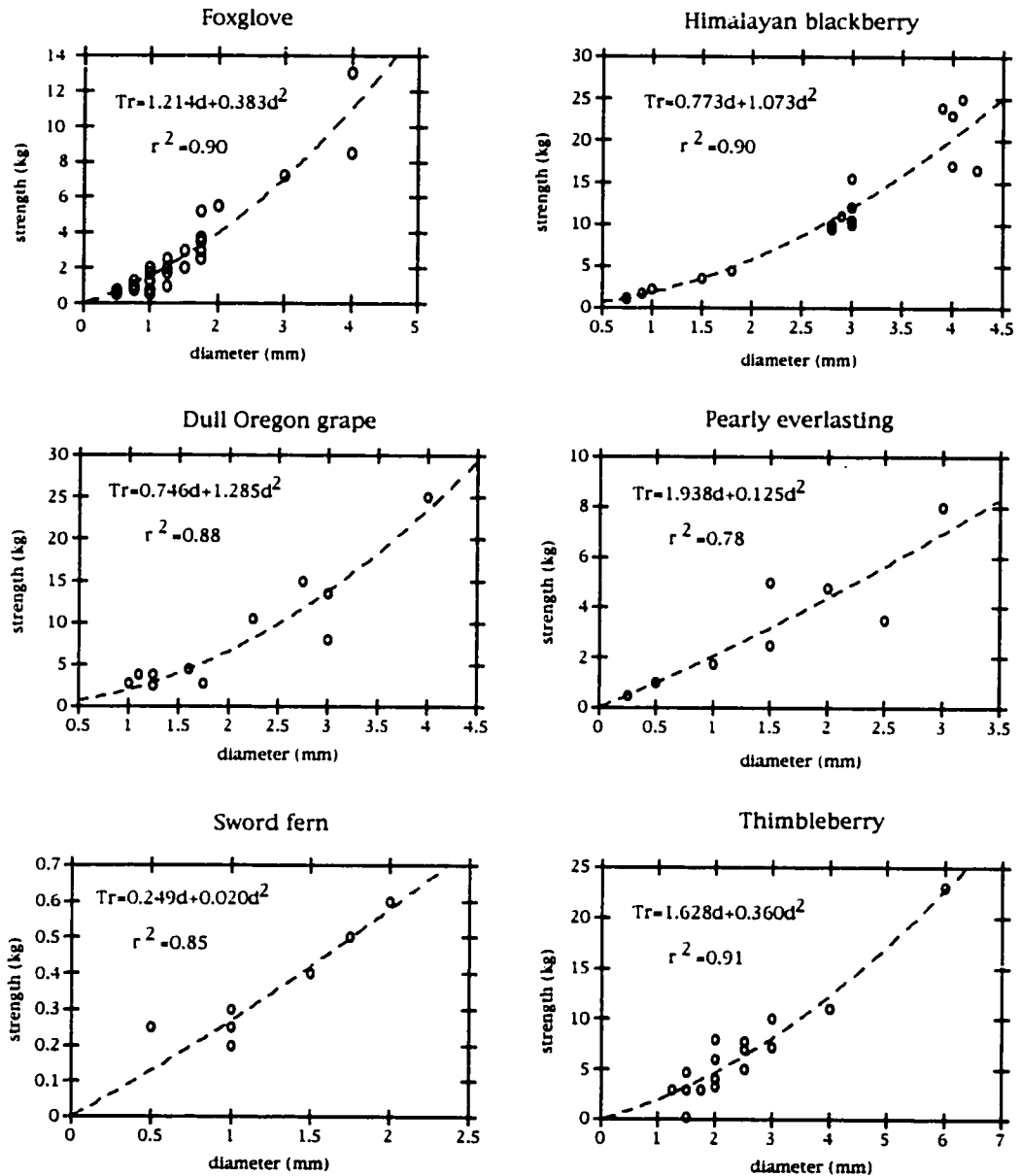
Figure 2.3 Critical tensile strength of individual root threads of varying diameter for the twelve primary species of vegetation (table 2.1). Second order polynomial regressions ( $T_r = ad + bd^2$ ) plotted as dashed line with associated regression coefficients; $T_r$ is the tensile strength of the individual root thread (kg), $d$ is the root thread diameter (mm), while $a$ and $b$ are constants. Root diameter measurements include outer bark.
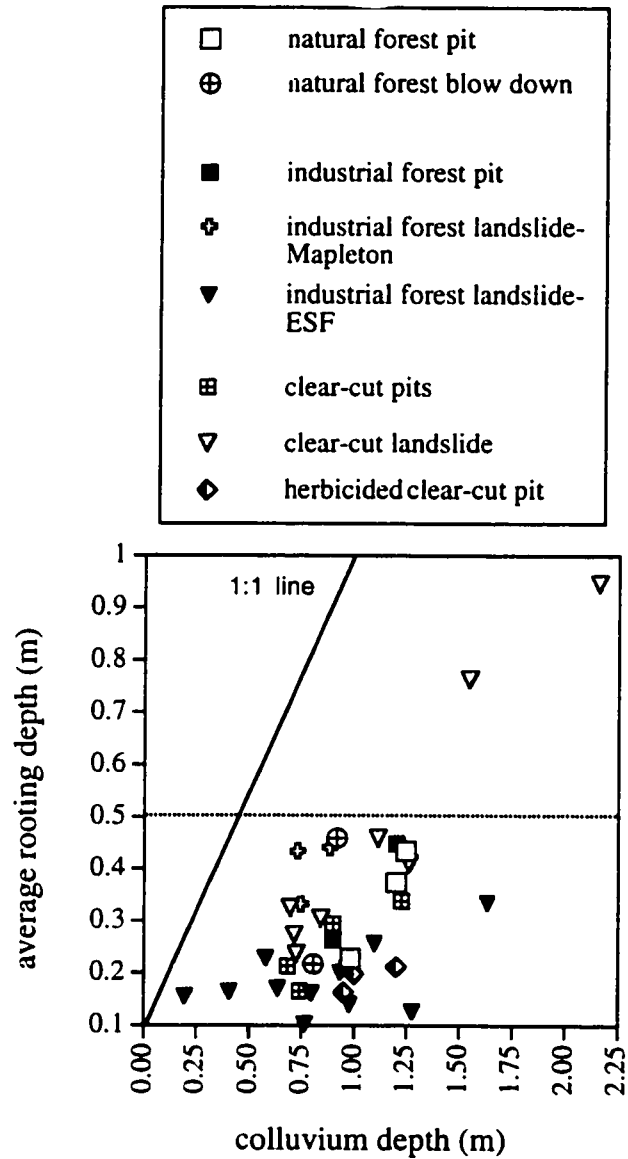
Figure 2.4    Average rooting depth vs. total colluvium depth for different vegetation communities showing that mean rooting depths generally are restricted to the upper 0.5 m of the regolith (dashed line). Root depth representative of a site was determined by averaging the depths of all roots both live and decaying. One-to-one relationship between rooting depth and colluvium depth is represented by solid line.
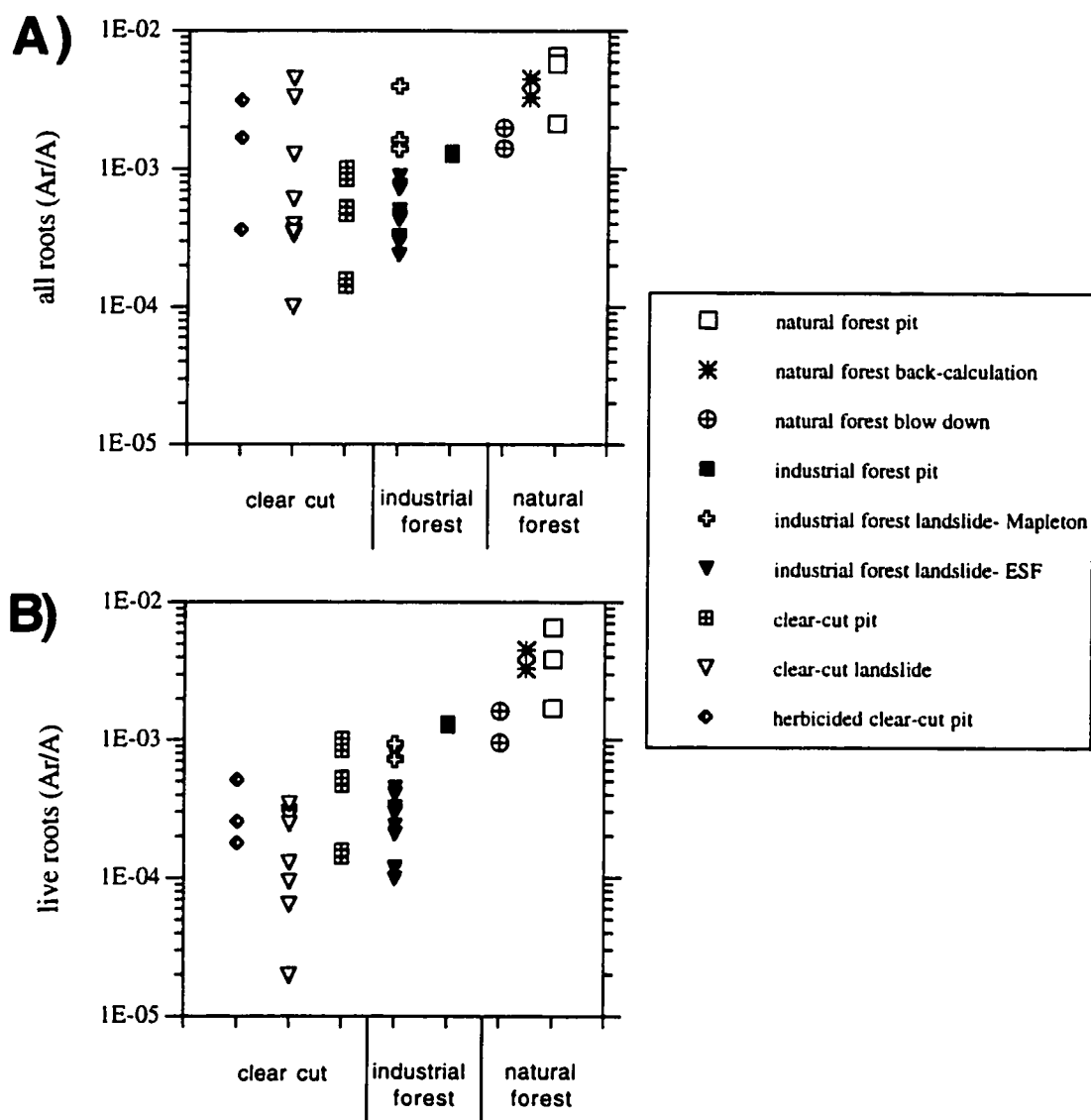
Figure 2.5    Semi-log plot of root area ratios ($A_r / A_s$) for different vegetation communities.  Square symbols represent soil pits while triangles depict landslides.  A)  The density of roots, both live and decaying, is similar between most communities with all communities expressing values > $10^{-3}$.  B)  Root area ratios of only live roots are greatly reduced indicating a significant fraction of decaying roots in clear cut and industrial forest sites.
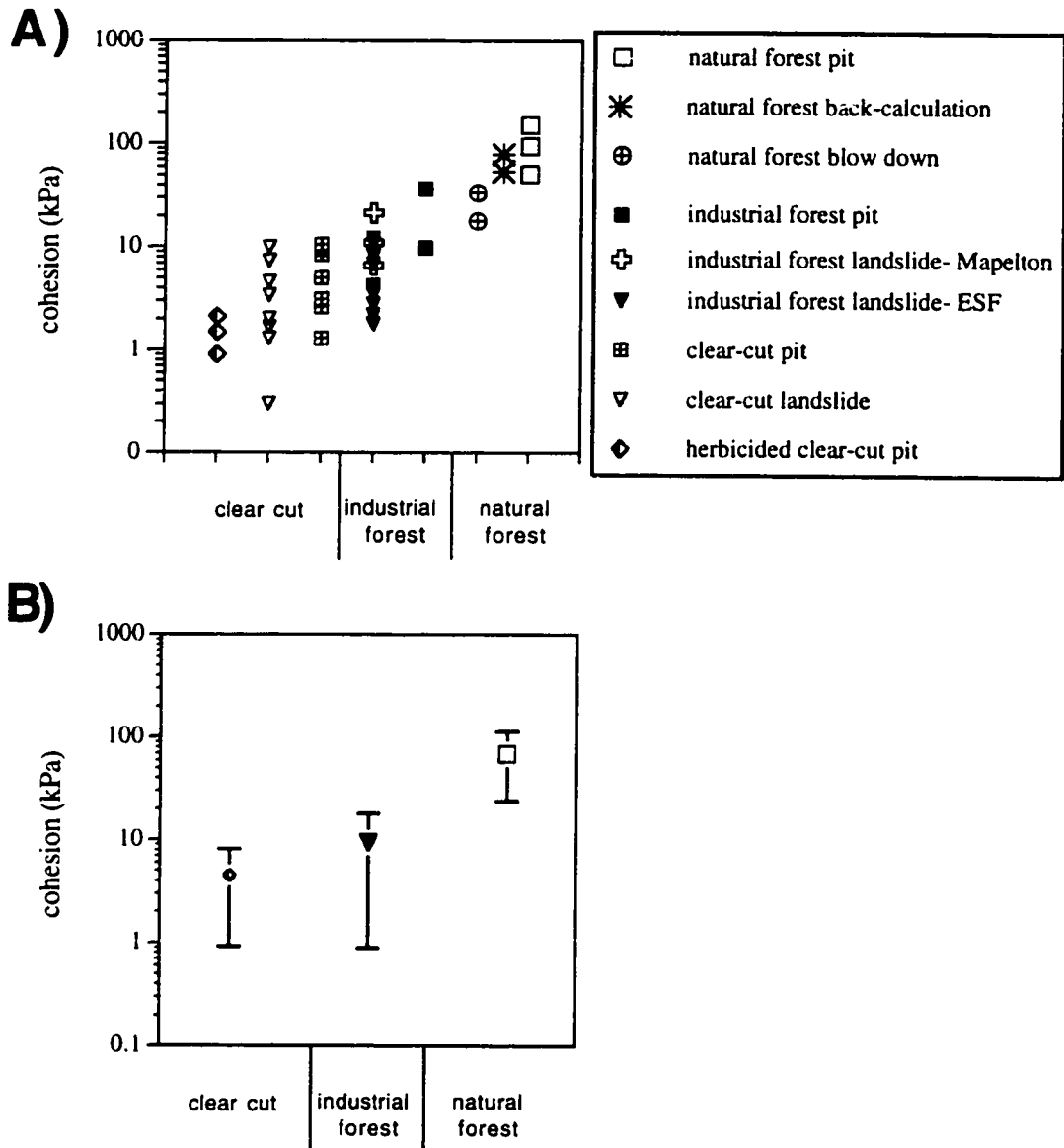
Figure 2.6    Semi-log plot of cohesion values for different vegetation communities. Square symbols represent soil pits while triangles depict landslides. A) The distribution of all 41 sites ranges over 3 orders of magnitude. B) Mean and standard deviations for clear cuts, industrial forests, and natural forest sites. Note, the offset of the brackets represents the standard deviations arises from the use of a logarithmic scale.
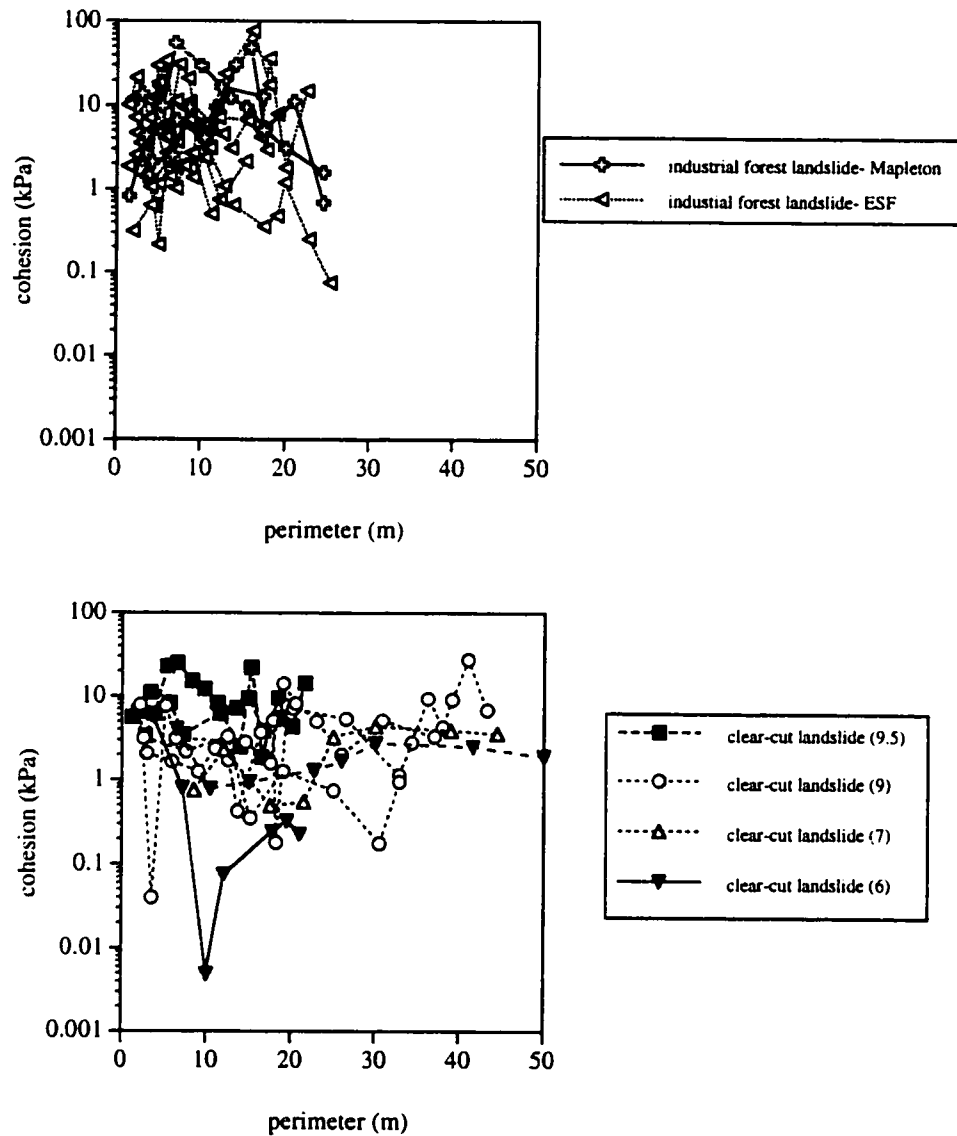
Figure 2.7    Along-scarp, spatial variation of cohesion along the perimeter of landslide source volumes.  Both industrial forests and clear cuts have a dense concentration of cohesion values between 1 and 10 kPa.  The localized high cohesion values for both industrial forests and clear cuts correspond to close proximity to hardwoods or conifers.  Clear cut cohesion maxima are positively associated with the longest time since harvesting.  The characteristic perimeter lengths of all landslides is about 25 m.  The mean perimeter length within industrial forests (16.9 m) is much less than clear cuts (33.6 m).  Age of clear-cut landslide shown in parenthesis.
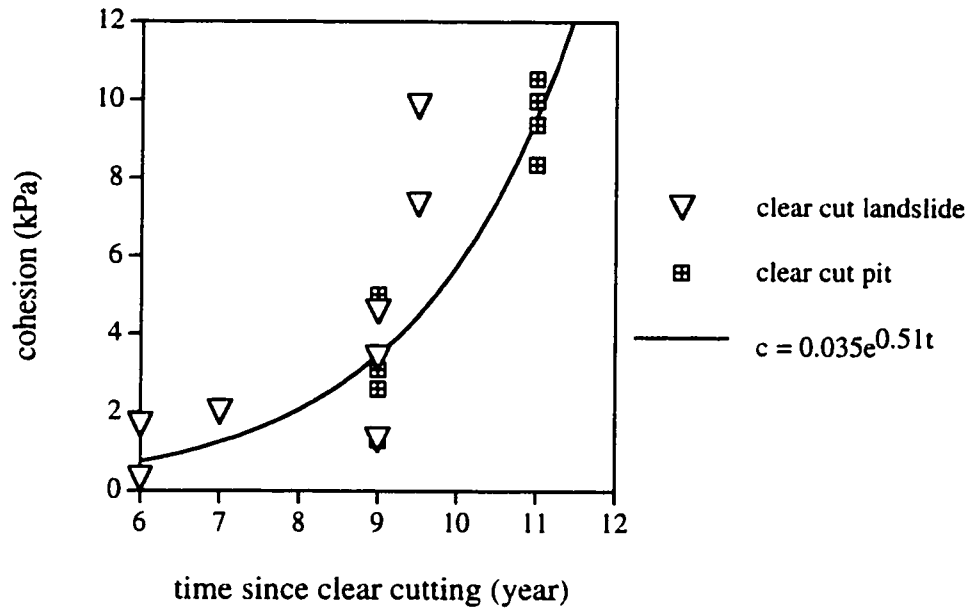
Figure 2.8    Cohesion values for clear cut landslides and pits as a function of time since cutting.  Regression equation (coefficient of determination $R^2$ = 0.73) is valid for time window expressed and should not be extrapolated beyond the data as cohesion does not indefinitely increase exponentially over time.
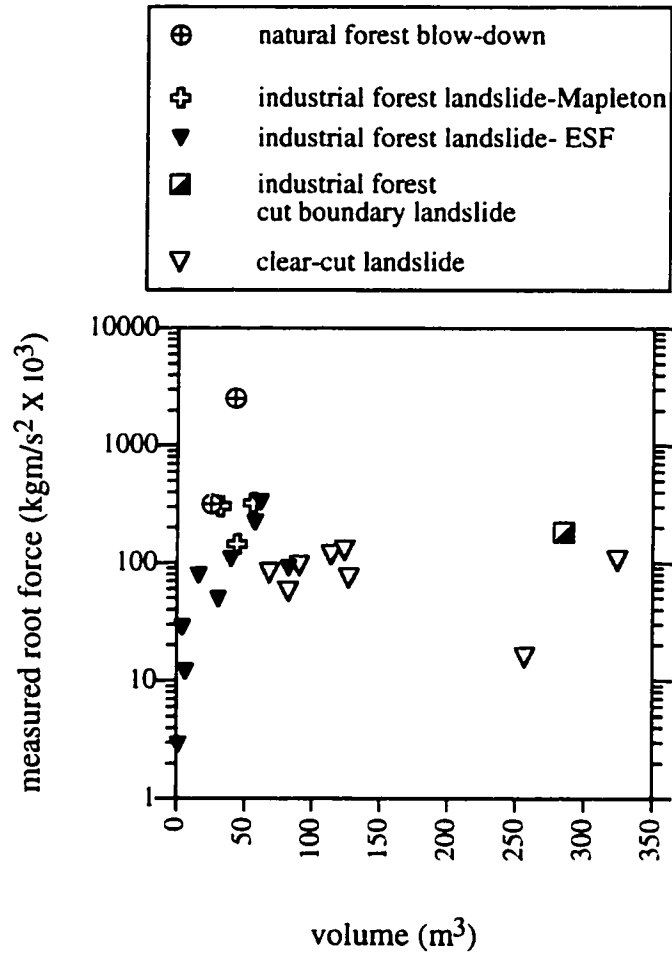
Figure 2.9    Variation in measured landslide source volumes with root force revealing greater volumes for clear cut landslides . The absolute root force is used in lieu of cohesion to avert spurious correlation between the area over which the root force acts and the source volume.
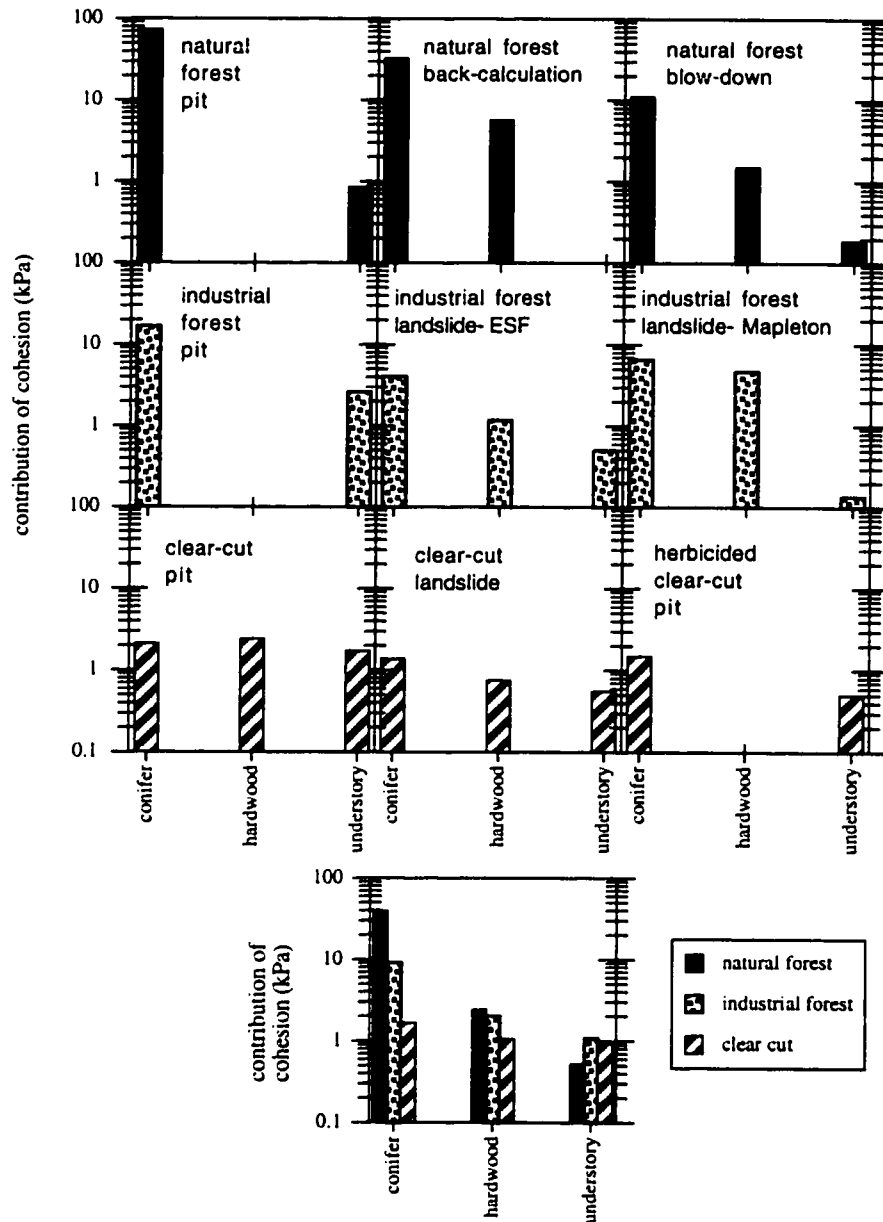
Figure 2.10    Semi-log plot of measured root cohesion and species composition in headscarps and pits. Top row represents natural forests, middle row industrial forests, and bottom row clear-cuts. Hardwood and understory vegetation species express a maximum cohesion of 12 kPa at any one site. Natural forests are dominated by conifers while industrial forests and clear cuts express reduced contributions from coniferous vegetation. Although the vegetation community designated as industrial forests represents vegetation > 43 years old, a significant contribution of cohesion originates from hardwood and understory species. Solitary graph at bottom of figure represents mean values for natural forests, industrial forests, and clear cuts.
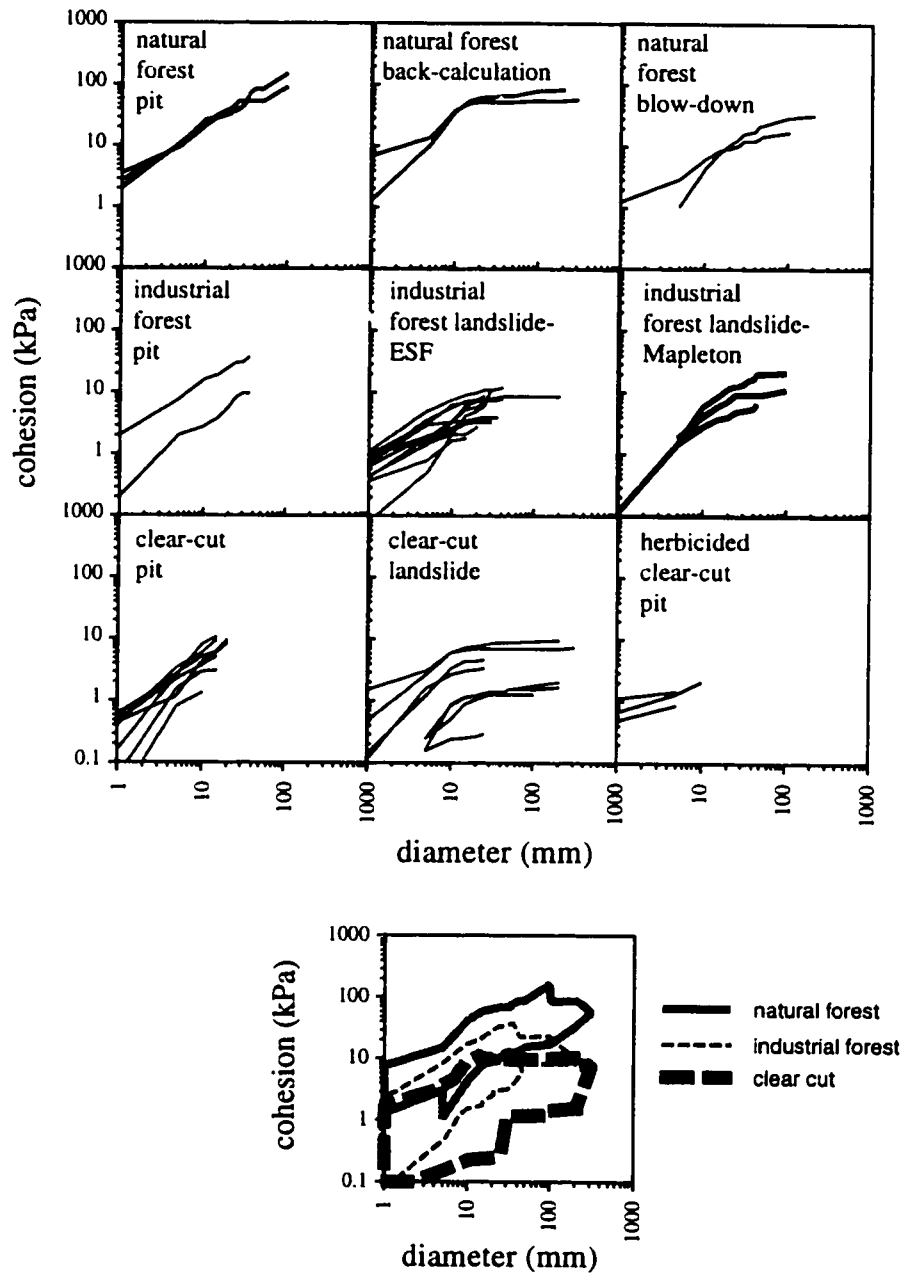
Figure 2.11    Semi-log plot of total cohesion provided by roots and size distribution for different vegetation communities. Top row represents natural forests, middle row industrial forests, and bottom row clear-cuts. Curves for individual sites are terminated at the maximum total cohesion. Natural forests exhibit higher cohesions for a suite of diameter roots and higher maximum values. Solitary graph at bottom of figure represents boundaries of curves plotted in above graphs.
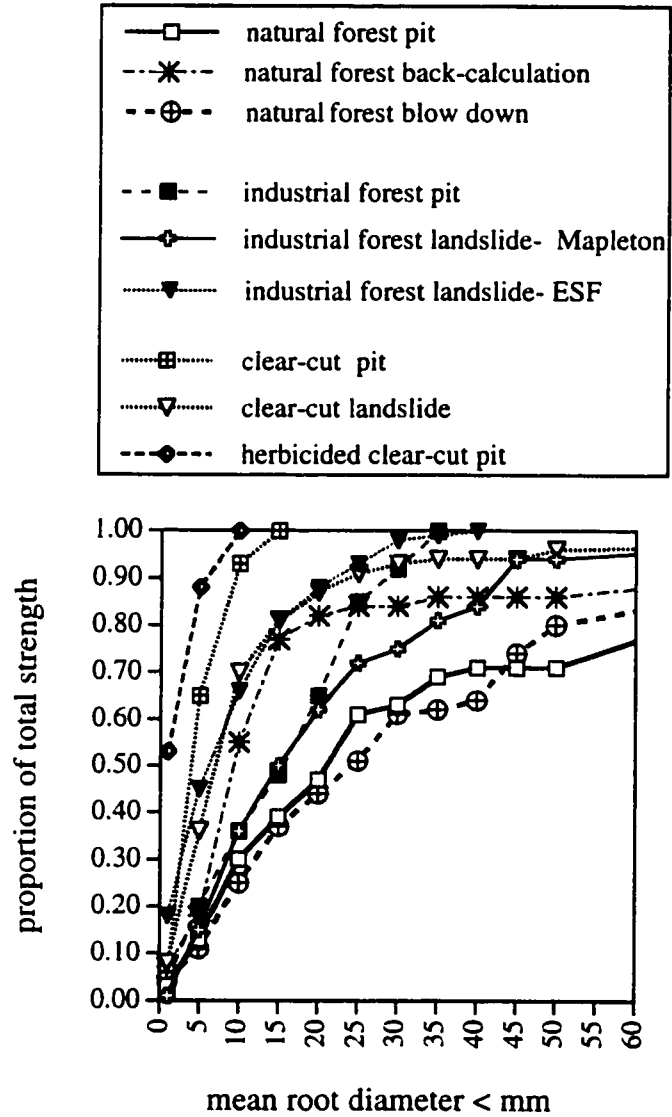
Figure 2.12    Proportion of total cohesion as a function of mean root diameter for the different vegetation communities.  Blow down sites and natural forest pits cluster together while herbicide sites and clear cuts comprise the low end of the distribution.  Significant overlap exists between clear-cut landslides and industrial forest landslides.
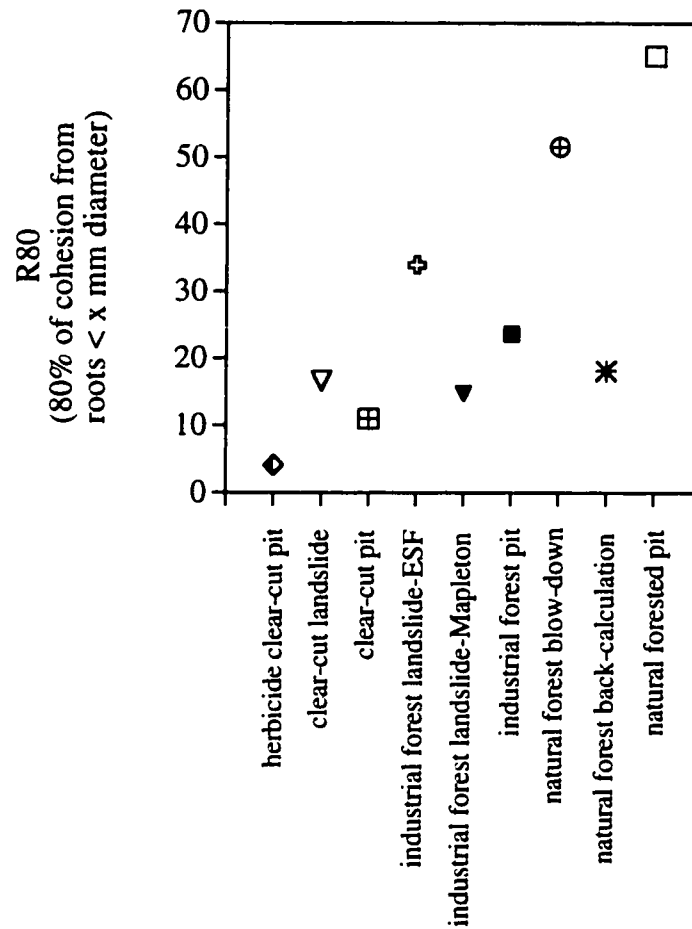
Figure 2.13    The maximum root diameter, $R_{80}$, for which 80% of the total cohesion at a site is provided by roots less than or equal to a given diameter.  An order of magnitude difference separates herbicided and unharvested sites.  Industrial forest landslides in the ESF have values comparable to those of clear cuts landslides.

$$h/z_s = \frac{q\,A}{T\,b\sin\theta}$$
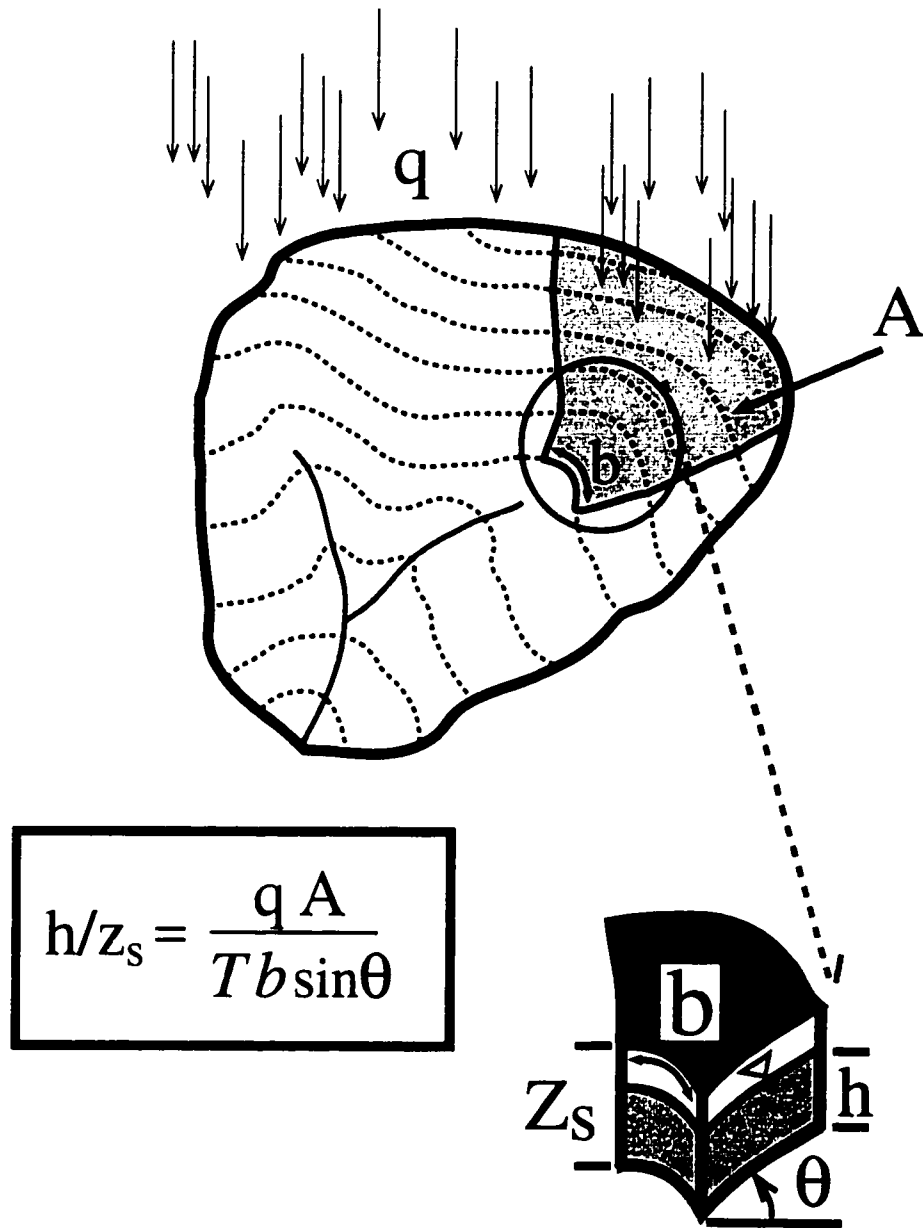
Figure 2.14    Conceptual model used to infer the degree of saturation where $M$ or $h/z_s$ is the saturated portion of regolith. The idealized topography receives a steady state rainfall ($q$) that contributes to an upslope drainage area ($A$) and flows through contour length ($b$). $T$ is the transmissivity, $z_s$ is the vertical regolith thickness, $h$ is the height of the piezometric surface above the base of the regolith, $\theta$ is slope of the ground surface. See discussion associated with equations 2.9 through 2.11.
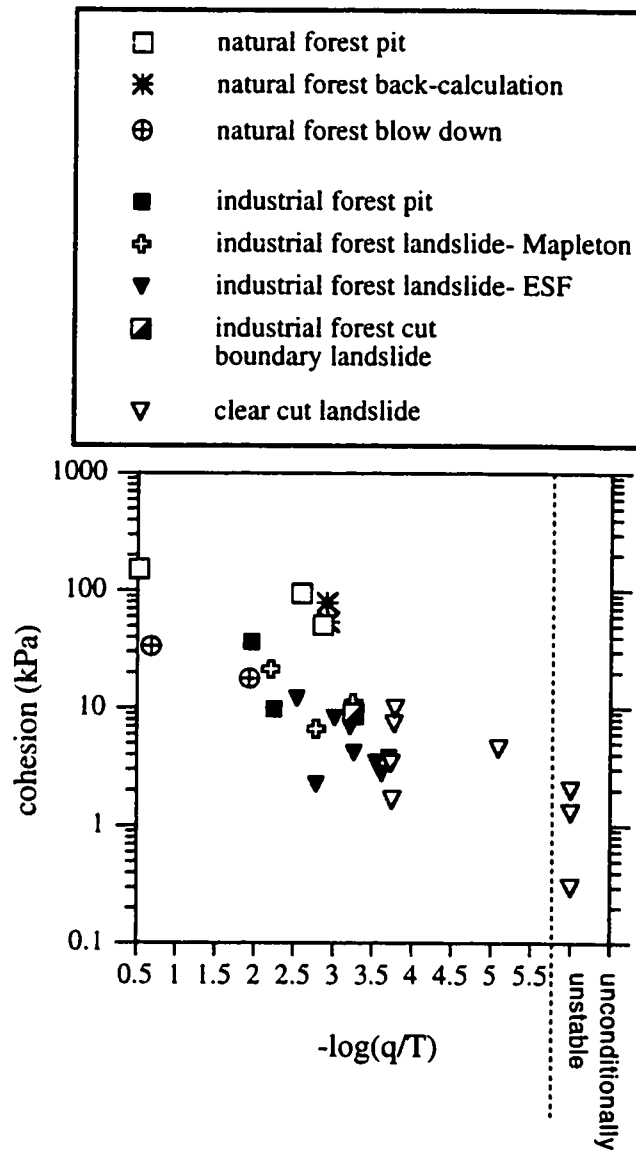
Figure 2.15 Semi-log plot of cohesion and back-calculated hydrologic properties, -log(q/T). Landsliding at clear cut sites requires higher values of -log(q/T) than industrial forest or natural forests. Assuming a transmissivity of 65 m²/day, clear cut landslides have a stability threshold equivalent to a steady state rainfall of 1.5 cm/day while industrial-forest landslides have a threshold equivalent to a steady state rainfall of 20.5 cm/day. Actual, maximum 24-hour rainfall totals for the two storms studied were between 8 to 15 cm.
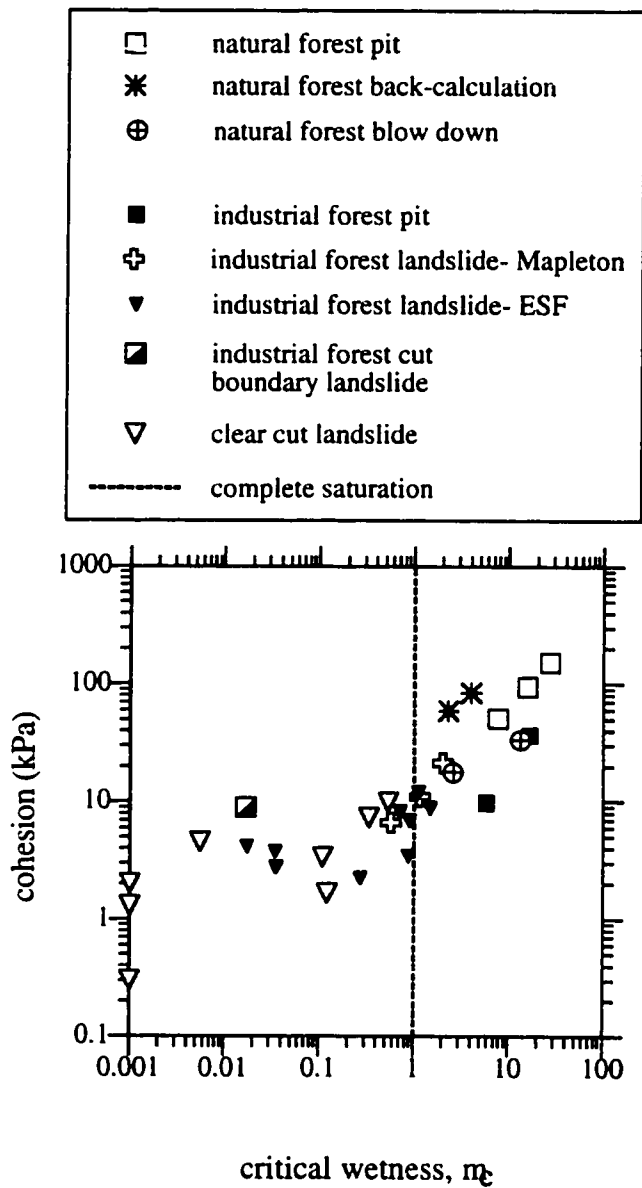
Figure 2.16    Log-log plot showing a rough positive correlation between cohesion and critical wetness (equation 2.10) necessary to initiate landsliding.  Clear cut sites require lower critical wetness levels than both disturbed and undisturbed forests.  Dashed line represents the complete saturation of colluvium.
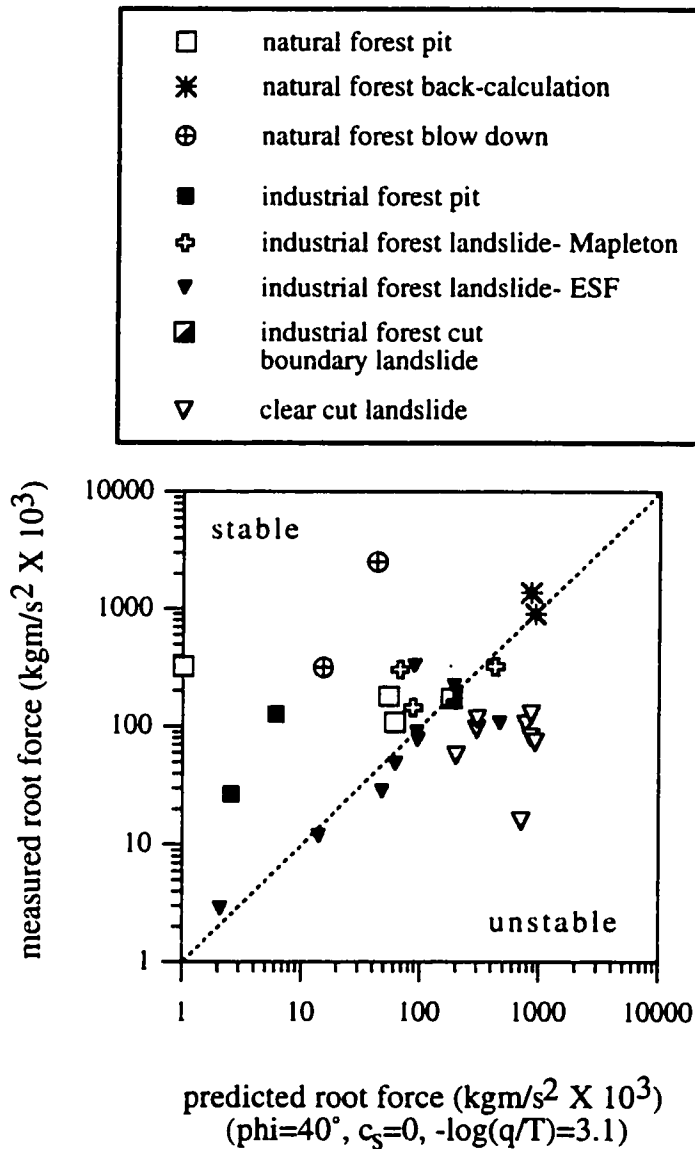
Figure 2.17   Log-log plot of measured and predicted root strengths using a two-dimensional slope stability model (equation 2.12), idealized hydrology from equation 2.10, and assuming uniform hydrologic conditions of $-\log(q/T) = 3.1$. Sites within industrial forests are the closest to the threshold of instability (dashed line) with clear cuts plotting well within the field of instability, presumably because of lower observed root strengths.
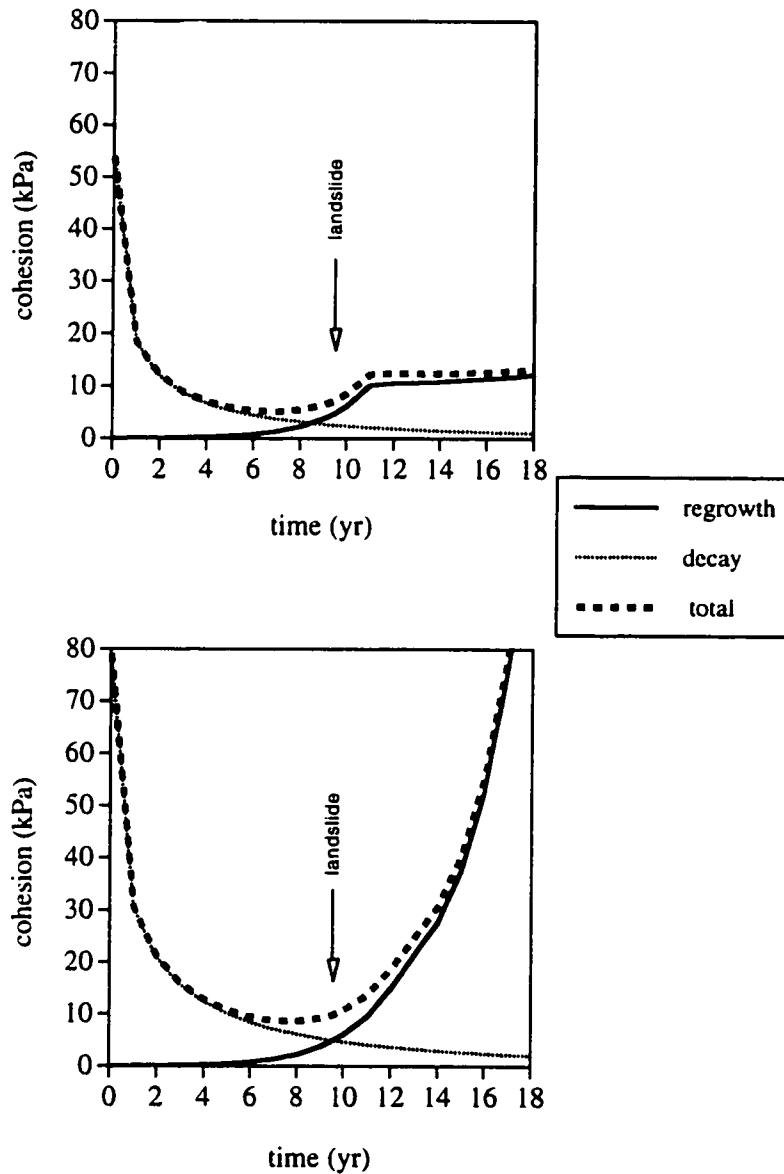
Figure 2.18    Regrowth and decay contributions of total cohesion for two sites that were clear cut in 1986 and that yielded debris flows in 1996. Roots examined immediately following the debris flow exposed an advanced state of decay. To illustrate the variability in regrowth at neighboring sites the regrowth curves (based on the first decade of vegetation reinstatement) are extrapolated past the time of the debris flow.

Table 2.1    The twelve dominant and sixteen associated species of conifer, hardwood, and understory vegetation in the Oregon Coast Range. Dominant vegetation is shown in bold lettering, while scientific names are in italics. For strength curves of the dominant species of roots, see figure 2.3. Strength curves for associated species of vegetation, shown indented in brackets, are tied to dominant species listed above.

| Coniferous Vegetation |
| --- |
| **Douglas-fir** (*Pseudotsuga menziesii*)<br><br>[grand fir (*Abies grandis*)]<br><br>**western hemlock** (*Tsuga heterophylla*) |

| Hardwood Vegetation |
| --- |
| **Oregon maple** (*Acer macrophyllum*)<br><br>[big leaf maple (*Acer macrophyllum*)]<br>[douglas maple (*Acer glabrum*)]<br>[cinquapin (*Castanopsis chrysophylla*)]<br>[madrone (*Arbutus menziesii*)]<br><br>**red alder** (*Alnus rubra*)<br><br>[beaked hazelnut (*Corylus cornuta var. californica*)]<br>[sitka willow (*Salix sitchensis*)]<br><br>**vine maple** (*Acer circinatum*)<br><br>[pacific rhododendron (*Rhododendron macrophyllum*)] |

| Understory Vegetation |
| --- |
| **blue elderberry** (*Sambucus caerulea*)<br><br>**foxglove** (*Digitalis purpurea*)<br><br>**himalayan blackberry** (*Rubus discolor*)<br><br>[salmonberry (*Rubus spectabilis*)]<br>[black raspberry (*Rubus leucodermis*)]<br>[trailing blackberry (*Rubus ursinus*)]<br>[black gooseberry (*Ribes lacustre*)]<br><br>**dull Oregon grape** (*Mahonia nervosa*)<br><br>[salal (*Gaultheria shallon*)]<br>[kinnikinnick (*Arctostaphylos uva-ursi*)]<br><br>**pearly everlasting** (*Anaphalis margaritacea*)<br><br>**sword fern** (*Polystichum munitum*)<br><br>[piggy-back plant (*Tolmmiea menziesii*)]<br><br>**thimbleberry** (*Rubus parviflorus*)<br><br>[red huckleberry (*Vaccinium parvifolium*)] |

**Table 2.2** Morphologic characteristics of landslides and pits with associated root attributes in different vegetation communities. Bold values in box at base of individual vegetation communities is mean cohesion and standard deviation. Cohesion measured on the basal surface of landslides ranges from 0.07 to 3.8 kPa values, overall equivalent to only a small fraction of the lateral cohesion.

| LAND USE TYPE | basal area (m²) | lateral area (m²) | depth (m) | volume (m³) | slope (degrees) | number of roots | cohesion (kPa) | tensile force (kgm/s²X10³) | mean root depth (m) | A/b (m) | A/bsin(slope) (m) |
|---|---|---|---|---|---|---|---|---|---|---|---|
| NATURAL | - | 2.12 | 1.25 | - | 34 | 351 | 151.9 | 321.5 | 0.43 | 50 | 89 |
| FOREST | - | 1.92 | 0.96 | - | 34 | 355 | 94.3 | 181.5 | 0.23 | 3492 | 6227 |
| PIT | - | 2.15 | 1.20 | - | 34 | 247 | 50.9 | 105.9 | 0.37 | 3122 | 5583 |
| **99.0±50.7** | | | | | | | | | | | |
| NATURAL FOREST | 132.0 | 15.40 | 0.96 | 126.7 | 37 | 95 | 53.9 | 804.9 | 0.22 | 1171 | 1846 |
| BACK-CALCULATION | 75.0 | 19.42 | 0.91 | 87.9 | 39 | 507 | 78.9 | 1377.1 | 0.19 | 2031 | 3227 |
| **66.4±17.7** | | | | | | | | | | | |
| NATURAL FOREST BLOW- | 42.0 | 75.52 | 1.01 | 42.4 | 43 | 514 | 33.4 | 2524.1 | 0.46 | 43 | 83 |
| DOWN INDUCED LANDSLIDE | 30.9 | 17.81 | 0.91 | 25.1 | 39 | 659 | 17.8 | 319.4 | 0.22 | 149 | 222 |
| **25.6±11.1** | | | | | | | | | | | |
| INDUSTRIAL | - | 3.46 | 1.20 | - | 32 | 425 | 36.5 | 85.9 | 0.45 | 798 | 1506 |
| FOREST PIT | - | 2.74 | 0.90 | - | 35 | 96 | 9.9 | 24.9 | 0.29 | 570 | 994 |
| **23.2±19.9** | | | | | | | | | | | |
| INDUSTRIAL | 72.2 | 21.75 | 1.14 | 62.2 | 44 | 100 | 4.2 | 90.5 | 0.14 | 22 | 32 |
| FOREST (ESF) | 31.6 | 13.07 | 0.96 | 30.3 | 46 | 780 | 3.6 | 49.3 | 0.16 | 125 | 174 |
| LANDSLIDE | 7.4 | 1.29 | 0.18 | 1.3 | 44 | 947 | 2.2 | 29 | 0.16 | 111 | 160 |
| \/ | 14.4 | 4.31 | 0.45 | 6.5 | 47 | 628 | 2.6 | 12.0 | 0.16 | 104 | 142 |
| \/ | 34.0 | 27.40 | 1.80 | 61.2 | 40 | 536 | 12.1 | 330.3 | 0.34 | 244 | 379 |
| \/ | 44.9 | 26.96 | 1.27 | 56.9 | 43 | 1281 | 6.3 | 222.4 | 0.20 | 500 | 733 |
| \/ | - | 6.61 | 0.76 | - | 43 | 355 | 1.9 | 12.2 | 0.10 | 500 | 733 |
| \/ | - | 5.54 | 1.26 | - | 43 | 138 | 10.9 | 60.2 | 0.13 | 500 | 733 |
| \/ | 11.4 | 11.30 | 1.38 | 15.8 | 45 | 2207 | 6.9 | 78.2 | 0.21 | 1029 | 1455 |
| \/ | 5.6 | 3.23 | 0.77 | 4.3 | 34 | 1050 | 8.8 | 28.6 | 0.17 | 1596 | 2854 |
| \/ | 40.2 | 31.27 | 0.96 | 39.5 | 32 | 563 | 3.5 | 108.2 | 0.26 | 1596 | 3012 |
| (CUT-BOUNDARY LANDSLIDE) | 179.2 | 19.44 | 1.59 | 284.8 | 42 | 2922 | 8.9 | 163.1 | 0.09 | 20 | 30 |
| INDUSTRIAL | 59.1 | 26.76 | 0.94 | 55.7 | 38 | 237 | 11.0 | 322.1 | 0.44 | 1250 | 2030 |
| FOREST (MAPLETON) | 35.8 | 14.29 | 0.89 | 31.8 | 44 | 245 | 21.3 | 304.1 | 0.43 | 222 | 320 |
| LANDSLIDE | 51.3 | 21.99 | 0.96 | 43.9 | 43 | 617 | 9.9 | 144.5 | 0.33 | 233 | 342 |
| **7.8±6.1** | | | | | | | | | | | |
| CLEAR | - | 0.73 | 0.73 | - | 34 | 20 | 1.3 | 0.9 | - | | |
| CUT | - | 0.50 | 0.50 | - | 44 | 20 | 2.6 | 1.3 | - | | |
| PIT | - | 0.69 | 0.69 | - | 38 | 47 | 3.1 | 2.1 | - | | |
| \/ | - | 1.10 | 1.10 | - | 45 | 50 | 5.0 | 5.5 | - | | |
| \/ | - | 2.58 | 1.23 | - | 41 | 123 | 9.4 | 19.5 | 0.34 | | |
| \/ | - | 1.38 | 0.90 | - | 40 | 124 | 8.3 | 16.5 | 0.29 | | |
| \/ | - | 1.65 | 0.74 | - | 46 | 108 | 10.0 | 18.4 | 0.17 | | |
| \/ | - | 1.71 | 0.69 | - | 39 | 109 | 10.5 | 19.0 | 0.21 | | |
| **6.3±3.7** | | | | | | | | | | | |
| CLEAR | 139.4 | 53.26 | 1.84 | 256.5 | 44 | 104 | 0.3 | 15.9 | 0.95 | 354 | 510 |
| CUT | 210.0 | 63.34 | 1.54 | 324.2 | 38 | 280 | 1.7 | 105.1 | 0.78 | 423 | 672 |
| LANDSLIDE | 65.0 | 43.90 | 1.26 | 82.0 | 44 | 206 | 1.3 | 57.2 | 0.41 | 288 | 414 |
| \/ | 105.9 | 63.42 | 1.17 | 123.5 | 45 | 345 | 2.0 | 127.7 | 0.46 | 1220 | 1726 |
| \/ | 98.0 | 20.79 | 0.92 | 90.3 | 44 | 363 | 4.6 | 95.0 | 0.33 | 484 | 688 |
| \/ | 135.3 | 34.40 | 0.84 | 113.7 | 42 | 1063 | 3.4 | 110.8 | 0.03 | 390 | 583 |
| \/ | 132.0 | 15.40 | 0.96 | 126.7 | 37 | 1961 | 7.3 | 74.2 | 0.24 | 1171 | 1846 |
| \/ | 75.0 | 19.42 | 0.91 | 87.9 | 39 | 909 | 9.9 | 817 | 0.27 | 2031 | 3227 |
| **3.8±3.3** | | | | | | | | | | | |
| HERBICIDED | - | 1.27 | 0.80 | - | 38 | 177 | 1.5 | 1.1 | 0.20 | | |
| CLEAR-CUT | - | 1.59 | 1.20 | - | 43 | 74 | 2.1 | 2.5 | 0.21 | | |
| PIT | - | 1.31 | 0.95 | - | 43 | 77 | 0.9 | 0.9 | 0.19 | | |
| **1.6±0.6** | | | | | | | | | | | |

Table 2.3    Quantity and size (dbh, diameter at breast height) of hardwood (red alder and Oregon maple) and coniferous (Douglas-fir and western hemlock) trees within 12 m surrounding landslide headscarps in the Mapleton District (n = 21) and Elliot State Forest (n = 12).

| site | hardwood live | hardwood dead | conifer live | conifer dead | conifer stumps |
|---|---|---|---|---|---|
| **# of trees per landslide** | | | | | |
| Mapleton | 6.7 | 0.2 | 1.1 | 0.7 | 0 |
| ESF | 2.8 | 0.1 | 3.5 | 0.8 | 0.8 |

| site | hardwood live | hardwood dead | conifer live | conifer dead | conifer stumps |
|---|---|---|---|---|---|
| **dbh of trees, mean and standard deviation (m)** | | | | | |
| Mapleton | 0.21 +/- 0.17 | 0.33 +/- 0.10 | 0.81 +/- 0.49 | 0.88 +/- 0.43 | n/a |
| ESF | 0.16 +/- 0.15 | 0.40 | 0.63 +/- 0.37 | 0.88 +/- 0.40 | 0.97 +/- 0.29 |

Table 2.4    Select literature review of cohesion values for different species of vegetation obtained by measuring root diameters and strength, direct shear tests in forest soils, and back-calculation.

| cohesion (kPa) | vegetation / location | source |
|---|---|---|
| **Measurement of root sizes and thread strength** | | |
| 3.5 - 7.0 | sphagnum moss / Alaska | Wu, 1984a |
| 5.6 - 12.6 | hemlock, sitka spruce, & yellow cedar / Alaska | Wu, 1984b |
| 5.7 | sugar maple / Ohio | Riestenberg and Sovonick-Dunford, 1983 |
| 5.9 | Alaska cedar, hemlock, & spruce / Alaska | Wu et al., 1979 |
| 7.5 - 17.5 | Douglas-fir / Oregon | Burroughs and Thomas, 1977 |
| ***In situ* direct shear test** | | |
| 1.0 - 5.0 | Japanese cedar / Japan | Abe and Iwamoto, 1987 |
| 2.0 - 12.0 | alder nursery / Japan | Endo and Tsuruta, 1969 |
| 3.0 - 21.0 | lodgepole pine / California | Ziemer, 1981 |
| 5.0 | pine seedlings in laboratory | Waldron and Dakessian, 1981 |
| 6.6 | beech / New Zealand | O'Loughlin and Ziemer, 1982 |
| 9.9 - 11.8 | 5-yr old pine seedlings in laboratory | Waldron et al., 1983 |
| **Back-calculation** | | |
| 1.6 - >3 | alder, hemlock, sword fern, Douglas-fir, & cedar / Washington | Buchanon and Savigny, 1990 |
| 2.2 | devil's club, blueberry, & dogwood / Alaska | Sidle and Swanston, 1982 |
| 2.8 - 6.2 | Ponderosa pine, Douglas-fir, & Engelmann spruce / Idaho | Gray and Megahan, 1981 |
| 3.4 - 4.4 | hemlock & spruce / Alaska | Swanston, 1970 |

# Chapter 3: Spatial Variability of Colluvium Depth and Slope Stability in a Steep Catchment

ABSTRACT

Colluvium depth measurements (n=721: 95 at < 0.4 m spacing; 626 at ≈ 5 m spacing) made with soil probe, auger, and shovel document great spatial variability in a landslide-prone headwall in the Oregon Coast Range. A semivariogram quantifies the correlation between depth measurements such that sites separated by short distances (5 m) are highly correlated (nugget effect = 0.07 m$^2$) while hollow/interfluve pairs and depth measurement separated by > 65 m are statistically distinct. Saprolite and colluvium distribution on the headwall is consistent with a process regime shift such that near the drainage divide landsliding is infrequent, saprolite is preserved, and the uprooting of trees creates depressions in the bedrock surface 1 to 2 m deep and up to 6 m in diameter. At large contributing drainage areas, a higher frequency of landsliding yields homogeneously thin deposits of colluvium, an absence of saprolite, and a relatively smooth bedrock surface. Comparing measured colluvium depths with depths predicted from solely a diffusion-based model of sediment transport reveals an over-estimation of predicted depths in regions of topographic concavity and large contributing drainage areas. A sediment transport power law, determined from topographic attributes at each colluvium depth measurement, was approximated by subtracting measured depths from predicted depths to appraise the material evacuated from the headwall. The form of the transport law representative of a steep catchment is approximated as: $\left(\dfrac{\partial z}{\partial t}\right)_{ls} = 0.08A^{0.5}S^1$, where $\left(\dfrac{\partial z}{\partial t}\right)_{ls}$ is expressed in units of m yr$^{-1}$ X 10$^{-4}$ and the constant has units of m$^{-1}$ yr$^{-1}$ X 10$^{-4}$. GIS-based, slope stability assessments using a detailed digital elevation model (< 3 m grid spacing), assumed homogeneous colluvium depths of 1 m, and predicted colluvial soil

depths tend to over-estimate the surface area of observed landslide source areas. Similar slope stability assessments using measured soil depths result in predictions of unstable areas that more closely correspond to observed landslides because the topographic influence of landslide potential is modified by site-specific conditions.

## INTRODUCTION

The spatial distribution of colluvium over a landscape influences the distribution of biota, hydrologic flow paths, and the potential for shallow-soil, slope instability. The thickness of colluvial cover may also influence the relative conversion rates of bedrock to colluvium (e.g., Gilbert, 1877; Culling, 1963; Ahnert, 1970; Kirkby, 1980) (chapter 4). Although landslide initiation typically results from multiple interrelated factors, colluvium depth tempers many facets of slope stability. For example, the spatial distribution of colluvium thickness regulates hydrologic response by controlling the relative magnitude of saturation for a given discharge of water (e.g., Dunne and Black, 1970; Dunne et al., 1975; Freeze and Cherry, 1979) and the partitioning of subsurface to overland flow (Dunne, 1978). A trade-off also exists between root cohesion and colluvium depth such that thick colluvial deposits require greater cohesion to retard landsliding (e.g., Reneau and Dietrich, 1987).

My field observations support the assertion that thick colluvial deposits require greater reinforcement from root cohesion to retain colluvium on steep, landslide-prone hillslopes (figure 3.1). In landslide headscarps of the Oregon Coast Range, for example, colluvium thickness reveals a weak positive, linear correlation with measured root cohesion (see Chapter 2 for further details of root strength measurements). Furthermore, colluvium thickness modulates whether roots penetrate into bedrock or are limited to growth in the overlying regolith.

Topographic concavities on hillslopes located at the upslope tips of the channel network, often referred to as hollows (Hack and Goodlett, 1960; Hack, 1965), are preferential source regions for landslides. For instance, Hack and Goodlett (1960) and Hack (1965) initially recognized the importance of hollows in the forested Appalachian Mountains of Virginia; Bogucki (1976) showed that landslides in Tennessee and New York originated at valley heads; Pierson (1977) and Dietrich and Dunne (1978) identified the importance of hollows for landslides in the Oregon Coast Range; Okunishi and Iida (1981), Iida and Okunishi (1983), as well as Tsukamoto et al. (1982) discussed their role as preferential landslide sites on hillslopes in Japan; while Lehre (1981), Reneau et al. (1990), and Montgomery (1991) further reinforced the connection between hollows, sediment transport, and channel evolution in the California Coast Ranges.

Although field observations and quantitative modeling support the inference that landsliding preferentially occurs in accumulations of thick colluvium, measurements of the spatial variation of colluvium depth over a landscape are not common. Noteworthy studies documenting colluvium depth include Trustrum and DeRose (1988), De Rose et al. (1991; 1993), and DeRose (1996) in Taranaki, New Zealand. Similarly, Okimura, (1983; 1989), Iida and Okunishi (1983), and Iida and Tanaka (1997) inferred "potential failure layers" and colluvium depth using cone penetrometers in Japan. The connection, however, between colluvium distribution and regional predictions of slope stability is unclear. Recent efforts to apply digital terrain-based models to estimate landslide susceptibility consistently predict areas of equivalent landslide hazard as being much larger than the actual area of instability in a given storm (Carrara et al., 1991; Ellen et al., 1993; Montgomery and Dietrich, 1994; Pack and Tarboton, 1997; Montgomery et al., 1998).

Dietrich et al. (1995), Wu and Sidle (1995), and Montgomery et al. (1997) suggested that spatial variability in factors such as soil depth, root strength, hydraulic conductivity, angle of internal friction, and cohesion can account for why specific sites are more landslide prone. Hence, landslide hazard maps generated from geographic information system (GIS)-based models using either assumed or modeled colluvium depths identify a large number of potential landslide source regions covering a significant portion of the landscape. Not all sites, though, have sufficient accumulations of colluvium to initiate landsliding. Typical landslide-producing storms tend to generate landslides in only a fraction of the total number of hollows in a region. Hence regional, GIS-based models smooth the natural irregularity in actual patterns of landsliding in response to a given storm. By applying regional, process-based landslide hazard analyses, a tension often exists between the long-term occurrence of landslides and analyses attempting to identify short-term landslide potential. Thus predicted, regional landslide distributions characteristic of geologic time scales should be interpreted in the context of local conditions to evaluate the signal of potential landsliding in response to a given storm.

Determining the distribution of colluvium depth over a landscape should help refine the regional identification of landslide source volumes. In application, however, colluvium depth in landslide-prone areas is rarely measured prior to failure because current techniques to measure colluvium depth on a regional basis are exceedingly time consuming. To depict the distribution and magnitude of spatial variability I measured colluvium depth with a soil probe in a steep, landslide-prone headwall of the Oregon Coast Range. The resulting colluvium depth distributions were evaluated in the context of topographic and biologic influences. Furthermore, the distribution of colluvium can be used to evaluate the applicability of deterministic predictive models of sediment generation and redistribution. Hence the model of Dietrich et al. (1995) is used to predict colluvium

depths based on two suites of model input parameters. The resulting spatial distribution of the difference between the predicted and measured colluvium depths is used to constrain a sediment transport law representative of a steep, landslide-prone headwall. To assess the magnitude of possible over-estimation of observed landslide source regions triggered by two storms, I use GIS-based, slope stability models (Montgomery and Dietrich, 1994; Dietrich et al., 1995; Montgomery et al., 1998) to compare model outputs based upon assumed, predicted, and field-measured colluvium depths.

## THEORY AND METHODS

The term colluvium is here used to represent surficial sediment that is derived from and mantles *in situ* weathered or fresh bedrock with negligible input from aeolian transport. The distribution of colluvium depth over a landscape is the result of a complex interplay between the bedrock-to-colluvium production rate (chapter 4), sediment transport via slow mass movement (chapter 4), aeolian transport, and incisional processes. While upslope contributing drainage area, ground surface gradient, and topographic curvature have served as proxies from which colluvium depth has been estimated (e.g., Dietrich et al., 1995), its distribution over a landscape is complicated by numerous factors including spatially variable biologic processes, prior evacuation of colluvium via landsliding, or possibly by overland flow at the tip of the channel network. The transport of colluvium resulting from these physical sediment transport mechanisms can be generally expressed as the sum of diffusive and incisive processes such that:

$$q_s = f(S) + f(A,S) \qquad (3.1)$$

where $q_s$ is the sediment flux, $S$ is the ground surface slope, and $A$ is the upslope contributing drainage area. The first term on the right side of equation 3.1 represents

sediment flux driven by slow mass movement or diffusional processes such as bioturbation while the second term denotes incisional processes that are a function of both slope and contributing drainage area. Thus colluvium depth across a landscape depends on the spatial distribution and rates of slow mass movement and incisional processes. If colluvial transport is driven largely by diffusional processes, the expected distribution of colluvium should be thickest in areas of topographic convergence (i.e., hollows) and thin over interfluves or areas of topographic divergence. Furthermore, the extent of the channel network and the corresponding distribution of colluvium thickness reflects the competing processes of continuous, diffusional infilling and stochastic removal of sediment from landsliding and/or channelized flow. The erosion rate via landsliding, $\left(\dfrac{\partial z}{\partial t}\right)_{ls}$, can be approximated as a power function of $A$ and $S$ such that:

$$\left(\frac{\partial z}{\partial t}\right)_{ls} = KA^m S^n \tag{3.2}$$

where $K$ is a constant representing the material's resistance to erosion while $m$ and $n$ are widely debated constants that are typically assumed $\geq 0$ (e.g., Kirkby, 1971; Smith and Bretherton, 1972; Howard, 1994). The exponent $m$ represents a discharge-drainage area relation that is weighted by the importance of discharge on landslide initiation while $n$ reflects the significance of topographic gradient on landslide initiation. Using predicted and observed distributions of colluvium depth I evaluate values for the exponents $m$ and $n$ in a landscape where slow mass movement and landsliding occur.

*Measuring colluvium depth*

As topographic data represented by large grid spacing (e.g., ≥ 30 m) does not accurately represent fine-scale hillslope textures characteristic of diffusive processes (Zhang and Montgomery, 1994), a digital representation of the topography and location of stumps was generated by field surveying almost 3,700 points with a total station theodolite at an approximate 2 - 3 m point spacing. Using a contour map depicting stump locations generated from the field surveyed topography, I measured 626 colluvium depths with a 1" diameter soil probe (figure 3.2) driven by a hand-powered slide hammer, soil auger, and/or shovel to dig pits at an approximate sampling grid of 5 m. Approximately 5% of the measurements made with probe or auger were substantiated by excavation. An additional 95 depths were measured to examine the influence of 2-D slope, 2-D curvature, and the presence of stumps and downed logs on colluvium depth. In general, the colluvium offered little resistance to penetration, while the unweathered bedrock was relatively impenetrable and therefore the colluvium/bedrock contact was easily identified. Those areas with intermediate layers of saprolite, *in situ* weathered bedrock, were identified by increased resistance to probe penetration and visual changes in color, texture, and relict bedrock structure in core samples. Colluvium depth was measured during the summer of 1995 after the occurrence of a debris flow producing storm in 1992 but prior to the storm of record in November 1996 that triggered widespread landsliding in the southern Oregon Coast Range, including two landslides in the area over which depth was measured.

*Modeling soil production and transport*

I use the soil production model proposed by Dietrich et al. (1995) to predict the spatial variation of colluvium based on a mass balance between soil production from the underlying bedrock and the divergence of diffusive soil transport. The change in the

colluvium thickness is related to the bedrock lowering rate and the local gradient in sediment flux through the continuity equation such that:

$$\frac{\partial(\rho_s z_s)}{\partial t} = \rho_s K \nabla^2 z - \rho_r \frac{\partial e}{\partial t} \tag{3.3}$$

where $z_s$ is the colluvium thickness, $\rho_s$ and $\rho_r$ are the bulk densities of colluvium and rock, $K$ is the diffusion coefficient, $z$ is the ground surface elevation, $\nabla^2 z$ is the topographic curvature, $e$ is the elevation of the bedrock-colluvium interface, and $t$ is time. The first term in equation 3.3 is the change in colluvium thickness with time, the second term is the divergence of colluvial transport assuming that sediment transport is driven by linear diffusion, and the last term is the conversion rate of bedrock to colluvium arising from the lowering of the elevation of the bedrock-colluvium interface, $-\partial e/\partial t$. A steady-state colluvium thickness develops when the downslope flux is balanced by the mass arriving from upslope plus the mass produced by the conversion of rock (e.g., Nikiforoff, 1942). Importantly, this approach does not consider the component of sediment transport resulting from chemical flux or landsliding. Application of the model requires high-resolution digital elevation data, estimates of the diffusion coefficient, a production law to describe the variation in colluvium production with overlying thickness of colluvium, and material bulk densities.

Values of $-\partial e/\partial t$ are estimated using a colluvium production law that expresses an exponential decline in production with increasing colluvial cover such that:

$$-\partial e/\partial t = P_o e^{-lz_s} \tag{3.4}$$

where $P_o$ and $l$ are empirical constants (e.g., Armstrong, 1976; Ahnert, 1977). Two suites of values for $P_o$ and $l$ are obtained through i) the magnitude of topographic divergence and the coefficient of diffusivity (chapter 4), and ii) dating by Heimsath (1999) using cosmogenic isotopes.

Colluvium depth is estimated using the production rate and subsequent transport expressed by equations 3.4 and 3.3. A digital elevation model (DEM) of the headwall derived from total station field surveys was used to route sediment. As bedrock surface morphology is usually unknown, the topographic surface is typically used to route sediment in GIS-based models. Where soil depth measurements constrain the bedrock surface morphology, however, a DEM of the bedrock surface can be used to route sediment. Model outputs were documented at 1 ka time steps for a total of 10 ka model years. All model runs begin with an initial, uniform colluvial cover of 0.1 m.

As the model of Dietrich et al. (1995) does not represent landslide processes, the difference between the predicted and the observed colluvium depths might provide a long term estimate of the material removed by landsliding in the absence of fluvial erosion. The difference between model outputs and measured colluvium depths at each measurement location is used to constrain the exponents in equation 3.2 for a debris flow transport law. Lastly, modeled colluvium depths at 10 ka model years are used to investigate the influence of colluvium depth on slope stability in a GIS-based analysis.

*Modeling slope stability*

Instability of colluvium arises through either i) a reduction of the effective normal stress of the material occurring in response to changes in water pressure, ii) increases in the interstitial pore pressure reducing the effective normal stress of the material, iii) decreases in the internal properties of the materials such as decreased cohesion driven by land use, fire, or climate change, or iv) increased colluvium thickness. To elucidate the importance of colluvium depth in the context of slope stability, the "infinite slope" analysis (e.g., Selby, 1993) can be solved for the critical colluvium depth at the threshold of landsliding. In a 1-D approximation of slope stability, the shear stress, $\tau$, acting over a unit width of the landslide can be represented by:

$$\tau = \rho_{ss} g z_s \sin\theta \cos\theta \tag{3.5}$$

where $\rho_{ss}$ is the saturated, sediment bulk density, $g$ is gravitational acceleration, $z_s$ is the vertical colluvium thickness, and $\theta$ is the ground surface slope. The resisting stress, $S_{sr}$, can be approximated as:

$$S_{sr} = c + (\rho_{ss} - \rho_w h/z_s) g z_s \cos^2\theta \tan\phi \tag{3.6}$$

where $c$ is the total cohesion provided by the colluvium and the root strength, $\rho_w$ is the bulk density of water, $h$ is the saturated portion of colluvium, and $\phi$ is the internal friction angle of the colluvium. For a factor of safety (ratio of the resisting to driving forces) of

unity, $\tau = S_{sr}$ and equations 3.5 and 3.6 are equal. Solving for the critical colluvium depth, $z_{sc}$, yields

$$z_{sc} = \frac{c}{\rho_{ss} g \cos\theta \left\{ \sin\theta - \cos\theta \tan\phi \left[ 1 - \left( \rho_w h/z_s \right)/\rho_{ss} \right] \right\}} \tag{3.7}$$

Figure 3.3 depicts the decreasing factor of safety with increasing colluvium depth for a hollow (CB1) in the Oregon Coast Range assuming that the colluvium is saturated to a height of 0.5 m; a constant $h$ value of 0.5 m independent of the value of $z_s$. In general, thin colluvium generates low driving stresses and the site is stable, independent of the magnitude of cohesion. For the field measured cohesion attributable to root strength along the lateral margin of a landslide at CB1 in 1996 (4.7 kPa), the gravity-induced stress generated by the weight of the material exceeds the resisting stress at colluvial depths greater than about 1.25 m and the factor of safety falls below unity (dashed horizontal line in figure 3.3).

The GIS-based slope stability model used here (SHALSTAB) is a steady-state runoff approximation that incorporates the topographic influence on subsurface discharge and hence positive pore pressure distribution (Dietrich et al., 1993; 1995; Montgomery and Dietrich, 1994). The version of the model applied accommodates spatially variable colluvium depth and root strength properties but the internal angle of friction, bulk density, and the saturated conductivity are assumed to be spatially invariant. The predicted patterns of slope stability are expressed in terms of the critical rainfall necessary to induce landsliding, $q_c$, such that:

$$q_c \geq \frac{T\sin\theta}{A/b}\left[\frac{c}{\rho_w g z_s \cos^2\theta\tan\phi} + \frac{\rho_{ss}}{\rho_w}\left(1 - \frac{\tan\theta}{\tan\phi}\right)\right] \qquad (3.8)$$

where $T$ is the transmissivity of the colluvium, $A$ is the upslope contributing area, while $b$ is the unit contour width through which subsurface discharge flows. Field measurements of hydraulic conductivity at the study site are used to estimate values of $T$. Where the value of $T$ is unconstrained by hydraulic conductivity measurements, a similar approach to equation 3.8 can be used to solve for the ratio $(q/T)_c$ as in equation 2.11. For more detailed discussions of the model, its assumptions, and performance see chapter 2, Dietrich et al. (1993; 1995), Montgomery and Dietrich (1994), and Montgomery et al. (1998). Resulting patterns of critical rainfall necessary to induce slope instability are evaluated using i) an assumed, homogeneous 1 m depth, ii) predicted depths using the model of Dietrich et al. (1995) and two suites of model input parameters, and iii) the field-measured colluvium depths.

*Manipulation of spatial data*

The ground and bedrock surfaces were characterized by fitting two-dimensional, second-degree polynomials to local subsets (314 m$^2$ area) of the ungridded x, y, z locations of the topographic data at an even 5 m spacing. The local gradient ($|\nabla z|$) and curvature (Laplacian operator, $\nabla^2 z$) were then calculated from the best-fit equations to the nine elevations of the 3 X 3 submatrix (e.g., Zaslavsky and Sinai, 1981; Zevenbergen and Thorne, 1987; Moore et al., 1991; 1993). Calculations were limited to those sites with at least 10 nearest neighbors within a 10 m radius. This limiting criteria eliminated thirty-one sites (5% of the data set located along the margins of the study area) from the analyses producing a data set of 595 colluvium depths. Digital elevation models (DEM) of the

topographic and bedrock surfaces as well as the digital data sets of curvature, hillslope gradient, colluvium depth, and saprolite depth were gridded and contoured using a minimum tension interpolation scheme in the *EarthVision* software package produced by Dynamic Graphics, Inc. The minimum tension, or more commonly referred to minimum curvature scheme, uses a third-order spline, such that a continuous function is found for all values of the independent variable (e.g., Briggs, 1974). The solution is forced to honor the value of the observation at the $(x, y)$ spatial position of the observation and hence the contouring process remains true to the original data.

*Spatial statistics*

Most natural features examined in earth sciences are distributed in space and typically express substantial variability. If a naturally occurring property is continuous, but cannot be represented by an ordinary function it is referred to as a "regionalized variable" (e.g., Davis, 1986; Oliver and Webster, 1990). Topographic and structural surfaces are examples of regionalized variables that embody characteristics intermediate between truly random variables and completely deterministic variables. Although spatially correlated over short distances, widely separated points of a regionalized variable tend to be statistically independent. As a measure of spatial continuity and a means to quantify the area-of-influence of a regionalized variable, the statistical technique of a semivariogram represents all possible pairs of data values whose locations are separated by a specific distance in a specific direction. Consider two numerical values $z(x)$ and $z(x+h)$, at two points $x$ and $x+h$ separated by the lag, or vector $\bar{h}$. The variability between this pair of points can be characterized by the semivariogram function, $\gamma^*(\bar{h})$:

$$\gamma^*(\bar{h}) = \frac{1}{2n} \sum_{i=1}^{n} [x_i - (x_i + h)]^2 \qquad (3.9)$$

where $n$ is the number of observations. The semivariogram function, half the mean-square of successive differences between the $x$ and $x + h$ coordinates of each data pair, increases as the values of the variable become less similar (e.g., Matheron, 1962, 1963; Isaaks and Srivastava 1989; Cressie, 1991). The relationship between the variogram function, $\gamma^*(\bar{h})$, and the separation distance of the points, $|\bar{h}|$, is called a semivariogram, a function of the variance of the increment. By varying $\bar{h}$, an ordered set of values is obtained that constitutes the semivariogram, a practice common in mining applications and frequently used in the context of soil properties (e.g., Vauclin, 1983). The variogram approach is sensitive to direction of sampling (vector $\bar{h}$) and the separation distance or lag spacing ($|\bar{h}|$) but not the location $x$ or a particular position in space.

Gradual changes in $\gamma^*(\bar{h})$ near the origin indicate strong spatial continuity while a sudden increase reflects significant short-scale variability. As the distance $|\bar{h}|$ approaches zero, each data point is paired with itself and hence the value of $\gamma^*(\bar{h})$ approaches zero. Although $\gamma^*(\bar{h}) = 0$ at $|\bar{h}| = 0$, sampling error and short scale variability will cause data pairs separated by short distances to be disparate, resulting in a discontinuity at the origin. The nugget effect represents the offset from the origin of the semivariogram to the value of $\gamma(h)$ at short separation lengths. With increasing values of $|\bar{h}|$, data typically become less similar and the value of $\gamma^*(\bar{h})$ increases. One of the salient features of a semivariogram is the sill, the limit at which the separation distance is no longer influenced by the

corresponding increase in the mean square of successive differences between data pairs. Hence, the variogram reaches the sill at the range that represents of the distance beyond which data pairs are no longer correlated.

Constructing a semivariogram requires the selection of an assumed spacing between data pairs and a sampling direction. The distance increment or lag spacing, $|\bar{h}|$, is selected based on the attributes of the data set. Since the colluvium depth measurements were obtained on a pseudo-regular grid, the lag spacing and the measurement spacing are roughly equivalent (i.e., 5 m). To examine variation of colluvium depth in all directions I used an omnidirectional variogram. The determination of an omnidirectional variogram does not assume that the spatial continuity is equivalent in all directions, rather, direction does not play a role allowing for the evaluation of distance parameters in all directions.

## STUDY AREA

Characteristic topography of the southern Oregon Coast Range is steep (up to 45°) and highly dissected into distinct hollows and interfluves (noses) resulting from a combination of diffusive (Roering et al., 1999), fluvial (Dietrich and Dunne, 1978), and mass wasting transport mechanisms (Pierson, 1977; Dietrich and Dunne, 1978; Benda and Dunne, 1987; Reneau and Dietrich, 1990). While mass wasting is often concentrated in topographic hollows (Dietrich and Dunne, 1978), diffusive processes may be active over the entire landscape. In the Oregon Coast Range diffusive transport of colluvium is demonstrated by accumulations upslope of trees and stumps, and by mounds and burrows created by mountain beavers (*Aplodontia rufa*) (Feldhamer and Rochelle, 1982). Field observations of well-established deer tracks and mountain beaver burrows attest to widespread bioturbation.

The study site (Mettman Ridge) is located 15 km northeast of Coos Bay, Oregon (figure 3.4) at an elevation of about 300 m a.s.l. The area was clear-cut logged in 1987 and replanted with Douglas-fir saplings in 1988. Situated on Mettman Ridge is CB1 (blue polygon in figure 3.4), an experimental study site examining the hydrologic response of a steep unchanneled valley to applied and natural rainfall (Anderson et al., 1997; Montgomery et al., 1997; Torres et al., 1998). Wooden catwalks anchored to cables over the ground surface were constructed throughout CB1 during 1989 to minimize disturbance due to walking and instrument installation.

As the parent material is an Eocene sandstone, siltstone, and mudstone (Lovell, 1969), the texture of the colluvium is relatively homogeneous throughout the hillslope; a sandy matrix with isolated clasts of sandstone up to tens of centimeters in diameter. Laboratory tests reveal a non-plastic colluvial material with a mean Atterberg plastic limit of about 56. A stress path analysis of low confining stress triaxial shear tests carried out on relatively undisturbed, 3" diameter colluvial soil samples from CB1 indicate that the material has a friction angle of 33° and is cohesionless. The present understory vegetation is dominated by a dense growth of thimbleberry, blue elderberry, vine maple, and sword fern with Douglas-fir and red alder up to about 4 m tall forming the canopy. The temperate, maritime climate is wet and relatively mild with mean annual precipitation totals of 1500 to 3000 mm (Corliss, 1973). Precipitation falls mainly as rain with infrequent subzero temperatures. During November 1996, the storm of record (66 years) hit the southern Oregon Coast Range triggering widespread landsliding. Rain gauge measurements from the CB1 site document that the storm of November 16 - 18, 1996 in the Coos Bay area produced 225 mm of rain with a maximum daily intensity of 150 mm day$^{-1}$ and a 48 hour average intensity of 85 mm day$^{-1}$.

RESULTS

Using a contour map generated from the field surveyed topography (figure 3.4), I measured 626 colluvium depths over 12,400 $m^2$ of the Mettman Ridge headwall (red polygon in figure 3.4) with a soil probe (figure 3.2), bucket auger, and/or shovel at an approximate sampling grid of 5 m (figure 3.5). The bedrock/colluvium contact was typically abrupt, characterized by distinct changes in color, texture, and compressive strength. Although the distribution of colluvium was expected to be thickest in hollows and thin over interfluves, the measured distribution shows significant spatial heterogeneity. Figure 3.6, a perspective view of an isopach map draped over of the DEM of the Mettman Ridge headwall, reveals that while pockets of colluvium up to 3 m deep are visible near drainage divide, the lower half of the headwall is mantled by a homogeneous cover of colluvium generally less than 0.25 m deep. The degree of weathering within the deep pockets of colluvium was often advanced such that pronounced oxidation and numerous charcoal layers were observed. In contrast, colluvium in the lower portion of the headwall was characterized by a thin cover of relatively unaltered mineral components indicative of a weathering limited environment (Carson and Kirkby, 1972). The total volume of colluvium, determined by subtracting the grid of the bedrock surface from the ground surface grid, is 7,400 $m^3$ distributed over the 12,400 $m^2$ area; a mean depth of 0.6 m. Cross section A - A' depicted in figures 3.5 and 7A reveals that along a topographic contour, the lateral edges of the two hollows, CB1 and CB2, are fairly distinct. Furthermore, although the bedrock surface defining CB1 is more deeply incised than CB2, it is filled with a thinner deposit of colluvium, retaining a more pronounced topographic concavity at the ground surface. Longitudinal cross sections B - B' and C - C' (figures 3.5, 3.7B, & 3.7C) show a progressive thinning of colluvium downslope to the confluence at the location of a prior (1992) debris flow deposit. The longitudinal cross sections show nearly smooth

bedrock surfaces on the lower portion of the slope while bedrock surfaces on the upper portion of the headwall have significant texture over the scale of meters to tens of meters.

While the isopach map and cross sections provide qualitative estimates of the length scale of spatial variability, colluvium depth variability can be quantified using spatial statistics. Overall, the spatial distribution of colluvium depth is relatively continuous such that two observations close to one another are more similar than data separated by large distances. That is, low values cluster near other low values and high values tend to be located near other high values. For example, the omnidirectional semivariogram for colluvium depth calculated with equation 3.9 reveals a modest gradient in $\gamma^*(\tilde{h})$ for values of $|\tilde{h}| < 40$ m, indicating moderately strong spatial continuity of colluvium depth (figure 3.8). The gradient in $\gamma^*(\tilde{h})$ near the origin represents the degree of spatial continuity of the colluvium depth such that the linearity of the variogram to the sill shows that colluvium depth varies in a spatially correlated fashion. The semivariogram stops increasing beyond a distance of about 65 m becoming more or less stable around the sill value of 0.46 m$^2$. The range of 87 m, greater than the separation distance between hollows, indicates that individual hollow/interfluve pairs are statistically distinct. Furthermore, the small discontinuity at the origin (nugget effect = 0.07 m$^2$), signifies strong spatial continuity over short length scales such that there is little variability at the length scale less than the sampling interval ($\approx$ 5 m grid).

In situ weathered bedrock or saprolite is commonplace near the drainage divide, occurring as distinct patches under thicker colluvial deposits and is uncommon on the lower half of headwall (figure 3.9). Saprolite, found in 48 exploratory holes (roughly 8% of the 626 sites), is located within both convergent and divergent topography and is

typically thinner than overlying colluvium (figure 3.10). Saprolite is located beneath moderate depths of colluvium, with the majority detected at sites with less than about 1.5 m of overlying colluvium (figures 3.10 and 3.11). Figure 3.11 is a histogram representing the depth of overlying colluvium at sites with and without saprolite. The calculated mean and median colluvium depths at sites with saprolite are 0.93 and 0.82 m whereas the mean and median colluvium depths at the sites without saprolite are 0.53 and 0.40 m. As the medians are not equivalent, it appears as if saprolite is preferentially produced or preserved under thicker colluvial deposits as often theoretically predicted. Saprolite, however, was not present at sites with > 2 m of overlying colluvium.

The topographic attributes of gradient and curvature are commonly thought to influence the magnitude and distribution of sediment transport (e.g., Kirkby, 1971; Dietrich et al., 1995). The DEM's of the topographic and bedrock surfaces allow for the correlation of colluvium depth measurements with topographic attributes. For example, a gradient map of the topographic surface for the headwall area depicts the steeper gradients ($> 0.90$ m m$^{-1}$) on the lower half of the headwall (orange to red hues on figure 3.12), corresponding to uniformly thin ($< 0.25$ m) colluvium (figure 3.6). The low-gradient region at the base of the headwall corresponds to the 1992 debris flow deposit. Although, the gradient of the bedrock surface expresses a broader range, its distribution and correlation with colluvium depth is roughly equivalent to that of the ground surface (figure 3.13). The relation between the topographic gradient of the bedrock surface, upslope contributing area, and colluvium depth (figure 3.14) discloses that the majority of sites with greater than 0.5 m of colluvium are located in regions with less than a 500 m$^2$ upslope contributing drainage area. Figures 3.13 and 3.14 show that colluvium depth has a rough normal distribution about equivalent mean gradients; $0.82 \pm 0.12$ m m$^{-1}$ and $0.82 \pm 0.10$ m m$^{-1}$ for the bedrock and ground surfaces, respectively. In the context of equation 3.2, it

appears as if increasing gradient has a minor influence on colluvium depth in a steep headwall while contributing drainage area has a more dominant control.

The influence of topographic curvature on sediment transport over the hillslope and hence colluvium depth is expressed in equation 3.3. Figure 3.15 is a perspective view of ground surface curvature draped over the DEM for the Mettman Ridge headwall. The threshold separating planar (yellow) from the divergent topography of the interfluves (green) occurs at a curvature of roughly - 0.025 $m^{-1}$. Strongly convergent regions (orange to red) appear as a dendritic pattern delineating the colluvial channels and pronounced hollows. Figure 3.16 reveals that the thickest colluvium occurs in areas of planar topography. For sites with greater than 1 m of colluvium the bedrock surface shows slightly greater curvature than the ground surface, reflecting the infilling of topographic concavities on the bedrock surface with colluvium. Hence, the bedrock hollows are largely filled, resulting in relatively planar topography at the ground surface. The filling of bedrock concavities is also expressed by the population statistics such that the ground surface is negatively skewed (- 1.1) with a mean curvature of 0.009 $m^{-1}$. The bedrock surface represents a lower negative skewness (- 0.4) with a slightly greater mean curvature of 0.012 $m^{-1}$. Furthermore, colluvium depth is negatively correlated with both divergent and convergent topography such that the upside-down, funnel-shaped distribution of colluvium depth is roughly centered about an axis of zero curvature (figure 3.16). A similar "funnel-shape" was observed by Iida and Tanaka (1997) where thin colluvium was observed on both convex and concave topography. The negative correlation between topographic divergence and colluvium thickness is consistent with transport by diffusive processes. Figure 3.17 depicts a histogram of colluvium depth and bedrock surface curvature for convergent, planar, and divergent topography. If sediment transport occurred solely by diffusive processes, the areas of strongly convergent topography would

theoretically have the thickest deposits of colluvium. Rather, planar topography has the highest median value of colluvium depth (0.60 m), while convergent topography expresses a median colluvium thickness (0.45 m) roughly equivalent to divergent topography (0.40 m). Hence, other transport processes other than slow mass movements, such as shallow landsliding of the colluvial mantle, may remove material from convergent topography, thereby decreasing mean soil depths.

To ascertain the relationship between colluvium depth and topographic form in convergent topography, I measured a detailed longitudinal profile 36 m long at an approximate 0.4 m interval down a colluvial channel axis (not shown on figure 3.5). Colluvium depth is not linearly correlated with the 2-D local longitudinal slope (figure 3.18A) but is positively related with the 2-D longitudinal curvature (figure 3.18B). Thus patterns of increased sediment deposition within colluvial channels appear to be related to positive longitudinal curvature or the change in longitudinal gradient.

Figures 3.6 through 3.18 show significant variation of colluvium and saprolite depth and the relative influence of morphologic attributes of the landscape on the depth of the deposits. Biological factors, however, are also responsible for variations in the depth of colluvium across the landscape. For example, root wads, stumps, and downed trees temporarily trap material as it moves downslope, thus increasing the colluvium depth. Figure 3.19 reveals that even on a 44° hillslope, the presence of a downed tree on a older colluvial surface can almost double the depth of colluvium from 0.87 m to 1.48 m. Similarly, the presence of in situ root wads of stumps effectively traps material moving downslope (figure 3.20). The relation depicted in figures 3.19 and 3.20 are not isolated instances, rather increased depths of colluvium upslope of trees and stumps were commonly observed throughout the study area. Alternatively, tree uprooting by blow down

efficiently redistributes colluvium by transporting blocks of colluvium downslope and sometimes introduces fresh bedrock into the colluvium. Lastly, bioturbation arising from mountain beaver disturbance appears to be responsible for the bulk of the material transported by the presently active diffusive processes (chapter 4). The spatial distribution of the above mentioned biologic processes is complex. For example, stumps are apparently concentrated on divergent topography, downed trees and the occurrence of tree throw were seemingly randomly distributed, while mountain beaver disturbance may concentrate in thicker colluvial deposits (chapter 4).

## Modeled colluvium depth and a landslide transport law

No efficient means of collecting regolith depth data currently exists and characterizing colluvium depth over a large area using a soil probe is a time-consuming, tedious process. In contrast, the use of process-based models in conjunction with high-resolution DEM's provides estimates of colluvium distribution on a regional basis in a timely manner and by modifying model input parameters a variety of boundary conditions can be readily evaluated. To relate predicted colluvium distribution based solely on transport by diffusive or slow mass movement processes with the actual distribution of colluvium for an environment exhibiting an amalgam of transport processes, I use the model of Dietrich et al. (1995) with two suites of input parameters to produce theoretical predictions of colluvium depth. The empirical constants, $P_o$ and $l$, expressed in equation 3.4, are assessed through measurements of i) the magnitude of topographic divergence and the coefficient of diffusivity (chapter 4) and ii) from dating of the colluvial profiles using cosmogenic isotopes (Heimsath, 1999). In chapter 4 I determined the colluvium production rate for Mettman Ridge is $-\partial e/\partial t = 0.071e^{-0.1z_s}$, where $\partial e/\partial t$ is expressed in mm yr$^{-1}$ and $z_s$ is measured in meters. For comparison, the colluvium production as a

function of overlying colluvium depth as calculated from concentrations of cosmogenic

$^{10}$Be and $^{26}$Al radionuclides is $-\partial e/\partial t = 0.28e^{-3z_i}$ (Heimsath, 1999). Thus input

parameters specific to measurements reported here (suite 1) are $-\partial e/\partial t = 0.071e^{-0.1z_i}$ and

$K = 20$ cm$^3$cm$^{-1}$yr$^{-1}$ (chapter 4). Input parameters based on measurements from

cosmogenic radionuclides (suite 2) are $-\partial e/\partial t = 0.28e^{-3z_i}$ and $K = 45$ cm$^3$cm$^{-1}$yr$^{-1}$.

Using the model of Dietrich et al. (1995) I generated outputs of colluvium depth

distribution at 1 ka intervals and ran the model for a total of 10 ka. All model runs use the

following material bulk densities: $\rho_s = 1.2$ tonnes m$^{-3}$, $\rho_r = 2.2$ tonnes m$^{-3}$ (see chapter 4

for discussion of bulk density measurements) and an initial colluvium thickness of 0.1 m

covering the DEM of the bedrock topography defined by field measurements of colluvium

depth. Rather than route sediment through the ground surface grid, predicted colluvium

depths are derived using the bedrock surface grid as it is thought to be more representative

of morphologic template routing diffusive sediment transport. At the catchment scale the

ground and bedrock surfaces share similar attributes such that they have comparable mean

gradients (both are 0.82; figure 3.13). Localized differences are expressed by the fact that

the mean curvature of the bedrock surface (0.012 m$^{-1}$) is slightly higher than the ground

surface (0.009 m$^{-1}$) (figure 3.16) and the bedrock surface curvature expresses a slightly

lower negative skewness resulting from the presence of concave depressions and more

convergent topography. As the bedrock surface is marked by localized concavities not

expressed by the ground surface, the use of the bedrock surface grid to predict soil depths

results in patterns that more closely resemble the actual soil depth distribution. That is,

pockets of deep colluvium on the upper half of the headwall (figure 3.6) cannot be

reproduced using the ground surface grid in the predictive model.

Model outputs based on the parameters in suite 1 (figure 3.21A) and suite 2 (figure 3.21B) produce thick deposits at the base of the hillslope with moderately deep colluvium concentrated in the topographic concavities. The pattern of colluvium deposition is similar for the two suites of parameters but differ in magnitude by nearly a factor of two. The predicted colluvial depths are thinner using the parameters from suite 1 because the bedrock-to-colluvium production rate and the coefficient of diffusivity are both lower (chapter 4). As the predicted colluvium depths are derived from a model that solely embodies diffusive processes, the predicted distributions in figure 3.21 do not match the actual distribution in figure 3.6 because the actual depths are the outcome of a mixture of transport processes.

Field observations at Mettman Ridge over a decade, including two debris flow producing storms (1992 and 1996), suggest that sediment is transported via diffusive, landslide, and channel processes. Debris flows triggered in CB1 and CB2 during storms in 1996 failed on the interface between the regolith and the unweathered bedrock surface. After the landsliding, the thin veneer of colluvium remaining on the shear surface was observed to be quickly eroded by overland flow during the next storms. Hence observations indicate that sediment is primarily removed from the basin via landsliding with infrequent overland flow. To compare the modeled depths based purely on diffusive transport with the measured colluvial depths representative of an aggregate of processes, I subtracted the measured depths from the predicted depths. The "missing depth" is depicted for the two suites of model parameters in figure 3.22A & B where green pixels represent regions where the modeled depth is approximately equivalent to the measured depths. Warm colors represent areas where there is a positive mis-match whereas cool colors represent regions where the model under-predicts the actual depth. The most notable differences occur near the ridgetop where the model under-predicts the colluvium

depth and in the pronounced topographic concavities where the model over-predicts the depth. In the prominent topographic concavities the missing depth likely results from sediment evacuation from the headwall via landsliding and/or channel processes. The spatial distribution of missing material in conjunction with the morphologic attributes of the landscape can be used to estimate the exponents of a landslide transport law.

Using only positive values of predicted minus observed thickness, figure 3.23 shows the relationship of the lowering rate, $\left(\dfrac{\partial z}{\partial t}\right)_{ls}$, expressed in equation 3.2 with the upslope contributing area, bedrock surface gradient, and product of $AS$ assuming that both exponents $m$ and $n$ are equal to unity. While there appears to be a strong correspondence with upslope contributing area (figure 3.23A), and hence with the product of $AS$ assuming that both $m$ and $n$ are equal to unity (figure 3.23C), no pronounced relationship between the local bedrock surface gradient and lowering rate is apparent (figure 3.23B). If the exponent on slope, $n$, assumed to be unity, the exponent on area, $m$, is calculated for each point estimate of the missing depth (n = 353) such that mean is 0.57 ± 0.23 with a median of 0.54. Similarly, if $n$ is assumed to be zero the mean value of $m$ is 0.55 ± 0.25 with a median of 0.51. The majority of the values for $m$ concentrate between values of 0.25 and 0.75, for either $n = 0$ or $n = 1$ (figure 3.24). Assuming that sediment transport via landsliding has a slope dependence of $S^1$ over the range of gradients examined, where $S$ has a mean value of 0.82 on Mettman Ridge, the relation between lowering rate, contributing upslope source area, and local bedrock surface slope can be expressed as:

$$\left(\frac{\partial z}{\partial t}\right)_{ls} = 0.08 A^{0.5} S^1 \qquad (3.10)$$

where $\left(\dfrac{\partial z}{\partial t}\right)_{ls}$ is expressed in (m yr$^{-1}$) X $10^{-4}$ and $K$ is expressed in (m$^{-1}$ yr$^{-1}$) X $10^{-4}$.

Equation 3.10 represents the mean hillslope gradient and the material resistance to landsliding including the time-integrated friction angle and the cohesion from the colluvium and root strength from vegetation. As a cautionary note, equation 3.10 does not represent the conditions necessary for an individual landslide, rather the average geomorphic attributes for long-term sediment removal via landsliding and possibly overland flow.

## GIS-based slope stability modeling

As landslide susceptibility determined from digital, terrain-based models consistently over-predicts areas of instability (Carrara et al., 1991; Ellen et al., 1993; Montgomery and Dietrich, 1994; Pack and Tarboton, 1997; Montgomery et al., 1998), I use four scenarios to investigate the influence of colluvium depth distribution on patterns of predicted instability: i) an assumed, homogeneous 1 m colluvial depth; ii) predicted colluvium depth using suite 1 parameters; iii) predicted colluvium depth using suite 2 parameters; and iv) the field-measured colluvium depth. Using a variant of the GIS-based slope stability model presented by Dietrich et al. (1993); Montgomery and Dietrich (1994); and Dietrich et al. (1995) patterns of slope stability are expressed in terms of the critical, steady state rainfall necessary to induce landsliding, $q_c$. In conjunction with the DEM (figure 3.4) and the measured and predicted colluvium depths (figures 3.6 and 3.21), all model outputs were generated using the following model inputs to equation 3.8: a depth-integrated, saturated soil transmissivity, $T = 65$ m$^2$ day$^{-1}$; saturated soil density, $\rho_{ss} = 1.6$ tonnes m$^{-3}$; a bulk density of water, $\rho_w = 1$ tonne m$^{-3}$; a friction angle, $\phi = 33°$; and a cohesion, $c$, of 2 and 4 kPa. Values of $T$, $\rho_{ss}$, and $\phi$ were determined from field and laboratory measurements specific to CB1.

Model outputs of the critical steady-state rainfall necessary to generate landsliding are depicted in figure 3.25 for the cases of an assumed 1 m soil depth, predicted soil depths (figure 3.21), and measured soil depths (figure 3.6). Warm colors in figure 3.25 represent regions that theoretically produce landslides under low rainfall intensities while cool colors represent areas requiring high intensities to trigger landsliding. The black pixels in figure 3.25 are unstable without rainfall at the prescribed cohesion such that:

$$\tan \theta \geq \frac{c}{\rho_{ss} g z_s \cos^2 \theta} + \tan \phi \qquad (3.11)$$

Similarly, the beige pixels are stable under all rainfall intensities at the prescribed cohesion such that:

$$\tan \theta \leq \frac{c}{\rho_{ss} g z_s \cos^2 \theta} + \tan \phi \left( 1 - \frac{\rho_w}{\rho_{ss}} \right) \qquad (3.12)$$

Patterns of predicted landslide susceptibility are strongly influenced by the spatial distribution of colluvium depth. For example, the numerous pixels representing low $q_c$ values in figures 3.25A & B are allied to an overestimation of colluvium depth in areas of topographic convergence or steep gradients. As the hydrologic response of the model is topographically driven, instability concentrates in the areas of topographic convergence. In addition, the widespread instability in figure 3.25A for the 2 kPa cohesion case arises from the association of thick soils in areas where the topographic gradient exceeds the friction angle. A relatively small increase in cohesion, though, from 2 to 4 kPa greatly reduces the proportion of unstable area. Similar to figure 3.25A, the low critical rainfall intensities

depicted in figure 3.25B concentrate in areas of topographic convergence where the predicted soil depths are thickest . A comparison of figures 3.6 and 3.25C reveals that the small number of pixels predicted to be unstable under moderate $q_c$ values correspond to regions that have large upslope contributing areas in association with thick deposits of colluvium. At present a relatively small percentage of the landscape is covered with sufficient colluvium to initiate landsliding under moderate rainfall intensities.

Fortuitously, I documented three landslide locations on Mettman Ridge since 1992. For example, the colluvium in the downslope portion of CB2 was removed via landsliding and deposited at the base of the headwall in 1992. The measurement of colluvium depth prior to the occurrence of landsliding in 1996 and the record of rainfall intensities at the time of landsliding provides for unique tests of the model outputs. Rain gauges situated on CB1 recorded 150 mm/day for a 1 day period or 85 mm/day averaged over a 2 day period for the storm of record in November, 1996. Moreover, the location of pixels in figure 3.25C with $q_c$ values between 0 to 200 mm yr$^{-1}$ correspond to the 1992 and 1996 landslide locations. The storm of record in November, 1996 initiated landslides in both hollows CB1 and CB2 which mobilized into debris flows removing a significant portion of the colluvium within the hollows, incorporating the 1992 debris flow deposit depicted at the base of figure 3.6, and transporting material out of the basin a distance of about 1.5 km. While topographic attributes may dictate the regional, long-term pattern of slope stability, site-specific soil depth may influence the actual distribution of landslides generated in a given storm.

The number of pixels within a given $q_c$ category represents the magnitude of predicted landslide susceptibility in response to a given storm for the four modeled cases

of homogenous, predicted, and measured colluvium depths. Figure 3.26 delineates a

significant shift in $q_c$ categories such that the assumed homogenous 1 m depth and the

predicted depths over-estimate the spatial extent of instability for low critical rainfall

intensities. In contrast, the measured colluvium depths produce patterns of potential

instability that are confined to the highest intensity $q_c$ categories or alternatively are stable

at the prescribed value of cohesion. For the case of $c$ = 2 kPa, only those predictions

determined from the measured soil depths identify a small proportion of the number of

pixels to be unstable. Alternatively, predictions based upon the measured depths identify

the largest percentage of stable pixels: 36% for the case of $c$ = 2 kPa and 68% for the case

of $c$ = 4 kPa(represented by beige pixels in figure 3.15 and equation 3.12). Slope stability

predictions determined from the homogeneous 1 m soil depth, however, uniformly under-

predict the percentage of stable ground (1% for $c$ = 2 kPa and 3% for $c$ = 4 kPa).

## DISCUSSION

Colluvium depth expresses a complex relation to morphologic attributes of the

landscape. For instance, in regions where diffusive transport is the primary sediment

transport mechanism colluvium thickness should theoretically increase with topographic

convergence. Likewise, if transport rates were spatially invariant, colluvium depth would

theoretically increase with upslope contributing area. Colluvium depth on Mettman Ridge,

and thus sediment transport, is not a simple function of topographic curvature and gradient

as expressed by equation 3.3. That is, thick deposits were identified in regions of moderate

gradient and planar topography (figures 3.6, 3.12 - 3.16). It would thus be difficult to infer

colluvium depth using the approach suggested by Dengler and Montgomery (1989) where

the ground surface expresses only a slight planform curvature. In addition, the longitudinal

profiles B - B' and C - C' (figures 3.5, 3.7B, & 3.7C) depict a smooth bedrock surface on

the lower half of the hillslope that is either exposed or covered by uniformly thin

colluvium. On the upslope portion of the hillslope, though, the profiles reveal significant texture in the bedrock surface where colluvium thickness exceeds 3 m. The downslope decrease in colluvium thickness (figures 3.6 and 3.7) reflects either spatially variable sediment transport or colluvium production rates.

If production rates do not decrease systematically with upslope drainage area, a sediment flux that increases with distance from drainage divide would result in thin colluvium and an absence of saprolite on the lower half of the headwall. Contrary to diffusive processes which are independent of contributing drainage area (e.g., Koons, 1989; Willgoose et al., 1991; Howard, 1994; Fernandes and Dietrich, 1997), it appears as if the transport process or processes operating on Mettman Ridge express an area dependence such that $m$ is roughly 0.5 while the dependency on slope is minimal such that $n = 1$, and can be represented by the mean hillslope gradient. Sediment transport laws similar to equation 3.2 have been used to characterize a number of environments such that the range of $m$ and $n$ exponents varies substantially depending on the process investigated. For instance, power law approximations for the process of soil creep indicate the exponent $m$ ranges between 0 and 1 while $n = 1$ (Davison, 1889; Culling, 1963; Kirkby, 1987). Similarly, the exponents for rainsplash are $0 < m < 1$ and $0 < n < 1$ (Schumm, 1964; Kirkby, 1971; 1987) while for soil wash the higher exponents vary between $1.3 < m < 1.7$ and $1.3 < n < 2$ (Zingg, 1940; Musgrave, 1947; Kirkby, 1971; 1987). Within bedrock channels of badlands topography, Howard and Kerby (1983) document that $m = 0.44$ and $n = 0.66$. Stock and Montgomery (1999) report that the exponents for rivers incising into bedrock with stable base levels in Australia are $0.3 < m < 0.5$ and $n = 1$. For the incision of bedrock rivers in coastal Oregon Seidl and Dietrich (1992) report that the ratio $m/n$ is equal to 1.0 for bedrock channels with gradients less than 0.2. On gradients steeper than 0.2 Seidl and Dietrich (1992) suggest the $m/n$ ratio is about 0.7, reflecting a greater slope

dependency for debris-flow dominated channels. The results reported here do not support the increased slope dependency in a relatively small, steep drainage basin where the topographic gradient typically exceeds 0.6 (i.e., figure 3.23). Rather the exponents for the transport law reported here most resemble those representative of creep and rainsplash. As the transport law reported here is determined from the difference between the predicted depths arising solely from slow mass movement and the actual depths arising from a combination of slow mass movement and landslide processes, it is thought that the form of the erosion law is dominantly representative of landslide and overland flow processes. Furthermore, field observations indicate that the occurrence of overland flow is limited to regions recently cleared of colluvium by landsliding.

The difference in predicted and observed colluvium thickness on the lower portion of the headwall was used to infer the removal of sediment by landsliding. A secondary influence on colluvium depth arises from the effect of tree uprooting, downed trees (figure 3.19), *in situ* stumps (figure 3.20), and recent bioturbation by mountain beaver (chapter 4). On the upper portion of the hillslope the increased roughness of the bedrock surface (figures 3.6 and 3.7) is representative of disturbance by tree uprooting. Floralturbation (Hole, 1961; Schaetzl et al., 1989) or arbroturbation (Beke and McKeague, 1984) is the mixing of regolith by the action of trees. Floralturbation driven by tree uprooting is caused by either strong winds, senescence as old roots die and decay, fire, or climate change. The uprooting of trees and the subsequent disturbance to the regolith is a natural process identified in almost all forest landscapes (Schaetzl et al., 1989). In North America, for instance, the influence of floralturbation has been well documented in the east (Denny and Goodlet, 1956; 1968; Lyford and MacLean, 1966; Beke and McKeague, 1984; Cremans and Kalisz, 1988), northern plains (Stearns, 1949; Kabrick et al., 1997), and Pacific Northwest (Reid, 1981; Swanson et al., 1982). In Alaska, where the occurrence of

wildfires is rare, tree throw is the predominant disturbance influencing forest stand development (McClellan et al., 1990).

On Mettman Ridge the deep pockets near the drainage divide express characteristic diameters of 6 m for an individual depression while assemblages of multiple depressions range up to 30 m in length (figure 3.6). Dimensions of pit and mound topography resulting from windthrow in the Deton Creek area near Mettman Ridge (Montgomery, unpublished data) document that a 1 m diameter tree is associated with a 6 m diameter pit extending vertically to a depth of 1 to 2 m (figure 3.27). Similarly, Reid (1981) measured dimensions of uprooted coniferous trees in the Olympic Mountains of Washington and determined that a 6 m diameter root wad, extending to a depth of 0.6 to 0.8 m, corresponds to a 1 m diameter tree with an average 4 $m^3$ volume of displaced sediment per tree throw. Swanson et al. (1982) estimate that in the Oregon Coast Range the density of tree uprooting is 11 sites ha$^{-1}$ while Reid (1981) reports an average of 18 uprooted trees per kilometer of channel over a 75 year period. At Mettman Ridge it is likely that relatively frequent landsliding in regions of large upslope drainage areas gives rise to a smooth bedrock surface covered by a thin veneer of colluvium while bedrock lowering in areas with small drainage areas occurs by floralturbation resulting in a bedrock surface marked by depressions as deep as 2 m. Even though microtopography at the ground surface resulting from floralturbation can persist for more than 1000 years (Schaetzl and Follmer, 1990), surficial expression of floralturbation on the steep topography of Mettman Ridge is absent, presumably erased by rheologic creep and diffusion via bioturbation (chapter 4).

As floralturbation entrains rock into the regolith, influencing the thickness and development of soil horizons [e.g., Lutz and Griswold 1939; Beke and McKeague 1984), tree uprooting is likely an important process of colluvium production. Furthermore, root

wads of large diameter trees can act as cantilevers, dislodging rock of great volume (1.4 m³) and mass (4.3 tonnes)(Lutz, 1960). The inference that floralturbation is an important colluvium production mechanism raises the issue of the long-term stability of colluvium mantles where tree throw no longer operates. For instance, the Holocene signal of colluvium production on Mettman Ridge is likely dominated by the occurrence of tree throw. Under current land use practices, though, trees are harvested prior to the onset of widespread tree uprooting, potentially decreasing rates of colluvium production. If land use practices increase sediment flux, as is widely reported, and decrease colluvium production, the practice of industrial forestry on steep, landslide-prone topography may not be sustainable.

Landslide recurrence intervals (average duration between landslides initiating from the same site on a hillslope) are a function of the time necessary to accumulate sufficient colluvium for instability (e.g., figure 3.3) and the return period of landslide-triggering rainstorms (e.g., Shimokawa, 1984; Trustrum and DeRose, 1988). During the period following sediment evacuation by landsliding, colluvium is thin, rock weathering and pedogenesis may occur, and the site is not prone to landsliding. The frequency of landsliding is thus a complex function of the time since the last event regulating the colluvium depth, the spatial distribution of vegetation and roots influencing cohesion, and the distribution of groundwater which may be associated with upslope drainage area or flow through local bedrock fractures. The distribution of deep pockets of colluvium in the headwall area near the drainage divide supports Dunne's (1991) interpretation that the upper portions of a basin fail less frequently. The presence of saprolite in the thickest accumulations of colluvium, indicative of a long duration without disturbance, is consistent with the inference that hollow source regions undergo partial removal of the available deposit. Hence basal colluvial ages should decrease in age with distance from divide.

Dating of colluvial and alluvial deposits in the Pacific Northwest, however, has resulted in a wide range of dates and subsequent interpretations. This discrepancy may stem from the fact that basal ages undoubtedly represent a wide range of upslope contributing areas. For example, a study specific to the southern Oregon Coast Range dated charcoal pieces within basal colluvium using radiocarbon techniques with upslope drainage areas ranging from 100 to 4100 m$^2$ (Reneau and Dietrich, 1991). Using similar techniques, Reneau and Dietrich (1990) report a clustering of basal radiocarbon dates between 4000 to 7500 years B. P. for sites in Oregon and Washington which the authors interpreted to indicate a change in mid-Holocene climate that favored landsliding. In another study specific to the Oregon Coast Range, Benda and Dunne (1987) dated basal radiocarbon in the lower portions of hollows at 1600 to 9500 years B. P. Dating of alluvial terraces throughout the Oregon Coast Range by Personious et al. (1993) imply a regional evacuation of sediment brought about by climate change during the Pleistocene-Holocene transition. Dunne (1991) suggested that under a constant climate, basal ages differ between the upper and lower portions of hollows because colluvium is evacuated more frequently from the lower portion of hollows. The results presented here support the hypothesis that published basal ages may simply represent the time necessary to refill hollows to a critical depth of colluvium in an unchanging climate. The evacuation, however, of the upper portions of hollows may demand changes in climate or fire regime as proposed by Reneau and Dietrich (1990) and Personious et al. (1993).

If the goal of landslide prediction is to determine the potential hazard related to specific hollows or sensitivity to land use practices, the inclusion of colluvium depth data greatly refines GIS-based predictions. In forest management, for example, the definition of harvest units may focus on the relevance of cutting individual trees which emphasizes the need for detailed measurements of both root strength and colluvium depth at the scale of

landslide source regions. The comparison of patterns of instability based on the measured colluvium depths with the observed locations of landslides from two debris flow producing rain storms at Mettman Ridge upholds the regional applicability of predictive models. As these model outputs can identify individual landslide source regions they are highly pertinent to land use management decisions. With the continued acquisition of high-resolution topographic data, there likely will be an increased demand for commensurate high-resolution coverage of the input parameters necessary for slope stability analyses. Hence, future investigations may benefit from applying techniques such as ground penetrating radar or shallow seismic reflection/refraction to appropriate colluvium depth data.

## CONCLUSION

The spatial variability of saprolite and colluvium over a steep, landslide-prone headwall in the Oregon Coast Range is a complex function of topographic curvature, upslope drainage area, frequency of landsliding, and tree uprooting. A semivariogram quantifies correlation between colluvium depth measurements such that measurements separated by short distances (5 m) are closely related (small nugget effect) but hollow/interfluve pairs separated by > 65 m are statistically distinct. The sporadic appearance of saprolite and the lack of developed soil horizons is thought to reflect frequent disturbance by mixing of the colluvium by tree uprooting and rapid sediment transport on steep slopes. The distribution of colluvium is consistent with a possible process regime shift roughly midway down the headwall such that near the drainage divide landsliding is infrequent, saprolite is preserved, and the uprooting of trees creates depressions in the bedrock surface up to 2 meters deep and 6 meters in diameter. A higher frequency of landsliding at larger contributing drainage areas results in uniformly thin deposits of colluvium, an absence of saprolite, and a smooth bedrock surface.

Comparison of predicted colluvium depths based on a sediment transport model representative solely of diffusive processes does not replicate the observed depths resulting from an amalgam of transport processes. Hence *a priori* predictions of the actual colluvium distribution over a landscape must incorporate all the operational processes of colluvium generation and redistribution. Based on a unique data set of two slide producing storms, the assumed and predicted colluvium depths used in a GIS-based assessment of slope stability tend to overestimate the area of observed landslide source regions. Patterns of modeled slope stability produced from the actual distribution of colluvium, though, correspond to observed landslide locations.

y = 5.85x + 0.046   $R^2$ = 0.58
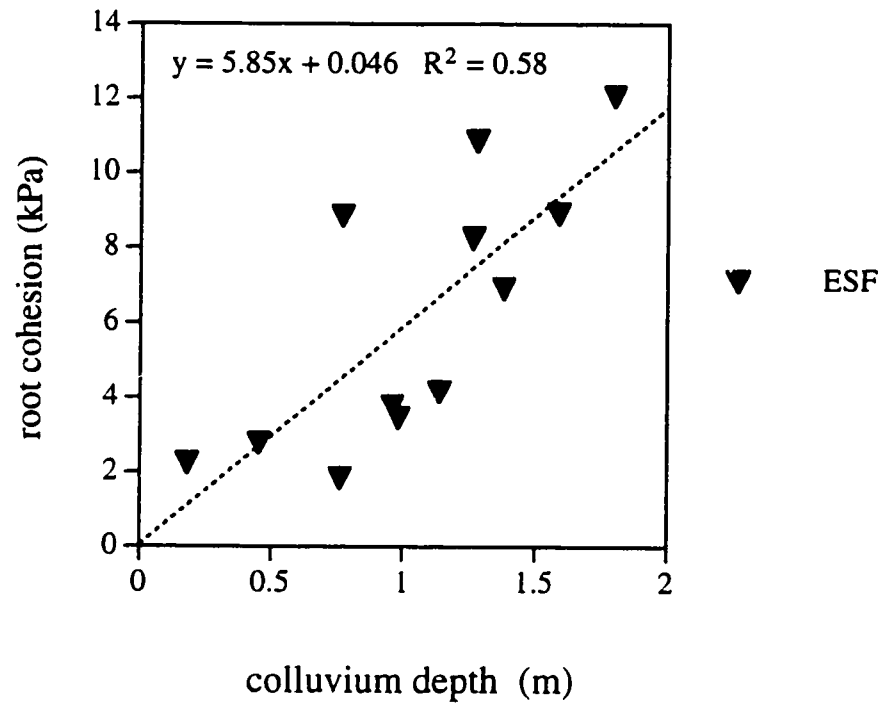
Figure 3.1    Positive correlation between mean landslide thickness and measured root cohesion for 12 landslides in the Elliot State Forest (ESF) of the Oregon Coast Range (see chapter 2 for more details). At the threshold of landsliding, sites with deep colluvial deposits are associated with greater reinforcement from root strength.

Figure 3.2    Photograph of soil probe used to measure colluvium depth.  Probe, hand-driven
with slide hammer, samples a 1" core of material such that color and texture is visible in cut-out
window.
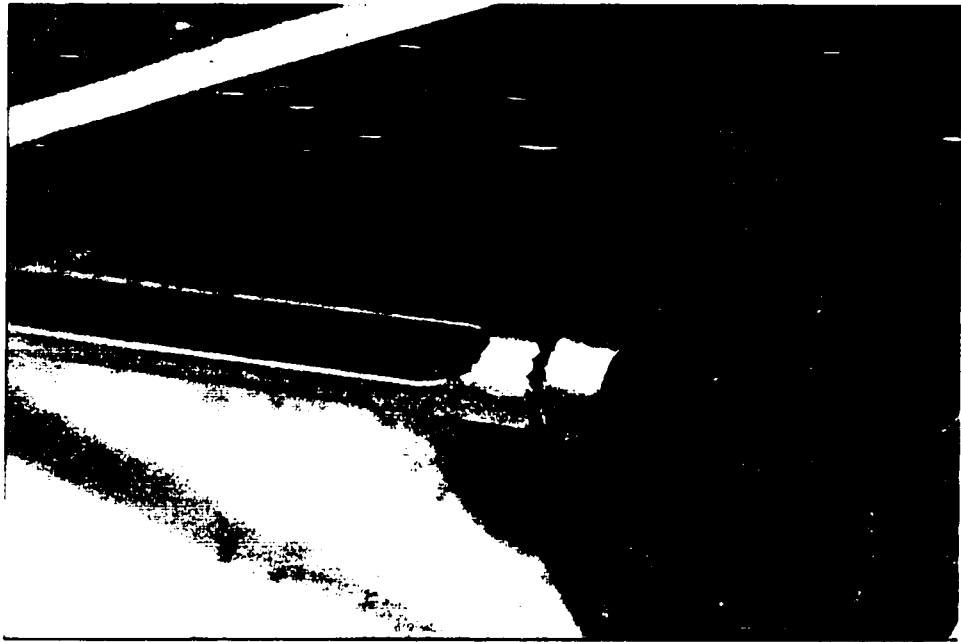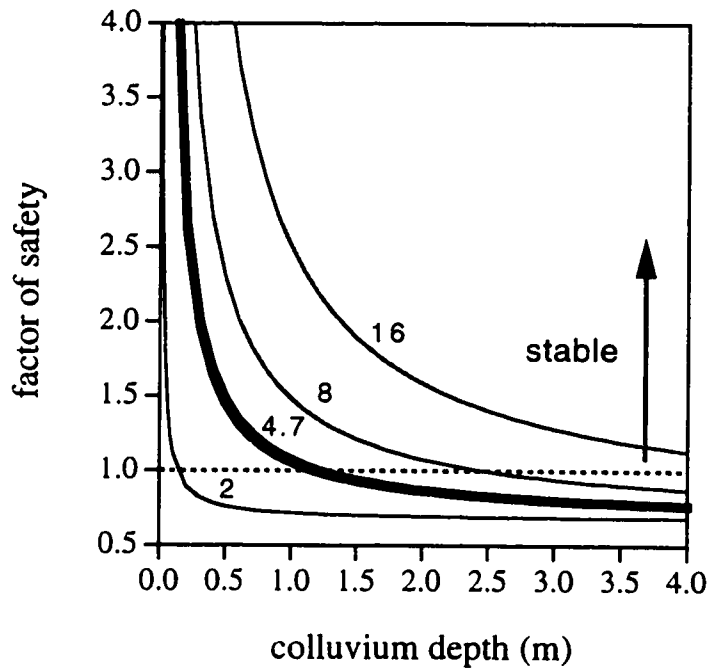
Figure 3.3    Inverse relationship between the factor of safety and colluvium depth for different cohesion values. Plot generated by holding all variables in equation 3.7 constant ($h$ = 0.5) except for $z_{sc}$ and $c$. Curves correspond to 2, 4.7 (field-measured root strength denoted by heavy line), 8, and 16 kPa of cohesive strength. The region on the plot above a factor of safety of unity (dashed, horizontal line) represents stable conditions. This hypothetical scenario is modeled after a specific study hollow (CB 1, see figure 3.4) in the Oregon Coast Range.

Figure 3.4     Study site located northeast of Coos Bay represented by asterisk in Oregon state map (lower). Contour lines on the perspective view (upper) of the DEM of the Mettman Ridge headwall at 10 m interval with heavy green contours every 50 m; view of DEM is due south at an inclination of 25° and no vertical exaggeration. The blue polygon draped over the DEM represents the 860 m² CB1 study site while the yellow polygon represents the hollow CB2. The red polygon demarcates the 12,400 m² area of colluvium depth measurements and calculations of topographic gradient, curvature, and upslope contributing area. Note, scale bar on perspective view varies with apparent distance toward the ridge top. Similarly, the contour interval cannot be used to determine absolute ground surface gradient. For planform view of area denoted by red polygon see figure 3.5.

300

CB1

CB2

250

200

40 m

OREGON

N

*
Coos Bay

0          200 km
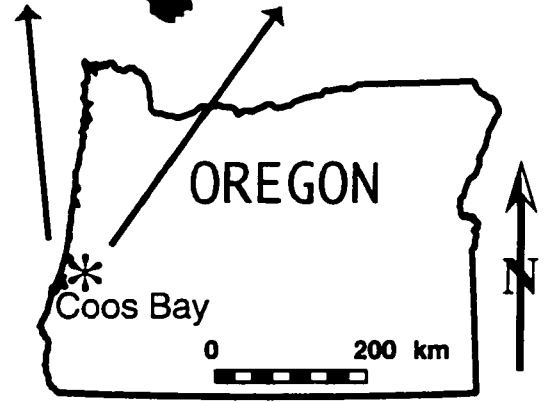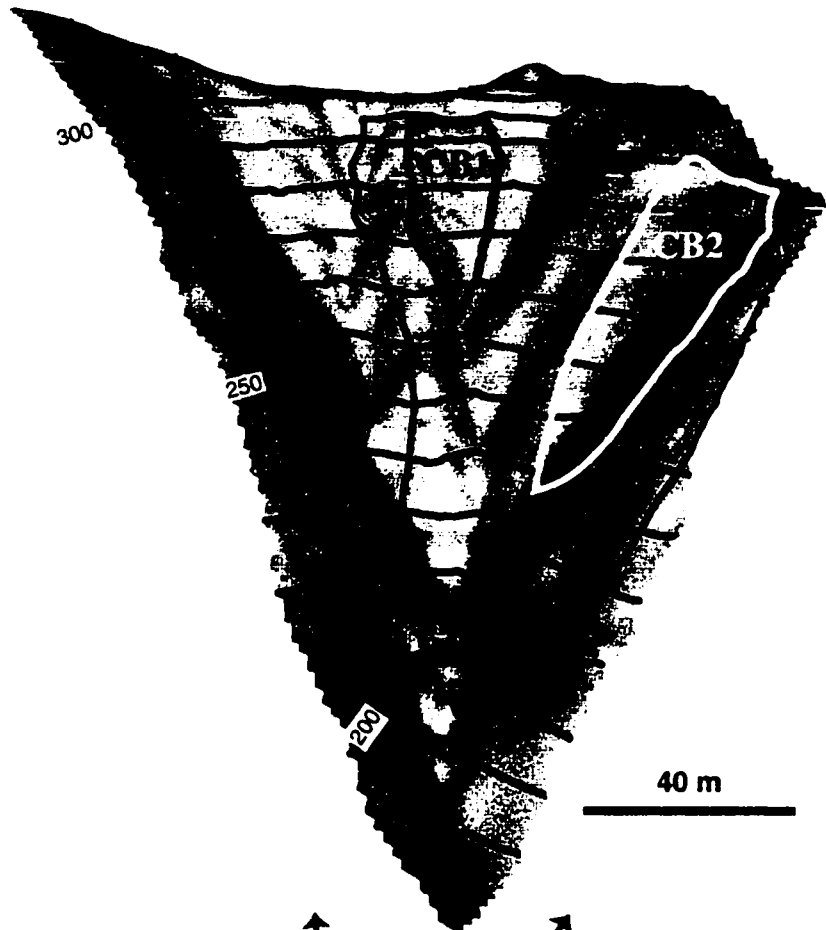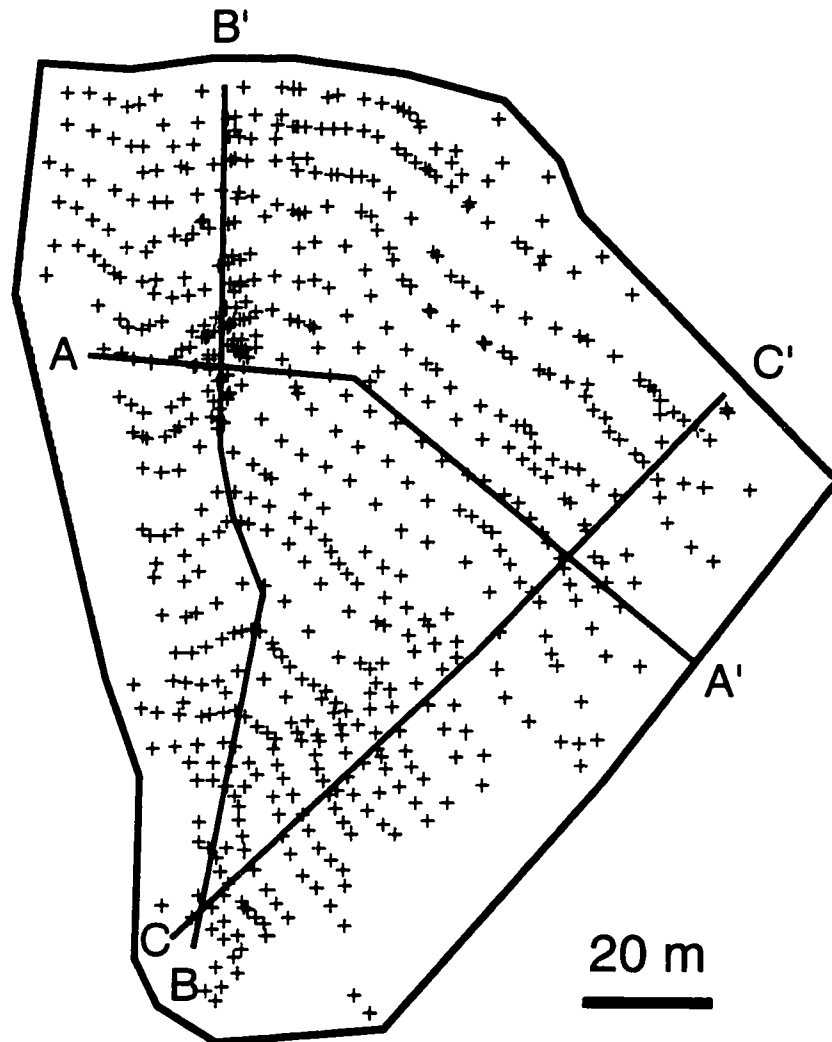
Figure 3.5    Plan view of 626 colluvium depth measurements marked by "+" symbols and cross sections A - A', B - B', and C - C' within red polygon denoted on figure 3.4.

Figure 3.6    Perspective view of colluvium depth distribution draped over the DEM (azimuth
= 155°, inclination: 10°, no vertical exaggeration). Thick deposits (red colors) are located near
drainage divide while the lower portion of the headwall is mantled with relatively thin deposits
(cool colors), except for the 1992 debris flow deposit at the base of the headwall at the
confluence.

meter

| | |
|---|---|
| | >3.0 |
| | 2.8 |
| | 2.6 |
| | 2.4 |
| | 2.2 |
| | 2.0 |
| | 1.8 |
| | 1.6 |
| | 1.4 |
| | 1.2 |
| | 1.0 |
| | 0.8 |
| | 0.6 |
| | 0.4 |
| | 0.2 |
| | 0.0 |

debris-
flow
deposit

20 m
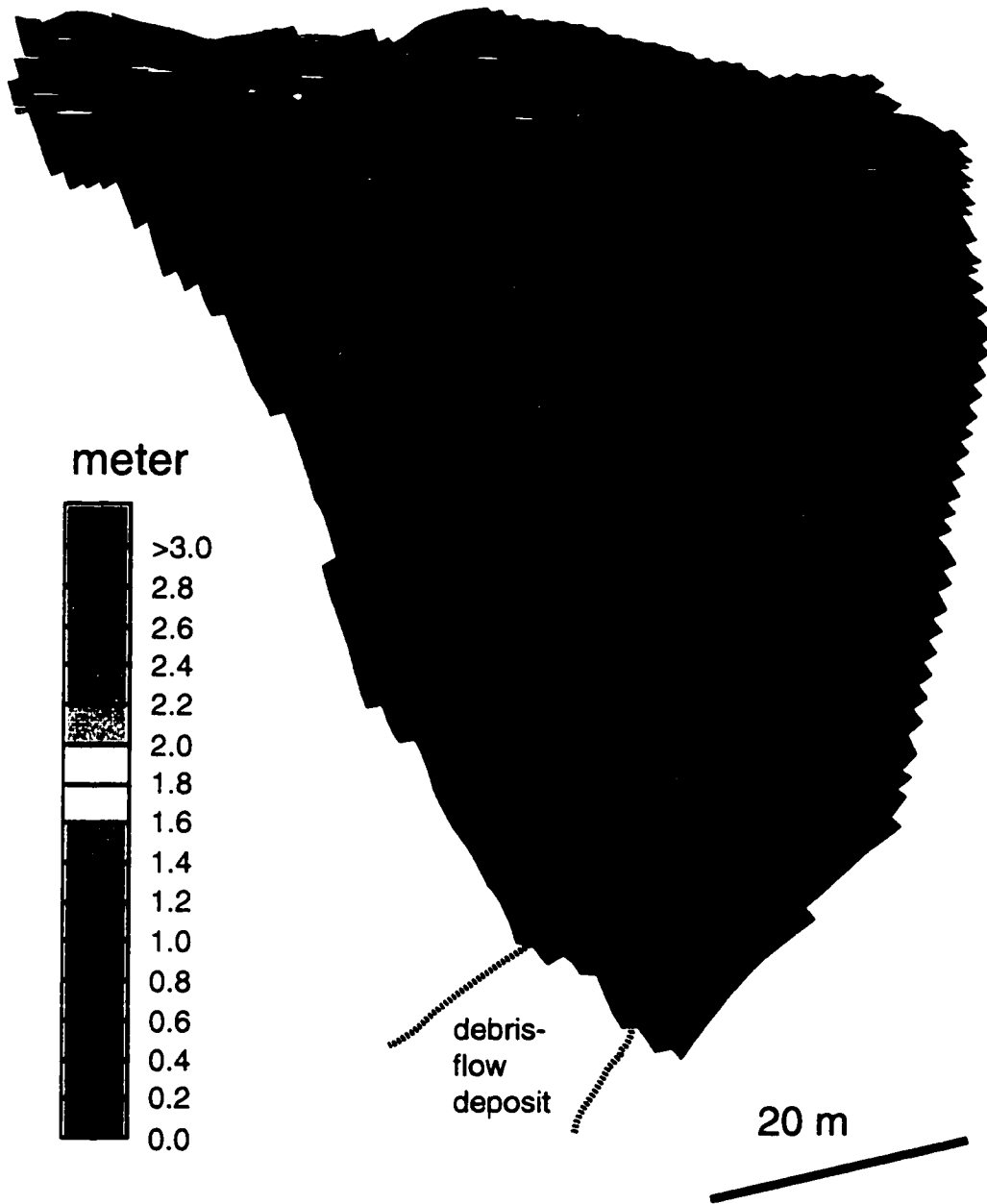
Figure 3.7A    Cross section A - A', depicting locations of hollows CB1 and CB2, colluvium (green), and bedrock (yellow) where the thickest deposits occur on the upper half of the hillslope (see figure 3.5 for cross section locations).

139
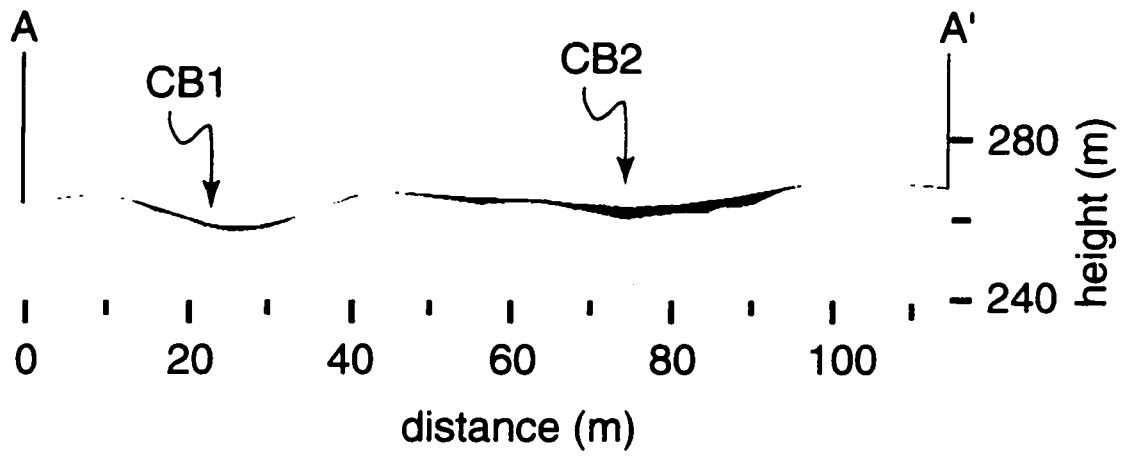
Figure 3.7B    Cross section B - B', depicting locations of hollows CB1 and CB2, colluvium (green), and bedrock (yellow) where the thickest deposits occur on the upper half of the hillslope (see figure 3.5 for cross section locations).

140
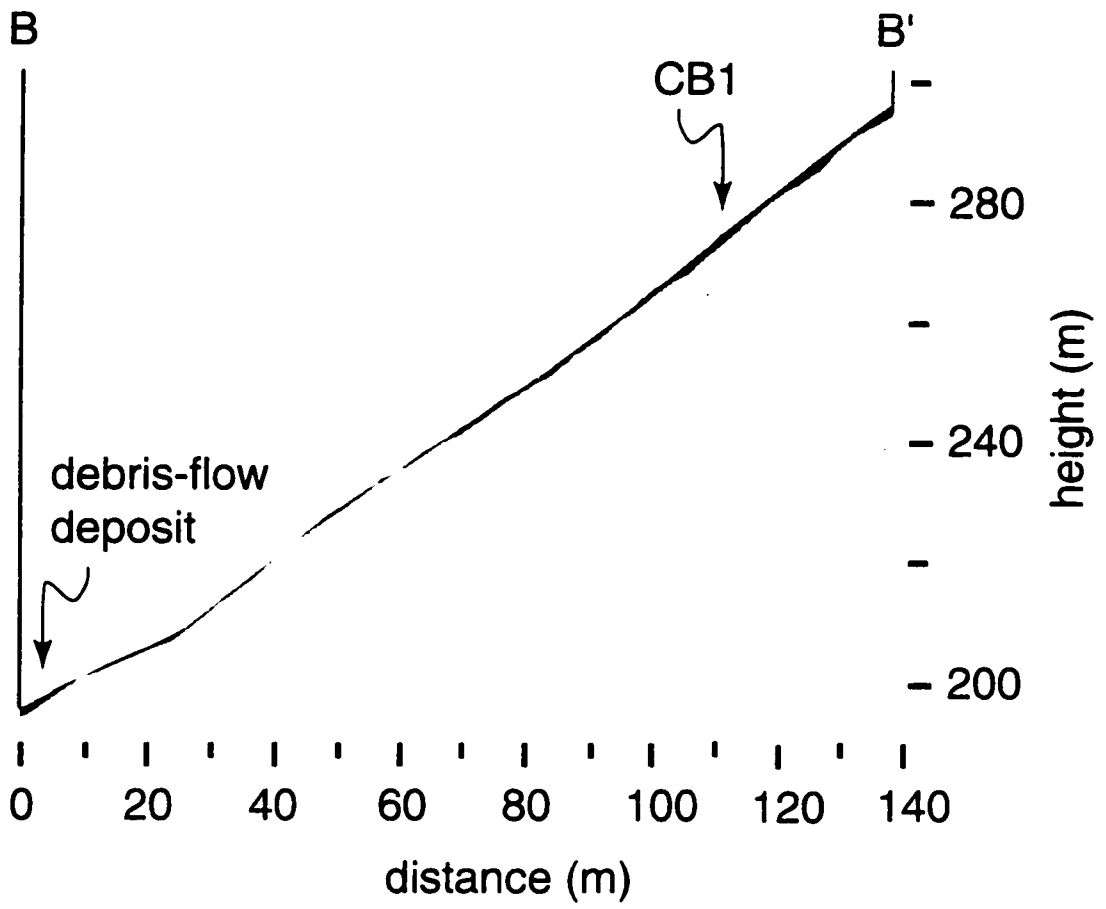
Figure 3.7C    Cross section C - C' depicting locations of hollows CB1 and CB2, colluvium (green), and bedrock (yellow) where the thickest deposits occur on the upper half of the hillslope (see figure 3.5 for cross section locations).

Semivariogram, spherical model
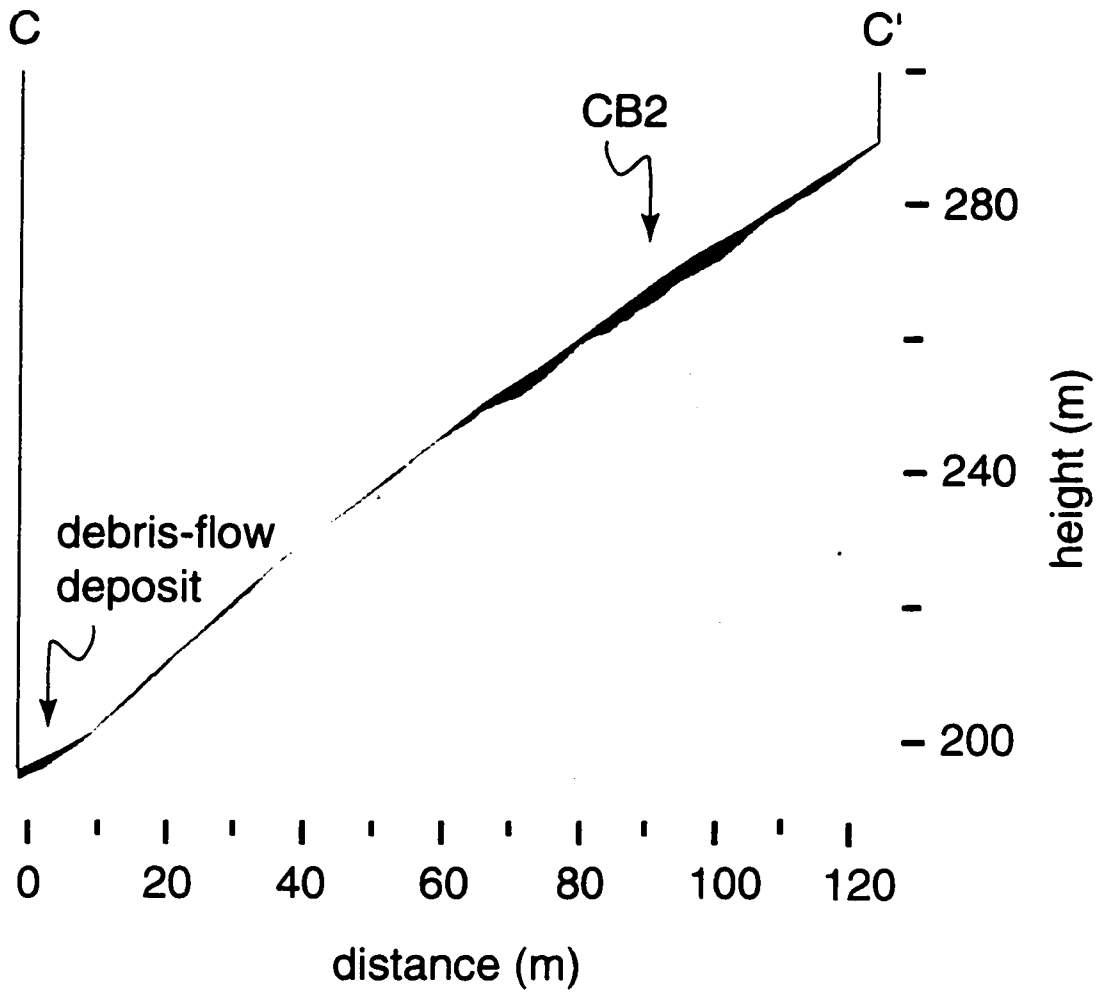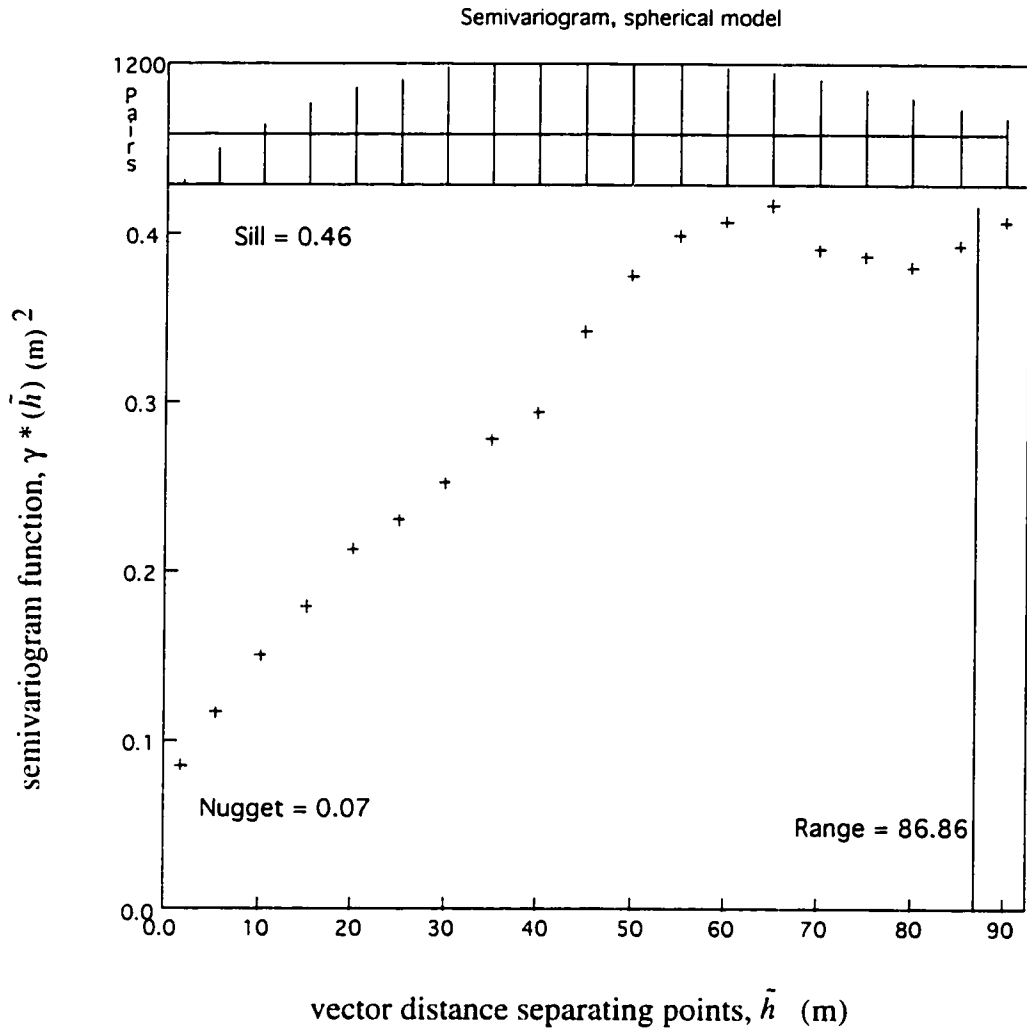


Figure 3.8    Omnidirectional semivariogram constructed using a 5 m lag spacing portraying spatial variability of colluvium depth. The salient features are a sill = 0.46 m$^2$, range = 87 m, nugget = 0.07 m$^2$, and a relative nugget effect (ratio of nugget to sill) of 0.15. Although colluvium depth is highly correlated over short distances, the plateau in semivariance around 65 m reveals that the colluvium depth of individual hollow/interfluve pairs are statistically distinct.

Figure 3.9    Perspective view of saprolite distribution draped over the DEM (azimuth = 155°, inclination: 10°, no vertical exaggeration). Thick deposits occur as distinct pockets located in areas of topographic convergence and divergence near drainage divide while the lower portion of the headwall is devoid of saprolite, represented by the shaded gray scale of the DEM.

meter

> 1.1
1.0
0.9
0.8
0.7
0.6
0.5
0.4
0.3
0.2
0.1
> 0.01

20 m
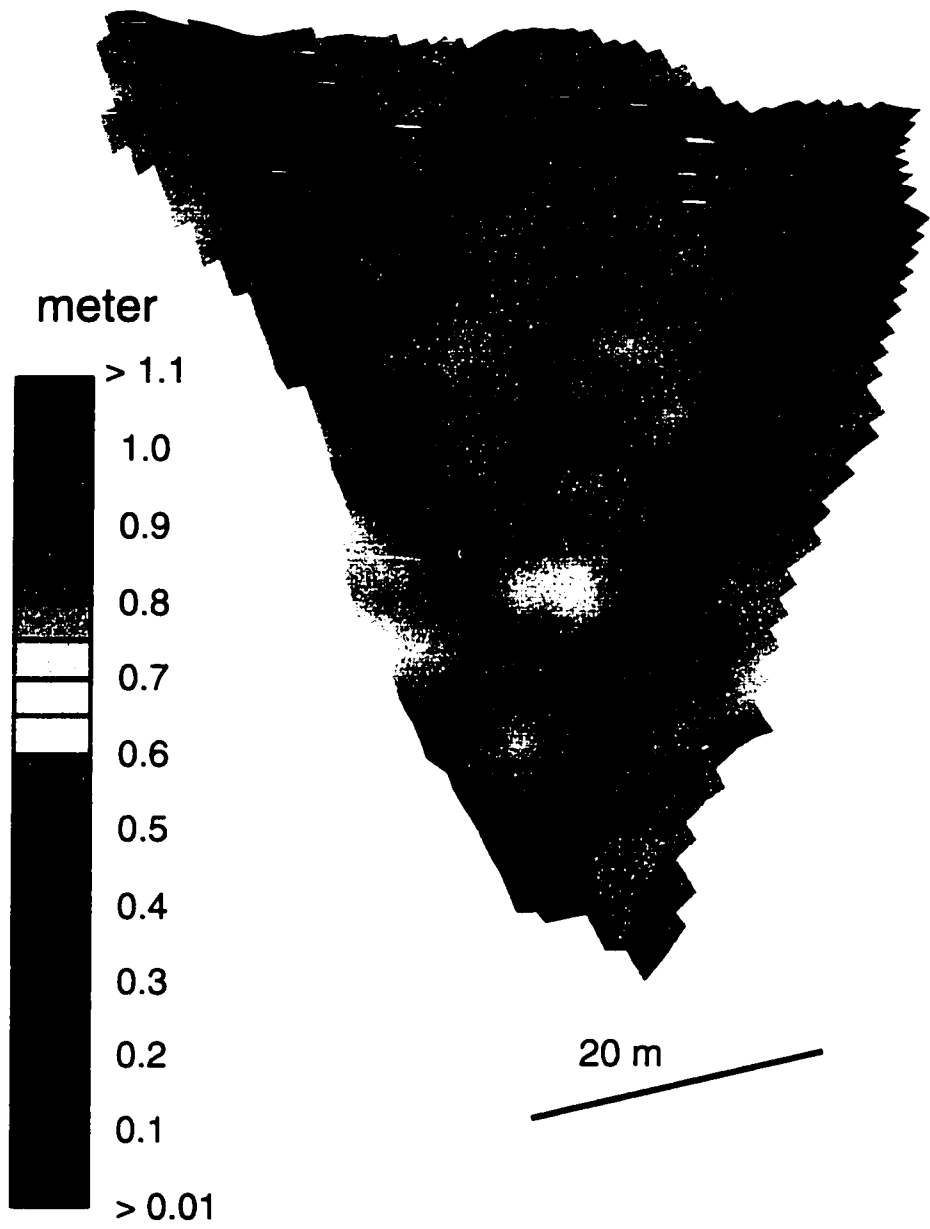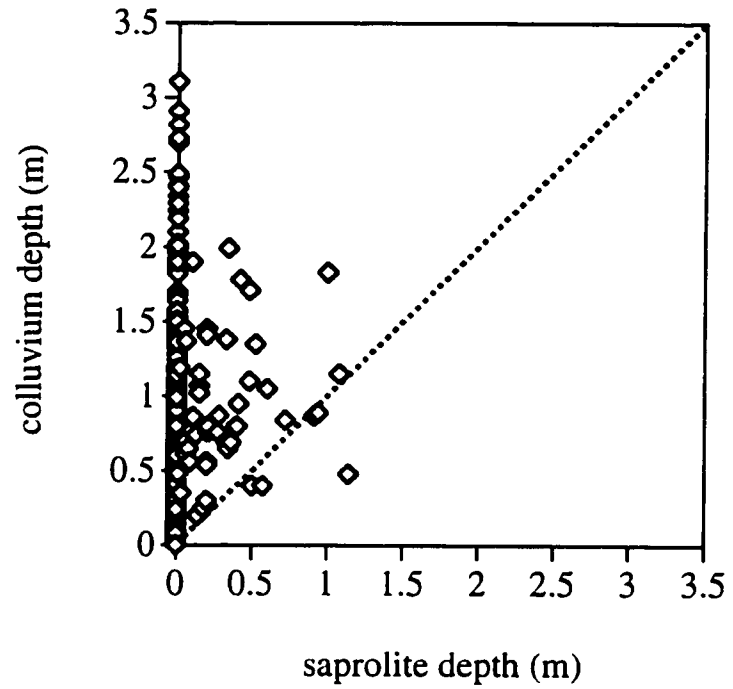
Figure 3.10    Relationship between saprolite and colluvium depth at locations where saprolite was present.  One-to-one relationship between saprolite and colluvium depth represented by dashed 45° line reveals that colluvium depth is generally greater than the underlying saprolite depth.
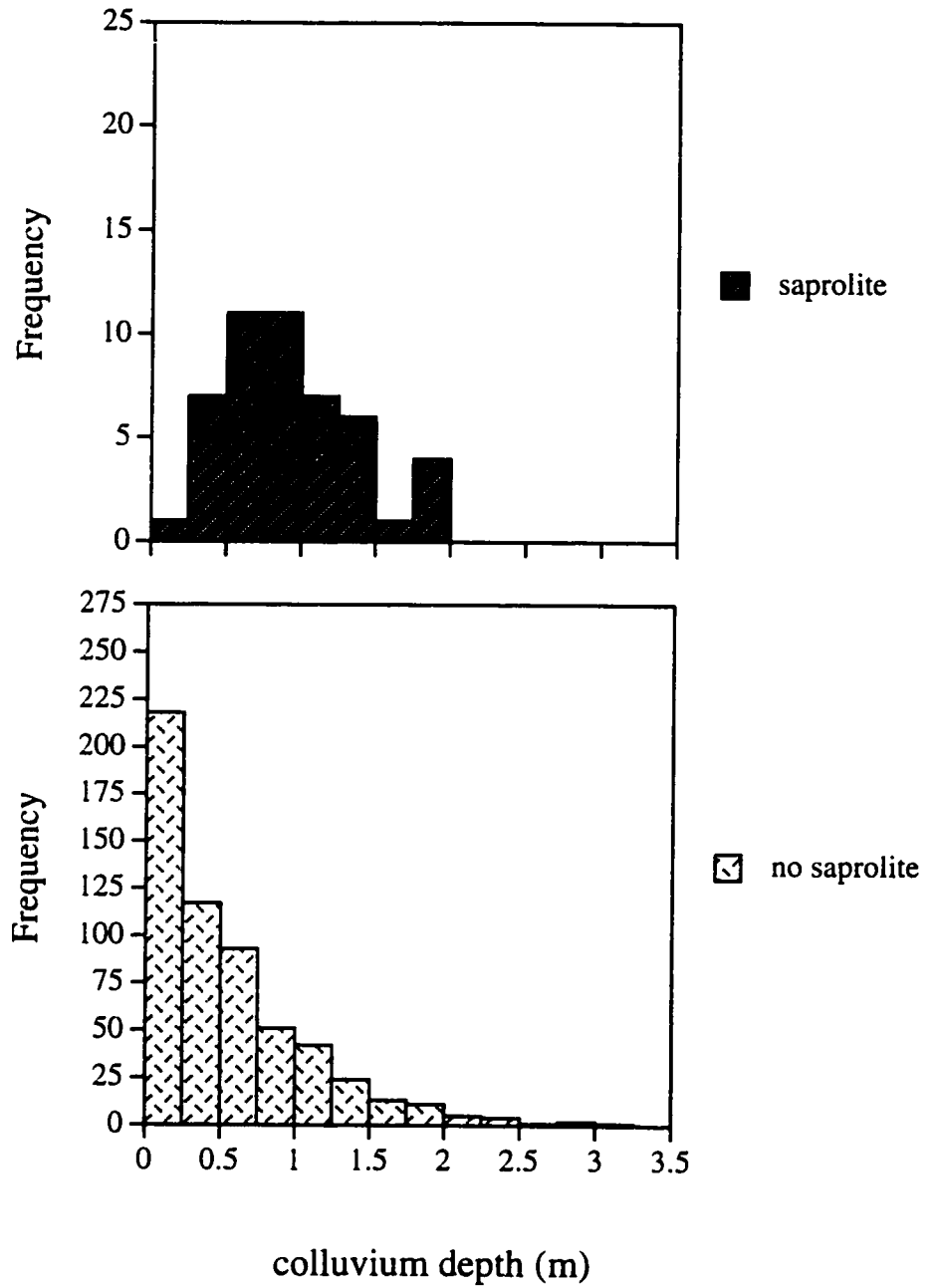
Figure 3.11    Histograms of overlying colluvial soil depth for sites with and without saprolite.

Figure 3.12     Perspective view of ground surface gradient ($|\nabla z|$) draped over the DEM

(azimuth = 155°, inclination: 10°, no vertical exaggeration). The lowest slopes are located near the drainage divide and on the 1992 debris flow deposit while the highest slopes are concentrated at the lower portion of the headwall.

m m$^{-1}$

>1.15
1.10
1.05
1.00
0.95
0.90
0.85
0.80
0.75
0.70
0.65
0.60
0.55
0.50
0.45
<0.40

20 m
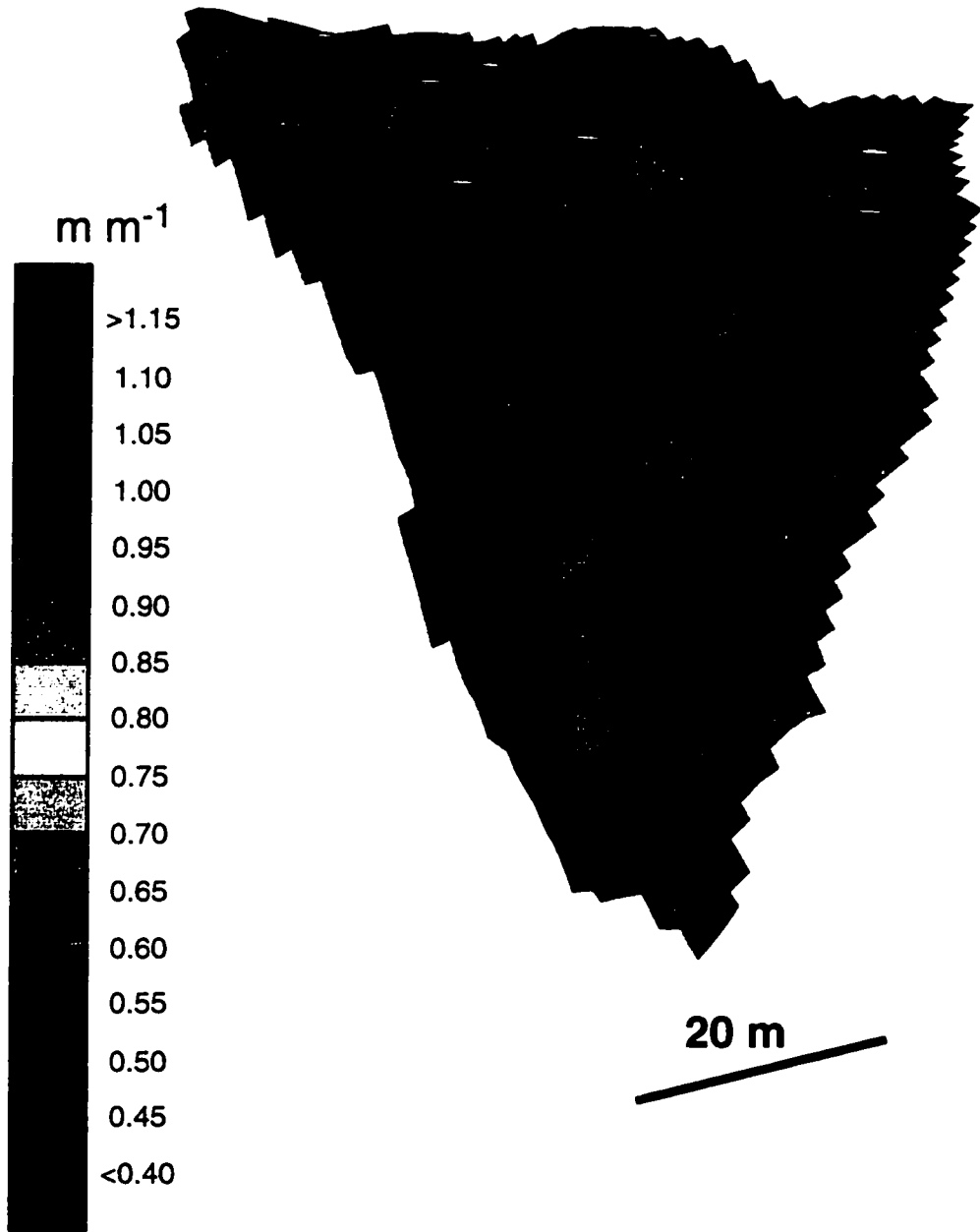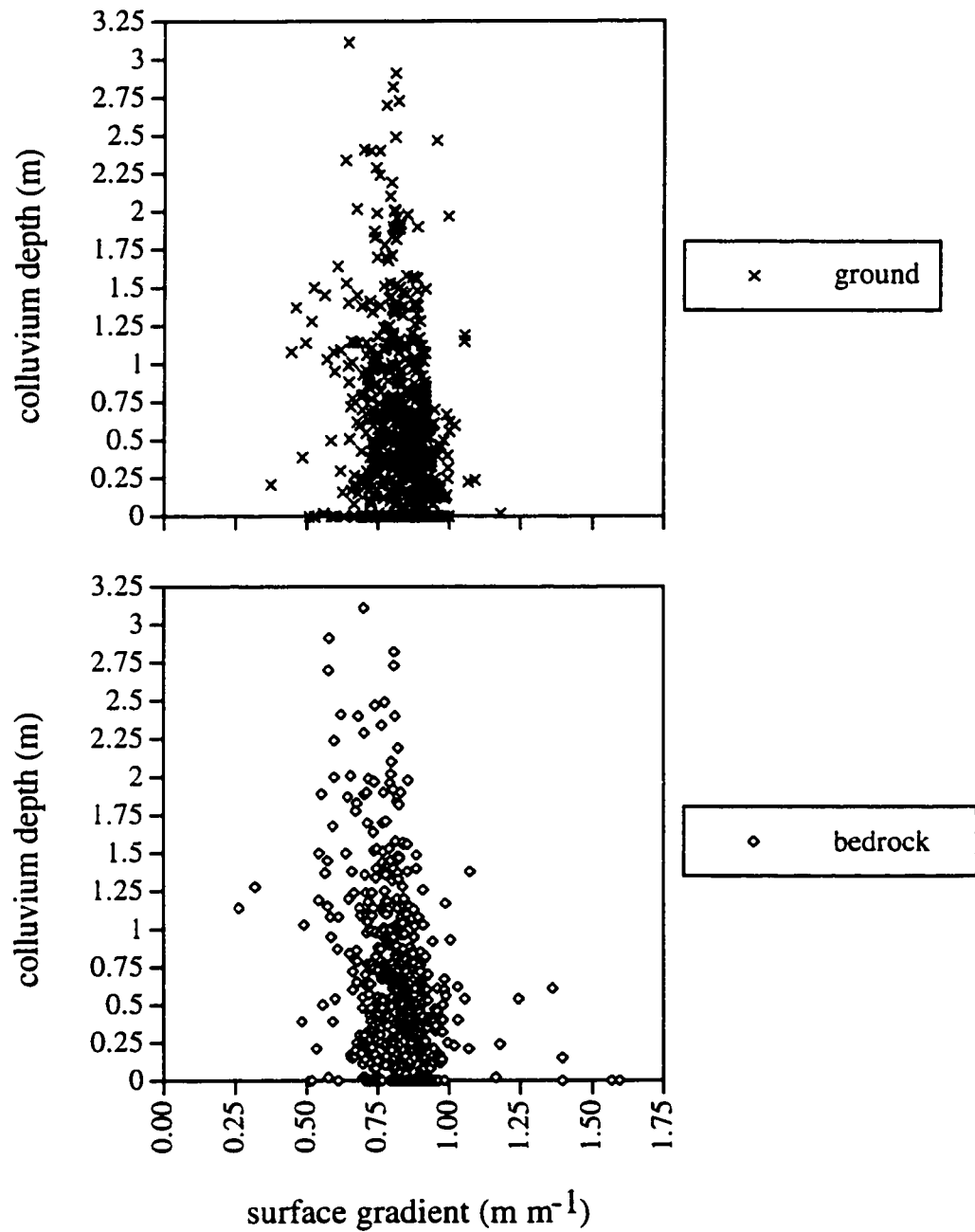
Figure 3.13    Plot of gradient for both the ground and bedrock surfaces in relation to colluvium depth. While the bedrock surface expresses both lower and higher extrema, the bulk of the distribution is located between gradients of 0.75 to 1.00 m m⁻¹ for both surfaces. The ground surface gradient has a negative skew of - 0.9, while the bedrock surface gradient is positively skewed (1.0).
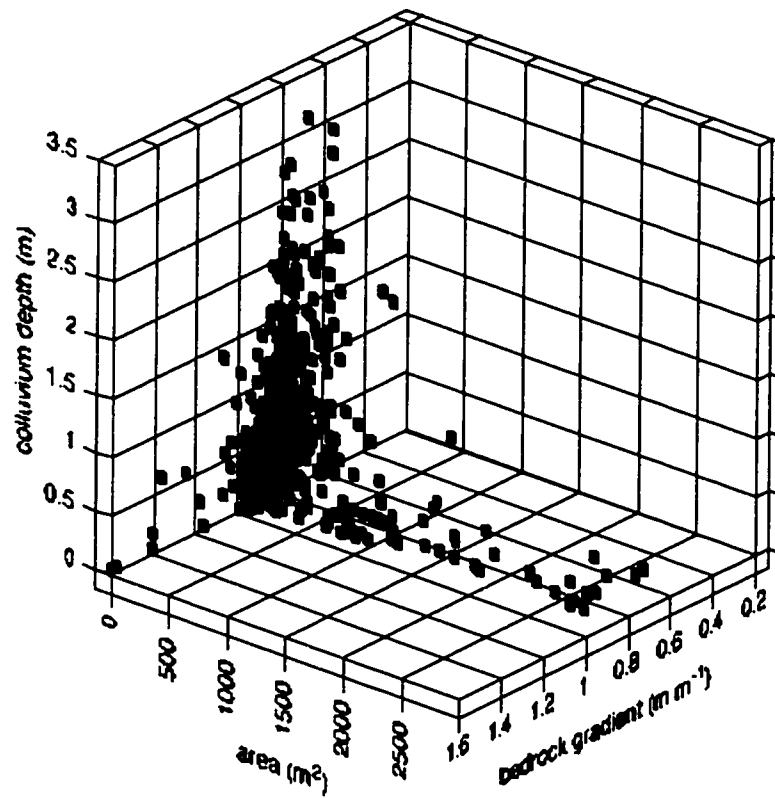
Figure 3.14    Plot of colluvium depth, bedrock surface gradient, and upslope contributing area that shows deep colluvial deposits concentrate in regions with relatively small upslope drainage areas (< 500 m²) and moderate gradients (0.8 m m⁻¹).

Figure 3.15     Perspective view of ground surface curvature ($\nabla^2 z$) draped over the DEM (azimuth = 155°, inclination: 10°, no vertical exaggeration). Divergent topography appears in green ($\nabla^2 z < -0.03$ m⁻¹), planar topography in yellow ($-0.03 > \nabla^2 z < 0.03$ m⁻¹), and convergent topography in orange ($\nabla^2 z > 0.03$ m⁻¹).

m⁻¹

>0.225
0.200
0.175
0.150
0.125
0.100
0.075
0.050
0.025
0.000
-0.025
-0.050
-0.075
-0.100
-0.125
-0.150
-0.175
-0.200
<-0.225

20 m
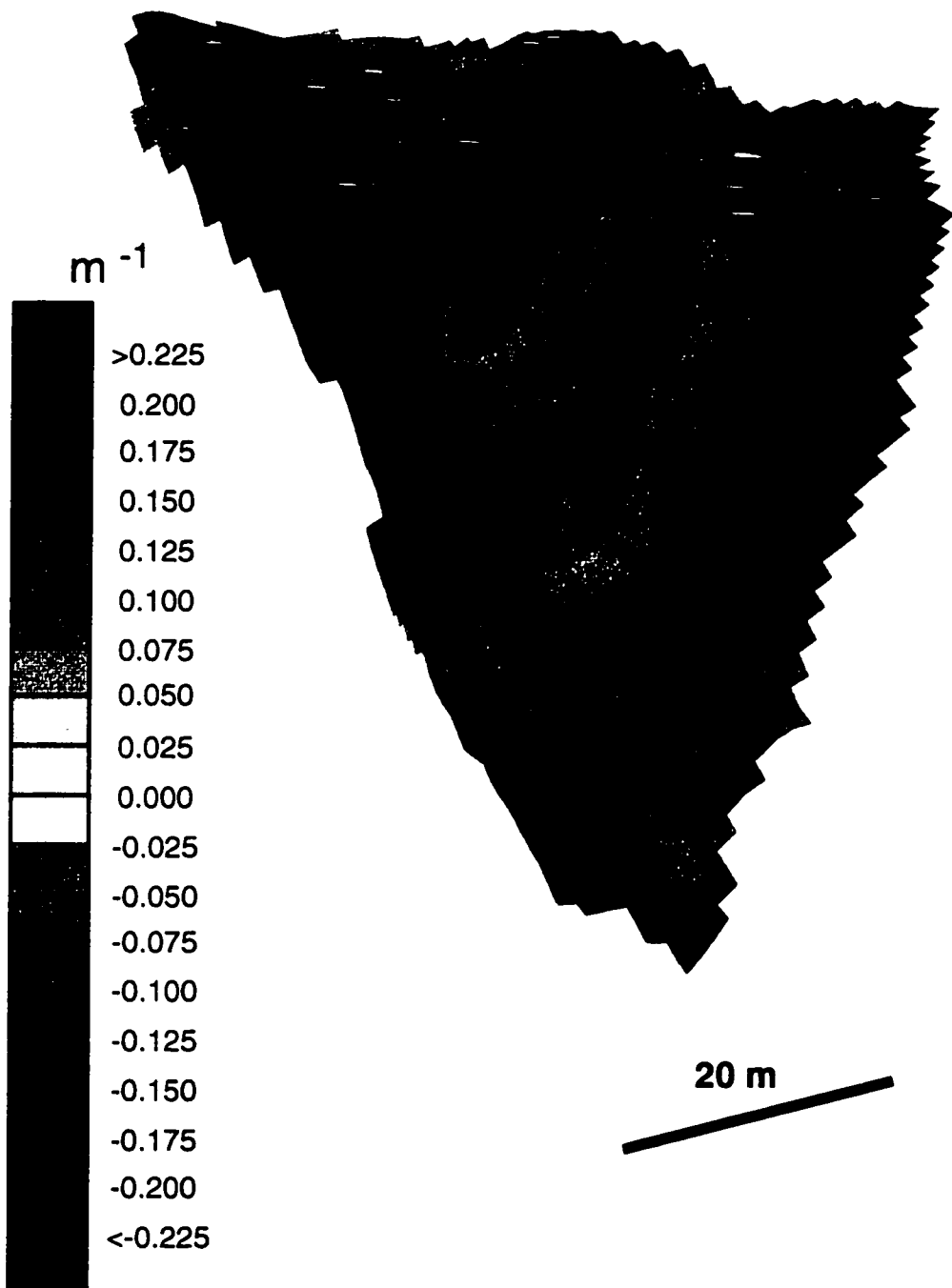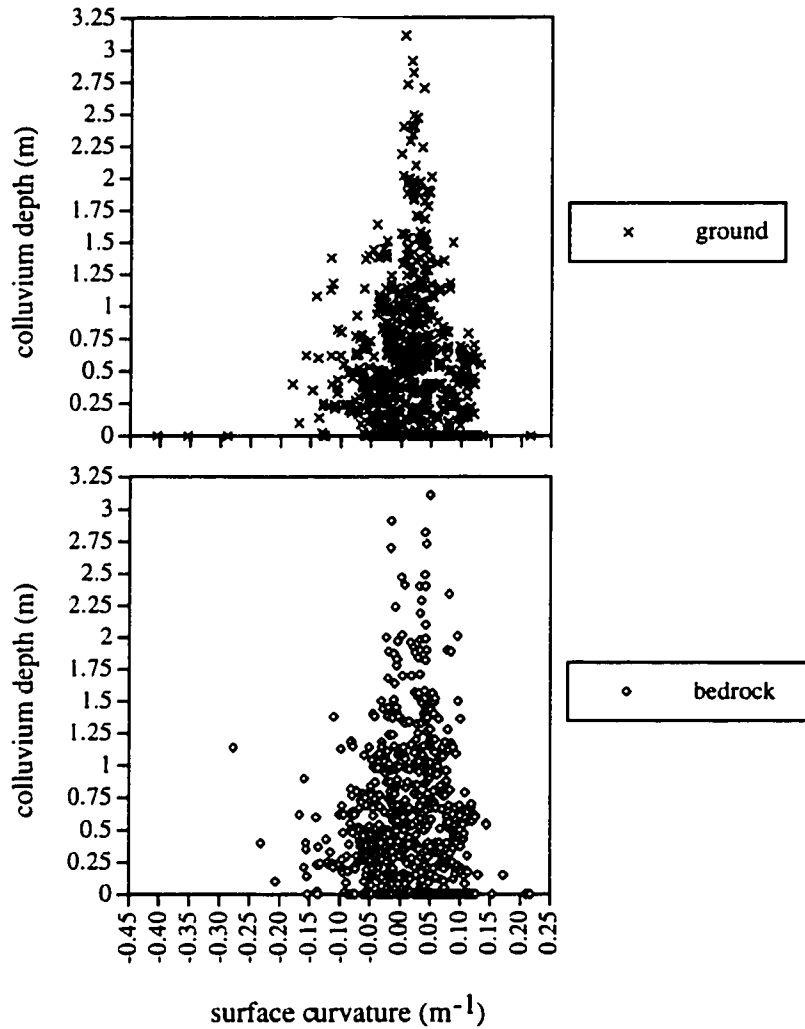
Figure 3.16    Plot of colluvium depth and surface curvature for both the bedrock and ground surfaces. Divergent topography is denoted by negative values while convergent topography is represented by positive values of surface curvature. Colluvium depth is negatively correlated with both increasing convergent and divergent topography with the thickest deposits (> 1 m) occurring in relatively planar topography.
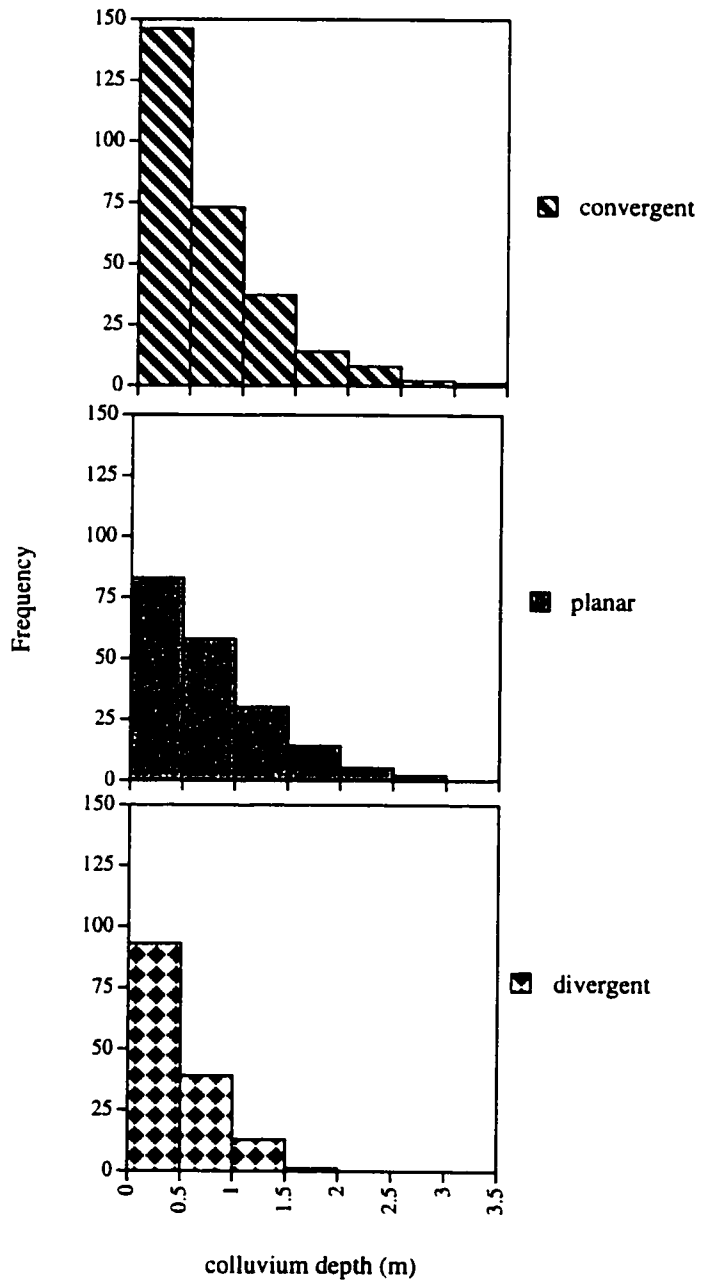
Figure 3.17    Histograms of colluvium depth for sites in convergent ($\nabla^2 z > 0.03$ m$^{-1}$),

planar ( -0.03 > $\nabla^2 z$ < 0.03 m$^{-1}$), and divergent ($\nabla^2 z$ < -0.03 m$^{-1}$) curvature of the bedrock surface.  As measurements were made over a headwall that is generally concave in morphology, the majority of sites are located within convergent topography.  Median values of soil depth are: convergent = 0.45 m, planar = 0.60 m, and divergent = 0.40 m.
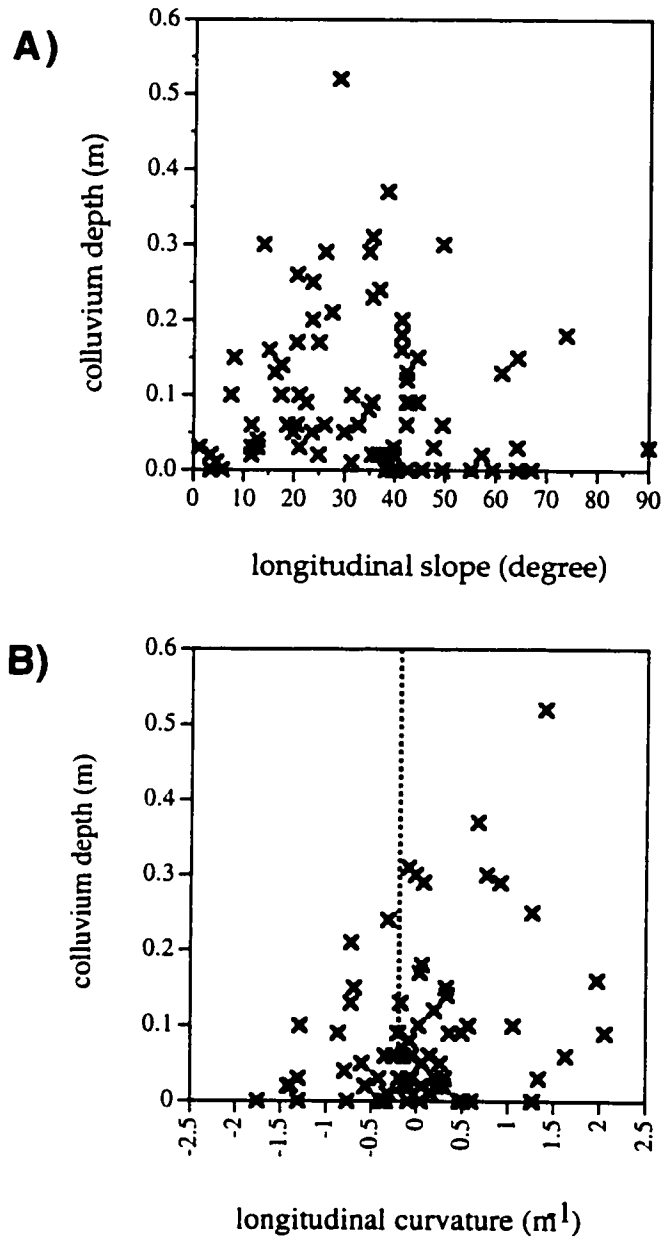
Figure 3.18    Relationship of colluvium depth with (A) 2-D longitudinal gradient and (B) 2-D longitudinal curvature for a 36 m profile with a measurement interval of approximately 0.40 m (n = 82).
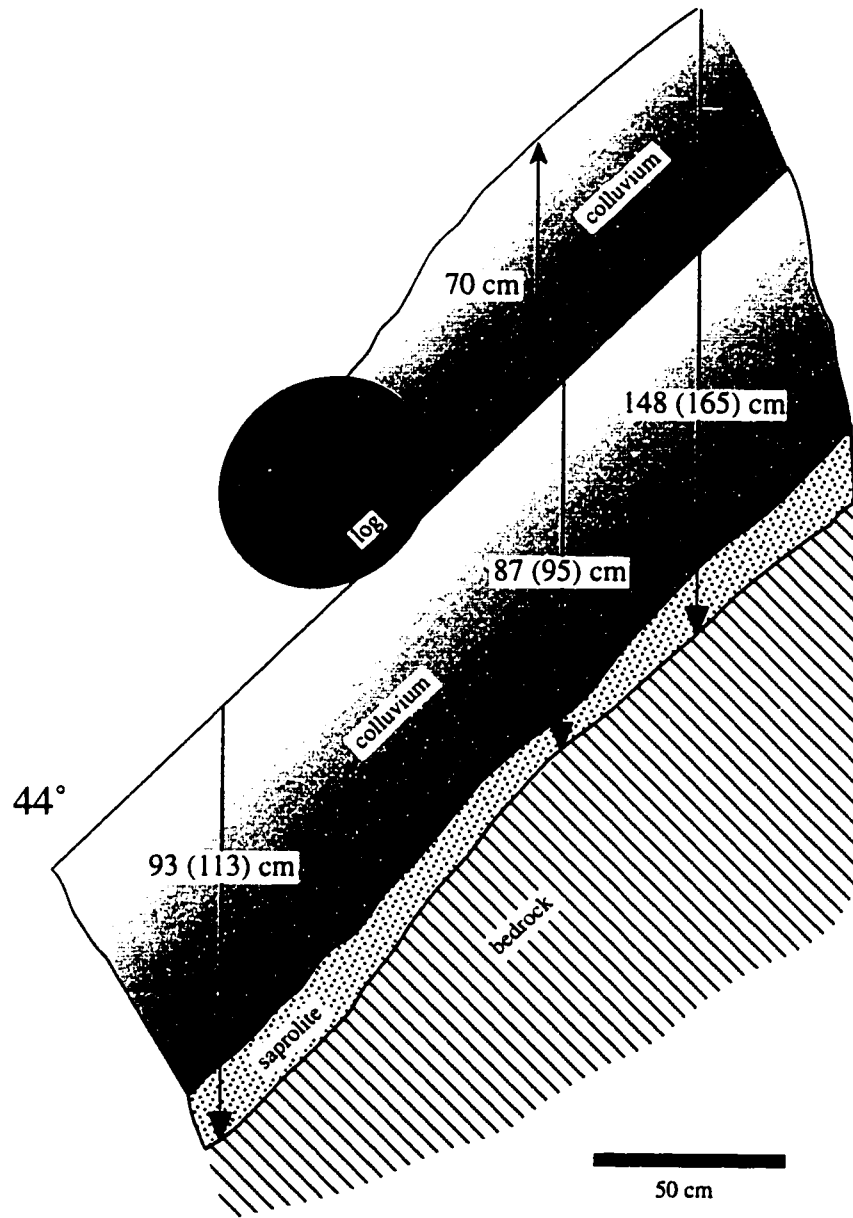
Figure 3.19    Cross section of bedrock, saprolite, and colluvium highlighting influence of downed trees on development of colluvial deposit.  Obstruction provided by tree almost doubles the deposit depth.  Profile located approximately 6 m vertically below ridge top.
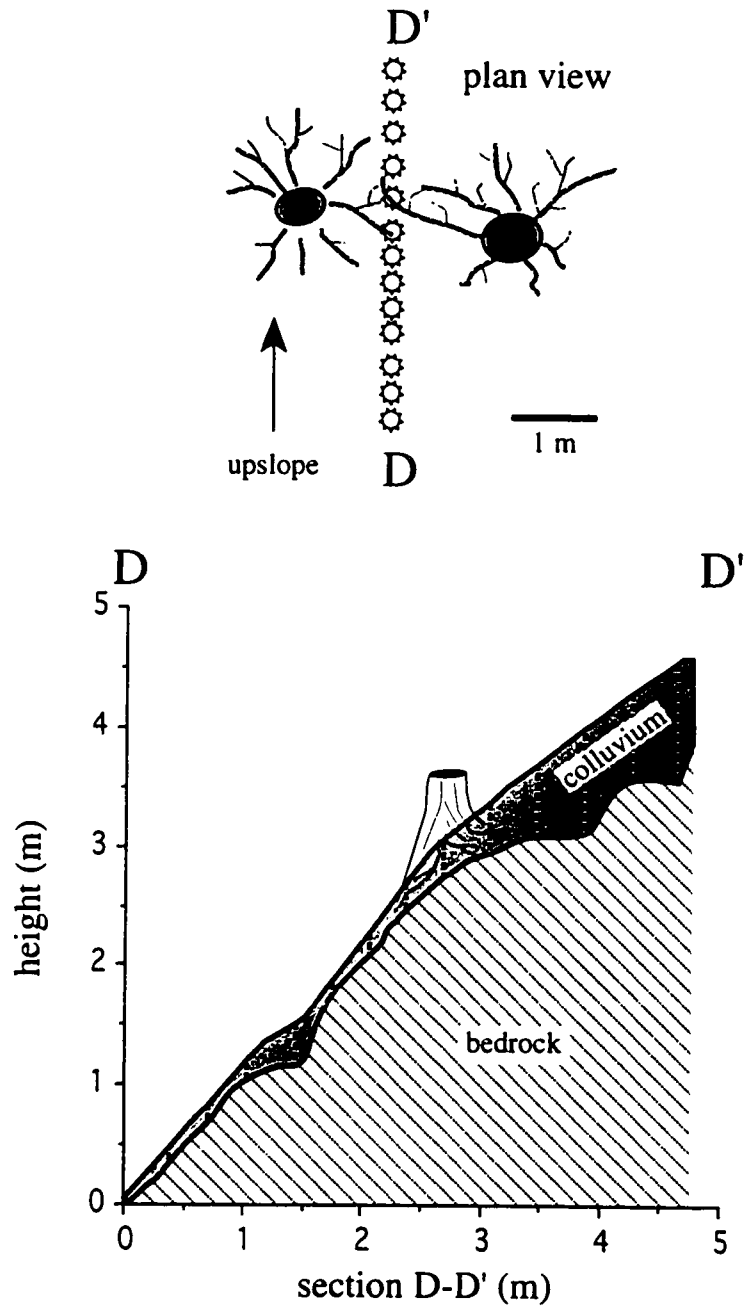
Figure 3.20    Plan view (upper) and cross section (lower) highlighting influence of root wads and stumps on the depth of colluvium. The 13 drill hole locations, represented by open circles surrounded by triangles, were used to depict the overall thickening of colluvium upslope of the root wad obstruction. Also note pronounced texture in bedrock surface at site located approximately 15 m vertically below ridge top on figure 3.6.

Figure 3.21    Perspective view of predicted colluvium depth draped over the DEM (azimuth = 155°, inclination: 10°, no vertical exaggeration). A) Upper figure, generated from suite 1 parameters, produces a maximum thickness of 3 to 4 m while predicted depths generated from suite 2 parameters (B) produces colluvial deposits > 6.5 m. For both cases thick deposits are located at the base of the headwall and in the regions of pronounced topographic concavity.

m

> 6.5
6.0
5.5
5.0
4.5
4.0
3.5
3.0
2.5
2.0
1.5
1.0
0.5
0
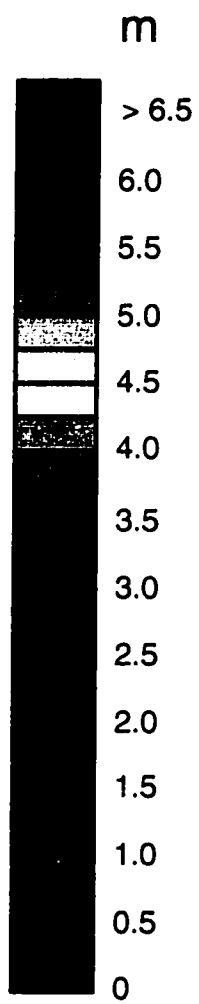
A)

suite 1

B)

suite 2

20 m

Figure 3.22     Perspective view of difference between predicted model output depths and observed colluvium depths draped over the DEM (azimuth = 155°, inclination:  10°, no vertical exaggeration) for (A) suite 1 parameters and (B) suite 2 parameters.  Notable deviations between the predicted and the observed depths occur near the drainage divide as negative values and within the pronounced concavities as positive values where the model over-predicts depth.

A)

suite 1

B)

suite 2

m

> 6.0
5.5
5.0
4.5
4.0
3.5
3.0
2.5
2.0
1.5
1.0
0.5
0
-0.5
-1.0
-1.5
-2.0
< -2.5

20 m
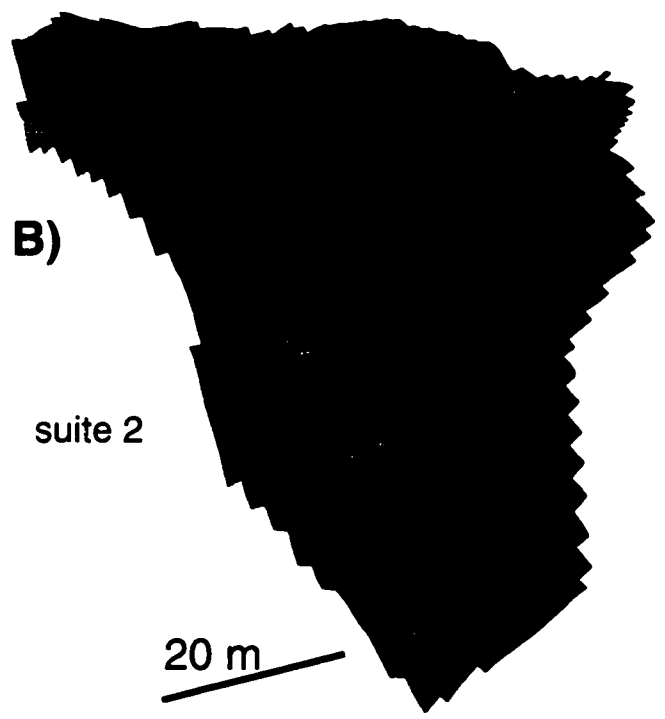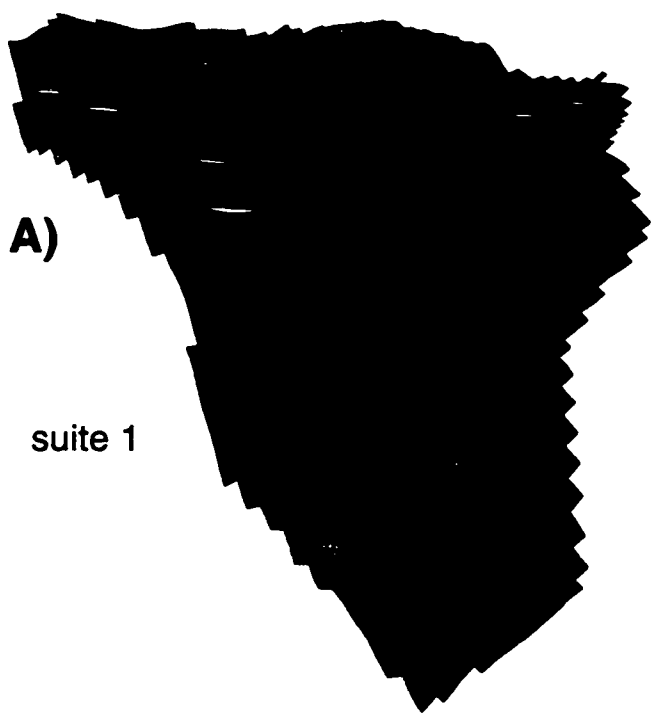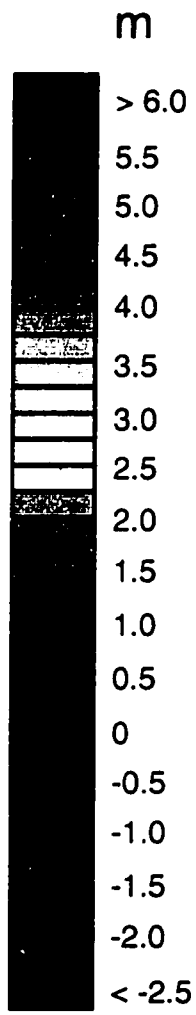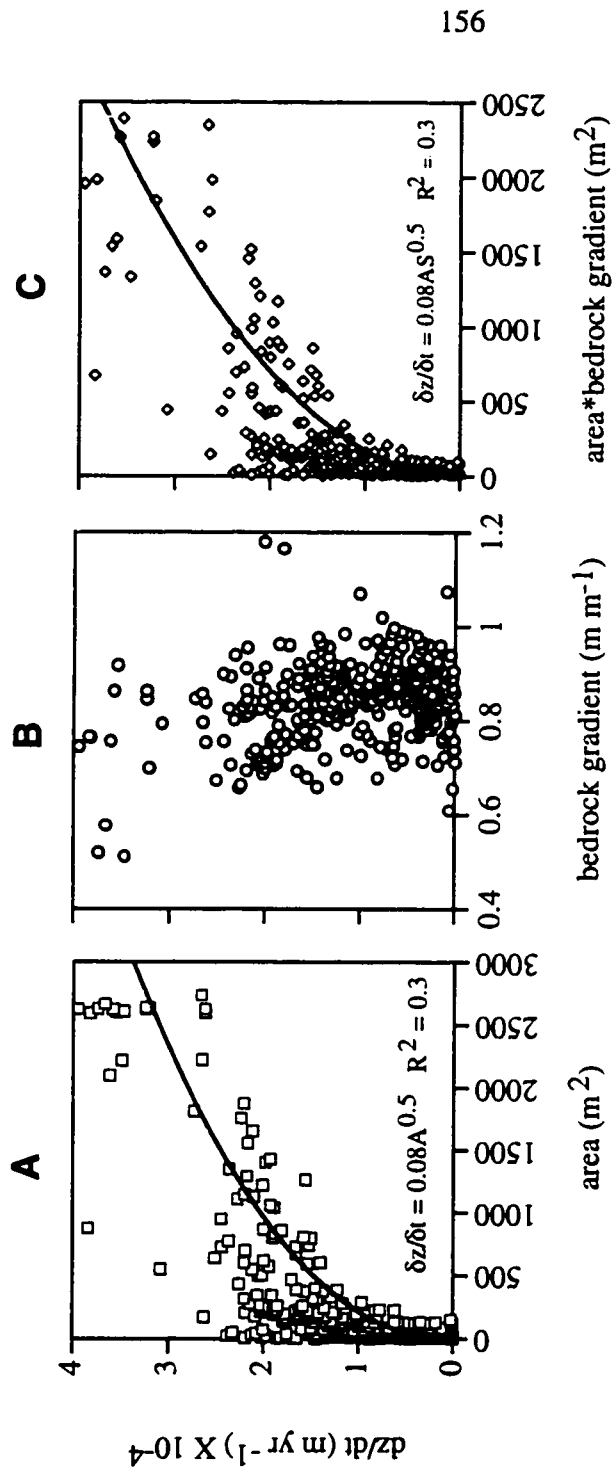
**Figure 3.23** Plots of (A) the lowering rate, $\left(\dfrac{\partial z}{\partial t}\right)_{ls}$, for a 10 ka period with upslope contributing area, (B) bedrock surface gradient, and

(C) the product of $AS$ assuming that both exponents $m$ and $n$ are equal to unity. While $\left(\dfrac{\partial z}{\partial t}\right)_{ls}$ shows no correlation with the local $S$, the

relation between $\left(\dfrac{\partial z}{\partial t}\right)_{ls}$ and $A$ or $AS$ approximates a power function to the 0.5 power.
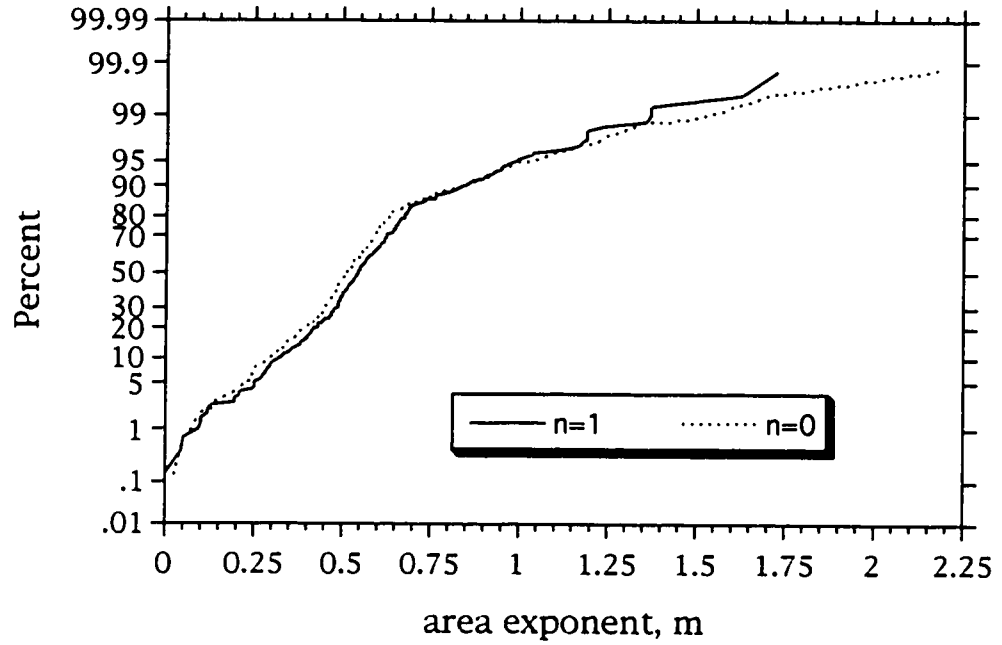
Figure 3.24    Cumulative frequency plot of the area exponent, *m*, derived from 353 estimates of the predicted minus observed colluvial depths assuming the exponent on slope, *n*, is equal to zero and unity.

Figure 3.25A    Maps of landslide location (dashed magenta curves) and critical rainfall calculated using equation 3.8 and cohesion values of 2 and 4 kPa in a GIS platform for an assumed, homogeneous colluvium depth of 1 m. Contour interval is 5 m.

c = 2 kPa                              c = 4 kPa

q_c (mm/day)

unstable
0 - 50
50 - 100
100 - 200
200 - 400
> 400
stable

N

50 m

Figure 3.25B    Maps of landslide location (dashed magenta curves) and critical rainfall
calculated using equation 3.8 and cohesion values of 2 and 4 kPa in a GIS platform. Predicted
soil depths using parameters from suites 1 and 2 are more spatially distributed than the assumed
1 m depth.  Contour interval is 5 m.

suite 1

suite 2

c = 2 kPa                    c = 4 kPa

$q_c$ (mm/day)

unstable
0 - 50
50 - 100
100 - 200
200 - 400
> 400
stable
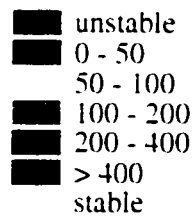
N

50 m

Figure 3.25C    Maps of landslide location (dashed magenta curves) and critical rainfall
calculated using equation 3.8 and cohesion values of 2 and 4 kPa in a GIS platform. Measured
colluvium depths depict focused regions of instability located within the areas of deep colluvial
deposits.  Bedrock outcrops appear in white.  Contour interval is 5 m.

c = 2 kPa                    c = 4 kPa

$q_c$ (mm/day)

unstable
0 - 50
50 - 100
100 - 200
200 - 400
> 400
stable

N

50 m
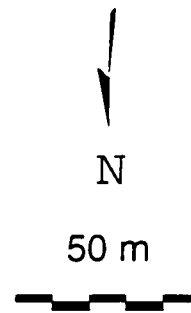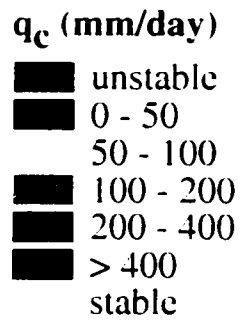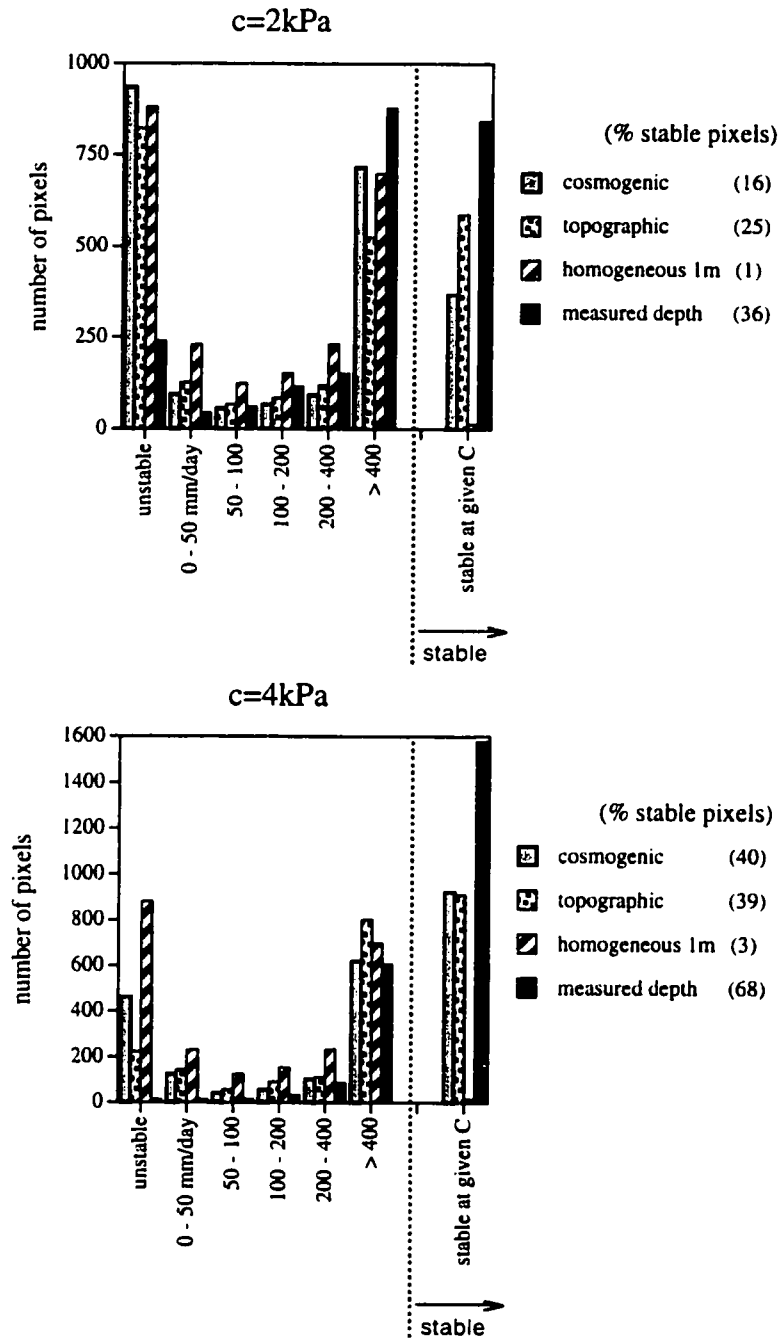
Figure 3.26    Histogram depicting number of pixels for critical rainfall categories based on the four scenarios of colluvium depth depicted in figure 3.25.  Upper figure represents distribution of critical rainfall categories for a cohesion of 2 kPa while the lower represents a cohesion of 4 kPa.  Percentage of landscape with stable pixels (category on right) shown in parenthesis to right of method used to determine colluvium depth.
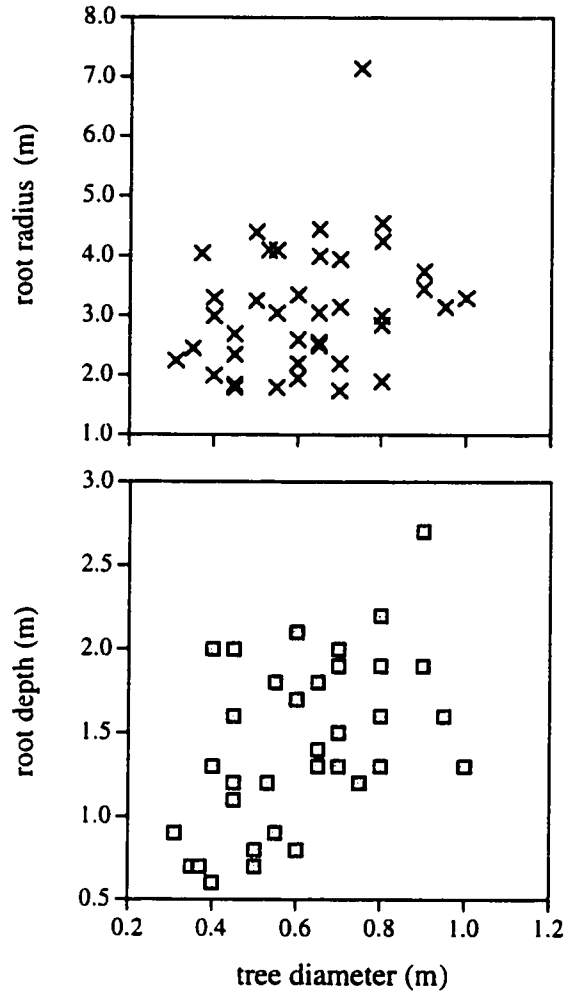
Figure 3.27    Dimensions of pit and mound topography in the Oregon Coast Range produced by wind throw of primarily coniferous trees.

# CHAPTER 4: VARIABILITY OF COLLUVIAL SOIL PRODUCTION AND TRANSPORT IN A STEEP CATCHMENT

ABSTRACT

Differential tilting of 212 polyvinylchloride (PVC) piezometer standpipes emplaced to varying depths within a steep, colluvium-mantled catchment in the southern Oregon Coast Range is used to infer rates of both slow mass movement or "soil creep" and bedrock-to-soil production. Measurements made over a 860 $m^2$ hollow (CB1) provide a four to nine year record of piezometer standpipe displacement resolved through angular measurements and simple trigonometric relations. Volumetric colluvial transport rates inferred from grouping together all 212 standpipes express a high degree of spatial variability, a weak exponential decline in velocity with length of below-ground pipe, and surface velocity in a downslope direction ranging from 0 to greater than 10 cm $yr^{-1}$. Highest velocities were observed adjacent to recent bioturbation by mountain beavers. An annual flux rate of 44 $cm^3 cm^{-1} yr^{-1}$ was determined from the integral of displacement for all piezometers on the hillslope with non-zero displacement. Using a site-specific density-depth function, the corresponding mass transport rate across a unit length of contour is 4.2 tonnes $m^{-1} yr^{-1}$, and the physical denudation rate is roughly 206 tonnes $km^{-2} yr^{-1}$. By assuming an exponential form to the velocity-depth profile for individual piezometers and integrating over the local soil depths, the mean and median annual volumetric fluxes characteristic of the short-term are 18.5 and 10.6 $cm^3 cm^{-1} yr^{-1}$. For comparison, long-term volumetric fluxes inferred through colluvial hollow infilling in the Oregon Coast Range are 32 ± 23 $cm^3 cm^{-1} yr^{-1}$ (Reneau and Dietrich, 1991). Estimates of the bedrock-to-soil conversion rate are determined through measurements of i) the gradient of the volumetric colluvial transport vector inferred from displaced piezometers and ii) the magnitude of

topographic divergence and the coefficient of diffusivity. Differentially displaced piezometer standpipes are used to infer an equivalent median bedrock-to-colluvium production rate of 0.14 mm yr$^{-1}$. Mapping of colluvium depth and detailed topographic surveying over a 12,400 m$^2$ area are used to calculate a median soil production rate of 0.053 mm yr$^{-1}$ for areas of topographic divergence surrounding bedrock outcrops. No correlation between bedrock-to-colluvium production rate and depth of overlying colluvium cover was discernible. In contrast, soil production rates reported by Heimsath (1999) inferred from cosmogenic isotope dating represent higher rates and a dependence with the depth of overlying colluvium.

## INTRODUCTION

Soil thickness is a function of the balance between sediment transport and production via conversion of bedrock to soil (e.g., Ahnert, 1970; Kirkby, 1980). Bedrock landscapes occur where rates of physical, biological, and chemical erosion exceed soil production rates. Conversely, soil-mantled landscapes occur where the conversion rate of bedrock-to-soil is equal to or greater than the rate of erosion. Besides being critical to supporting a broad variety of flora and fauna, a persistent soil cover is essential to agriculture. In addition, the magnitude of soil production and transport rates are central to modeling landscape evolution or soil depth variation across a landscape.

Colluvial soil on steep hillslopes lacks relict bedrock structure and is typically devoid of classic soil horizons because of frequent downslope transport via slow mass movement. On steep hillslopes, processes responsible for converting bedrock to colluvial soil and sediment transport include tree throw, biogenic mixing, and *in situ* physical and chemical weathering (Paton et al., 1995). Hence, short-term, event-based production and transport rates representative of bio-mechanical disturbance are likely to exhibit great

spatial and temporal variability. Furthermore, rates may vary substantially with the underlying parent lithology and its degree of weathering as well as the local plant and animal communities, climate, and elevation.

Sediment transport via slow mass movement or creep processes is commonly conceived as a discontinuous, downslope movement of soil resulting from a disturbance of particles in the presence of gravity (Sharpe, 1938; Young, 1960; Culling, 1963; Kirkby, 1967; Carson and Kirkby, 1972; Selby, 1993). Based upon theoretical considerations Davison (1889) attributed creep to an expansion of a sloping soil mass and subsequent deflation of the soil resulting from repeated cycles of freeze-thaw. Davis (1892) suggested that creep rates are highest at the ground surface and increase with hillslope gradient. Following Davis's suggestion, Gilbert (1909) demonstrated how creep can produce convex hillslope profiles by assuming creep rates are a function of ground-surface slope. Recent research by Martin and Church (1997) and Roering et al. (1999), however, indicates that the relation between sediment transport and surface slope in certain environments may be non-linear. If transport processes driving slow mass movement are not uniformly distributed throughout the landscape, hillslope-scale sediment flux may not be a simple function of slope and may express a high degree of spatial variability. Although studies have documented short-term rates of slow mass movement (Young, 1960; Kirkby, 1967; Owens, 1969; Fleming and Johnson, 1975; Lewis, 1976; Moeyersons, 1988; Clarke et al., 1999) and long-term rates of slow mass movement (Reneau et al., 1989; Reneau and Dietrich, 1991; McKean et al., 1993), the spatial variability of sediment transport rates over 10's to 100's of meters is relatively unconstrained.

Numerous sediment transport processes are commonly attributed to the term "slow mass movement" with regional variations arising from differences in climate and

environment. "Particle creep" is defined as the movement of single particles over exposed bedrock or soil surface driven by freeze-thaw, wetting cycles, rainsplash, and/or overland flow (Leopold et al., 1966; Schumm, 1967; Abrahams et al., 1984). "Continuous creep" is the slow, but uninterrupted movement produced by transport of rigid material above a zone of deformation (Terzaghi, 1936; Van Asch et al., 1989). Continuous creep is driven solely by the force of gravity where the applied stress is produced by the weight of overlying material. Typical engineering definitions often refer to continuous creep. "Soil creep," the transport process addressed in this paper, is the downslope movement of superficial colluvium and/or rock debris driven by a mixture of biotic and abiotic processes: a) continuous creep in a rheologic sense and/or b) transport of individual particles initiated by moisture fluctuations, temperature fluctuations, or bioturbation in the presence of gravity-induced downhill shear stress (e.g., Carson and Kirkby, 1972). Yamada (1997) noted that the processes driving sediment transport on forested hillslopes of northern Japan are seasonal; transport during the summer is driven by the shrinking and swelling of clay rich material while transport during the winter is driven by frost action. Previous research documents that bioturbation, for example, can be a common transport process acting over much of the landscape, but ordinarily represents low rates of transport (Darwin, 1882; Fleming and Johnson, 1975; Imeson, 1976; Thorn, 1978; Black and Montgomery, 1991). Studies examining the variability of soil creep rates in different environments recognized increased rates in anthropogenically disturbed areas while no creep was observed over a 12-year period in mature forests on 30° slopes (Jahn, 1981; 1989). In Oregon, Gray (1973) recognized higher near-surface creep rates of colluvial soil in areas of dead trees and clear cuts relative to creep in colluvium beneath live trees. In a global compilation, Saunders and Young (1983) indicated that acceleration of natural erosion rates by anthropogenic disturbance ranges from 2 - 3 times for moderate land use and about 10 times for intensive land use.

Although numerous conceptual arguments regarding soil production have been proposed, few quantitative measurements of production rates exist. For instance, it is commonly theorized that the overlying regolith thickness influences bedrock-to-soil conversion rates (Gilbert, 1877; 1909; Culling, 1963; Young, 1963; Carson and Kirkby, 1972; Young, 1972; Armstrong, 1976; Ahnert, 1977; Cox, 1980; Ahnert, 1987). In particular, Armstrong (1976) and Ahnert (1977) suggested an exponential relationship between bedrock lowering and overlying soil thickness represents the decreased efficacy of processes converting rock to soil with increasing cover. A "humped" or bell-shaped polynomial function proposed by Gilbert (1877), Ahnert (1967), and Carson and Kirkby (1972) is thought to portray the maximum soil production occurring under moderate cover depths. Where mechanical disruption displaces rock, a finite soil cover is necessary to allow for the burrowing of animals or growth of large tree roots. Under these scenarios exposed rock produces little soil. Similarly, Young (1963) and Culling (1963) proposed hyperbolic relationships for the relationship between colluvium production and depth of overlying colluvium cover. Quantitative estimates of the colluvial soil production rate and its variability with overlying cover, however, are uncommon and limited to coastal California (e.g., Monaghan et al., 1992; McKean et al., 1993; Heimsath et al., 1997).

Two principal methods have been used to determine the variation of production rate with depth of overlying soil: 1) dating of the soil profile using radionuclides and 2) theoretical calculations based on mass conservation and topographic form. *In situ* radionuclide concentrations, commonly $^{14}$C, $^{10}$Be, and $^{26}$Al, are used to infer soil production rates. For example, production rates were assessed from $^{14}$C ages of charcoal deposited at the bedrock-colluvium interface (Reneau et al., 1986; 1989; 1990; Benda and Dunne, 1987; Reneau and Dietrich, 1990; 1991). Furthermore, recent advances in dating techniques

provide a means to determine cosmogenic radionuclide concentrations in vertical pits and in the bedrock at the colluvium-rock interface (Pavich et al., 1984; Monaghan et al., 1992; McKean et al., 1993; Heimsath et al., 1997). Radionuclide concentration can provide estimates of the production rate in the context of steady-state models used to describe mass- and radionuclide conservation on the hillslope by examining the ratio of the radionuclide delivery rate from the atmosphere relative to the average concentration of radionuclides in the colluvium.

The relationship between colluvial soil production and transport can be portrayed by a continuity equation; a statement describing the conservation of mass such that if more material is transported into a section of hillslope than is removed, the soil column will thicken. Conversely, if less material is transported into than out of a section of hillslope, net erosion of the soil arises. Process-response, hillslope evolution models customarily assume conservation of mass and use transport laws to quantify sediment transport (e.g., Culling, 1963 ; Ahnert, 1967; Kirkby, 1971; Fernandes and Dietrich, 1997). A method proposed by Dietrich et al. (1995), utilizes the topographic form of the ground surface in the context of mass conservation to estimate bedrock-to-colluvium production rates. If the conversion of rock to soil exceeds the transport rate, the colluvium/bedrock contact decreases in elevation leading to an increase in the overlying colluvium thickness. Changes in colluvium thickness can thus be related to the bedrock lowering rate and the local gradient in sediment flux through the continuity equation:

$$\frac{\partial(\rho_s z_s)}{\partial t} = -\rho_r \frac{\partial e}{\partial t} - \nabla \cdot \rho_s \bar{q}_s$$

(4.1)

where $z_s$ is the vertical colluvium thickness (L), $e$ is the elevation of the bedrock-colluvium interface (L), $t$ is time (T), $\rho_s$ and $\rho_r$ are the bulk densities of colluvium and rock (M L$^{-3}$), and the volumetric colluvial transport vector, $\vec{q}_s$, has the units of volume per unit contour length per time (L$^3$ L$^{-1}$ T$^{-1}$). The first term in the mass conservation of equation 4.1 is the change in colluvium thickness and bulk density with time, the second term is the conversion rate of bedrock to colluvium arising from the lowering of the elevation of the bedrock-colluvium interface, $-\partial e/\partial t$ (L T$^{-1}$), and the last term is the divergence of colluvial transport. A steady-state colluvium thickness develops when the downslope flux is balanced by the mass arriving from upslope plus the mass produced by the conversion of rock (e.g., Nikiforoff (1942)).

Culling (1960; 1963) first suggested that an expression for a purely slope-dependent transport law characteristic of long-time scales can be portrayed by:

$$\vec{q}_s = -K\nabla z \tag{4.2}$$

in which $K$ is the diffusion coefficient (L$^3$ L$^{-1}$ T$^{-1}$), $z$ is the ground surface elevation (L), and $\nabla z$ is the topographic gradient (L L$^{-1}$). Most landscape evolution models assume sediment transport on hillslopes is driven by linear diffusion such that diffusive processes lower topographic highs, fill topographic lows, and are not dependent on upslope contributing drainage area (e.g., Koons, 1989; Willgoose et al., 1991; Howard, 1994; Fernandes and Dietrich, 1997). Although field measurements of sediment flux on moderate slopes are consistent with equation 4.2 (Schumm, 1967; McKean et al., 1993; Granger et al., 1996), measured transport rates on slopes greater than 20° are lacking.

Sediment flux, $\bar{q}_s$, may also be expressed as a function of velocity (L T$^{-1}$), $u_*$, integrated over the local colluvium depth, $z_s$, where:

$$\bar{q}_s = \int_0^{z_s} u_* dz_{s*} \tag{4.3}$$

where $z_{s*}$ is the distance below the ground surface. Previous research specific to coastal Oregon demonstrates that $z_s$ ranges from < 0.5 m on topographic noses to < 2 - 3 m in hollows (chapter 3; Pierson, 1977; Montgomery et al., 1997) but little is known about the variation in $u_*$. Thus adequately characterizing the variability of $\bar{q}_s$ requires knowledge of both $u_*$ and $z_s$ to construct landscape evolution models or estimate the magnitude of the mass flux. Velocity-depth profiles typically exhibit complex patterns of deformation within the colluvial cover (Young, 1960; Kirkby, 1967; Selby, 1974; Lewis, 1976; Young, 1978; Jahn, 1981; Moeyersons, 1988; Yamada, 1997; and Clarke et al., 1999). As sediment transport by soil creep is slow and often discontinuous, its measurement requires either long-term monitoring projects (Young, 1978; Jahn, 1981; 1989; Clarke et al., 1999), measurements over a large area where the goal is to substitute space for time, or dating of basal colluvium to infer hollow infilling rates (Reneau et al., 1989; Reneau and Dietrich, 1991).

Here I examine rates and depth profiles of sediment transport and bedrock-to-colluvial soil production in a steep, colluvium-mantled hillslope in the southern Oregon Coast Range (figure 3.4). I estimate the magnitude and variability of sediment velocity and flux from differentially displaced, polyvinylchloride (PVC) piezometer standpipes emplaced in the ground to varying depths and compare short-term values determined here

with those representative of longer time scales determined through dating of colluvial deposits. The piezometer standpipes were intended to measure near-surface pore-water pressures (Montgomery et al., 1997), rather than to infer rates and depth profiles of sediment transport. Progressive tilting of PVC standpipes, though, provides a means to infer sediment transport at individual piezometers and therefore over the entire basin. As the piezometer standpipes were installed over a large area, I circumvent some of the sampling problems often associated with short term monitoring programs that are limited in space thus providing a means to estimate the spatial variability of short-term transport rates. I also use the distribution of $\bar{q}_s$ inferred from differentially displaced standpipes, local colluvium depth measurements, and topographic curvature calculated over a 12,400 m$^2$ headwall area to infer bedrock-to-colluvial soil production rates ($-\partial e/\partial t$).

## STUDY AREA

Characteristic topography of the southern Oregon Coast Range is steep (up to 45°) and highly dissected into distinct hollows and interfluves (noses) resulting from a combination of slow mass movement (Roering et al., 1999), fluvial (Dietrich and Dunne, 1978), and rapid mass movement transport mechanisms (Pierson, 1977; Dietrich and Dunne, 1978; Benda, 1987; Benda and Dunne, 1987; Reneau and Dietrich, 1990). While rapid mass movement characterized by landsliding often concentrates in topographic hollows, slow mass movement processes may act over the entire landscape. In the Oregon Coast Range evidence for slow mass movement is demonstrated by an accumulation of soil upslope of trees and stumps, and by the conspicuous presence of mounds and burrows created by mountain beavers (*Aplodontia rufa*) (Feldhamer and Rochelle, 1982). Field observations of well-established deer tracks and mountain beaver burrows attest to widespread bioturbation.

Mettman Ridge is located 15 km northeast of Coos Bay, Oregon at an elevation of about 300 m a.s.l. (figure 3.4). Situated on Mettman Ridge is CB1, an experimental site used to examine the hydrologic response of a steep unchanneled valley. This 43° topographic hollow has a drainage area of 860 m$^2$ that was clear-cut logged in 1987 and replanted with Douglas-fir saplings in 1988. Wooden catwalks anchored to cables over the ground surface were constructed throughout the site during 1989 to minimize disturbance due to walking and instrument installation. Hydrologic studies included the installation of 224 PVC piezometer standpipes for monitoring groundwater response to sprinkler-applied and natural rainfall (Anderson et al., 1997; Montgomery et al., 1997; Torres et al., 1998). While 25% of the standpipe inlets are anchored within bedrock, the majority are located at varying depths throughout the colluvium. As the parent material is an Eocene sandstone and mudstone (Lovell, 1969), the texture of the colluvium is relatively homogeneous throughout the study site: a sandy matrix with isolated clasts of sandstone up to tens of centimeters in mean diameter. The presence of a thin, discontinuous *in situ* weathering profile (saprolite) and the absence of defined soil horizons is thought to reflect frequent disturbance by biogenic mixing or other slow mass movement processes. The present vegetation is dominated by a dense understory of thimbleberry (*Rubus parviflorus*), blue elderberry (*Sambucus caerulea*), vine maple (*Acer circinatum*), and sword fern (*Polystichum munitum*) with Douglas-fir (*Pseudotsuga menziesii*) and red alder (*Alnus rubra*) up to about 4 m tall (in 1998) forming the canopy. The temperate, maritime climate is wet and relatively mild with mean annual precipitation totals of 1500 to 3000 mm (Corliss, 1973). Precipitation falls mainly as rain with infrequent subzero temperatures.

Short-term, modern values of sediment transport from CB1 are readily evaluated in a geologic time frame because the region has been the focus of much geomorphic study. Previous research examining hollow infilling rates (Reneau et al., 1989; Reneau and

Dietrich, 1991) and the soil production function (Heimsath et al., 1996), and non-linear, diffusive sediment transport (Roering et al., 1999) constrain long-term values for both the diffusivity constant, $K$, and bedrock lowering rates.

## METHODS

Short-term (4 - 9 year) measurements of tilted piezometer standpipes are used to infer downslope sediment velocity and flux. A total of 224 schedule 40 PVC piezometer standpipes (1" diameter with a pipe stiffness of 17.5 MPa) were installed in the summers of 1989, 1990, and 1992 to monitor pore-water pressure response to natural and sprinkler-applied rainfall (for a location map showing piezometer locations see figure 4.4). Because the standpipes were installed roughly vertical (± approximately 5°), the lever arm influence arising from the above-ground length of pipe should be minimal. Differential tilting of 212 PVC standpipes was measured with a Brunton compass to ± 1° during the summer of 1996. Subsequent repeat measurements of 81 pipes were made during the autumn of 1998. The record length thus varies between four and over nine years depending on the duration the standpipe remained undisturbed in the ground. The 9-year record contains 81 measurements, the 7-year record contains 139 measurements, the 6-year record contains 10 measurements, and the 4-year record contains 63 measurements. The 139 sites of the 7-year record, 10 sites of the 6-year record, and 63 sites of the 4-year record were measured during the summer of 1996. The 9-year record represents the second field campaign to measure standpipe inclination in 1998 such that the 81 measurements are a subset of the 212 sites measured in 1996. Horizontal displacements are resolved by simple trigonometric relations (figure 4.1) where the angle $\alpha_p$ (inclination of the standpipe from vertical) was measured in the field. The horizontal length between the initial top of the ground surface to the present pipe location, $h_1$, is calculated by:

$$h_1 = Z \tan \alpha_p \qquad (4.4)$$

where $Z$ is the underground length of standpipe. I used the law of sines to determine the slope parallel displacement length, $L_s$, such that:

$$L_s = \frac{\sin \upsilon h_1}{\sin \omega} \qquad (4.5)$$

With estimates of the local slope, $\theta$, (defined by the mean of four measurements within a 2 m contour interval or roughly 2 m planform distance straddling individual standpipes) I calculate the length of horizontal displacement, $L_h$, such that:

$$L_h = L_s \cos \theta \qquad (4.6)$$

Velocity of the displaced standpipes is assumed to equal sediment transport velocity, $u_*$, resolved by dividing $L_h$ by the duration the standpipe remained in the ground $t$:

$$u_* = \partial L_h / \partial t \qquad (4.7)$$

The PVC standpipes function as inclinometers to provide minimum estimates of ground deformation, an approach similar to Kirkby's (1967) "T-peg". The displacements represent a minimum estimate because I do not consider the material resistance (bending moment of PVC pipe), the amount of material that possibly bypassed the pipes, or how far the pipe anchor point (inlet depth) migrated downslope.

*Inferring rates of slow mass movement*

To obtain a velocity-depth profile of $u_*$ in the downslope direction I assume that:
1) the inlet locations of all the standpipes are fixed in space, whether anchored into bedrock or colluvium; 2) the standpipe deformations between the inlet and ground surface are linear [a constant angle ($\alpha_p$) of deformation; figure 4.1]; and 3) the displacements of bedrock piezometers are limited to the local thickness of overlying colluvium. Assumption #1 is probably valid at the cm scale as field observations reveal that the standpipes did not migrate 10's of cm from their initial surveyed position. If entire standpipes were transported downslope, displacing the inlet locations in addition to tilting the pipes, the displaced locations would not coincide with the initial surveyed positions. Excavating PVC pipes within the colluvium indicated that the pipes were not bent, validating assumption #2. Velocity, $u_*$, depends on the duration the pipe was left undisturbed in the ground, ranging from 4 to 9 years. To determine a sediment flux, $\bar{q}_s$, I integrate $u_*$ over the depth of colluvium as in equation 4.3 assuming the volume of sediment is moved across a vertical plane of unit area that is parallel to the contour of the slope, for a unit horizontal distance along the plane.

As the piezometer standpipes were located over most of the 860 m$^2$ hollow, I had a rare opportunity to scale up from point measurements of individual piezometers to hillslope-scale transport rates. From $\bar{q}_s$ I determine a hillslope-scale coefficient of diffusion, $K$, by rearranging equation 4.2 such that:

$$K = -\bar{q}_s \Big/ \nabla_z$$

(4.8)

Alternatively, local values of $K$ are determined for each standpipe based on local slope and an assumed depth profile of colluvium velocity for individual standpipes. The downslope sediment mass transport rate ($M L^{-1} T^{-1}$), $\tilde{q}_m$, is defined as the product of the velocity profile, $u_*$, and the bulk density of the colluvium measured in the field ($M L^{-3}$), $\rho_s$, integrated with respect to soil depth such that:

$$\tilde{q}_m = \int_0^{z_t} u_* \rho_s dz_s \ast \qquad (4.9)$$

Colluvium was sampled at 20, 40, 60, and 80 cm depth increments (4 samples per depth increment, total = 16) to determine the vertical variation in $\rho_s$. Similarly, 6 samples (3 at a mean depth of 30 cm and 3 at mean depth of 70 cm) were used to characterize the Atterberg limits of the colluvial soil.

The landscape denudation rate or sediment production rate ($M L^{-2} T^{-1}$), $Q_{spr}$, is calculated by multiplying $\tilde{q}_m$ by the ratio of the hillslope length to the total hillslope area such that:

$$Q_{spr} = \tilde{q}_m \frac{2 \sin \beta l_h}{A_c} \qquad (4.10)$$

where following Reneau et al. (1989), $\beta$ is the convergence angle representing the angle between the orientation of the hollow axis and the down-gradient orientation of the adjacent side slopes, $l_h$, is the planform length of the hollow axis, and $A_c$ is the area over which slow mass movement acts. The approach presented here accounts only for physical, not chemical transport and denudation.

*Inferring colluvial soil production rates*

Bedrock-to-soil production rates are inferred using variants of the continuity equation expressed by equation 4.1. Analyses are restricted solely to strongly divergent topography where the long-term thickness of colluvial soil has a higher likelihood to be approximately constant. Areas of divergent topography are typically mantled with a thin cover of colluvium, and are potential sediment sources not sinks. Assuming a steady state colluvium thickness $\left(\partial z_s/\partial t = 0\right)$ and a temporally constant bulk density of colluvium($\partial \rho_s/\partial t = 0$) on divergent topography, the colluvium production rate, $-\partial e/\partial t$, is equal to the divergence of sediment flux modified by the respective bulk densities of the materials:

$$-\frac{\partial e}{\partial t} = \frac{\rho_s}{\rho_r}\nabla \cdot \tilde{q}_s \qquad (4.11)$$

Although the colluvium production rate can be determined directly from equation 4.11, values of $\tilde{q}_s$ are rarely known. Determining $\nabla \cdot \tilde{q}_s$ requires either i) known colluvium thickness and the form of the vertical velocity profile or ii) the adoption of a specific transport law for colluvium flux relating transport rate to topographic form.

Where values of $\tilde{q}_s$ are unconstrained by independent measurements, calculation of $-\partial e/\partial t$ requires the assumption of a transport law. The most general hillslope transport law is that where sediment transport is portrayed as being simply slope-dependent (equation 4.2). Assuming colluvial transport has a linear slope dependence, a steady state

colluvium thickness, and that $K$ is spatially and temporally constant, $-\partial e/\partial t$ can also be determined from topographic form resulting in:

$$-\frac{\partial e}{\partial t} = \frac{\rho_s}{\rho_r} K \nabla^2 z$$

(4.12)

where $\nabla^2 z$ is the topographic curvature ($L^{-1}$). The spatial distribution of bedrock outcrops and colluvium depth ($z_s$) over a landscape can be used to evaluate conversion rates of bedrock-to-colluvium by rearranging equation 4.12 to yield the association of local curvature surrounding bedrock outcrops. For the case where bedrock is exposed, the transport divergence exceeds the colluvium production rate such that:

$$-\frac{\partial e}{\partial t} < \frac{\rho_s}{\rho_r} K \nabla^2 z$$

(4.13)

Hence, for areas where $K$, $\rho_s$, and $\rho_r$ are known the production rate can be constrained through the patterns of local topographic curvature associated with bedrock outcrops.

As topographic data measured with a large grid spacing (i.e., > 30 m) cannot accurately represent small-scale hillslope textures characteristic of slow mass movement processes (Zhang and Montgomery, 1994), a digital representation of the topography was generated by field surveying almost 3700 points at an approximate 2 - 3 m spacing with a total station theodolite (figure 3.4). Using a contour map generated from this field survey, I took 626 colluvium depth measurements over 12,400 m$^2$ of the Mettman Ridge headwall (red polygon in figure 3.4) with a soil probe, bucket auger, and/or shovel at an approximate sampling grid of 5 m (chapter 3). The ground and bedrock surfaces were characterized by

fitting two-dimensional, second-degree polynomials to local subsets (314 m² area) of the ungridded x, y, z locations of the topographic data at an even 5 m spacing. The local gradient ($|\nabla z|$) and curvature (Laplacian operator, $\nabla^2 z$) were then calculated from the best-fit equations to the nine elevations of the 3 X 3 submatrix (e.g., Zaslavsky and Sinai, 1981; Zevenbergen and Thorne, 1987; Moore et al., 1991). Calculations were limited to those sites with at least 10 nearest neighbor elevations within a 10 m radius. This limiting criteria eliminated thirty-one sites (5% of the data set located along the margins of the study area) from the analyses producing a data set of 595 colluvium depths.

Estimates of the colluvium production rate, $-\partial e/\partial t$, are thus determined from i) short-term (< 9 yrs), local (860 m² area of CB1) measurements of the volumetric transport rate, $\bar{q}_s$, using equation 4.11 and ii) long-term, regional (12,400 m² area) patterns of divergent topography and bedrock outcrops assuming a linear transport law and a value for the coefficient of diffusivity, $K$, using equations 4.12 and 4.13. Determining $-\partial e/\partial t$ using method (i) requires knowledge of the material densities (assuming spatially and temporally invariant properties) and spatial distribution of the gradient of colluvial flux vector, $\nabla \cdot \bar{q}_s$. The distribution of $\nabla \cdot \bar{q}_s$ was calculated with a geographic information system (GIS) from all 212 sites using the neighboring 8 $\bar{q}_s$ values in a 3 X 3 sampling submatrix. From the spatially continuous field of $\nabla \cdot \bar{q}_s$ over CB1, the GIS was used to interpolate values of $\nabla \cdot \bar{q}_s$ specific to each standpipe location (excluding the 12 standpipes that exhibited small upslope displacements). To satisfy the assumed condition of a steady-state colluvium depth, $\partial z_s/\partial t = 0$, only those piezometer standpipes situated on strongly divergent topography, $\nabla^2 z < -0.03$ m⁻¹, were used in the following analyses. As most of the measurements of $\bar{q}_s$ are located within a topographic hollow, the limiting condition of

$\nabla^2 z < $ -0.03 m$^{-1}$ significantly reduces from sample size from 212 to 8. This small sample

size pertains only to production rates determined from the divergence of volumetric

transport.

Necessary input requirements to estimate values of $-\partial e/\partial t$ using method (ii)

include detailed topographic information to calculate $\nabla^2 z$, material bulk densities assuming

spatially and temporally invariant properties, estimates of the local diffusivity ( $K$ ), and a

known colluvium depth ( $z_s$ ) distribution. To satisfy the condition of a steady-state

colluvium depth $\left(\partial z_s/\partial t = 0\right)$ only those measurements of colluvium depth situated on

strongly divergent topography, $\nabla^2 z < $ -0.03 m$^{-1}$, were used in the following analyses

decreasing the data set from 626 to 134 measurements. Available estimates of the local

coefficient of diffusivity, $K$, are provided by 1) differentially displaced PVC pipes at CB1

reported here and 2) radiocarbon dating of basal colluvium within hollows of the Oregon

Coast Range that indicate mean colluvial transport rates of 34 ± 23 cm$^3$ cm$^{-1}$ yr$^{-1}$ (Reneau

and Dietrich, 1991); all mean values reported at 95% confidence interval. Measurements of

colluvium depth, $z_s$, including bedrock outcrop locations are discussed in chapter 3. The

methods used address the component of colluvium production from physical disturbance

but cannot address the flux arising from chemical weathering. Critical assumptions in

these calculations are that colluvium thickness is constant over time and that loss arising

from chemical dissolution is minor. Furthermore, this approach does not account for

tectonically driven changes in elevation.

## RESULTS

Colluvial soil on Mettman Ridge is composed of a dark-brown, silty sand matrix

surrounding isolated clasts of sandstone parent material. Laboratory tests of six samples

depict a non-plastic material with a mean Atterberg plastic limit of 56 and a plasticity index

of zero. Hence the material expresses little to no plastic deformation characteristic of clay-

rich material. Rather the stress-strain behavior determined through triaxial strength testing

reveals elastic deformation at low applied stress. There is, however, a moderately distinct

peak in the stress-strain plot demarcating the transition from elastic to non-elastic

deformation at axial strains of only 1 - 2%. Mean material bulk densities determined from

samples obtained from the field site are $\rho_s$= 1.2 tonnes m$^{-3}$ (n = 16, moisture content of

roughly 20 - 30%) and $\rho_r$= 2.2 tonnes m$^{-3}$ (n = 5). Soil bulk density, though, increases

with depth which is approximated as:

$$\rho_s = 0.640\,z_{s*}^{\,2} - 0.113\,z_{s*} + 0.864 \qquad (4.14)$$

where $z_{s*}$ is the distance below the ground surface in meters and $\rho_s$ is in tonnes m$^{-3}$.

Equation 4.14 was determined by fitting a 2$^{nd}$ order polynomial (R$^2$ = 0.94) to the mean

value of binned bulk densities at a given depth below the ground surface.

*Slow mass movement rates*

Standpipes were predominantly displaced downslope and inclination varied

inversely with the depth of emplacement. Table 4.1 lists piezometer inlet depths, rotation

angle, local soil depth, record length, and annual, horizontal velocity in the downslope

direction. Figure 4.2 depicts a piezometer nest at CB1 exhibiting an inverse relationship

between angular displacement, $\alpha_p$, and depth of standpipe emplacement, Z. The high

degree of tilt exhibited by the shallow piezometer in figure 4.2 (far right) is not necessarily

indicative of rapid creep of surficial material. For standpipes emplaced at varying depths to

exhibit the same amount of downslope movement at the surface, shallower pipes must

display greater angular rotations. A comparison of the rotation angle, representing downslope displacement, and length of above-ground length of PVC standpipe for all pipes shows no relationship, indicating that the pipes were not artificially displaced by a lever-arm influence induced by the above-ground pipe length (figure 4.3). There are, though, 12 standpipes that displayed inclinations in the upslope direction, 7 of which are anchored into bedrock. As the rotation angles are small, it is probable that the standpipes were initially installed with a slight upslope tilt.

The spatial distribution of inferred horizontal, surface velocity, at CB1 (figure 4.4) is characterized by distinct high velocity ($> 7$ cm yr$^{-1}$) regions separated by low velocities ($<$ 2 cm yr$^{-1}$) characteristic of a larger area. The mean, median, and standard deviation of all the surface, non-negative transport rates (including zero values) are 1.9, 1.3, and 2.2 cm yr$^{-1}$, respectively. Although the highest velocities are located in the axis of the hollow where colluvial thickness is typically greatest, a plot of horizontal surface velocity, $u_*$, and local colluvial soil depth reveal no systematic relationship (figure 4.5A). Figure 4.5B, a plot of $u_*$ and local hillslope gradient, exhibits a rough normal distribution of $u_*$ centered about the mean hollow gradient of 43°. The highest surface velocities are neither located in regions of the thickest soil or steepest surface gradient.

Surface velocity varied with emplacement depth in several ways for piezometer nests with 3 to 5 standpipes (figure 4.6). Although, not a true depth profile, these plots express the variation in surface displacement for 6 archetype piezometer nests (12% of the total data set). The non-unique relation between surface displacement and depth of emplacement within individual nests, in addition to the planform velocity distribution of figure 4.4, illustrates the great spatial variation in the transport processes. Although the greatest downslope tilt of an individual piezometer within a nest occurs at all depths

throughout the colluvial deposit, three general styles of deformation are present. For piezometer nests with > 3 standpipes, surface displacement rates varied with a total of six nests showing the highest displacement rates in the shallowest pipes similar to the top 2 plots in figure 4.6, eight nests showing highest rates in moderate-depth pipes similar to the middle 2 plots, and eleven nests showed the highest surface displacement rates in the deepest pipes similar to the bottom 2 plots. Surface displacements of the nest shown in figure 4.2 are depicted in the lower right corner of figure 4.6, with the highest rates occurring in the deepest piezometers. Furthermore, the highest magnitude of surface displacement (up to 8 cm yr$^{-1}$) is expressed by the deeper piezometers. If however the inlet depths of shallow pipes migrated downslope, the resulting rates of inferred transport would be artificially low.

To extrapolate the inferred surface velocities presented in figures 4.4 - 4.6 into a velocity-depth profile requires numerous assumptions. That is, below-ground displacements in a velocity-depth profile represent calculated displacements rather than measured displacements. To infer a velocity-depth profile I assume: 1) the standpipe inlets are fixed in space, 2) the angle $\alpha_p$ is a constant, and 3) displacements for standpipes anchored in bedrock are resolved solely within the overlying colluvium. I calculate horizontal velocity, $u_*$, using equation 4.7 at the following selected depths: the ground surface, 15 cm below surface, as well as at 2, 8, 32, and 128 cm above the standpipe inlet depth. As it is impossible to fit exponential regression curves through data with negative or zero values, I omitted the 30 standpipes exhibiting small upslope or zero displacements (0° = $\alpha_p$ > -10°) from the subsequent analysis of hillslope-scale transport. Combining the remaining 182 standpipes on the hillslope with positive displacements reveals a general trend of decreasing horizontal velocity with increasing depth of pipe emplacement (figure

4.7). The 3 regression equations applied correspond to an exponential curve as suggested by the theory of Davison (1889), the modified exponential suggested by Kirkby (1967) and Carson and Kirkby (1972), and a simple linear curve fit. The modified exponential velocity profile suggested by Kirkby (1967) is intended to represent zero shear at the ground surface corresponding to the absence of soil overburden. The resulting curve fits uniformly express low correlation coefficients ($0.12 < R^2 < 0.26$) because the inferred $u_*$ values embody a large degree of variability.

The exponential regression equation in figure 4.7 expresses the greatest correlation coefficient and the residuals of the curve fit display the weakest systematic variation with the independent variable (depth below ground surface). Figure 4.8 is a plot of the curve-fit residuals (difference between inferred velocities and velocities predicted by regression equations) and depth below surface. Residuals to the exponential and modified exponential ("Kirkby") curves were determined by calculating the difference between the base 10 logarithm of the inferred velocities and the base 10 logarithm of the velocities predicted by regression equations. In performing the curve-fit regressions certain assumptions about the residuals are made: they are independent, have a zero mean, a constant variance, and follow a normal distribution. Figure 4.8 shows that these assumptions have been violated to varying degrees. While residual variance is relatively constant for the exponential and "Kirkby" regression curves, the variance is not constant for the linear equation. The variance of the residuals to the linear regression systematically decreases with depth below the surface. The mean value of the residuals to the exponential, "Kirkby," and linear regressions equations are -0.06, -0.31, and 0.04 respectively. Only the residuals to the exponential regression, though, are normally distributed. The residuals to the linear regression violate the curve-fit assumptions. Although the residuals to the exponential and "Kirkby" equations display similar variance, the simple exponential fit

has the highest correlation coefficient, a mean close to zero, and a normal distribution. Hence the regression equation with the best fit to the velocity data representative of the entire site is:

$$u_* = 1.1e^{-0.02z_{s*}}$$

(4.15)

where $u_*$ is expressed in cm yr$^{-1}$, $z_{s*}$ represents positive values of depth below the ground surface in cm. The velocity-depth profile of the colluvial soil appears to behave as a non-Newtonian fluid such that velocity does not vary linearly from zero at the bedrock contact to a maximum at the ground surface.

I use the exponential vertical velocity profile of equation 4.15 to calculate a sediment flux of volumetric colluvium transport rate, $\tilde{q}_s$, (cm$^3$ cm$^{-1}$ yr$^{-1}$). Integrating the velocity-depth profile over a mean colluvium depth of 80 cm (determined from drill hole data of piezometer standpipes) yields:

$$\tilde{q}_s = 1.1 \int_0^{80} e^{-0.02z_{s*}} dz_{s*} = 44 \text{ cm}^3 \text{cm}^{-1} \text{yr}^{-1}$$

(4.16)

If $\tilde{q}_s$ is solely slope-dependent of the form expressed by equation 4.2 as often assumed, the corresponding hillslope-scale diffusion coefficient, $K$, is calculated to be 47 cm$^3$ cm$^{-1}$ yr$^{-1}$; using a mean hollow gradient of 43° in equation 4.8. The hillslope-scale $\tilde{q}_s$ can also be used to calculate the sediment mass transport rate, $\tilde{q}_m$, through equation 4.9. Using the velocity-depth profile of equation 4.15, the site-specific density-depth function expressed by equation 4.14 to account for the low density material near the ground surface,

and a mean colluvium depth of 0.8 m the sediment mass transport rate, $\bar{q}_m$, is 4.2 tonnes m⁻¹ ka⁻¹.

Assuming the exponential form of the velocity-depth profile, representative of the site as a whole, is characteristic of any location within the hollow, I calculate local values of $\bar{q}_s$ based upon the displacement of individual standpipes. The general form of equation 4.15 is used to compute local fluxes by integrating over the local soil depth for each standpipe as in equation 4.3. I use the inferred surface velocity depicted in figure 4.4 and assume the velocity is zero at the base of the soil to constrain values of the two constants in equation 4.15. The resulting spatial distribution of depth-integrated flux, $\bar{q}_s$, (figure 4.9) closely resembles the pattern of inferred surface velocities (figure 4.4). While the hillslope-scale transport rate (44 $cm^3 cm^{-1} yr^{-1}$) is based on a mean soil depth and a velocity-depth profile characteristic of the entire site, transport rates depicted in figure 4.9 are calculated from local measurements of soil depth and velocity. Sites with $\bar{q}_s$ values less than 30 $cm^3 cm^{-1} yr^{-1}$ are evenly distributed over the entire study site; throughout the hollow axis and over sideslopes from near the ridgetop downslope to the transition of the hollow with the first order channel (figures 3.4 and 4.9). Sites with $\bar{q}_s$ values greater than 100 $cm^3 cm^{-1} yr^{-1}$, on the other hand, are focused within 3.5 m of the hollow axis. The highest fluxes occur where the colluvial deposits are thick with rapid surface velocities.

Local, annual sediment fluxes calculated for individual standpipes (figure 4.9) are not a simple linear function of ground surface slope (figure 4.10) as theoretically predicted. Rather, the highest sediment yields occur in conjunction with the mean hollow gradient of 43°. The mean and median of the sediment fluxes calculated from local soil depths and velocities are 18.5 and 10.6 $cm^3 cm^{-1} yr^{-1}$, respectively (lower and upper quartile values of

4.4 and 20.4 $cm^3 cm^{-1} yr^{-1}$). The corresponding mean and median of the coefficient of

diffusion calculated from local soil depths and velocities are 20.2 and 11.6 $cm^3 cm^{-1} yr^{-1}$,

respectively (lower and upper quartile values of 4.8 and 23.1 $cm^3 cm^{-1} yr^{-1}$). The Pearson

correlation coefficient (a dimensionless index ranging between -1 and 1) value of -0.04

corroborates the poor linear fit between $\tilde{q}_s$ and the ground surface slope. The cumulative

distribution function (cdf) for the local topographic gradient resembles an approximate

Gaussian distribution (figure 4.11A). The cdf's for $\tilde{q}_s$ and $K$, however, are not Gaussian

but rather express pronounced positive skewnesses indicative of lognormal distributions

(figures 4.11B, C, & D). If sediment flux were simply slope dependent, the cdf's of $\tilde{q}_s$

and $K$ would be Gaussian similar to the distribution of gradient. The median, lower

quartile, and upper quartile values of $\tilde{q}_s$ and $K$ are depicted in figure 4.11D.


In spatial statistics $\gamma^*(\tilde{h})$, the semivariogram function, is used to measure the

continuity of data in specific directions and distances (see chapter 3 for more detailed

discussion). The semivariogram function, defined as half the average squared difference

between the $x$ and $y$ coordinates of a select data pair, increases as sample pairs become

more disparate (Hohn, 1988; Isaaks and Srivastava, 1989). Figure 4.12 is a semivariogram

or plot of $\gamma^*(\tilde{h})$ vs. lag or distance between data pairs ($\tilde{h}$) used to examine the spatial

continuity of $\tilde{q}_s$. The steep rise in values of $\gamma^*(\tilde{h})$ reflects a large magnitude discontinuity

at the origin (a nugget effect) and thus great spatial variation in $\tilde{q}_s$. In addition, the

decrease in values of $\gamma^*(\tilde{h})$ at values of $\tilde{h}$ greater than about 17 m indicates that the values

of $\tilde{q}_s$ separated by 30 m are more similar than paired values separated by a 15 m spacing.

Often referred to as a hole effect, this feature of a semivariogram is characteristic of spatial

distributions with discrete lenses or pockets of similar values separated by regions with

relatively homogeneous background values (figures 3.4 and 4.9). Hole effects also occur

in data sets expressing natural cyclicity where values do not increase monotonically.

Furthermore, the large nugget effect [nugget = 272 $(cm^3 cm^{-1} yr^{-1})^2$] portrays the fact that

$\bar{q}_s$ varies greatly over short distances.


To evaluate the relative contributions from different transport processes, I use

equation 4.10 to compare denudation rates, $Q_{spr}$, attributed to short-term, modern soil creep

and landsliding. While soil creep may transport material over the entire landscape,

landsliding delivers sediment directly into the fluvial domain. The mass deposition rate

attributable to recent soil creep determined from the colluvium bulk density-depth function

is 4.2 tonnes $km^{-1} yr^{-1}$. Using a $\beta$ value of 25°, a hollow-axis length, $l_h$, of 50 m, and a

hollow area, $A_c$, of 860 $m^2$, the physical denudation rate in the hollow is 206 tonnes $km^{-2}$ yr

$^{-1}$. In a companion study located in the same region as this study (Montgomery et al.,

submitted), landslide surveys over a ten year period identified 35 landslides representing a

surface area 8700 $m^2$ within a 0.43 $km^2$ area. Using the density-depth function discussed

earlier and assuming a mean colluvium depth of 1m, the denudation rate attributed to

modern landsliding is 2064 tonnes $km^{-2} yr^{-1}$. Thus, current denudation rates arising solely

from soil creep are about 10% of the modern landsliding denudation rate. In summary,

present denudation rates arising from soil creep are similar to geologic rates inferred

through hollow infilling, but present denudation rates due to landsliding may be an order of

magnitude greater.


Dethier (1986), in an examination of chemical denudation rates from the West Fork

of the Millicoma River nearby to my study area, reports that dissolved silica accounts for

15.5 tonnes $km^{-2} yr^{-1}$ while cations and anions account for an additional 14.2 tonnes $km^{-2}$

$yr^{-1}$. Hence, total denudation, both physical and chemical, from my study area approaches

236 tonnes $km^{-2}yr^{-1}$. For comparison, Reneau and Dietrich (1991) report a mean

denudation rate of $150 \pm 53$ tonnes $km^{-2}yr^{-1}$ for the Oregon Coast Range, including the

chemical denudation rate contribution of nearly 30 tonnes $km^{-2}yr^{-1}$ (Dethier, 1986).

Similarly, Benda and Dunne (1987) calculated a physical sediment production rate for 1st

order basins of 28 tonnes $km^{-2}yr^{-1}$.

*Colluvial soil production rates*

The gradient of the volumetric fluxes inferred from differentially displaced

piezometer standpipes (figure 4.9) is used to estimate colluvium production rates over the

hollow CB1 for a 9 year period. In addition, longer term production rates in areas of

bedrock outcrops and areas mantled with colluvium are determined from the magnitude of

topographic divergence and the coefficient of diffusivity over a 12,400 $m^2$ area of colluvium

depth mapping (red polygon on figure 3.4). The production rates inferred from these two

divergent methods, representative of short and long term measurements rates, are of similar

magnitude and show no dependency of production rate and overlying soil thickness.

*i) Rates of $-\partial e/\partial t$ calculated from spatial distribution of $\tilde{q}_s$*

The displaced piezometer standpipes provide a unique opportunity to characterize

the short-term spatial gradient of sediment flux ($\nabla \cdot \tilde{q}_s$) over the scale of a hillslope hollow.

The gradient in sediment flux ($\nabla \cdot \tilde{q}_s$) was determined from the spatial distribution of local

$\tilde{q}_s$ inferred from individual standpipe displacements (figure 4.9) using a GIS. Values of

$-\partial e/\partial t$ determined from $\nabla \cdot \tilde{q}_s$ using equation 4.11 are roughly 0.1 mm $yr^{-1}$ and express

no correlation with the depth of overlying colluvium (figure 4.13). The lower quartile,

median, and upper quartile values of $-\partial e/\partial t$ are 0.092, 0.14, and 0.26 mm $yr^{-1}$, respectively

(n = 8). Since no correlation with overlying soil depth is observed, the function describing

production rate may be simplified to $-\partial e/\partial t \cong 0.1$. As the subset of $\bar{q}_s$ used to calculate

$-\partial e/\partial t$ are based on locally divergent topography ($\nabla^2 z < -0.03$ m$^{-1}$) within a hollow,

values of $-\partial e/\partial t$ in figure 4.13 may have a small, unknown component arising from

changing colluvium depth over time. For example, if the assumption that $\partial z_s/\partial t = 0$ is

incorrect, a thickening colluvium cover (increasing value of $\partial z_s/\partial t$ in equation 4.1)

increases the inferred values of $-\partial e/\partial t$ in equation 4.11. Thus, I estimate maximum values

for $-\partial e/\partial t$ derived from inferred sediment fluxes.

*ii) Rates of $-\partial e/\partial t$ calculated from spatial distribution of $\nabla^2 z$*

      The occurrence of bedrock outcrops within a landscape provides constraints on

where the long-term erosion rate exceeds the bedrock-to-colluvium production rate. At the

Mettman Ridge headwall, bedrock outcrops occur in both convergent and divergent

topography ranging in elevation from the drainage divide to the local confluence (figures

4.14 & 4.15). Irregularly shaped blocks of resistant rock appear at the ground surface

throughout the hillslope with dimensions ranging up to 20 m in length (figure 4.14).

Bedrock outcrops were primarily exposed on the lower half of the hillslope as broad sheets

in areas of topographic convergence, often revealing exfoliation lenses that range up to

several centimeters in thickness. These broad exposures are likely to be exhumed by rapid

sediment flux on steep slopes (Roering et al., 1999) and by the occurrence of observed

landsliding of the overlying soil. Unexpectedly, bedrock outcrops and colluvium mantled

sites do not express statistically distinct populations with respect to topographic curvature

(figures 4.15). The Mann-Whitney U test, a nonparametric version of the unpaired *t*-test

used to evaluate whether the means of two groups are equal, reveals that the mean

topographic curvatures for bedrock outcrops and sites mantled with colluvium are

statistically significant within the small data set (P < 0.0001; where test results of P = 1 indicate equivalent means). Bedrock outcrops on convergent ground surface topography ($\nabla^2 z > 0$ m$^{-1}$), accounting for 63 of the 86 bedrock outcrops, are presumably exposed by shallow landsliding and infrequent overland flow (figure 4.15A). Bedrock is exposed in 23 divergent areas ($\nabla^2 z < 0$ m$^{-1}$) where shallow landslides and overland flow are rare and the rate of diffusive transport presumably exceeds the conversion rate of bedrock to colluvium. For exposed bedrock, the median $\nabla^2 z$ value of 0.05 m$^{-1}$ in figure 4.15A reveals that under the current climatic, tectonic, and land use regimes mass movement and channel processes expose a larger area of bedrock to surficial weathering processes on convergent topography than diffusive processes removing colluvium from divergent topography. Furthermore, after completion of the colluvium depth mapping in the summer of 1996, additional extensive areas of bedrock outcrops were exhumed by debris flows within the colluvial channels and hollows during the storm of record in November 1996.

Focusing my analysis only on the subset of colluvium depth measurements located on planar and divergent topography (negative $\nabla^2 z$ values, n = 235) reveals that colluvium depth has no relationship with hillslope curvature (figure 4.16). While colluvium attains an equilibrium depth of generally < 1.5 m on the interfluves, no systematic decrease in soil depth was observed with increasing curvature of divergent topography. All sites with $\nabla^2 z$ less than -0.3 are exposed bedrock.

Values of $-\partial e/\partial t$ calculated from equation 4.12 using a mean coefficient of diffusion from figure 4.11D of $K = 20$ cm$^3$cm$^{-1}$yr$^{-1}$ reveal no correlation with the depth of overlying colluvium (figure 4.17A). The lower quartile, median, and upper quartile values of $-\partial e/\partial t$ calculated from sites of exposed bedrock using equation 4.11 are 0.040, 0.053,

and 0.14 mm yr$^{-1}$, respectively (n = 16) while the lower quartile, median, and upper quartile

values of $-\partial e/\partial t$ determined using all the sites (both exposed bedrock and areas mantled

with colluvium) are 0.044, 0.065, and 0.094 mm yr$^{-1}$, respectively (n = 134) (figure 4.17B).

As values of $\partial e/\partial t$ show no relation to $z_s$, the regression equation depicted in figure 4.17A

can be simplified to $-\partial e/\partial t \cong 0.07$. Production rates, though, differ over an order of

magnitude for both exposed bedrock and colluvium mantled areas because of the wide

range in $\nabla^2 z$. Besides the evident association with the magnitude of topographic

divergence, no systematic spatial pattern in the values of $-\partial e/\partial t$ was discernible over the

study region.


## DISCUSSION

I document great spatial variability of hillslope sediment flux based upon

measurements limited to a short time frame in a geologic context but spanning a large area

(almost $10^3$ m$^2$). Variation is expressed by regression equations with low coefficients of

determination ($R^2$), great ranges in the curve-fit residuals, and a large nugget effect in the

semivariogram of sediment flux. Similarly, Moeyersons (1988) and Clarke et al. (1999)

recognized great spatial and temporal variability of transport even within the same

"Young" pit over successive measurements. These results cast doubt on the use of a

simple linear transport relation expressed by equation 4.2 to predict short-term transport in

steep, highly bioturbated landscapes. If particle-motion depends on spatially variable

processes such as with bioturbation, the magnitude of the flux may be non-linear with an

exponent < 1 (E. J. Gabet, personal communication) or > 1 Roering et al. (1999). Once a

particle is dislodged from its neighbors, however, the distance traveled is some function of

slope because of the local gravity-induced downhill shear stress.

The evidence representative of specific sediment transport processes operating at my study site is varied. A lush vegetation canopy and thick layer of detritus retard significant transport by rainsplash. In the temperate climate of coastal Oregon the frequency and depth of frost within the ground is minimal, limiting the process of freeze-thaw. At present, there is no transport from tree throw because the trees are not yet large enough to fall over. No overland transport of water was seen to occur even during heavy rains as the colluvium is highly conductive (Montgomery et al., 1997). Although shear stress arising from the colluvial overburden theoretically increases with depth, the upper 50 cm of surface material shows highest displacement rate, a region with little overburden-induced shear. Hence the velocity-depth profile suggested by Kirkby (1967) does not apply at this site. The profile arising from pure continuous or rheologic creep as suggested by Kirkby (1967) would resemble a Z-curve with an exponential form at depth superimposed with plug flow at shallow depths. Even though the exponential form of my depth profile data is inconsistent with pure rheologic creep, some component of rheologic creep may be expected on hillslopes such as these with mean slopes of 43°. The granular nature of the colluvium and the absence of a plastic behavior denoted by the Atterberg tests, however, precludes the occurrence of widespread rheologic creep characteristic of more clay-rich materials.

Ample evidence of bioturbation exits at my study area. Bioturbation induces diffusion of particles from regions of high particle concentrations to regions of low concentration by either the growth and decay of plant roots or by burrowing animals such as worms, ants, bees, and mountain beavers. The high rates of displacement measured at shallow depths (low gravitational stress) and low bulk density suggest that bioturbation transports material from depth to the surface. An abundance of recently deposited mounds of disrupted colluvium and an intricate network of tunnels attest to widespread particle

movement by mountain beavers. In areas of focused mountain beaver activity, a void produced by a mountain beaver hole downslope of a standpipe will be filled in by material in an upslope mound or by a displaced PVC pipe. Mountain beaver burrows are typically 10 to 20 centimeters in diameter and range in depth up to 1.5 m (Ingles, 1965; Martin, 1971; Feldhamer and Rochelle, 1982).

Repeat measurements of standpipe tilt over a 2 year period indicate that accelerated diffusion of particles or groups of particles is directly associated with mountain beaver activity. The reoccupation of 81 sites reveals that 27% of the pipes accelerated during a 2 year period between 1996 and 1998 and that those pipes that accelerated were located in areas of abundant, recently created mountain beaver mounds and tunnels characterized by loose soil devoid of vegetation. The amount of material within a single mound can be large. For example, one mountain beaver mound that was deposited directly on top of a catwalk in 1996 was $91000\,cm^3$ in volume. The mountain beaver burrow opening was located immediately adjacent to the catwalk and the area over which the mound was deposited was $5000\ cm^2$ providing a downslope transport rate of $18\ cm\ yr^{-1}$, the same order of magnitude as my maximum surface displacement in figures 4.4 and 4.5. Similarly, Reid (1981) reports that the mean mountain beaver mound volume in the Clearwater basin, Washington is $130,000\ cm^3$. The variability displayed in figures 4.4, 4.7, and 4.9 is consistent with spatially discontinuous, rapid transport initiated by mountain beaver disturbance.

If the hillslopes in the study area are in equilibrium, the transport capacity must increase with distance from the drainage divide in order to maintain homogeneous colluvium thickness on the divergent topography (Gilbert, 1909). My measurements in primarily convergent topography record no monotonic increase in transport capacity with

distance from the drainage divide. An examination of the variation of volumetric transport rate with distance from the drainage divide reveals that the highest transport rates are located midway from the ridgetop. Furthermore, high rates of surface transport occur over the full range of colluvial depths. If mountain beavers represent the primary transport agent, the spatial locus of their activity may be allied more closely with the location of prime roots for feeding as opposed to ground slope or distance from the ridgetop. Thus, in areas where the transport agent is spatially heterogeneous, such as with bioturbation, sediment flux should be concentrated in areas of high biologic disturbance.

The exponential or convex-upward form of the regression curves (equation 4.15) is consistent with the theory of Davison (1889) and with previous field studies (Young, 1960; Fleming and Johnson, 1975; Yamada, 1997). Furthermore, the short-term volumetric transport rate determined by grouping together all the standpipes in the hollow ($44$ $cm^3 cm^{-1} yr^{-1}$) and the mean and median rates calculated from local standpipe locations and colluvium depths in ($18.5$ and $10.6$ $cm^3 cm^{-1} yr^{-1}$, respectively) are strikingly similar to geologic rates inferred through colluvial hollow infilling in the Oregon Coast Range [$32 \pm 23$ $cm^3 cm^{-1} yr^{-1}$; Reneau and Dietrich (1991)] and western Washington [$34$ $cm^3 cm^{-1} yr^{-1}$; Reneau et al (1989)]. In addition, Reneau and Dietrich (1991) report a mean mass transport rate of $3.0 \pm 3.1$ tonnes $m^{-1} ka^{-1}$, a value similar to that reported here ($4.2$ tonnes $m^{-1} ka^{-1}$). Volumetric transport rates measured in the steep, headwaters of the Oregon Coast Range, though, are typically higher than those measured elsewhere. For instance, sediment flux measurements from Europe, New Zealand, and Puerto Rico span the range from $0.25$ to $8.5$ $cm^3 cm^{-1} yr^{-1}$ (Darwin, 1882; Young, 1960; Kirkby, 1967; Owens, 1969; Lewis, 1976; Young, 1978). In contrast, McKean, et al. (1993) report a larger mean diffusion coefficient ($360 \pm 55$ $cm^3 cm^{-1} yr^{-1}$), determined from cosmogenic isotopes for expansive soils in northern California.

Even though the modern sediment fluxes reported here are typically an order of magnitude higher than most flux rates, I believe my estimates represent a minimum bound to the actual transport in the Oregon Coast Range. The basis for this interpretation is several fold: 1) an unknown quantity of material bypassed the standpipes, 2) Kirkby (1967) reported that measurement of soil displacement via stake rotation similar to the approach adopted here may be up to five times less than the mean shear rate determined from "Young" pits, and 3) standpipe inlets within the colluvium may have migrated downslope.

While short-term, modern fluxes reported here are similar to Holocene fluxes for the same region (Reneau and Dietrich, 1991), the specific transport processes likely changed. For instance, the conversion of vegetation from established forests to regenerating industrial forests alters the processes driving sediment transport. The process of tree throw, which is thought to be instrumental in transporting sediment in steep catchments (Grant, 1963), does not happen without trees large enough and/or weak enough to fall over, uproot, and displace colluvium. The decrease in transport by tree-throw may be offset by: 1) a higher degree of mountain beaver activity spawned by the presence of numerous, young roots; 2) increased rates of rheologic creep resulting from the removal of trees and subsequent relative increase of stored water in the colluvium (Gray, 1973); or 3) fewer large-diameter, high-strength roots within the upper 50 cm of colluvium to bind the colluvium together. I suspect that the decrease in sediment transport by tree throw may be offset by increased transport by mountain beavers.

Colluvium production rates based on i) colluvium flux over less than a 9 year period are roughly equivalent to ii) production rates representative of the longer time scales

required to diffuse sediment from divergent topography. For example, colluvium production rates are i) 0.041 to 0.44 mm yr$^{-1}$ for rates determined from the local volumetric colluvium flux and ii) from 0.034 to 0.44 mm yr$^{-1}$ for rates calculated from the magnitude of topographic divergence (figures 4.13 and 4.17). As these ranges were determined through different methods and are representative of different time scales, the similarity of their minimum and maximum values lends credence to using the techniques discussed here to determine colluvium production rates. Likewise, published values of the colluvium production rate for other regions are of a similar magnitude. For example, Monaghan et al. (1992) report local production rates of 0.15 to 0.27 mm yr$^{-1}$ for Eocene shales exposed to the Mediterranean climate of central California. McKean et al. (1993) document an average rate of colluvium production of 0.26 ± 0.07 mm yr$^{-1}$ for comparable Eocene marine shales in central California. Heimsath et al. (1997), report bedrock-to-colluvium conversion rates of generally < 0.1 mm yr$^{-1}$ for the Franciscan assemblage in central, coastal California.

The production values reported here address the component of colluvium production from physical disturbance but do not address the component arising from the chemical weathering of bedrock. In conjunction with chemical denudation rates from Dethier (1986), Reneau and Dietrich (1991) estimate that roughly 11% of the denudation on a typical hillslope in the Oregon Coast Range is by dissolution of bedrock. As only a portion of the chemical flux deposits within the colluvium, the resulting contribution to the production rate from chemical dissolution of bedrock is less than 11%.

Although numerous studies assume conversion of bedrock to colluvium decreases with increasing colluvium cover, the relationship determined here for the Oregon Coast Range does not support this assumption (figures 4.13 and 4.17). No correlation between

the production rate and depth of overlying colluvium cover is apparent in either the values

inferred from the volumetric colluvium flux or topographic divergence. In contrast, the

colluvium production function depicted in figure 4.17 $\left(-\partial e/\partial t = 0.071 e^{-0.1 z_s}\right)$ has both a

lower y-axis intercept and a smaller negative slope than the relation calculated from

cosmogenic radionuclides sampled at Mettman Ridge $\left(-\partial e/\partial t = 0.28 e^{-3 z_s}\right)$ (Heimsath,

1999); where $-\partial e/\partial t$ is expressed in mm yr$^{-1}$ and $z_s$ is measured in meters. For bedrock

exposures where $z_s = 0$, the regression equation determined here predicts a production rate

of 0.071 mm yr$^{-1}$ while the cosmogenic isotope research predicts a rate of 0.28 mm yr$^{-1}$.

Contrary to the relation observed here, Heimsath et al. (1997) recognize an exponential

decline of colluvium production rates with increasing colluvium depth from measurements

of *in situ* produced cosmogenic concentrations in central coastal California. The lack of a

strong relationship between production rate and overlying colluvium depth or the spatial

position on the hillslope indicates that the processes converting rock to colluvium are

relatively insensitive to the overburden thickness of colluvium, possibly a result of the

active biogenic mixing at the site. Furthermore, figures 4.13 and 4.17 indicate that there is

no threshold thickness of overlying colluvium necessary to physically weather the bedrock.

Hence, neither an exponential nor a bell-shaped polynomial function fit the data presented

here, as colluvium production rates are uniform over the total range of colluvium depth.

The lack of a depth dependency in the production rate may arise because the

primary disturbance mechanism introducing bedrock into the overlying colluvium over

geologic time is likely to be tree uprooting. Although disturbances arising from mountain

beavers are frequent, mountain beaver burrows appear to be limited to the overlying

colluvium with minor upheaval of bedrock. Mountain beavers also appear to be less

prominent in old growth forests. Furthermore, the length scale of disturbance is relatively

small compared to pit and mound topography generated by tree throw. Where roots penetrate bedrock, tree throw causes a decrease in the bedrock surface elevation that is equal to or greater in magnitude than the overlying colluvium thickness. For instance, measurements of coniferous root wads in the Oregon Coast Range reveal thicknesses commonly over 1 m (chapter 3) and measurements of root wads adjacent to tree throw pits in the Olympic Mountains of Washington by Reid (1981) document thicknesses up to 1 m. Considering soil depth is generally less than 1.5 m, the thickness of material entrained into the colluvium from tree throw may exceed the colluvium thickness. The process of tree throw thus serves to displace bedrock and create pits in both the bedrock and soil. If tree throw is the primary mechanism responsible for colluvium production, the influence arising from industrial forestry on the rate of soil production may be considerable as trees are typically harvested prior to the onset of widespread tree throw. Hence, soil production rates may be suppressed in response to industrial forestry.

## CONCLUSION

Changes in the inclination of 212 piezometer standpipes over a 4 to 9 year period within a steep, colluvium-mantled catchment show great variability in sediment flux. The volumetric flux calculated by grouping together all the piezometer standpipes and integrating over the mean hollow soil depth ($44 \ cm^3 cm^{-1} yr^{-1}$) exceeds the volumetric fluxes calculated with a velocity-depth profile that decreases exponentially with depth and local soil depths measurements (mean and median of 18 and 11 $cm^3 cm^{-1} yr^{-1}$). Sediment transport rates inferred from a 860 $m^2$ hollow compare closely to hollow infilling rates determined from basal colluvium charcoal dating in the same geographic area and bedrock lithology (Reneau and Dietrich, 1991). Although the present, mean volumetric transport rates are similar to the geologic rate determined through basal colluvium charcoal dating, the processes driving slow mass movement have changed in response to industrial forestry.

The exponential form to the velocity profile and the field observations linking mountain beaver activity to high displacement standpipes are consistent with a bioturbation-driven transport process. Although the sample sites express a Gaussian distribution with respect to topographic gradient, my volumetric transport rates, however, are inconsistent with the commonly assumed linear function of local slope.

Within convex or divergent topography of the Oregon Coast Range the magnitude of topographic divergence has no apparent relationship with the thickness of the overlying colluvium depth. Similarly, the calculated colluvium production function also has no apparent relationship with overlying colluvium depth such that locations of high production rates are asymmetrically distributed over the hillslope. Bedrock-to-colluvium production rates determined from colluvium flux measurements have a similar range as those rates calculated from the magnitude of topographic divergence. Hence, given the distribution of bedrock outcrops and detailed topographic maps one can determine colluvium production rates.

$$h_1 = Z \tan \alpha_p$$

$$L_s = \frac{\sin \upsilon h_1}{\sin \omega}$$

$$L_h = L_s \cos \theta$$
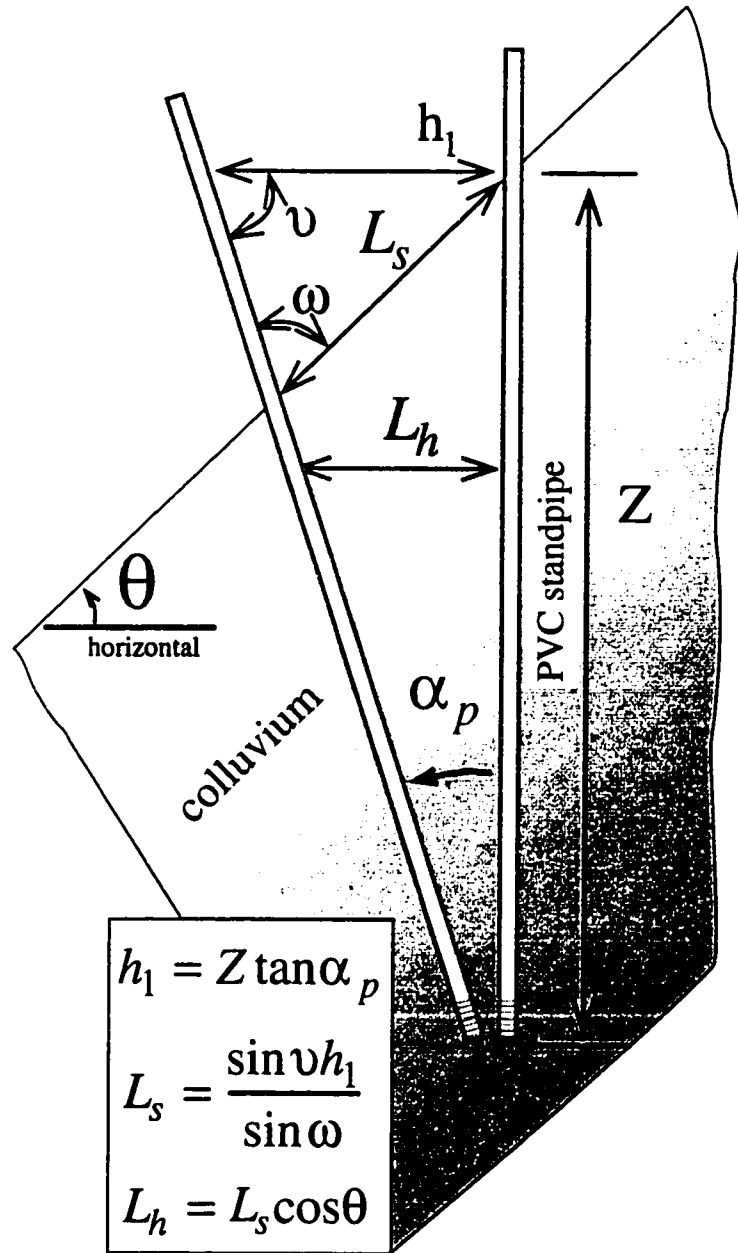
Figure 4.1    Schematic cross section of PVC piezometer standpipe deflection with exaggerated displacements to show geometric relations. Standpipes were initially installed roughly vertical on a local ground slope of $\theta$ and were deflected downslope by angle $\alpha_p$. Z is the underground length of standpipe, $L_s$ is the slope parallel displacement length, $L_h$ is the horizontal displacement length of interest, $\omega$ is the angle between the ground surface and the present pipe orientation, and $\upsilon$ is the angle between the present pipe location and $L_h$.

Figure 4.2    Annotated photograph showing differential tilting of PVC pipes within a piezometer nest at CB1. Hachured line approximates ground surface slope. Bold values in boxes adjacent to pipes represent surface, horizontal transport (cm yr$^{-1}$) while below ground lengths of PVC (cm) are shown in italics. Although standpipes show decreasing angles of rotation from vertical with increasing depth of emplacement, the highest transport rate is expressed by the deepest piezometer in the nest. Note catwalk and clipboard on left of photograph.

**catwalk**

| 5.0 | 7.9 | | 3.8 |
| --- | --- | --- | --- |
| *91* | *198* | | *47* |

| 7.7 |
| --- |
| *151* |
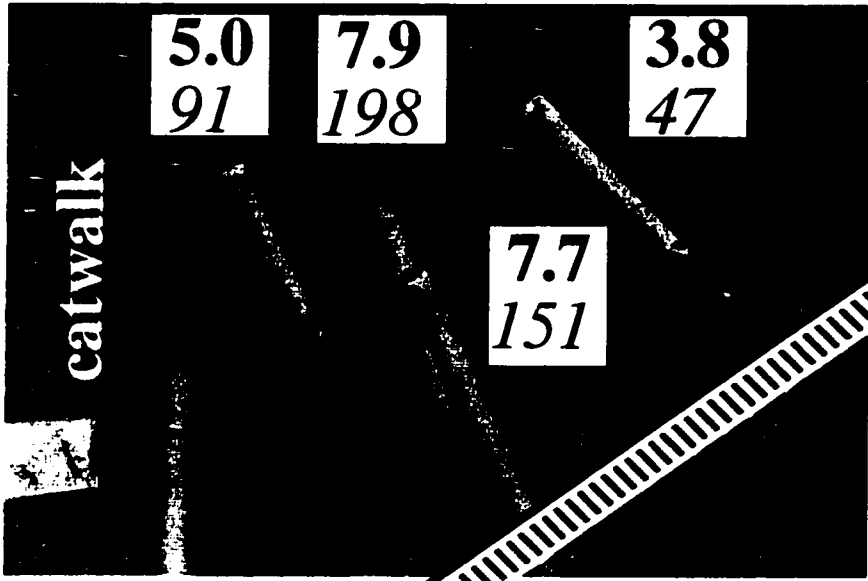
*ground surface*
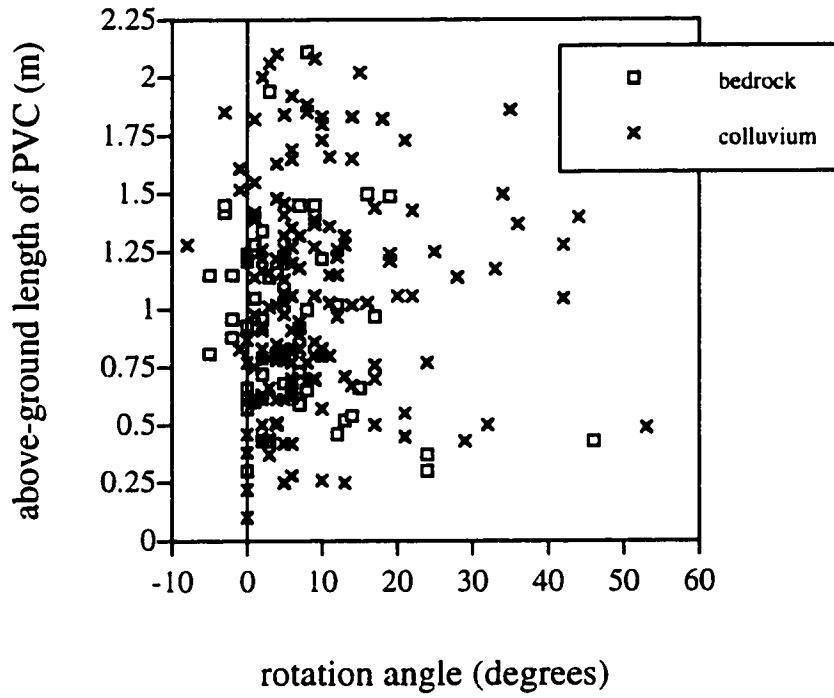
Figure 4.3    Plot of above-ground length and rotation angle of PVC piezometer standpipes showing no apparent lever-arm influence of long above-ground pipe lengths. Vertical black line corresponds to $\alpha_p = 0$.

Figure 4.4    Planform map showing distribution of surface velocity, $u_*$, at CB1. Standpipe location denoted by "+" symbol. Upslope, negative, velocities depicted in dark blue while the greatest downslope velocities appear in red.

surface velocity (cm/yr)
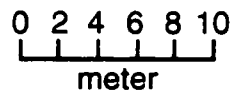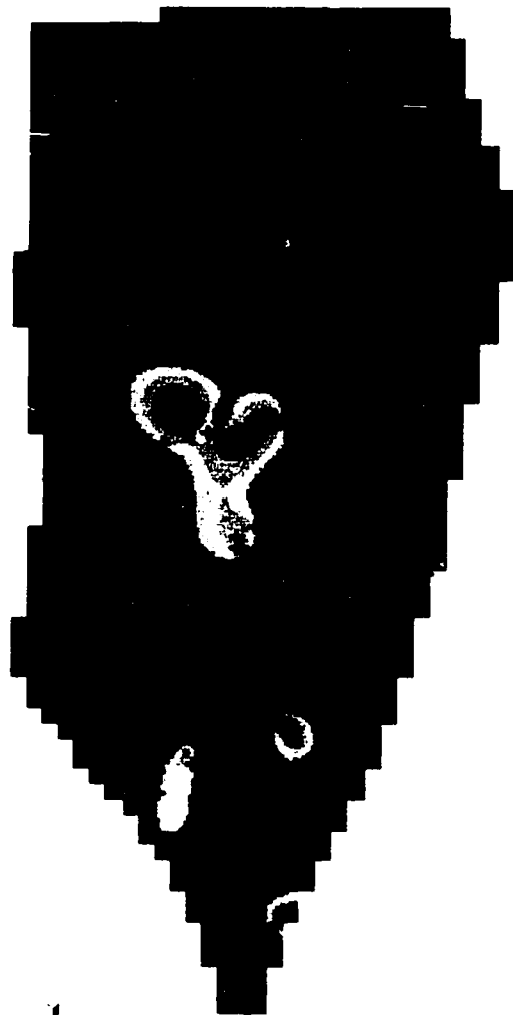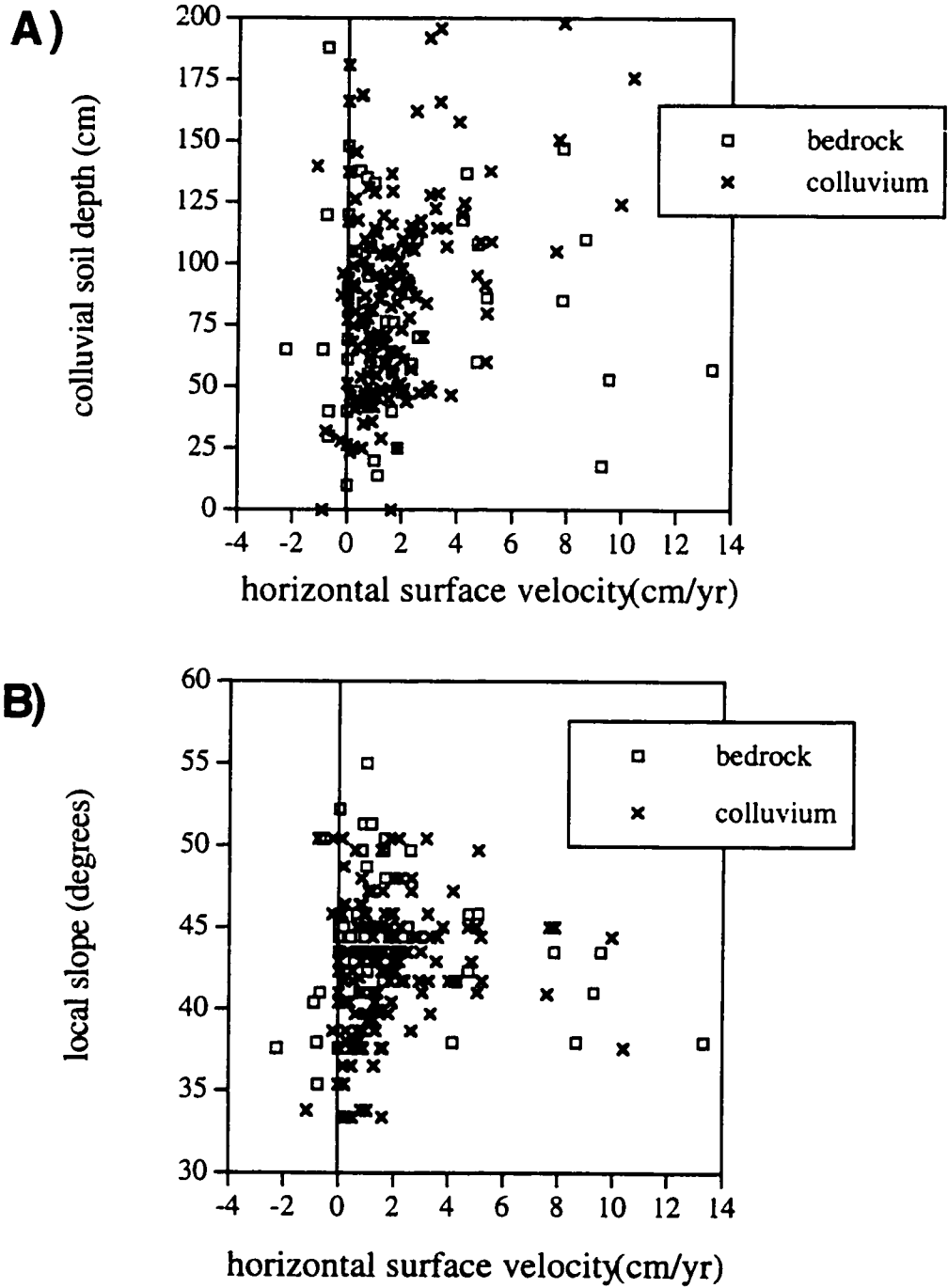
Figure 4.5 Plot of surface velocity versus (A) local colluvial soil depth and (B) local hillslope gradient for piezometer inlets anchored in colluvium and bedrock. Zero velocity depicted by vertical line.
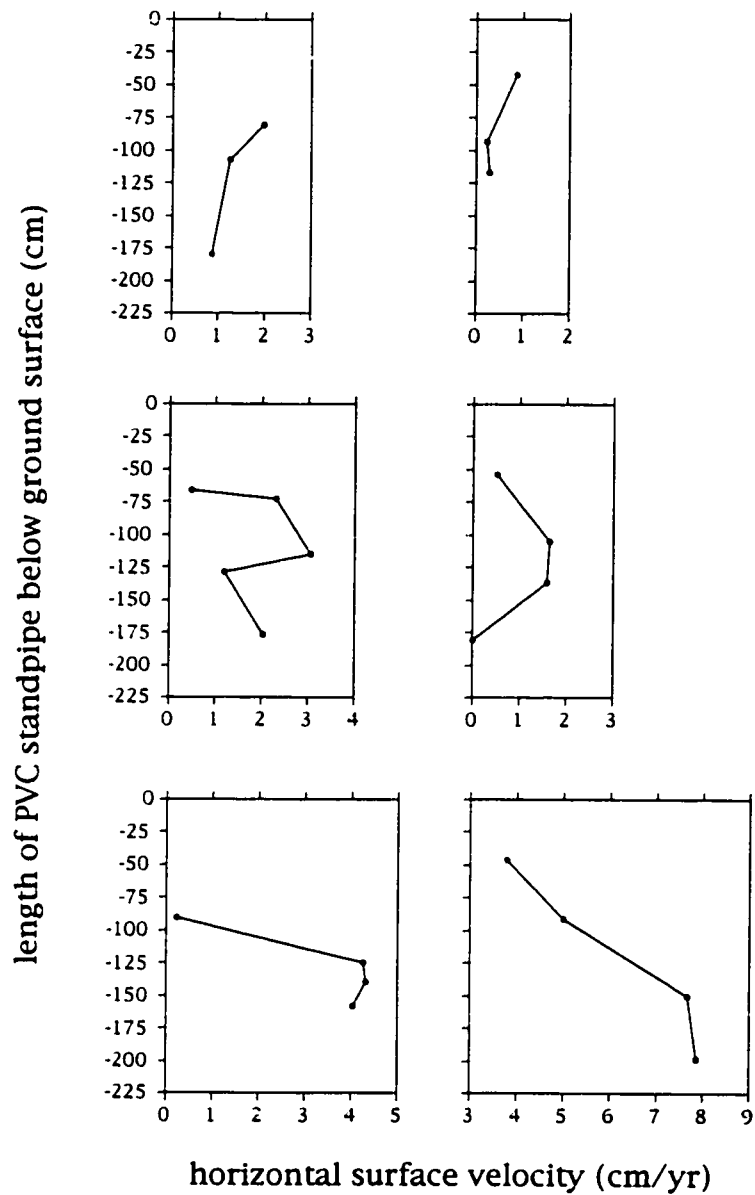
Figure 4.6    Surface velocity, $u_*$, inferred from angle of rotation, $\alpha_p$, measured at the ground surface for 6 archetype piezometer nests. Line segments link individual PVC standpipes, anchored at varying depths within a single piezometer nest. Depth of individual standpipes shown as open circles connecting line segments. Six nests exhibit highest rates in the shallowest pipes similar to the upper two plots, eight nests exhibit highest rates in the moderate-depth pipes similar to the middle two plots, and eleven nests showed the highest transport rates in the deepest pipes of a nest similar to the lower two plots.

A) $u_* = 1.1e^{-0.02z_s}$

exponential
regression

$R^2 = 0.26$

B) $u_* = 1.1(1 + 0.02z_{s*})e^{-0.02z_{s*}}$

"Kirkby"
regression

$R^2 = 0.12$

C) $u_* = 1.7 - 0.014z_s$

linear
regression

$R^2 = 0.19$

depth below surface (cm)
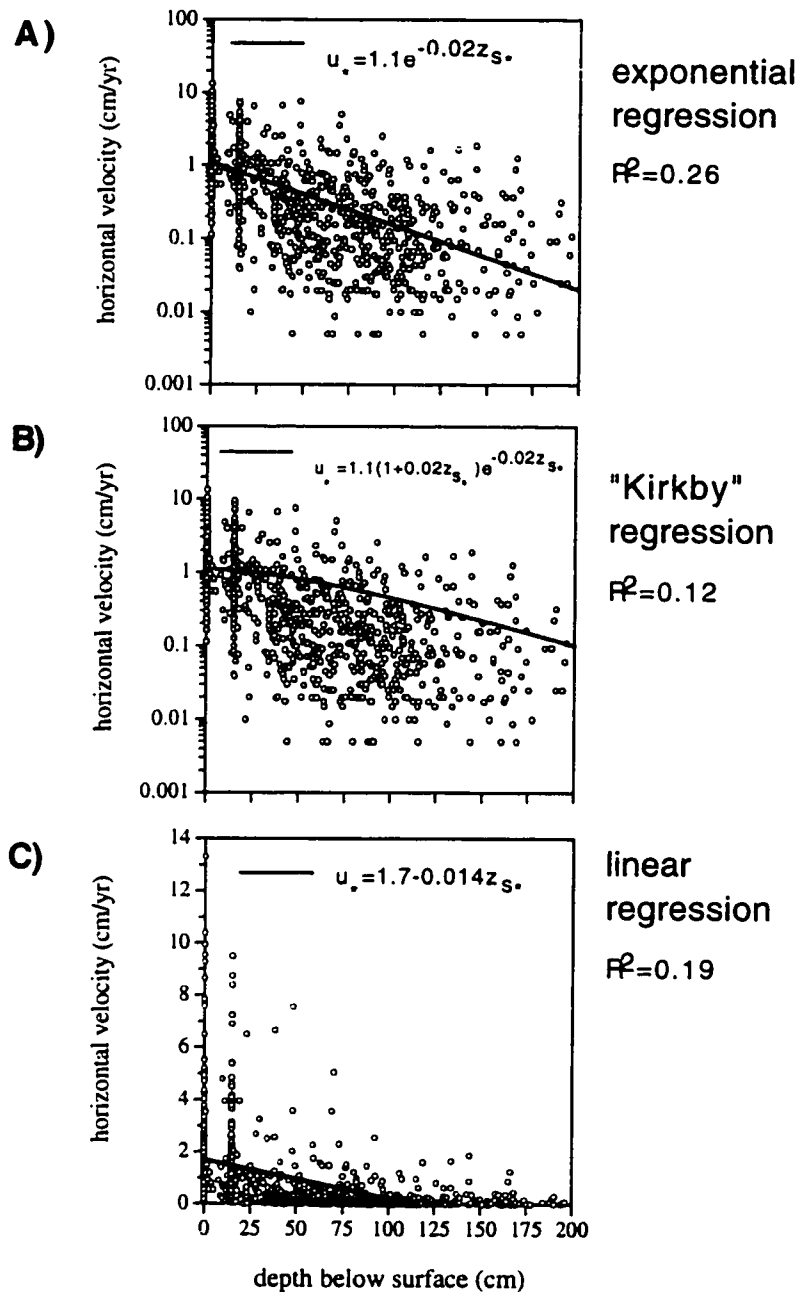
Figure 4.7    A 4 to 9 year record of horizontal velocity for all PVC piezometer standpipes at CB1 as a function of depth below the ground surface with A) an exponential regression, B) a regression suggested by Kirkby (1967), and C) a linear regression. Horizontal, transport rates were determined at the ground surface, 15 cm below surface, as well as at 2, 8, 32, and 128 cm above the inlet depth. Note decreasing transport rate with increasing depth of PVC below the ground surface and the absence of a distinct shear zone. Maximum depth of colluvium in the hollow is 1.98 m. Rotation of standpipes anchored into bedrock is resolved within the overlying colluvium.

208
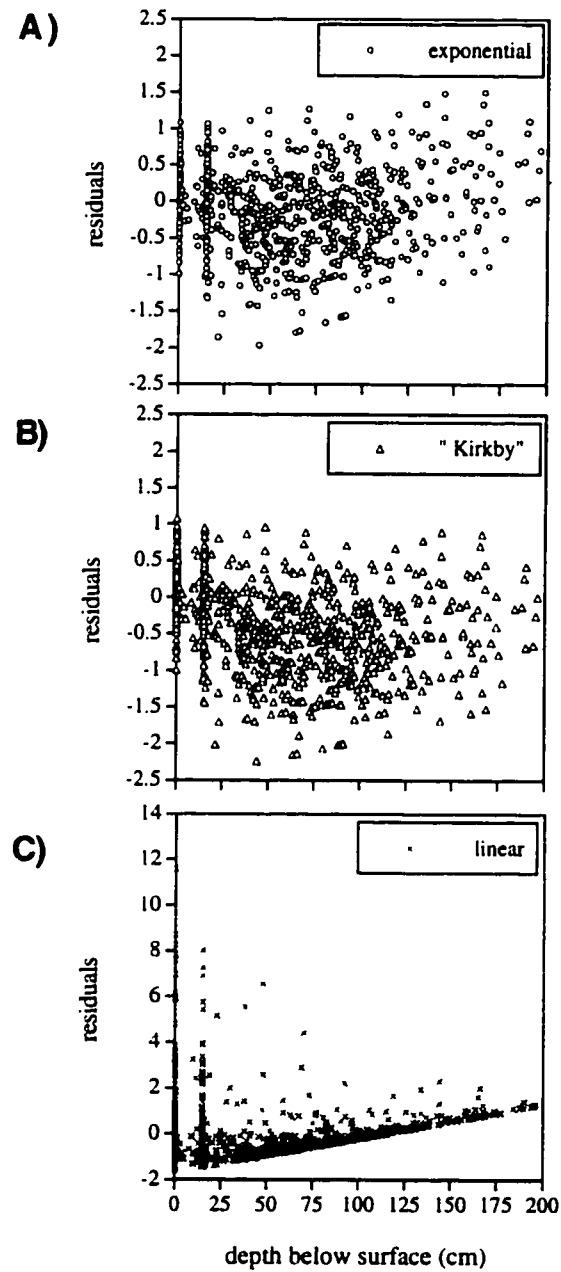


Figure 4.8    Plot of the independent variable (depth below ground surface) and residuals or difference between the inferred and predicted horizontal soil velocities for exponential, modified exponential ("Kirkby"), and linear regressions. Note different range of dependent variable on plot (C).

Figure 4.9    Planform map showing spatial distribution of sediment flux, $\bar{q}_s$, at CB1.

Regions of high flux roughly correspond to regions of high velocity, $u_*$, depicted in figure 4.4.

sediment flux (cm$^3$ cm$^{-1}$ yr$^{-1}$)

> 150
140
130
120
110
100
90
80
70
60
50
40
30
20
< 10

N

0 2 4 6 8 10
meter
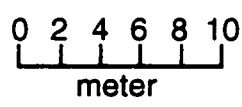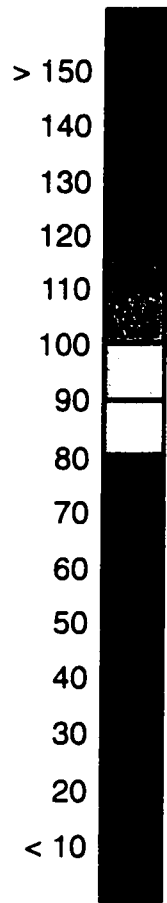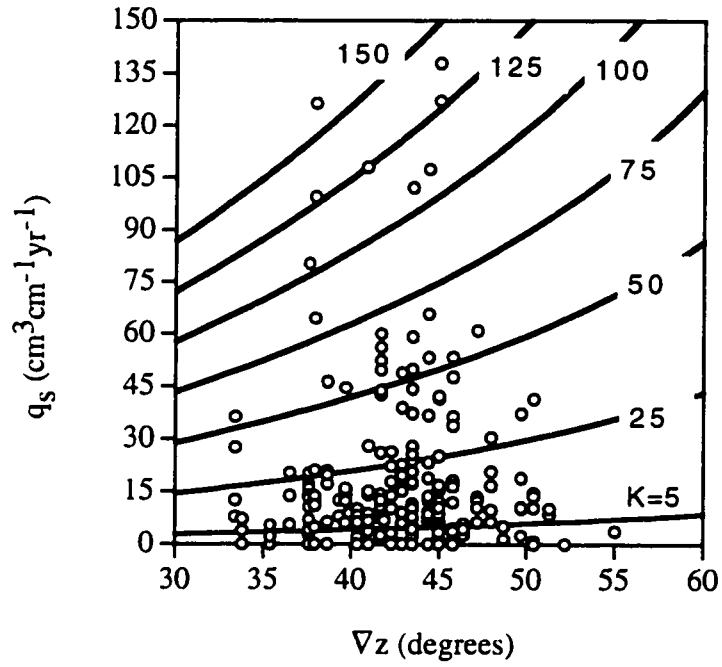
Figure 4.10    Annual volumetric transport rate, local slope, and lines of equal diffusivity for individual standpipes (n = 212) assuming displacement decreases exponentially with depth.
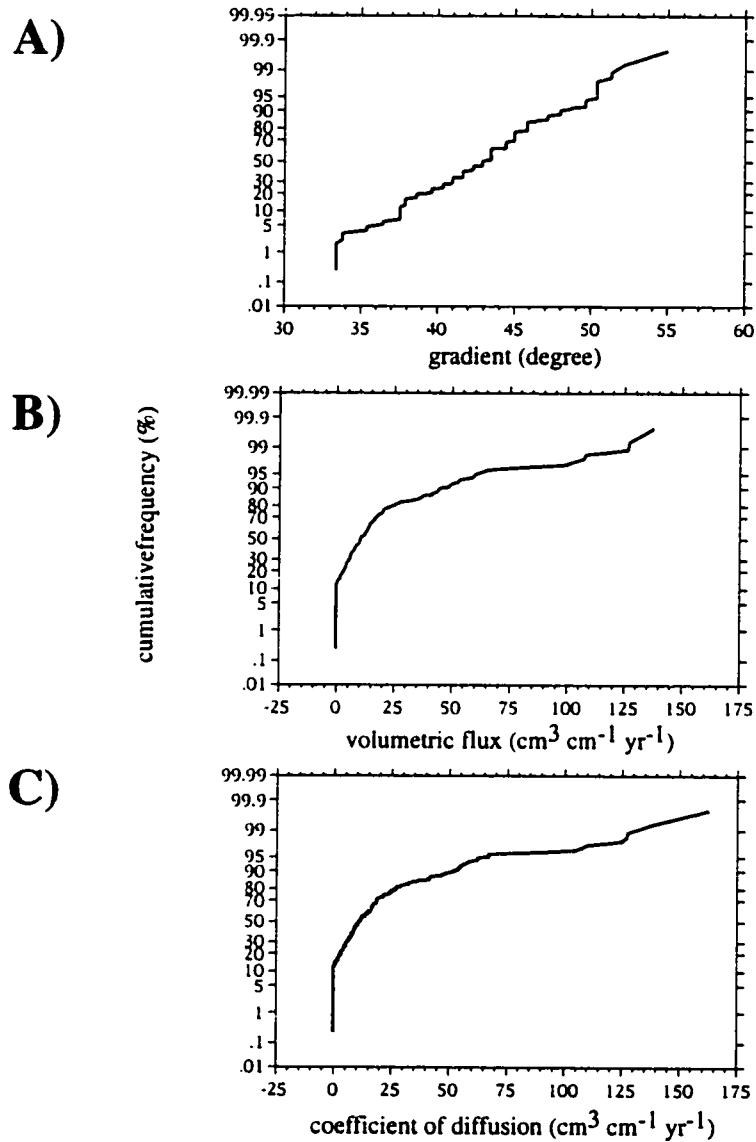
Figure 4.11    A) Cumulative distribution function (cdf) of $\nabla z$ revealing an approximate Gaussian distribution (skewness = 0.007) where the mean and median are almost identical; 42.8° and 42.9° respectively.  B)  Positively skewed (skewness = 2.6) cdf of $\bar{q}_s$ depicting a median value (11 $cm^3 cm^{-1} yr^{-1}$) that is less than the mean (18 $cm^3 cm^{-1} yr^{-1}$).  C)  Cumulative distribution function of $K$ that is positively skewed (skewness = 2.7) such that the median is less than the mean; 12 and 20 $cm^3 cm^{-1} yr^{-1}$, respectively.  Although the cdf for the entire distribution is clearly non-Gaussian, the cdf for all non-zero $K$ values reveals an approximate lognormal distribution (not depicted).  Hence sediment transport is not solely slope dependent as postulated in equation 4.2 and that hillslope-scale measurements express variability in $\bar{q}_s$ and $K$ ranging over two orders of magnitude.
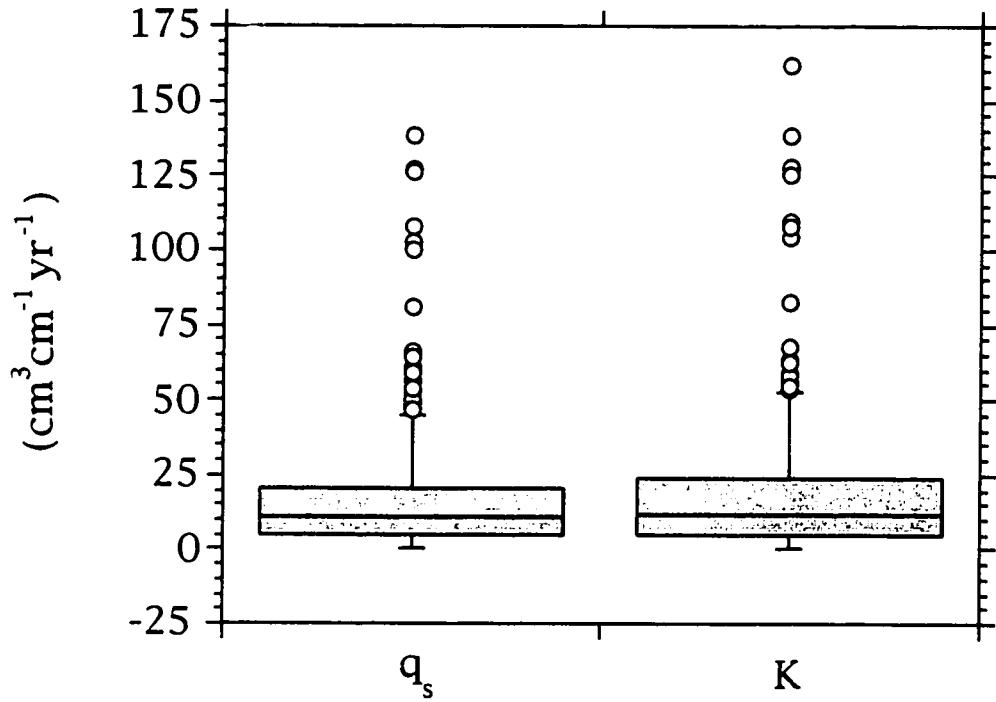
Figure 4.11    D) "Box" plot for $\tilde{q}_s$ and $K$ values where the median is displayed as horizontal line in box and the top and bottom of the box mark the limits of ± 25% of the variation. "Whiskers" mark minimum and maximum values within acceptable range. Values, exceeding 90th percentile, plotted as open circles. Variance of $\tilde{q}_s$ and $K$ are 573 and 712 $cm^6 cm^{-2} yr^{-2}$, respectively.

Semivariogram, spherical model



vector distance separating points, $\tilde{h}$ (m)
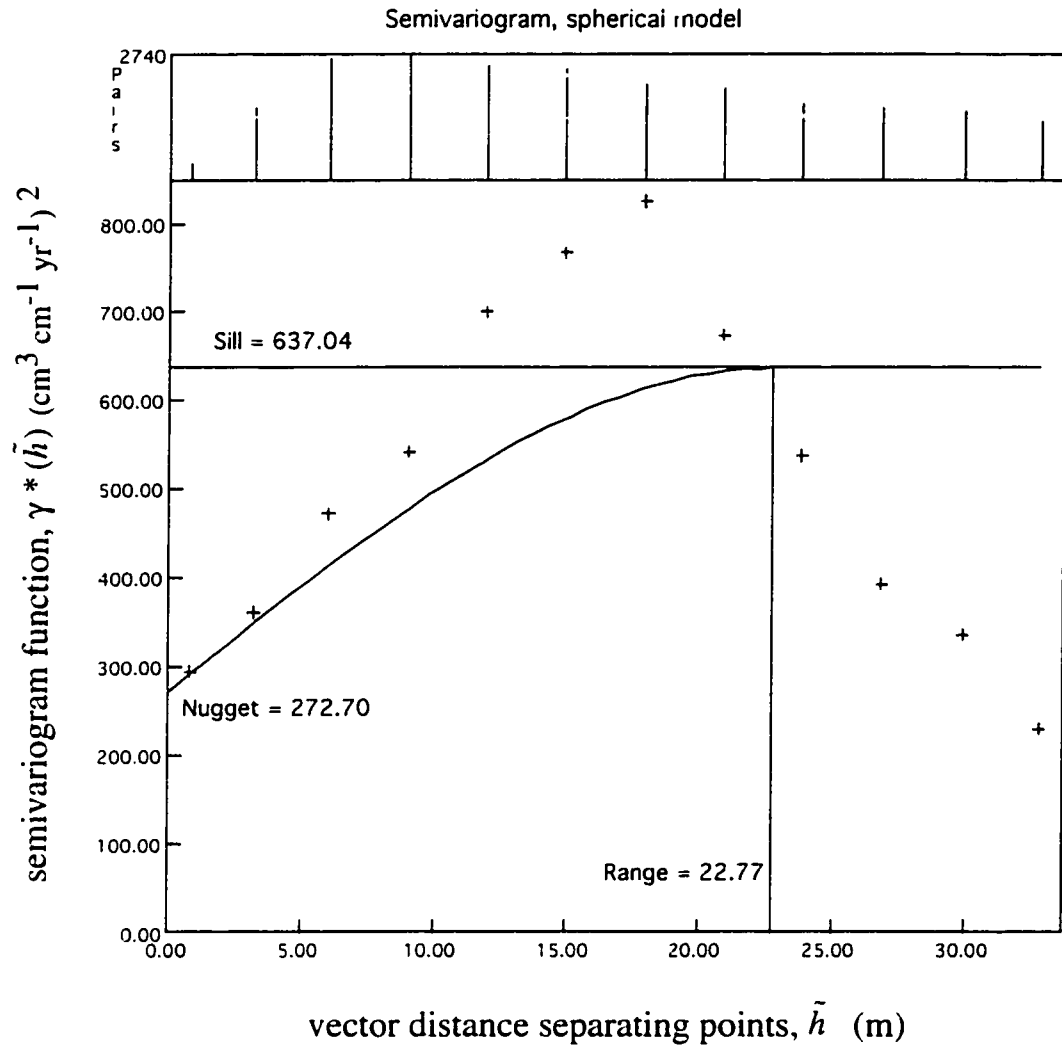
Figure 4.12     Omnidirectional semivariogram of $\tilde{q}_s$ for CB1 calculated using a lag increment of 3 m reflecting a great spatial variability in $\tilde{q}_s$ over short distances and a greater similarity of values at distances of 30 m than 15 m. The salient features are a sill = 637 ($cm^3$ $cm^{-1} yr^{-1})^2$, range = 23 m, and nugget = 273 ($cm^3 cm^{-1} yr^{-1})^2$. The relative nugget effect (ratio of nugget to sill) is 0.43.
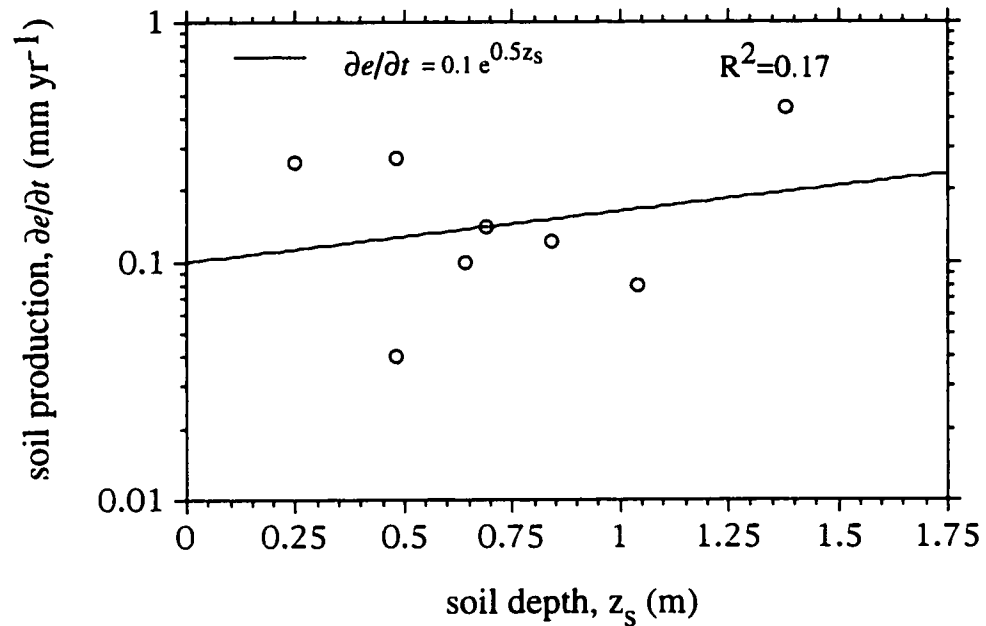
Figure 4.13    Semi-log plot of colluvium production rate ($-\partial e/\partial t$) determined from the divergence of the volumetric sediment flux ($\nabla \cdot \tilde{q}_s$) on divergent topography ($\nabla^2 z < -0.03$) revealing a weak positive relationship with the overlying colluvium depth, $z_s$. The production rate variation with depth was calculated using equation 4.11 and the following variables: $\rho_s = 1.2$ tonnes m$^{-3}$, $\rho_r = 2.2$ tonnes m$^{-3}$, and local $\tilde{q}_s$ values based on displaced piezometer standpipes is $-\partial e/\partial t = 0.1 e^{0.5 z_s}$ where $\partial e/\partial t$ is expressed in mm yr$^{-1}$ and $z_s$ is measured in meters. As the volumetric colluvium fluxes are depth integrated, values of $-\partial e/\partial t$ increase with increasing colluvium depth. Hence, the weak positive correlation between $-\partial e/\partial t$ and $z_s$ may be a spurious correlation.

Figure 4.14      Bedrock outcrop map of a portion of the Mettman Ridge headwall showing bedrock (orange) and overlying colluvium (gray). Region corresponds to 12,400 $m^2$ area represented by blue polygon in figure 3.4. The view is azimuth 155°, inclination 10°, and no vertical exaggeration. Map was generated by draping a contour map of zero soil depth ( $z_s$ = 0) on to the topography to create a perspective view looking up from the local confluence to the drainage divide. Bedrock outcrops, irregularly shaped orange polygons, occur in both convergent and divergent topography. Contour lines, shown in black, depicted at 5 m interval. As the view is a perspective, the contour spacing does not represent ground surface gradient.
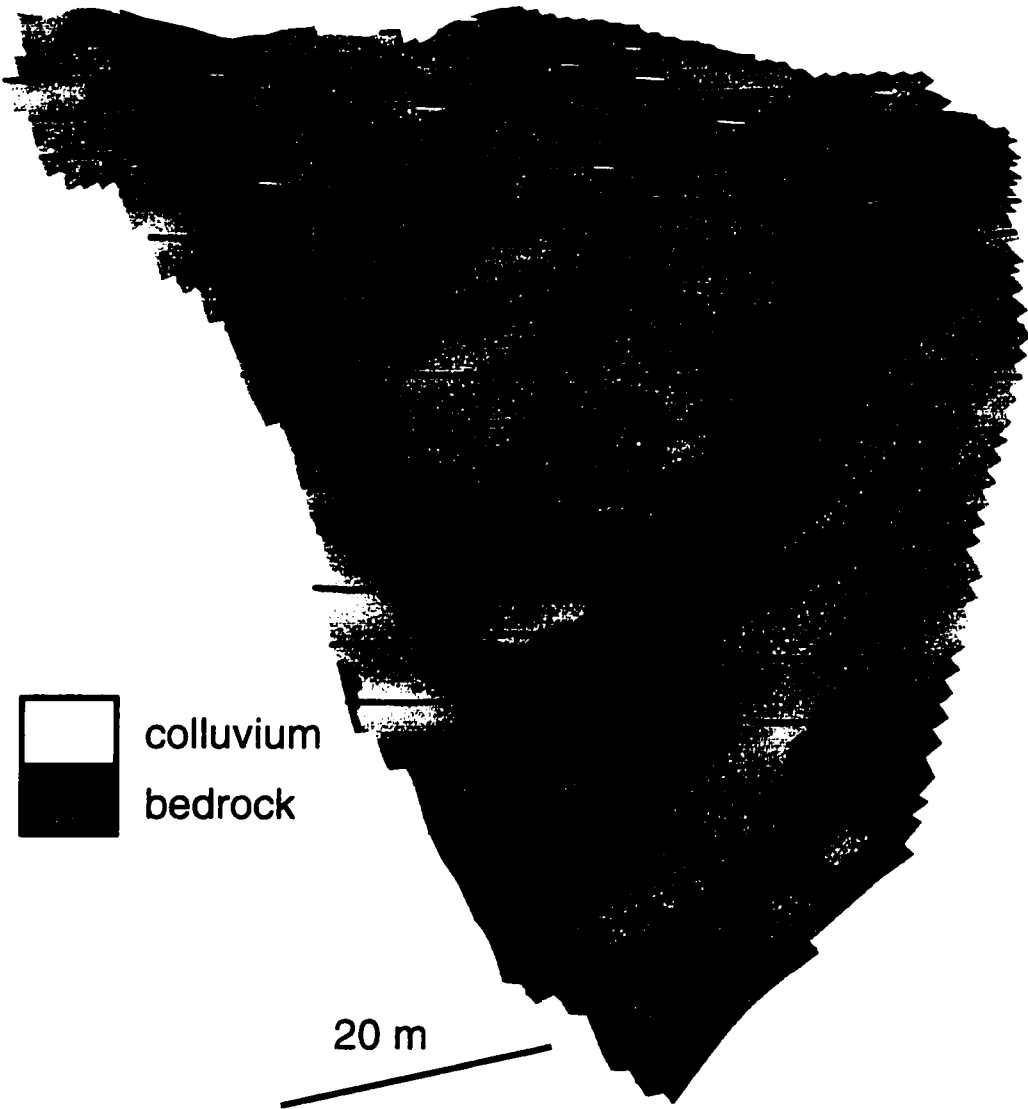
colluvium
bedrock

20 m
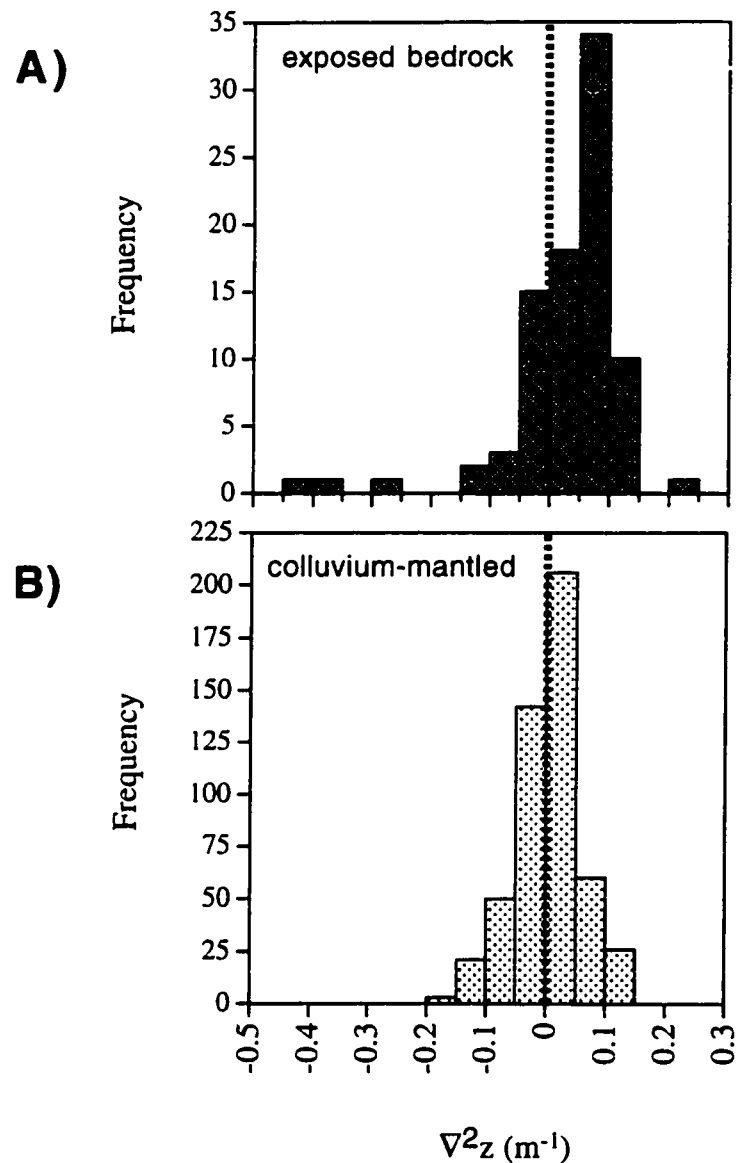
Figure 4.15    Histogram of (A) sites of bedrock outcrops ($z_s = 0$, n = 86) and (B) sites mantled by colluvium ($z_s > 0$, n = 509) with respect to topographic curvature of ground surface. Vertical, dashed line separates divergent topography ($\nabla^2 z < 0$, interfluves or topographic noses) from convergent topography ($\nabla^2 z > 0$, hollows and low-order channels). The median value in figure 4.15A is 0.05 m$^{-1}$ while the median value in 4.15B is 0.010 m$^{-1}$. The 86 bedrock outcrops in figure 4.15A are distributed such that 27% of the sites occur in divergent topography and 73% occur in convergent topography.
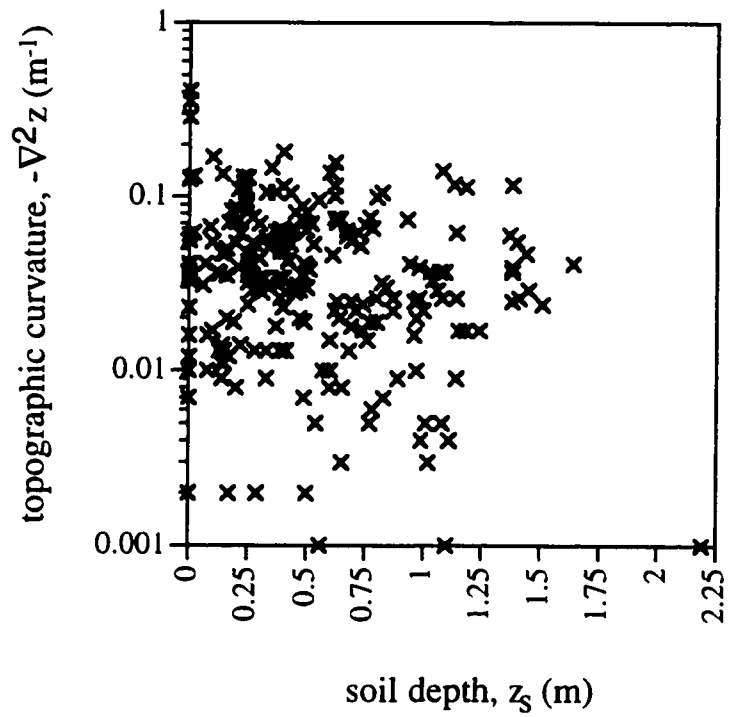
Figure 4.16    Distribution of colluvium depth relative to negative hillslope curvature ( $\nabla^2 z$ < 0) revealing no relationship (n = 235).

**A)**

soil production, $-\partial e/\partial t$ (mm yr$^{-1}$)

$\partial e/\partial t = 0.7\,e^{0.1z_s}$     $R^2=0.02$

soil depth, $z_s$ (m)

**B)**

cumulative frequency (%)

$-\partial e/\partial t$ (mm yr$^{-1}$)
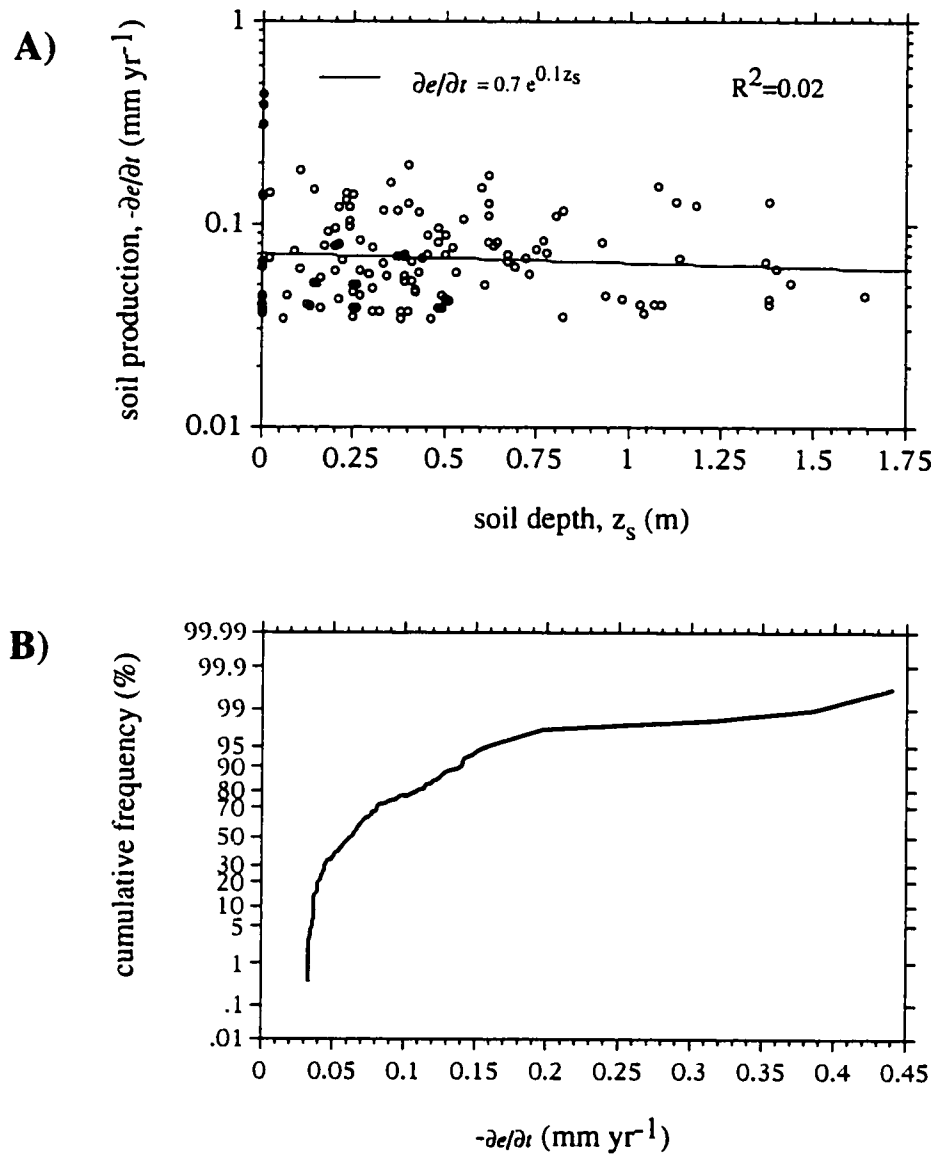
Figure 4.17    A)  Semi-log plot showing the distribution of colluvium depth ($z_s$) relative to bedrock-to-colluvium production rate ($-\partial e/\partial t$) for strongly divergent topography ($\nabla^2 z < -0.03$) revealing a weak inverse relationship (n = 134). The production rate variation with depth was calculated using equation 4.12 and the following variables: $\rho_s = 1.2$ tonnes m$^{-3}$, $\rho_r = 2.2$ tonnes m$^{-3}$, and $K = 20$ cm$^3$cm$^{-1}$yr$^{-1}$ where $\partial e/\partial t$ is expressed in mm yr$^{-1}$ and $z_s$ is measured in meters. For comparison, the colluvium production as a function of overlying colluvium depth as calculated from concentrations of cosmogenic radionuclides ([10]Be and [26]Al) is $-\partial e/\partial t = 0.28e^{-3z_s}$ (Heimsath, 1999). B) Cumulative distribution function of $-\partial e/\partial t$ for divergent topography, depicting a median value of 0.065 mm yr$^{-1}$, is neither normally or lognormally distributed.

Table 4.1   Piezometer identification, inlet depth, rotation angle, maximum soil depth, record length, and inferred annual horizontal surface velocity

| piezometer ID | inlet depth of piezometer (cm) | rotation angle of pipe (degrees) | maximum soil depth (cm) | record length (year) | annual horizontal surface velocity (cm/yr) |
|---|---|---|---|---|---|
| 0-1 | 61.4 | 6 | 70 | 7 | 0.84 |
| 0-1A | 56.9 | 14 | | 7 | 1.64 |
| 0-2 | 85.6 | -3 | 40 | 7 | -0.68 |
| 0-2A | 46 | 1 | | 7 | 0.11 |
| 0-3 | 86.4 | 9 | 40 | 7 | 1.64 |
| 0-3A | 32 | -8 | | 7 | -0.77 |
| 0-4 | 50 | -5 | 30 | 7 | -0.68 |
| 0-4A | 29 | 22 | | 7 | 1.24 |
| 0-6 | 34 | 16 | 20 | 7 | 0.99 |
| 1-0 | 59.3 | 17 | 59 | 6 | 2.33 |
| 1,1 | 57 | 21 | 57 | 7 | 2.33 |
| 1,1A | 25 | 10 | | 7 | 0.54 |
| 1,1B | 50 | 33 | | 7 | 2.94 |
| 1,2 | 50 | 19 | 50 | 7 | 1.84 |
| 1,2A | 49 | 10 | | 6 | 1.23 |
| 1,3 | 70 | 5 | 79 | 7 | 0.81 |
| 1,3A | 60 | 9 | | 6 | 1.39 |
| 1,4 | 25 | 44 | 64 | 7 | 1.84 |
| 1,5 | 74 | 19 | 70 | 7 | 2.59 |
| 1,6 | 47 | 10 | 47 | 7 | 0.99 |
| 2,1 | 66.8 | 9 | 69 | 7 | 1.33 |
| 2,1A | 25.4 | 4 | | 7 | 0.24 |
| 2,1B | 51 | 19 | | 7 | 1.94 |
| 2,2 | 48 | 36 | 51 | 7 | 3.05 |
| 2,2A | 60 | 42 | | 6 | 5.05 |
| 3,0 | 61 | 17 | | 7 | 2.05 |
| 3,0A | 70 | 17 | 73 | 6 | 2.75 |
| 3,1 | 117.5 | 9 | 149 | 6 | 2.64 |
| 3,1A | 90.4 | 10 | | 6 | 2.22 |
| 3,1B | 47.6 | 24 | | 7 | 2.03 |
| 3,1C | 71 | 5 | | 7 | 0.81 |
| 3,2 | 116.9 | 3 | 107 | 7 | 0.82 |
| 3,2A | 63.9 | 12 | | 7 | 1.55 |
| 3,2B | 35 | 8 | | 7 | 0.60 |
| 3,3 | 112 | 5 | 112 | 4 | 2.25 |
| 3,3A | 114.4 | 2 | | 4 | 0.97 |
| 3,4 | 77.7 | 4 | 81 | 7 | 0.73 |
| 3,4A | 45.5 | 6 | | 4 | 1.08 |

| piezometer ID | inlet depth of piezometer (cm) | rotation angle of pipe (degrees) | maximum soil depth (cm) | record length (year) | annual horizontal surface velocity (cm/yr) |
|---|---|---|---|---|---|
| 3,5 | 28 | -3 | 28 | 7 | -0.22 |
| 3,6 | 62.5 | 13 | 56 | 7 | 1.62 |
| 3,6A | 79.6 | 20 | | 4 | 5.07 |
| 3,7 | 54.7 | 9 | 56 | 7 | 1.06 |
| 3,7A | 82.3 | 9 | | 7 | 1.59 |
| 4,-1 | 99 | -2 | 65 | 4 | -0.89 |
| 4,-1A | 45 | 2 | | 4 | 0.38 |
| 4,0 | 105.5 | 6 | 108 | 7 | 1.44 |
| 4,0A | 51 | 0 | | 7 | 0.00 |
| 4,1 | 95 | 28 | 102 | 7 | 4.71 |
| 4,1A | 55 | 5 | | 6 | 0.74 |
| 4,2 | 71 | 9 | 78 | 7 | 1.39 |
| 4,2A | 97 | 6 | | 6 | 1.54 |
| 4,3 | 62 | 6 | 66 | 7 | 0.84 |
| 4,4 | 49 | 22 | 53 | 7 | 2.07 |
| 4,4A | 23.5 | 2 | | 7 | 0.11 |
| 4,5 | 128 | 11 | 128 | 7 | 3.00 |
| 4,5A | 89 | 6 | | 7 | 1.22 |
| 4,5B | 46 | 6 | | 7 | 0.63 |
| 5,0 | 68 | 1 | | 7 | 0.17 |
| 5,1 | 44.8 | 17 | 60 | 7 | 1.52 |
| 5,1A | 26.3 | 0 | | 7 | 0.00 |
| 5,2 | 94.5 | 5 | 95 | 4 | 1.90 |
| 5,2A | 46.1 | 1 | | 7 | 0.11 |
| 5,3 | 181 | 0 | 190 | 7 | 0.00 |
| 5,3A | 136.8 | 5 | | 7 | 1.58 |
| 5,3B | 104.7 | 7 | | 7 | 1.65 |
| 5,3C | 53.7 | 4 | | 7 | 0.50 |
| 5,4 | 91.6 | 1 | 97 | 7 | 0.22 |
| 5,4A | 49.8 | 7 | | 7 | 0.77 |
| 5,5 | 112 | 0 | 87 | 7 | 0.00 |
| 5,5A | 87 | -1 | | 7 | -0.22 |
| 5,5B | 42 | 11 | | 7 | 0.97 |
| 6,0 | 78 | 14 | 78 | 7 | 2.25 |
| 6,0A | 36 | 12 | | 7 | 0.91 |
| 6,1 | 137.8 | 10 | 138 | 4 | 5.18 |
| 6,1A | 107 | 17 | | 7 | 3.60 |
| 6,1B | 124.3 | 25 | | 4 | 9.95 |
| 6,2 | 103.3 | 6 | 104 | 7 | 1.41 |
| 6,2A | 108.9 | 12 | | 4 | 4.83 |
| 6,3 | 114.5 | 8 | 115 | 4 | 3.56 |

| piezometer ID | inlet depth of piezometer (cm) | rotation angle of pipe (degrees) | maximum soil depth (cm) | record length (year) | annual horizontal surface velocity (cm/yr) |
|---|---|---|---|---|---|
| 6,3A | 91.8 | 6 | | 4 | 2.20 |
| 6,4 | 65.6 | 1 | 65 | 7 | 0.16 |
| 6,4A | 58.5 | 6 | | 4 | 1.39 |
| 6,5 | 109 | 13 | | 4 | 5.22 |
| 6,6 | 91 | 4 | | 4 | 1.50 |
| 7,2 | 64 | 12 | 64 | 7 | 1.63 |
| 7,3 | 41.5 | 24 | 25 | 7 | 1.84 |
| 7,4 | 108.4 | 24 | 108 | 7 | 4.73 |
| 7,5 | 198 | 21 | 198 | 7 | 7.85 |
| 7,5A | 150.7 | 29 | | 7 | 7.68 |
| 7,5B | 91.1 | 32 | | 7 | 5.00 |
| 7,5C | 46.5 | 53 | | 7 | 3.79 |
| 7,6 | 139.3 | 15 | 137 | 7 | 4.30 |
| 7,6A | 90.1 | 1 | | 7 | 0.22 |
| 7,6C | 124.8 | 14 | | 6 | 4.24 |
| 7,6D | 158 | 12 | | 7 | 4.03 |
| 7,7 | 170.7 | 1 | 138 | 7 | 0.42 |
| 7,7A | 83.7 | 9 | | 4 | 2.87 |
| 7,8 | 103.9 | 5 | 104 | 7 | 1.19 |
| 7,8A | 47.3 | 34 | | 7 | 2.64 |
| 7,9 | 97 | 8 | 76 | 7 | 1.68 |
| 8,-1 | 122.6 | 18 | 138 | 9 | 3.18 |
| 8,-1A | 64.1 | 21 | | 9 | 1.87 |
| 8,-1B | 44 | 44 | | 9 | 2.18 |
| 8,0 | 86.5 | 19 | 97 | 9 | 2.49 |
| 8,0A | 93.2 | 9 | | 6 | 2.14 |
| 8,1 | 135.9 | 3 | 95 | 9 | 0.76 |
| 8,1A | 137.5 | 0 | | 6 | 0.00 |
| 8,2 | 109.9 | 3 | 110 | 9 | 0.61 |
| 8,2A | 95.3 | 4 | | 6 | 1.05 |
| 8,3 | 117.3 | 0 | 125 | 9 | 0.00 |
| 8,3A | 93 | 0 | | 9 | 0.00 |
| 8,3B | 42.6 | 7 | | 9 | 0.53 |
| 8,4 | 85.4 | 8 | 96 | 9 | 1.16 |
| 8,4A | 120.1 | 15 | | 6 | 4.16 |
| 8,5 | 139.9 | -4 | 143 | 9 | -1.14 |
| 8,5A | 112.4 | 5 | | 9 | 1.03 |
| 8,5B | 43.8 | 11 | | 9 | 0.84 |
| 9,1 | 45.3 | 11 | 48 | 9 | 0.83 |
| 9,1A | 41 | 4 | | 9 | 0.30 |
| 9,2 | 102.5 | 0 | 69 | 9 | 0.00 |

| piezometer ID | inlet depth of piezometer (cm) | rotation angle of pipe (degrees) | maximum soil depth (cm) | record length (year) | annual horizontal surface velocity (cm/yr) |
|---|---|---|---|---|---|
| 9,2A | 44.2 | 9 | | 9 | 0.67 |
| 9,3 | 179.3 | 0 | 89 | 9 | 0.00 |
| 9,3A | 107.5 | 4 | | 9 | 0.79 |
| 9,3B | 80.9 | 4 | | 6 | 0.89 |
| 9,4 | 162.1 | 9 | 184 | 9 | 2.48 |
| 9,4A | 109.9 | 11 | | 9 | 2.00 |
| 9,4B | 59 | 15 | | 9 | 1.40 |
| 9,5 | 177.3 | 2 | 135 | 9 | 0.66 |
| 9,5A | 114.5 | 19 | | 9 | 3.24 |
| 9,5B | 66.1 | 8 | | 9 | 0.90 |
| 9,5C | 73.1 | 18 | | 9 | 1.98 |
| 9,5D | 129 | 4 | | 9 | 0.94 |
| 9,6 | 188.4 | -2 | 188 | 9 | -0.75 |
| 9,6A | 81.8 | 0 | | 9 | 0.00 |
| 9,6B | 74.7 | 1 | | 6 | 0.21 |
| 9,7 | 195.8 | 10 | 196 | 9 | 3.35 |
| 9,7A | 84 | 13 | | 9 | 1.81 |
| 9,7B | 68.7 | 8 | | 9 | 0.96 |
| 9,8 | 192 | 9 | 192 | 9 | 2.96 |
| 9,8A | 105.5 | 14 | | 9 | 2.39 |
| 10,1 | 103.1 | 3 | 76 | 9 | 0.57 |
| 10,1A | 94 | 0 | | 6 | 0.00 |
| 10,2 | 145.6 | 1 | 153 | 9 | 0.28 |
| 10,2A | 96 | -1 | | 9 | -0.19 |
| 10,2B | 211.4 | 2 | | 6 | 0.87 |
| 10,3 | 76 | 4 | 78 | 9 | 0.56 |
| 10,3A | 117.7 | 1 | | 6 | 0.34 |
| 10,4 | 97.6 | 4 | 98 | 9 | 0.72 |
| 10,4A | 49.2 | 20 | | 9 | 1.55 |
| 10,6B | 166.3 | 0 | 170 | 7 | 0.00 |
| 10,7 | 80.3 | 2 | 96 | 9 | 0.30 |
| 10,7A | 105 | 1 | | 9 | 0.20 |
| 10,8 | 71.6 | 9 | 73 | 9 | 1.12 |
| 10,8A | 91.8 | 5 | | 6 | 1.25 |
| 11,2 | 119.5 | 6 | 124 | 9 | 1.29 |
| 11,2A | 99.1 | 1 | | 9 | 0.19 |
| 11,2B | 168.6 | 1 | | 6 | 0.48 |
| 11,3 | 155.9 | 1 | 105 | 9 | 0.30 |
| 11,3A | 129.5 | 7 | | 9 | 1.61 |
| 11,3B | 101.2 | 3 | | 9 | 0.57 |
| 11,3C | 175.9 | 26 | | 6 | 10.39 |

| piezometer ID | inlet depth of piezometer (cm) | rotation angle of pipe (degrees) | maximum soil depth (cm) | record length (year) | annual horizontal surface velocity (cm/yr) |
|---|---|---|---|---|---|
| 11,4 | 158.4 | 6 | 110 | 6 | 2.51 |
| 11,4A | 88.5 | 8 | | 6 | 1.82 |
| 11,5 | 162.4 | 1 | 48 | 9 | 0.31 |
| 11,5A | 126.4 | 1 | | 9 | 0.24 |
| 11,5B | 169 | 1 | | 6 | 0.49 |
| 11,5C | 116.2 | 5 | | 6 | 1.60 |
| 12,1 | 90.8 | 46 | 86 | 9 | 5.06 |
| 12,1A | 55 | 21 | | 9 | 1.68 |
| 12,2 | 115.5 | 12 | 120 | 9 | 2.29 |
| 12,2A | 100.9 | 11 | | 9 | 1.86 |
| 12,2B | 128.7 | 10 | | 6 | 3.27 |
| 12,3 | 131.1 | 3 | 145 | 9 | 0.73 |
| 12,3A | 94.6 | 8 | | 9 | 1.33 |
| 12,3B | 113.1 | 9 | | 6 | 2.65 |
| 12,4 | 146.1 | 2 | 84 | 9 | 0.55 |
| 12,4A | 96.8 | 4 | | 9 | 0.71 |
| 12,4B | 86.8 | 4 | | 9 | 0.64 |
| B-3 | 287 | 4 | 60 | 4 | 4.72 |
| B-3A | 123 | 2 | 60 | 4 | 1.04 |
| B-4 | 269 | 1 | 69 | 4 | 1.15 |
| B-4A | 105 | 2 | 60 | 4 | 0.88 |
| B-5 | 335 | 7 | 18 | 4 | 9.29 |
| B-5A | 55 | 5 | 14 | 4 | 1.12 |
| B-6 | 203 | 0 | 40 | 4 | 0.00 |
| B-7 | 239 | 0 | 10 | 4 | 0.00 |
| B-8 | 285 | 7 | 85 | 4 | 7.84 |
| B-8A | 164 | 2 | 76 | 4 | 1.39 |
| B-9 | 308 | 8 | 53 | 4 | 9.55 |
| B-9A | 113 | 5 | 88 | 4 | 2.28 |
| B-10 | 239 | 0 | 61 | 4 | 0.00 |
| B-10A | 91 | 2 | 42 | 4 | 0.77 |
| B-11 | 66 | 2 | 170 | 6 | 0.37 |
| B-12 | 253 | 8 | 147 | 4 | 7.84 |
| B-13 | 505 | 0 | 148 | 4 | 0.00 |
| B-13A | 218 | 1 | 133 | 4 | 0.94 |
| B-13B | 166 | 5 | | 4 | 3.34 |
| B-14 | 183 | 0 | 120 | 4 | 0.00 |
| B-15 | 292 | 12 | 57 | 4 | 13.31 |
| B-15A | 166 | 14 | 110 | 4 | 8.66 |
| B-16 | 197 | 8 | 118 | 6 | 4.16 |
| B-16A | 130 | -2 | 120 | 6 | -0.78 |

| piezometer ID | inlet depth of piezometer (cm) | rotation angle of pipe (degrees) | maximum soil depth (cm) | record length (year) | annual horizontal surface velocity (cm/yr) |
|---|---|---|---|---|---|
| B-17 | 165 | -3 | 65 | 4 | -2.25 |
| 9,9 | 92 | 7 | | 7 | 1.46 |
| 13,1 | 105 | 42 | | 7 | 7.59 |
| 9,10 | 81 | 4 | | 7 | 0.76 |
| B-1 | 98 | 5 | | 4 | 1.98 |
| B-1A | 106 | 5 | | 4 | 2.14 |
| B-1B | 66 | 3 | | 4 | 0.82 |
| | 69 | 8 | | 7 | 1.23 |
| | 77 | 0 | | 4 | 0.00 |

# List of References

Abe, K., and Iwamoto, M., 1986, An evaluation of tree-root effect on slope stability by tree-root strength: Journal of Japanese Forestry Science, v. 69, p. 505-510.

Abrahams, A.D., Cook, R.U., and Reeves, R.W., 1984, Stone movement on hillslopes in the Mojave Desert, California: A 16 year record: Earth Surface Processes and Landforms, v. 9, p. 365-370.

Ahnert, F., 1967, The role of the equilibrium concept in the interpretation of landforms of fluvial erosion and deposition, Symposium International de Géomorphologie, Volume 40: Congrés et Colloques de l'Université de Liége, p. 22-41.

Ahnert, F., 1970, A comparison of theoretical slope models with slopes in the field: Zeitschrift für Geomorphologie Supplempentband, v. 9, p. 88-101.

Ahnert, F., 1977, Some comments on the quantitative formulation of geomorphological processes in a theoretical model: Earth Surface Processes and Landforms, v. 2, p. 191-201.

Ahnert, F., 1987, Approaches to dynamic equilibrium in theoretical simulations of slope development: Earth Surface Processes and Landforms, v. 12, p. 3-15.

Amaranthus, M.P., Rice, R.M., Barr, N.R., and Ziemer, R.R., 1985, Logging and forest roads related to increased debris flows in southwestern Oregon: Journal of Forestry, v. 83, p. 229-233.

Anderson, C.J., Coutts, M.P., Ritchie, R.M., and Campbell, D.J., 1989, Root extraction force measurements for Sitka Spruce: Forestry, v. 62, p. 127-137.

Anderson, S.P., Dietrich, W.E., Torres, R., Montgomery, D.R., and Loague, K., 1997, Concentration-discharge relationships in runoff from a steep, unchanneled catchment: Water Resources Research, v. 33, p. 211-225.

Armstrong, A.C., 1976, A three dimensional simulation of slope forms: Zeitschrift für Geomorphologie Supplementband, v. 25, p. 20-28.

Bannan, M.W., 1940, The root systems of northern Ontario conifers growing in sand: American Journal of Botany, v. 27, p. 108-114.

Beke, G.J., and McKeague, J.A., 1984, Influence of tree windthrow on the properties and classification of selected forested soils from Nova Scotia: Canadian Journal of Soil Science, v. 64, p. 195-207.

Benda, L., 1987, Debris flows in the Oregon Coast Range [Unpublished M.S. thesis], University of Washington, 135 p.

Benda, L., and Dunne, T., 1987, Sediment routing by debris flow, in Beschta, R.L., Blinn, T., Grant, G.E., Ice, G.G., and Swanson, F.J., eds., Erosion and Sedimentation in the Pacific Rim, International Association of Hydrological Sciences Publication 165, p. 213-223.

Beschta, R.L., 1978, Long-term patterns of sediment production following road construction and logging in the Oregon Coast Range: Water Resources Research, v. 14, p. 1011-1016.

Beschta, R.L., 1984, River channel reponses to accelerated mass soil erosion, in O'Loughlin, C.L., and Pearce, A.J., eds., Effects of Forest Land Use on Erosion and Slope Stability: Honolulu, HI, East-West Environmental Policy Institute, p. 155-163.

Beven, K.J., and Kirkby, M.J., 1979, A physically based, variable contributing area model of basin hydrology: Hydrological Sciences Bulletin, v. 24, p. 43-69.

Bishop, D.M., and Stevens, M.E., 1964, Landslides on logged areas in southeast Alaska: Northern Forest Experiment Station, U. S. Forest Service, Research Paper NOR-1, 18 p.

Black, T.A., and Montgomery, D.R., 1991, Sediment transport by burrowing mammals, Marin County, California: Earth Surface Processes and Landforms, v. 16, p. 163-172.

Bogucki, D.J., 1976, Debris slides in the Mt. LeConte area, Great Smoky Mountains National Park, U.S.A.: Geografiska Annaler, v. 58A, p. 179-191.

Böhm, W., 1979, Methods of studying root systems: Berlin, West Germany, Springer-Verlag, 270 p.

Brabb, E.E., Pampeyan, E.H., and Bonilla, M.G., 1972, Landslide susceptibility in San Mateo County, California, U. S. Geological Survey, Miscellaneous Field Studies Map, MF-360, scale 1:62,500.

Briggs, I.C., 1974, Machine contouring using minimum curvature: Geophysics, v. 39, p. 39-48.

Brown, G.W., and Krygier, J.T., 1971, Clear-cut logging and sediment production in the Oregon Coast Range: Water Resources Research, v. 7, p. 1189-1199.

Brown, L.R., and Wolf, E.C., 1984, Soil erosion: Quiet crisis in the world economy: Worldwatch Institute, Washington, D. C., Paper No. 60, 50 p.

Buchanon, P., and Savigny, K.W., 1990, Factors controlling debris avalanche initiation: Canadian Geotechnical Journal, v. 27, p. 659-675.

Burroughs, E.R.J., 1985, Landslide hazard rating for the Oregon Coast Range, in Jones, E.B., and Ward, T.J., eds., Watershed Management in the Eighties, American Society of Civil Engineers, p. 132-139.

Burroughs, E.R.J., and Thomas, B.R., 1977, Declining root strength in Douglas-fir after felling as a factor in slope stability: Forest Service, U.S. Department of Agriculture, Research Paper INT-190, 27 p.

Caine, N., 1980, The rainfall intensity-duration control on shallow landslides and debris flows: Geografiska Annaler, v. 62A, p. 23-27.

Campbell, R.H., 1975, Soil slips, debris flows and rainstorms in the Santa Monica Mountains and vicinity, southern California, U.S. Geological Survey Professional Paper 851, 51 p.

Cannon, S.H., 1988, Regional rainfall-threshold conditions for abundant debris-flow activity, in Ellen, S.D., and Wieczorek, G.F., eds., Landslides, Floods, and Marine Effects of the Storm of January 3-5, 1982, in the San Francisco Bay Region, California, U.S. Geological Survey Professional Paper 1434, p. 35-42.

Cardone, A.J., and Kelley, D.E., 1961, The influence of inorganic sediment on the aquatic life of streams: California Fish and Game, v. 47, p. 189-228.

Carrara, A., 1983, Multivariate models for landslide hazard evaluation: Mathematical Geology, v. 15, p. 403-426.

Carrara, A., Cardinali, M., Detti, R., Guzzetti, F., Pasqui, V., and Reichenback, P., 1991, GIS techniques and statistical models in evaluating landslide hazard: Earth Surface Processes and Landforms, v. 16, p. 427-445.

Carrara, A., Pugliese Carratelli, E., and Merenda, L., 1977, Computer-based bank and statistical analysis of slope instability phenomena: Zeitschrift für Geomorphologie, v. 21, p. 187-222.

Carrara, A., Sorriso-Valvo, M., and Reali, C., 1982, Analysis of landslide form and incidence by statistical techniques, southern Italy: Catena, v. 9, p. 35-62.

Carson, M.A., and Kirkby, M.J., 1972, Hillslope Form and Process: London, Cambridge University Press, 475 p.

Clarke, M.F., Williams, M.A.J., and Stokes, T., 1999, Soil creep: problems raised by a 23 year study in Australia: Earth Surface Processes and Landforms, v. 24, p. 151-175.

Commandeur, P.R., and Pyles, M.R., 1991, Modulus of elasticity and tensile strength of Douglas-fir roots: Canadian Journal of Forestry Research, v. 21, p. 48-52.

Coppin, N.J., and Richards, I.G., 1990, Use of vegetation in civil engineering: London, Construction Industry Research and Information Association, Butterworths, 292 p.

Corliss, J.F., 1973, Soils survey of Alsea area, Oregon: U. S. Department of Agriculture, Soil Conservation Service, U. S. Forest Service Survey, 82 p.

Coutts, M.P., 1983, Root architecture and tree stability: Plant and Soil, v. 71, p. 171-188.

Cox, N.J., 1980, On the relationship between bedrock lowering and regolith thickness: Earth Surface Processes, v. 5, p. 271-274.

Cremans, D.W., and Kalisz, P.J., 1988, Distribution and characteristics of windthrow microtopography on the Cumberland Plateau of Kentucky: Soil Science Society of America, v. 52, p. 816-821.

Cressie, N.A.C., 1991, Statistics for Spatial Data: New York, John Wiley & Sons, Inc., 900 p.

Croft, A.R., and Adams, J.A., 1950, Landslides and sedimentation in the North Fork of Ogden River, May 1949: U. S. Forest Service, Intermountain Forest and Range Experiment Station, Research Paper INT-21, 4 p.

Culling, W.E.H., 1960, Analytical theory of erosion: Journal of Geology, v. 68, p. 336-344.

Culling, W.E.H., 1963, Soil creep and the development of hillside slopes: The Journal of Geology, v. 71, p. 127-161.

Cumberland, K.B., 1947, Soil Erosion in New Zealand: A Geographic Reconnaissance: Christchurch, Whitcombe & Tombs Limited, 228 p.

Darwin, C., 1882, The formation of vegetable mould through the action of worms, with observations on their habits: Edinburgh, John Murray, 298 p.

Davis, J.C., 1986, Statistics and data analysis in geology: New York, John Wiley & Sons, Inc., 646 p.

Davis, W.M., 1892, The convex profile of bad-land divides: Science, v. 20, p. 245.

Davison, C., 1889, On the creeping of the soil-cap through the action of frost: Geological Magazine, v. 6, p. 255-261.

De Rose, R.C., 1996, Relationships between slope morphology, regolith depth, and the incidence of shallow landslides in eastern Taranaki hill country: Zeitschrift für Geomorphologie, v. 105, p. 49-60.

De Rose, R.C., Trustrum, N.A., and Blaschke, P.M., 1991, Geomorphic change implied by regolith-slope relationships on steepland hillslopes, Taranaki, New Zealand: Catena, v. 18, p. 489-514.

De Rose, R.C., Trustrum, N.A., and Blaschke, P.M., 1993, Post-deforestation soil loss from steepland hillslopes in Taranaki, New Zealand: Earth Surface Processes and Landforms, v. 18, p. 131-144.

Deans, J.D., and Ford, E.D., 1983, Modelling root structure and stability: Plant and Soil, v. 71, p. 189-195.

Dengler, L., and Montgomery, D.R., 1989, Estimating the thickness of colluvial fill in unchanneled valleys from surface topography: Bulletin of the Association of Engineering Geologists, v. 26, p. 333-342.

Denny, C.S., and Goodlet, J.C., 1956, Microrelief resulting from fallen trees: U. S. Geological Survey, Professional Paper 288, p. 59-65.

Denny, C.S., and Goodlett, J.C., 1968, Tree-throw origin of patterned ground on beaches of the ancient Champlain Sea nea Plattsburgh, New York: U. S. Geological Survey Professional Paper 600B, p. B157-164.

Derbyshire, E., van Asch, T., Billard, A., and Meng, X., 1995, Modelling the erosional susceptibility of landslide catchments in thick loess: Chinese variations on a them by Jan de Ploey: Catena, v. 25, p. 315-331.

Dethier, D.P., 1986, Weathering rates and the chemical flux from catchments in the Pacific Northwest, U.S.A., in Colman, S.M., and Dethier, D.P., eds., Rates of Chemical Weathering of Rocks and Minerals: Orlando, Academic Press, p. 503-530.

Dietrich, W.E., and Dunne, T., 1978, Sediment budget for a small catchment in mountainous terrain: Zeitschrift für Geomorphologie Suppl., v. 29, p. 191-206.

Dietrich, W.E., Reiss, R., Hsu, M.-L., and Montgomery, D.R., 1995, A process-based model for colluvial soil depth and shallow landsliding using digital elevation data: Hydrological Processes, v. 9, p. 383-400.

Dietrich, W.E., Wilson, C.J., Montgomery, D.R., and McKean, J., 1993, Analysis of erosion thresholds, channel networks, and landscape morphology using a digital terrain model: Journal of Geology, v. 101, p. 259-278.

Dudal, R., 1981, An evaluation of conservation needs, in Morgan, R.P.C., ed., Soil Conservation, Problems and Prospects: Chichester, England, John Wiley & Sons, p. 3-12.

Dunne, T., 1978, Field studies of hillslope flow processes, in Kirkby, M.J., ed., Hillslope Hydrology: Chichester, John Wiley & Sons, p. 227-293.

Dunne, T., 1991, Stochastic aspects of the relationships between climate, hydrology and landform evolution: Transactions of the Japanese Geomorphological Union, v. 12, p. 1-24.

Dunne, T., and Black, R.G., 1970, An experimental investigation of runoff production in permeable soils: Water Resources Research, v. 6, p. 478-490.

Dunne, T., Dietrich, W.E., and Brunengo, M.J., 1978, Recent and past erosion rates in semi-arid Kenya: Zeitschrift für Geomorphologie Supplementband, v. 29, p. 130-140.

Dunne, T., Moore, T.R., and Taylor, C.H., 1975, Recognition and prediction of runoff-producing zones in humid regions: Hydrological Sciences Bulletin, v. 20, p. 305-327.

Dyrness, C.T., 1967, Mass soil movements in the H. J. Andrews Experimental Forest: U. S. Department of Agriculture, Forest Service Research Paper PNW-42, 12 p.

Eis, S., 1974, Root system morphology of Western Hemlock, Western Red Cedar, and Douglas-fir: Canadian Journal of Forestry Research, v. 4, p. 28-38.

Eis, S., 1987, Root systems of older immature hemlock, cedar, and Douglas-fir: Canadian Journal of Forestry, v. 17, p. 1348-1354.

Ellen, S.D., Mark, R.K., Cannon, S.H., and Knifong, D.L., 1993, Map of debris-flow hazard in the Honolulu District of Oahu, Hawaii: U. S. Geological Survey Open-File Report 93-213, 25 p.

Ellen, S.D., Wieczorek, G.F., Brown, W.M., and Herd, D.G., 1988, Landslides, floods, and marine effects of the storm of January 3-5, 1982, in the San Francisco Bay region, California, in Ellen, S.D., and Wieczorek, G.F., eds., Landslides, Floods, and Marine Effects of the Storm of January 3-5, 1982, in the San Francisco Bay Region, California, U.S. Geological Survey Professional Paper 1434, p. 1-5.

Endo, T., and Tsuruta, T., 1969, Effects of trees' roots upon the shearing strengths of soils: Annual Report of the Hokkaido Branch Government Forest Experimental Station Tokyo, 1968, v. 18, p. 167-179.

Ennos, A.R., 1990, The anchorage of leek seedlings: the effect of root length and soil strength: Annals of Botany, v. 65, p. 409-416.

Everest, F.H., and Meehan, W.R., 1981, Forest management and anadromous fish habitat productivity, *in* Sabol, K., ed., Transactions of the Fourty-sixth North American Wildlife and Natural Resources Conference: Washington, DC, Wildlife Management Institute, p. 521-530.

Fahey, T.J., and Arthur, M.A., 1994, Further studies of root decomposition following harvest of a northern hardwoods forest: Forest Science, v. 40, p. 618-629.

Fahey, T.J., Hughes, J.W., Pu, M., and Arthur, M.A., 1988, Root decomposition and nutrient flux following whole-tree harvest of northern hardwood forest: Forest Science, v. 34, p. 744-768.

Feldhamer, G.A., and Rochelle, J.A., 1982, Mountain Beaver, *in* Chapman, J.A., and Feldhamer, G.A., eds., Wild Mammals in North America: Baltimore, MD, Johns Hopkins University Press, p. 167-176.

Fernandes, N.F., and Dietrich, W.E., 1997, Hillslope evolution by diffusive processes: The timescale for equilibrium adjustments: Water Resources Research, v. 33, p. 1307-1318.

Fleming, R.W., and Johnson, A.M., 1975, Rates of seasonal creep of silty clay soil: Quarterly Journal of Engineering Geology, v. 8, p. 1-29.

Fleming, R.W., and Taylor, F.A., 1980, Estimating the cost of landslide damage in the United States: U. S. Geological Survey Circular 832, 21 p.

Franklin, J.F., and Dyrness, C.T., 1969, Vegetation of Oregon and Washington: U. S. Department of Agriculture, Forest Service Research Paper PNW-80, 216 p.

Freeze, R.A., and Cherry, J.A., 1979, Groundwater: New Jersey, Prentice-Hall, Inc., 604 p.

Gilbert, G.K., 1877, Report on the geology of the Henry Mountains: Washington, D.C., U.S. Geographical and Geological Survey of the Rocky Mtn Region, 229 p.

Gilbert, G.K., 1909, The convexity of hilltops: The Journal of Geology, v. 17, p. 344-350.

Granger, D.E., Kirchner, J.W., and Finkel, R., 1996, Spatially averaged long-term erosion rates measured from *in situ*-produced cosmogenic nuclides in alluvial sediment: Journal of Geology, v. 104, p. 249-257.

Grant, P.J., 1963, Forests and recent climatic history of the Huiarau Range, Urewera region, North Island: Transactions, Royal Society of New Zealand, Botany, v. 2, p. 144-172.

Gray, D.H., 1970, Effects of forest clear-cutting on the stability of natural slopes: Bulletin of the Association of Engineering Geologists, v. 7, p. 45-66.

Gray, D.H., 1973, Effects of forest clear-cutting on the stability of natural slopes: results of field studies: University of Michigan, Dept. of Civil Engineering Report, 119 p.

Gray, D.H., and Leiser, A.T., 1982, Biotechnical Slope Protection and Erosion Control: New York, Van Nostrand Reinhold Co., 271 p.

Gray, D.H., and Megahan, W.F., 1981, Forest vegetation removal and slope stability in the Idaho Batholith: Forest Service, U. S. Dept. of Agriculture, Research Paper INT-271, 23 p.

Gray, D.H., and Ohashi, H., 1983, Mechanics of fiber reinforcement in sand: Journal of Geotechnical Engineering, v. 109, p. 335-53.

Gresswell, S., Heller, D., and Swanston, D.N., 1979, Mass movement response to forest management in the central Oregon Coast Ranges: U. S. Department of Agriculture, Forest Service Resources Bulletin PNW-84, 26 p.

Hack, J.T., 1965, Geomorphology of the Shenandoah Valley, Virginia and West Virginia, and origin of the residual ore deposits: U. S. Geological Survey Professional Paper 484, 84 p.

Hack, J.T., and Goodlett, J.C., 1960, Geomorphology of forest ecology of a mountain region in the central Appalachians: U. S. Geological Survey Professional Paper 347, 66 p.

Hathaway, R.L., and Penny, D., 1975, Root strength in some Populus and Salix clones: New Zealand Journal of Botany, v. 13, p. 333-344.

Heimsath, A.M., 1999, The soil production function [Ph.D. thesis]: Berkeley, CA, University of California, 324 p.

Heimsath, A.M., Dietrich, W.E., Nishiizumi, K., and Finkel, R.C., 1996, Soil production and landscape equilibrium: hillslope analysis using cosmogenic nuclides in northern California and coastal Oregon: EOS, Transactions, American Geophysical Union, v. 77, p. 245-246.

Heimsath, A.M., Dietrich, W.E., Nishiizumi, K., and Finkel, R.C., 1997, The soil production function and landscape equilibrium: Nature, v. 388, p. 358-361.

Hendrick, R.L., and Pregitzer, K.S., 1993, Patterns of fine root mortality in two sugar maple forests: Nature, v. 361, p. 59-61.

Herbert, D.W.M., and Merkens, J.C., 1961, The effect of suspended mineral solids on the survival of trout: International Journal of Air and Water Pollution, v. 5, p. 46-55.

Hohn, M.E., 1988, Geostatistics and petroleum geology: New York, Van Nostrand Reinhold, 264 p.

Hole, F.D., 1961, A classification of pedoturbations and some other processes and factors of soil formation in relation to isotropism and anisotropism: Soil Science, v. 91, p. 375-377.

Hollingsworth, R., and Kovacs, G.S., 1981, Soil slumps and debris flows: prediction and protection: Bulletin of the Association of Engineering Geologists, v. 18, p 17-28.

Howard, A.D., 1994, A detachment-limited model of drainage basin evolution: Water Resources Research, v. 30, p. 2261-2285.

Howard, A.D., and Kerby, G., 1983, Channel changes in badlands: Geological Society of America Bulletin, v. 94, p. 739-752.

Hsi, G., and Nath, J.H., 1970, Wind drag within a simulated forest: Journal of Applied Meteorology, v. 9, p. 592-602.

Ifju, G., and Kennedy, R.W., 1962, Some variables affecting microtensile strength of Douglas-fir: Forest Products Journal, v. 12, p. 213-217.

Iida, T., and Okunishi, K., 1983, Development of hillslopes due to landslides: Zeitschrift für Geomorphologie, v. 46, p. 67-77.

Iida, T., and Tanaka, K., 1997, The relationship between topography and soil depth measured with the portable penetration test apparatus: Transactions, Japanese Geomorphological Union, v. 18, p. 61-78.

Imeson, A.C., 1976, Some effects of burrowing animals on slope processes in the Luxemburg Ardennes: Geografiska Annaler, v. 58A, p. 115-125.

Ingles, L.G., 1965, Mammals of the Pacific States: California, Oregon, and Washington: Stanford, CA, Stanford University Press, 506 p.

Isaaks, E.H., and Srivastava, R.M., 1989, Applied Geostatistics: New York, Oxford University Press, 561 p.

Iverson, R.M., and Major, J.J., 1986, Groundwater seepage vectors and the potential for hillslope failure and debris flow mobilization: Water Resources Research, v. 22, p. 1543-1548.

Iverson, R.M., Reid, M.E., and LaHusen, R.G., 1997, Debris-flow mobilization from landslides: Annual Review of Earth and Planetary Science, v. 25, p. 85-138.

Jahn, A., 1981, Some regularities of soil movement on the slope as exemplified by the observations in Sudety Mts.: Transactions, Japanese Geomorphological Union, v. 2, p. 321-328.

Jahn, A., 1989, The soil creep on slopes in different altitiudinal and ecological zones of the Sudetes Mountains: Geografiska Annaler, v. 71A, p. 161-170.

Jewell, R.A., and Wroth, C.P., 1987, Direct shear tests on reinforced sand: Geotechnique, v. 37, p. 53-68.

Johnson, A.M., and Rahn, P.H., 1970, Mobilization of debris flows: Zeitschrift für Geomorphologie Suppl., v. 9, p. 168-186.

Judson, S., 1981, What's happening to our continents, in Skinner, B.J., ed., Use and Misuse of Earth's Surface: Los Altos, California, William Kaufman, Inc., p. 12-139.

Kabrick, J.M., Clayton, M.K., McBratney, A.B., and McSweeney, K., 1997, Cradle-knoll patterns and characteristics on drumlins in northeastern Wisconsin: Soil Science Society of America Journal, v. 61, p. 595-603.

Kassiff, G., and Kopelovitz, A., 1968, Strength properties of soil-root systems: Israel Institute of Technology, CV-256, 44 p.

Keefer, D.K., Wilson, R.C., Mark, R.K., Brabb, E.E., Brown, W.M., Ellen, S.D., Harp, E.L., Wieczorek, G.F., Alger, C.S., and Zatkin, R.S., 1987, Real-time landslide warning during heavy rainfall: Science, v. 238, p. 921-925.

Keller, E.A., and Swanson, F.J., 1979, Effects of large organic material on channel form and fluvial processes. Earth Surface Processes, v. 4, p. 361-380.

Kelsey, H.M., and Bockheim, J.G., 1994, Coastal landscape evolution as a function of eustasy and surface uplift rate, Cascadia margin, southern Oregon: Geological Society of America Bulletin, v. 106, p. 840-854.

Kelsey, H.M., Engebretson, D.C., Mitchell, C.E., and Ticknor, R.L., 1994, Topographic form of the Coast Ranges of the Cascadia Margin in relation to coastal uplift rates and plate subduction: Journal of Geophysical Research, v. 99, p. 12,245-12,255.

Ketcheson, G.L., and Froehlich, H.A., 1978, Hydrology factors and environmental impacts of mass soil movements in the Oregon Coast Range: Water Resources Research Institute, Oregon State University, Corvallis, 94 p.

Kirkby, M.J., 1967, Measurement and theory of soil creep: The Journal of Geology, v. 75, p. 359-378.

Kirkby, M.J., 1971, Hillslope process-response models based on the continuity equation, *in* Brunsden, D., ed., Slope form and process, Volume Special Publication #3, Institute of British Geographers, p. 15-30.

Kirkby, M.J., 1980, The Problem, *in* Kirkby, M.J., and Morgan, R.P.C., eds., Soil erosion: Chichester, John Wiley & Sons, p. 1-16.

Kirkby, M.J., 1987, Modelling some influences of soil erosion, landslides and valley gradient on drainage density and hollow development: Catena Supplement, v. 10, p. 1-14.

Koons, P.O., 1989, The topographic evolution of collisional mountain belts: A numerical look at the Southern Alps, New Zealand: American Journal of Science, v. 289, p. 1041-1069.

Krogstad, F., 1995, A physiology and ecology based model of lateral root reinforcement of unstable hillslopes [Master of Science thesis]: Seattle, Washington, University of Washington, 44 p.

Lal, R., 1982, Effective conservation farming systems for the humid tropics, *in* Kussow, W., ed., Soil Erosion and Conservation in the Tropics: Fort Collins, Colorado, American Society of Agronomy Soil Science Society of America, p. 57-76.

Lee, I.W.Y., 1985, A review of vegetative slope stabilization: Hong Kong Engineer, v. 13, p. 9-21.

Lehre, A.K., 1981, Sediment budget of a small California Coast Range drainage basin near San Francisco, *in* Davies, T.R.H., and Pearce, A.J., eds., Erosion and sediment transport in Pacific Rim steeplands, International Association of Hydrological Sciences Publication 132, p. 123-139.

Lehre, A.K., 1982, Sediment mobilization and production from a small mountain catchment: Lone Tree Creek, Marin County, California [Ph.D. thesis]: Berkeley, University of California, Berkeley, 187 p.

Leopold, L.B., Emmett, W.W., and Myrick, R.M., 1966, Channel and hillslope processes in a semiarid area, New Mexico: U. S. Geological Survey, Professional Paper 352-G, p. 193-252.

Lewis, L.A., 1976, Soil movement in the tropics- a general model: Zeitschrift für Geomorphologie, Suppl., v. 25, p. 132-144.

Loudermilk, W.C., 1950, Conquest of the land through seven thousand years: U. S. Department of Agriculture Soil Conservation Service, MP-32.

Lovell, J.P.B., 1969, Tyee formation: undeformed turbidites and their lateral equivalents: mineralogy and paleogeology: Geological Society of America Bulletin, v. 80, p. 9-22.

Lutz, H.J., 1960, Movement of rocks by uprooting of forest trees: American Journal of Science, v. 258, p. 752-756.

Lutz, H.J., and Griswold, F.S., 1939, The influence of tree roots on soil morphology: American Journal of Science, v. 237, p. 389-400.

Lyford, W.H., and MacLean, D.W., 1966, Mound and pit microrelief in relation to soil disturbance and tree distribution in New Brunswick, Canada: Harvard University, Harvard Forest Paper No. 15, 18 p.

Manbeian, T., 1973, The influence of soil moisture suction, cyclic wetting and drying, and plant roots on the shear strength of cohesive soil [Ph.D. thesis]: Berkeley, CA, University of California, Department of Soil Science.

Mark, R.K., 1992, Map of debris-flow probability, San Mateo County, California, U. S. Geological Survey, Miscellaneous Investigations Map I-1267-M, scale 1:62,500.

Martin, K., Skaugset, A., and Pyles, M.R., 1996, Forest management of landslide prone sites: the effectiveness of headwall leave areas, part II: COPE Report, v. 9, p. 8-12.

Martin, P., 1971, Movements and activities of the Mountain Beaver (Aplodontia rufa): Journal of Mammalogy, v. 52, p. 717-723.

Martin, Y., and Church, M., 1997, Diffusion in landscape development models: on the nature of basic transport relations: Earth Surface Processes and Landforms, v. 22, p. 273-279.

Matheron, G., 1962, Traité de géostatistique appliquée, tome I, Théorie générale: Paris, Editions Technip, 333 p.

Matheron, G., 1963, Principles of geostatistics: Economic Geology, v. 58, p. 1246-1266.

McCaskill, L.W., 1973, Hold this land: a history of soil conservation in New Zealand: Wellington, A. H. & A. W. Reed, 274 p.

McClellan, M.ïl., Bormann, B.T., and Cromack Jr., K., 1990, Cellulose decomposition in southeast Alaskan forests: effects of pit and mound microrelief and burial depth: Canadian Journal of Forest Research, v. 20, p. 1242-1246.

McKean, J.A., Dietrich, W.E., Finkel, R.C., Southon, J.R., and Caffee, M.W., 1993, Quantification of soil production and downslope creep rates from cosmogenic $^{10}$Be accumulations on a hillslope profile: Geology, v. 21, p. 343-346.

McMinn, R.G., 1974, Characteristics of Douglas-fir root systems: Canadian Journal of Botany, v. 41, p. 105-122.

Moeyersons, J., 1988, The complex nature of creep movements on steeply sloping ground in southern Rwanda: Earth Surface Processes and Landforms, v. 13, p. 511-524.

Monaghan, M.C., McKean, J., Dietrich, W., and Klein, J., 1992, $^{10}$Be chronometry of bedrock-to-soil conversion rates: Earth and Planetary Science Letters, v. 111, p. 483-492.

Montgomery, D.R., 1991, Channel initiation and landscape evolution [Ph.D. thesis], University of Calif., Berkeley, 421 p.

Montgomery, D.R., 1994, Road surface drainage, channel initiation, and slope stability: Water Resources Research, v. 30, p. 1925-1932.

Montgomery, D.R., and Dietrich, W.E., 1994, A physically based model for the topographic control on shallow landsliding: Water Resources Research, v. 30, p. 1153-1171.

Montgomery, D.R., Dietrich, W.E., Torres, R., Anderson, S.P., Heffner, J.T., and Loague, K., 1997, Hydrologic response of a steep, unchanneled valley to natural and applied rainfall: Water Resources Research, v. 33, p. 91-109.

Montgomery, D.R., Schmidt, K.M., Greenberg, H.M., and Dietrich, W.E., submitted, Forest clearing and regional landsliding: Geology.

Montgomery, D.R., Sullivan, K., and Greenberg, H.M., 1998, Regional test of a model for shallow landsliding: Hydrological Processes, v. 12, p. 943-955.

Moore, I.D., Gessler, P.E., Nielsen, G.A., and Peterson, G.A., 1993, Soil attribute prediction using terrain analysis: Soil Science Society of America Journal, v. 57, p. 443-452.

Moore, I.D., Grayson, R.B., and Ladson, A.R., 1991, Digital terrain modelling: a review of hydrological, geomorphological, and biologic applications: Hydrologic Processes, v. 5, p. 5-30.

Musgrave, G.W., 1947, The quantitative evaluation of factors in water erosion: a first approximation: Journal of Soil and Water Conservation, v. 2, p. 133-138.

Neuland, H., 1976, A prediction model of landslips: Catena, v. 3, p. 215-230.

Nikiforoff, C.C., 1942, Fundamental formula of soil formation: American Journal of Science, v. 240, p. 847-66.

O'Loughlin, C., 1974a, A study of tree root strength deterioration following clearfelling: Canadian Journal of Forest Research, v. 4, p. 107-113.

O'Loughlin, C., and Ziemer, R.R., 1982, The importance of root strength and deterioration rates upon edaphic stability in steepland forests, in Waring, R.H., ed., Carbon Uptake and Allocation in Subalpine Ecosystems as a Key to Management: Corvallis, Oregon, Oregon State University, p. 70-78.

O'Loughlin, C.L., 1974b, The effect of timber removal on the stability of forest soils: Journal of Hydrology (N.Z.), v. 13, p. 121-134.

O'Loughlin, E.M., 1986, Prediction of surface saturation zones in natural catchments by topographic analysis: Water Resources Research, v. 22, p. 794-804.

Okimura, T., 1982, Quantitative analysis of the relation between groundwater movement and slope failure: Journal of Natural Disaster Science, v. 4, p. 51-68.

Okimura, T., 1983a, Rapid mass movement and groundwater level movement: Zeitschrift für Geomorphologie, v. 46, p. 35-54.

Okimura, T., 1983b, A slope stability method for predicting rapid mass movements on granite mountain slopes: Natural Disaster Science, v. 5, p. 13-30.

Okimura, T., 1989, Prediction of slope failure using the estimated depth of the potential failure layer: Journal of Natural Disaster Science, v. 11, p. 67-79.

Okimura, T., and Ichikawa, R., 1985, A prediction method for surface failures by movements of infiltrated water in a surface soil layer: Natural Disaster Science, v. 7, p. 41-51.

Okimura, T., and Nakagawa, M., 1988, A method for predicting surface mountain slope failure with digital landform model: Shin Sabo, v. 41, p. 48-56.

Okunishi, K., and Iida, T., 1981, Evolution of hillslopes including landslides: Japanese Geomorphological Union Transactions, v. 7, p. 81-92.

Oliver, M.A., and Webster, R., 1990, Kriging: a method of interpolation for geographical information systems: International Journal of Geographical Information Systems, v. 4, p. 313-332.

Owens, I.F., 1969, Causes and rates of soil creep in the Chilton Valley, Cass, New Zealand: Arctic and Alpine Research, v. 1, p. 213-220.

Pack, R.T., and Tarboton, D.G., 1997, New developments in terrain stability mapping in B.C., 11th Vancouver Geotechnical Society Symposium: Vancouver, B.C., Forestry Geotechnique and Resource Engineer, 12 p.

Paton, T.R., Humphreys, G.S., and Mitchell, P.B., 1995, Soils: A new global view: New Haven and London, Yale University Press, 213 p.

Pavich, M.J., Brown, L., Klein, J., and Middleton, R., 1984, $^{10}$Be accumulation in a soil chronosequence: Earth and Planetary Science Letters, v. 68, p. 198-204.

Personious, S.F., Kelsey, H.M., and Grabau, P.C., 1993, Evidence for regional stream aggradation in the central Oregon Coast Range during the Pleistocene-Holocene transition: Quaternary Research, v. 40, p. 297-308.

Phillips, R.W., 1971, Effects of sediment on the gravel environment and fish production, *in*: Forest Land Use and Stream Environment: Corvallis, Oregon State University, p. 64-74.

Pierson, T.C., 1977, Factors controlling debris-flow initiation on forested hillslopes in the Oregon Coast Ranges [Ph.D. thesis]: Seattle, WA, University of Washington, 166 p.

Pyles, M.R., and Froehlich, H.A., 1987, Rates of landsliding as impacted by timber management activities in northwestern California: Bulletin of the Association of Engineering Geologists, v. 24, p. 425-431.

Reeves, G.H., Benda, L.E., Burnett, K.M., Bisson, P.A., and Sedell, J.R., 1995, A disturbance-based ecosystem approach to maintaining and restoring freshwater habitats of evolutionarily significant units of anadromous salmonids in the Pacific Northwest, *in* Nielsen, J.L., ed., Evolution and the Aquatic Ecosystem: Defining Unique Units in Population Conservation, Volume American Fisheries Society Symposium 17, American Fisheries Society, p. 334-349.

Reid, L.M., 1981, Sediment production from gravel-surfaced forest roads, Clearwater basin, Washington: University of Washington, College of Fisheries, Fisheries Research Institute, FRI-UW-8108, 247 p.

Reid, L.M., and Dunne, T., 1984, Sediment production from forest road surfaces: Water Resources Research, v. 20, p. 1753-1761.

Reid, L.M., Dunne, T., and Cederholm, C.J., 1981, Application of sediment budget studies to the evaluation of logging road impact: Journal of Hydrology (NZ), v. 20, p. 49-62.

Reid, M.E., and Iverson, R.M., 1992, Gravity-driven groundwater flow and slope failure potential 2. Effects of Slope morphology, material properties, and hydraulic heterogeneity: .

Reid, M.E., Nielson, H.P., and Dreiss, S.J., 1988, Hydrologic factors triggering a shallow hillslope failure: Bulletin of the Association of Engineering Geologists, v. 25, p. 349-361.

Reneau, S.L., and Dietrich, W.E., 1987, Size and location of colluvial landslides in a steep forested landscape, in Beschta, R.L., Blinn, T., Grant, G.E., Ice, G.G., and Swanson, F.J., eds., Erosion and Sedimentation in the Pacific Rim, International Association of Hydrological Sciences Publication 165, p. 39-48.

Reneau, S.L., and Dietrich, W.E., 1990, Depositional history of hollows on steep hillslopes, Coastal Oregon and Washington: National Geographic Research, v. 6, p. 220-230.

Reneau, S.L., and Dietrich, W.E., 1991, Erosion rates in the southern Oregon coast range: evidence for an equilibrium between hillslope erosion and sediment yield: Earth Surface Processes and Landforms, v. 16, p. 307-322.

Reneau, S.L., Dietrich, W.E., Donahue, D.J., Jull, A.J.T., and Rubin, M., 1990, Late Quaternary history of colluvial deposition and erosion in hollows, central California Coast Ranges: Geological Society of America Bulletin, v. 102, p. 969-982.

Reneau, S.L., Dietrich, W.E., Dorn, R.I., Berger, C.R., and Rubin, M., 1986, Geomorphic and paleoclimatic implications of latest Pleistocene radiocarbon dates from colluvium-mantled hollows, California: Geology, v. 14, p. 655-658.

Reneau, S.L., Dietrich, W.E., Rubin, M., Donahue, D.J., and Jull, A.T.J., 1989, Analysis of hillslope erosion rates using dated colluvial deposits: Journal of Geology, v. 97, p. 45-63.

Rice, R.M., and Krammes, J.S., 1970, Mass wasting processes in watershed management, Proceedings of the Symposium on Interdisciplinary Aspects of Watershed Management, American Society of Civil Engineers, p. 231-260.

Richter, E., 1968, Druckversuche *in situ* zur Bestimmung von Verformungs- und Festigkeitsparametern des kluftigen Gebirges: Bergakademie, v. 20, p. 721-724.

Riestenberg, M.M., 1987, Anchoring of thin colluvium on hillslopes by roots of sugar maple and white ash [Ph.D. thesis]: Cincinnati, OH, University of Cincinnati, .

Riestenberg, M.M., 1994, Anchoring of thin colluvium by roots of sugar maple and white ash on hillslopes in Cincinnati, U.S. Geological Survey Bulletin 2059-E, 25 p.

Riestenberg, M.M., and Sovonick-Dunford, S., 1983, The role of woody vegetation in stabilizing slopes in the Cincinnati area, Ohio: Geological Society of America Bulletin, v. 15, p. 3-45.

Robison, E.G., Mills, K., and Dent, L., 1997, Oregon Department of Forestry 1996-1997 storms impact monitoring project, preliminary results regarding landslides on managed and unmanaged forestland: EOS, Transactions, American Geophysical Union, v. 78, p. 314.

Robison, E.G., Mills, K., Paul, J., Dent, L., and Skaugset, A., 1999, Oregon Department of Forestry storm impacts and landslides of 1996: final report: Oregon Department of Forestry Technical Report Number 4, 145 p.

Roering, J.J., Kirchner, J.W., and Dietrich, W.E., 1999, Evidence for non-linear, diffusive sediment transport on hillslopes and implications for landscape morphology: Water Resources Research, v. 35, p. 853-870.

Saunders, I., and Young, A., 1983, Rates of surface processes on slopes, slope retreat and denudation: Earth Surface Processes and Landforms, v. 8, p. 473-501.

Schaetzl, R.J., and Follmer, L.R., 1990, Longevity of treethrow microtopography: implications for mass wasting: Geomorphology, v. 3, p. 113-123.

Schaetzl, R.J., Johnson, D.L., Burns, S.F., and Small, T.W., 1989, Tree uprooting: review of terminology, process, and environmental implications: Canadian Journal of Forest Research, v. 19, p. 1-11.

Schietchtl, H.M., 1980, Bioengineering for land reclamation and conservation: Edmonton, Alberta, Canada, University of Alberta Press, 404 p.

Schmidt, K.M., Roering, J.J., Stock, J.D., Schaub, T., Dietrich, W.E., and Montgomery, D.R., 1997, Spatial variability of root strength in forested landscapes and susceptibility to shallow landsliding: EOS (American Geophysical Union Transactions), v. 76, p. 314.

Schmidtke, R.H., and Lajtai, E.Z., 1985, The long-term strength of Lac du Bonnet Granite: International Journal of Rock Mechanics and Mineral Sciences and Geomechanical Abstracts, v. 22, p. 461-465.

Schroeder, W.L., and Alto, J.V., 1983, Soil properties for slope stability analysis; Oregon and Washington Coastal Mountains: Forest Science, v. 29, p. 823-833.

Schumm, S.A., 1964, Seasonal variations of erosion rates on hillslopes in Western Colorado: Zeitschrift für Geomorphologie, v. 5, p. 215-238.

Schumm, S.A., 1967, Rates of surficial rock creep on hillslopes in western Colorado: Science, v. 155, p. 560-561.

Schumm, S.A., 1971, Fluvial geomorphology: channel adjustments and river metamorphosis, *in* Shen, H.W., ed., River Mechanics: Ft. Collins, CO, ???, p. 5.1 - 5.22.

Schumm, S.A., 1973, Geomorphic thresholds and complex response of drainage systems, *in* Morisawa, M.E., ed., Fluvial Geomorphology: Binghampton, NY., State University of New York, p. 299-310.

Seeley, M.W., and West, D.O., 1990, Approach to geologic hazard zoning for regional planning, Inyo National Forest, California and Nevada: Bulletin of the Association of Engineering Geologists, v. 27, p. 23-35.

Seidl, M.A., and Dietrich, W.E., 1992, The problem of channel erosion into bedrock, *in* Schmidt, K.H., and de Ploey, J., eds., Functional Geomorphology, Catena Supplement 23: Cremlingen-Destedt, Germany, Catena-Verlag, p. 101-124.

Selby, M.J., 1974, Rates of creep in pumaceous soils and deposits, central North Island, New Zealand: New Zealand Journal of Science, v. 17, p. 47-48.

Selby, M.J., 1976, Slope erosion due to extreme rainfall: A case study from New Zealand: Geografiska Annaler, v. 58A, p. 131-138.

Selby, M.J., 1993, Hillslope materials and processes: Oxford, Oxford University Press, 451 p.

Sharpe, C.F.S., 1938, Landslides and related phenomena: a study of mass movements of soil and rock: New York, Columbia University Press, 136 p.

Shewbridge, S.E., and Sitar, N., 1989, Deformation characteristics of reinforced sand in direct shear: Journal of Geotechnical Engineering, American Society of Civil Engineers, v. 115, p. 1134-1147.

Shewbridge, S.E., and Sitar, N., 1990, Deformation-based model for reinforced sand: Journal of Geotechnical Engineering, American Society of Civil Engineers, v. 116, p. 1153-1170.

Shimokawa, E., 1984, A natural recovery process of vegetation on landslide scars and landslide periodicity in forested drainage basins, *in* O'Loughlin, C.L., and Pearce, A.J., eds., Effects of Forest Land Use on Erosion and Slope Stability: Honolulu, HI, East-West Environmental Policy Institute, p. 99-107.

Sidle, R.C., 1991, A conceptual model of changes in root cohesion in response to vegetation management: Journal of Environmental Quality, v. 20, p. 43-52.

Sidle, R.C., 1992, A theoretical model of the effects of timber harvesting on slope stability: Water Resources Research, v. 28, p. 1897-1910.

Sidle, R.C., Pearce, A.J., and O'Loughlin, C.L., 1985, Hillslope stability and land use: Washington, D.C., American Geophysical Union Water Resources Monograph Series 11, 140 p.

Sidle, R.C., and Swanston, D.N., 1982, Analysis of a small debris slide in coastal Alaska: Canadian Geotechnical Journal, v. 19, p. 167-174.

Skaugset, A., Froehlich, H., and Lautz, K., 1993, The effectiveness of headwall leave areas: COPE Report, v. 6, p. 3-6.

Smith, J.H., 1964, Root spread can be estimated from crown width of Douglas fir, Lodgepole pine, and other British Columbia tree species: Forestry Chronicle, v. 40, p. 456-473.

Smith, T.R., and Bretherton, F.P., 1972, Stability and the conservation of mass in drainage basin evolution: Water Resources Research, v. 8, p. 1506-1529.

Snavely, P.D., Wagner, H.C., and MacLeod, N.S., 1964, Rhythmic-bedded eugeosynclinal deposits of the Tyee Formation, Oregon Coast Range: Kansas Geological Survey Bulletin, v. 169, p. 462-480.

Stearns, F.W., 1949, Ninety years change in a northern hardwood forest in Wisconsin: Ecology, v. 30, p. 350-358.

Stock, J.D., and Montgomery, D.R., 1999, Geologic constraints on bedrock river incision using the stream power law: Journal of Geophysical Research, v. 104, p. 4983-4993.

Stokes, A., and Mattheck, C., 1996, Variation of wood strength in tree roots: Journal of Experimental Botany, v. 47, p. 693-699.

Stolzy, L.H., and Barley, K.P., 1968, Mechanical resistance encountered by roots entering compact soils: Soil Science, v. 105, p. 297-301.

Stout, B.B., 1956, Studies of the root systems of deciduous trees: Harvard University, Cambridge, MA, Black Rock Forest Bulletin No. 15.

Swanson, F.J., and Dyrnesss, C.T., 1975, Impact of clearcutting and road construction on soil erosion by landsliding in the western Cascade Range, Oregon: Geology, v. 3, p. 393-396.

Swanson, F.J., Fredriksen, R.L., and McCorison, F.M., 1982, Material transfer in a western Oregon forested watershed: US/IBP Synthesis Series, v. 14, p. 233-266.

Swanson, F.J., and Lienkaemper, 1978, Physical consequences of large organic debris in Pacific Northwest streams: USDA Forest Service General Technical Report PNW-69, Pacific Northwest Forest and Range Experimental Station, 12 p.

Swanson, F.J., Swanson, M.M., and Woods, C., 1977, Inventory of mass erosion in the Mapleton Ranger District: Suislaw National Forest, Forest Science Laboratory, Corvallis, Oregon, 62 p.

Swanson, F.J., Swanson, M.M., and Woods, C., 1981, Analysis of debris-avalanche erosion in steep forest lands: An example from Mapleton, Oregon, USA, *in* Davies, T.R.H., and Pearce, A.J., eds., Erosion and Sediment Transport in Pacific Rim Steeplands, International Association of Hydrological Sciences Publication 132, p. 67-75.

Swanston, D.N., 1967, Soil-water piezometry in a southeast Alaska landslide area: U. S. Department of Agriculture, Forest Service Research Note PNW-68, 17 p.

Swanston, D.N., 1969, Mass-wasting in coastal Alaska: U. S. Department of Agriculture, Forest Service Research Paper PNW-83, 15 p.

Swanston, D.N., 1970, Mechanics of debris avalanching in shallow till soils of southeast Alaska: Pacific Northwest Forest and Range Experiment Station, U.S. Department of Agriculture, USDA Forest Service Research Paper PNW-103, 17 p.

Swanston, D.N., and Swanson, F.J., 1976, Timber harvesting, mass erosion, and steepland forest geomorphology in the Pacific Northwest, *in* Coates, D.R., ed., Geomorphology and Engineering: New York, Van Nostrand Reinhold, p. 199-221.

Takahashi, K., 1968, Studies of the forest facilities to prevent landslides: Bulletin of the Faculty of Agriculture, Shizuoka University, v. 18, p. 85-101.

Terwilliger, V.J., and Waldron, L.J., 1991, Effects of root reinforcement on soil-slip patterns in the Transverse Ranges of southern California: Geological Society of America Bulletin, v. 103, p. 775-785.

Terzaghi, K., 1936, The shearing resistance of saturated soils, Proceedings, First International Conference on Soil Mechanics, v. 1, p. 54-60.

Thorn, C.E., 1978, A preliminary assessment of the geomorphic role of pocket gophers in the alpine zone of the Colorado Front Range: Geografiska Annaler, v. 60A, p. 181-187.

Torres, R., Dietrich, W.E., Montgomery, D.R., Anderson, S.P., and Loague, K., 1998, Unsaturated zone processes and the hydrologic response of a steep, unchanneled catchment: Water Resources Research, v. 34, p. 1865-1879.

Trustrum, N.A., and De Rose, R.C., 1988, Soil depth-age relationship of landslides on deforested hillslopes, Taranaki, New Zealand: Geomorphology, v. 1, p. 143-160.

Tsukamoto, Y., Ohta, T., and Noguchi, H., 1982, Hydrological and geomorphological studies of debris flows on forested hillslopes in Japan, in Walling, D.E., ed., Recent developments in the explanation and prediction of erosion and sediment yield, International Association of Hydrological Sciences Publication 137, p. 89-98.

Van Asch, T.W.J., Deimel, M.S., Haak, W.J.C., and Simon, J., 1989, The viscous creep component in shallow clayey soil and the influence of tree load on creep rates: Earth Surface Processes and Landforms, v. 14, p. 557-564.

Varnes, D.J., 1978, Slope movement types and processes, in Schuster, R.L., and Krizek, R.J., eds., Landslide analysis and control: Washington, D.C., National Research Council, Transportation Research Board, Special Report 176, p. 11-33.

Vauclin, M., Vieira, S.R., Vachaud, G., and Nielsen, D.R., 1983, The use of cokriging with limited field soil observations: Soil Science Society of America Journal, v. 47, p. 175-184.

Waldron, L.J., 1977, The shear resistance of root-permeated homogenous and stratified soil: Soil Science Society of America Journal, v. 41, p. 843-849.

Waldron, L.J., and Dakessian, S., 1981, Soil reinforcement by roots: calculation of increased soil shear resistance from root properties: Soil Science, v. 132, p. 427-435.

Waldron, L.J., and Dakessian, S., 1982, Effect of grass, legume, and tree roots and soil shearing resistance: Soil Science Society of America Journal, v. 46, p. 894-899.

Waldron, L.J., Dakessian, S., and Nemson, J.A., 1983, Shear resistance enhancement of 1.22-meter diameter soil cross sections by pine and alfalfa roots: Soil Science of America Journal, v. 47, p. 9-14.

Willgoose, G., Bras, R.L., and Rodriguez-Iturbe, I., 1991, A coupled channel network growth and hillslope evolution model: I. Theory: Water Resources Research, v. 27, p. 1671-1684.

Wu, T.H., 1976, Investigation of landslides on Prince of Wales Island, Alaska: Department of Civil Engineering, Ohio State University, Geotechnical Engineering Report No. 5, 94 p.

Wu, T.H., 1984a, Effect of vegetation on slope stability, Soil Reinforcement and Moisture Effects on Slope Stability, Volume Transportation Research Record 965: Washington, D.C., Transportation Research Board, p. 37-46.

Wu, T.H., 1984b, Soil movements on permafrost slopes near Fairbanks, Alaska: Canadian Geotechnical Journal, v. 21, p. 699-709.

Wu, T.H., 1995, Slope stabilization, in Morgan, R.P.C., and Rickson, R.J., eds., Slope Stabilization and Erosion Control: a Bioengineering Approach: London, E. & F.N. Spon, p. 221-264.

Wu, T.H., Beal, P.E., and Lan, C., 1988a, In-situ shear test of soil-root systems: Journal of Geotechnical Engineering, v. 114, p. 1376-1394.

Wu, T.H., McKinnell III, W.P., and Swanston, D.N., 1979, Strength of tree roots and landslides on Prince of Wales Island, Alaska: Canadian Geotechnical Journal, v. 16, p. 19-33.

Wu, T.H., McOmber, R.M., Erb, R.T., and Beal, P.E., 1988b, Study of soil-root interaction: Journal of Geotechnical Engineering, v. 114, p. 1351-1375.

Wu, W., and Sidle, R.C., 1995, A distributed slope stability model for steep forested basins: Water Resources Research, v. 31, p. 2097-2110.

Yamada, S., 1997, Seasonal variation in soil creep on a forested hillslope near Sapporo, Hokkaido, Northern Japan: Transactions, Japanese Geomorphological Union, v. 18, p. 117-130.

Yee, C.S., and Harr, D.R., 1977, Influence of soil aggregation on slope stability in the Oregon Coast Range: Environmental Geology, v. 1, p. 367-377.

Young, A., 1960, Soil movements by denudational processes: Nature, v. 188, p. 120-122.

Young, A., 1963, Deductive models of slope evolution: Nachrichten der Akademie der Wissenshaften in Göttingen, v. II, p. 45-66.

Young, A., 1972, Slopes: Edinburgh, Oliver and Boyd, 288 p.

Young, A., 1978, A twelve-year record of soil movement on a slope: Zeitschrift für Geomorphologie, Suppplementband, v. 29, p. 104-110.

Záruba, R., and Mencl, V., 1982, Landslides and their Control: Amsterdam, Elsevier Scientific, 324 p.

Zaslavsky, D., and Sinai, G., 1981, Surface hydrology: I- explanation of phenomena: Journal of the Hydraulics Division, Proceedings of the American Society of Civil Engineers, v. 107, p. 1-16.

Zavitkovski, J., and Stevens, R.D., 1972, Primary productivity of red alder ecosystems: Ecology, v. 53, p. 235-242.

Zevenbergen, L.W., and Thorne, C.R., 1987, Quantitative analysis of land surface topography: Earth Surface Processes and Landforms, v. 12, p. 47-56.

Zhang, W., and Montgomery, D.R., 1994, Digital elevation model grid size, landscape representation, and hydrologic simulations: Water Resources Research, v. 300, p. 1019-1028.

Ziemer, R.R., 1981, Roots and the stability of forested slopes, *in* Davies, T.R.H., and Pearce, A.J., eds., Erosion and Sediment Transport in Pacific Rim Steeplands, International Association of Hydrological Sciences Publication 132, p. 343-361.

Ziemer, R.R., and Swanston, D.N., 1977, Root strength changes after logging in southeast Alaska: Forest Service, U.S. Department of Agriculture, Research Note PNW-306, 10 p.

Zingg, A.W., 1940, Degree and length of land slope and it affects soil loss in runoff: Agricultural Engineering, v. 21, p. 59-64.

## Curriculum Vitae
# Kevin Michael Schmidt

*born: July 9, 1966   San Diego, CA.*

## Education

Ph.D., University of Washington, Seattle          August 20, 1999
*Root Strength, Colluvial Soil Depth, and Colluvial Transport on Landslide-Prone Hillslopes*

M.S., University of Washington, Seattle, 1994
*Mountain scale strength properties, deep-seated landsliding, and relief limits*

B.A., University of California, Berkeley, 1989, with highest honors in geology
*The effects of fire on erosion with a case study of the "49'er Fire" of Grass Valley, California.*

## Positions Held

Research Assistant and Teaching Assistant, Dept. of Geological Sciences, Univ. of Washington, 1991 - 1999 (Advisors: Dr. D. R. Montgomery and Dr. T. Dunne)

Geologist, U.S. Geological Survey, FY 1998 - 99 (Investigating Quaternary faulting in Pahrump Valley, Nevada & California.

Geologist, U.S. Geological Survey, Branch of Geologic Risk Assessment, Menlo Park, CA. August 1989 - September 1991 (Hillslope hydrology research including instrument design and construction, establishment and maintenance of five field sites, interpretation of hydrologic data. Loma Prieta earthquake research including field mapping, landslide monitoring, and interpretation of coseismic damage patterns; Supervisor: Dr. S.D. Ellen)

Geologist/N.A.G.T Appointment, U.S. Geological Survey, Branch of Sedimentary Processes, Lakewood, CO. June - August 1989 (Examination of radon emissions in the Colorado Rockies and northern Great Plains; Supervisor: Dr. R.R. Schumann)

## Scholarship Awards                                                      Univ.
of Wash., Dept. of Geological Sciences, Howard A. Coombs Fellowship, 1997
AGU Outstanding Student Paper Award, Tectonophysics Section, Fall 1996 Meeting
Univ. of Wash., Dept. of Geological Sciences, Graduate Research Fund, 1996
Univ. of Wash., Dept. of Geological Sciences, David Johnston Award, 1996
Univ. of California, Berkeley, George D. Louderbach Award, 1989
Univ. of California, Berkeley, Departmental Citation, 1989
Golden Key National Honor Society, elected 1989
Phi Beta Kappa, elected 1989
California Federation of Mineralogical Societies, Mineralogical Award, 1988

## Special Training

Washington Forest Practices Methodology for Conducting Watershed Analysis, 1995

## Invited Talks

National Science Teachers Association Global Summit on Science and Science Education, 1996

## Select Publications

Schmidt, K.M., Ellen, S.D., Haugerud, R.A., and Peterson, D.M., 1995, Breaks in pavement and pipes as indicators of range-front faulting resulting from the 1989 Loma Prieta earthquake near the southwest margin of the Santa Clara Valley, California, U.S. Geological Survey Open-File Report 95-820, 33 p.

Schmidt, K.M., and Montgomery, D.R., 1995, Limits to relief, Science, v. 270, p. 617-620.

Schmidt, K.M., and Montgomery, D.R., 1996, Rock mass strength assessment for bedrock landsliding, Environmental & Engineering Geoscience, v. II, Fall 1996, p. 325-338.

Langenheim, V.E., and Schmidt, K.M., 1996, Thickness and storage capacity of basin fill of the northern part of the Eldorado Valley, Nevada, and the extent of the Boulder City pluton, U.S. Geological Survey Open-File Report 96-512, 27 p.

Langenheim, V.E., Schmidt, K.M., and Jachens, R.C., 1997, Coseismic deformation during the 1989 Loma Prieta earthquake and range-front thrusting along the southwest margin of the Santa Clara Valley, California, Geology, v. 25 p. 1091-94.

Langenheim, V.E., Jachens, R.C., and Schmidt, K.M., 1997, Preliminary location and geometry of the Las Vegas Valley shear zone based on gravity and aeromagnetic data, U.S. Geological Survey Open-File Report 97-441, 25 p.

McLaughlin, R. J., Langenheim, V. E., Schmidt, K. M., Jachens, R. C., Stanley, R. G., Jayko, A. S., McDougall, K. A., Tinsley, J. C., and Valin, Z. C., 1999, Neogene contraction between the San Andreas fault and Santa Clara Valley, San Francisco Bay Region, California, International Geology Review, v. 41, p. 1-30.

Montgomery, D.R., Buffington, J.M., Smith, R.D., Schmidt, K.M., and Pess, George, 1995, Pool Frequency in Forest Channels, Water Resources Research, v. 31, p. 1097-1105.

Blakely, R. J., Morin, R. L., McKee, E. H., Schmidt, K.M., Langenheim, V. E., Dixon, G., 1998, Three-dimensional model of Paleozoic basement beneath Amargosa Desert and Pahrump Valley, California and Nevada: Implications for tectonic evolution and water-resources, U. S. Geological Survey Open-File Report 98-496, 29 p.

Montgomery, D.R., Abbe, T.B., Buffington, J.M, Peterson, N.P., Schmidt, K.M., and Stock, J.D., 1996, Distribution of bedrock and alluvial channels in forested mountain drainage basins, Nature, v. 381, p. 587-589.

Aalto, R., Montgomery, D.R., Hallet, B., Abbe, T.B., Buffington, J.M., Cuffey, K.M., and Schmidt, K.M., 1997, A hill of beans, Science, v. 277, no. 5334, p. 1911-12.